2017

Vapor grown Perovskite solar cells

Hisham Abdussamad Abbas
Iowa State University

Recommended Citation

Abdussamad Abbas, Hisham, "Vapor grown Perovskite solar cells" (2017). *Graduate Theses and Dissertations*. 15239.
https://lib.dr.iastate.edu/etd/15239

Vapor grown Perovskite solar cells

by

Hisham Abdussamad Abbas

A dissertation submitted to the graduate faculty

in partial fulfillment of the requirements for the degree of

DOCTOR OF PHILOSOPHY

Major: Electrical Engineering

Program of Study Committee:
Vikram L. Dalal, Major Professor
Kristen P. Constant
Joseph Shinar
Rana Biswas
Mani Mina

The student author and the program of study committee are solely responsible for the content of this dissertation. The Graduate College will ensure this dissertation is globally accessible and will not permit alterations after a degree is conferred.

Iowa State University

Ames, Iowa

2017

DEDICATION

To my Beautiful family

TABLE OF CONTENTS

CHAPTER 3 PROCESS DEVELOPMENT AND SYSTEM BUILDING 55

CHAPTER 4 METHYL AMMONIUM IODIDE PEROVSKITES 84

LIST OF FIGURES

NOMENCLATURE

TW	Terra Watt
PV	Photovoltaic
U.S. A	United States of America
C-Si	Crystalline Silicon
CdTe	Cadmium Telluride
MA	Methyl Ammonium
MAI	Methyl Ammonium Iodide
FA	Formamidinium
FAI	Formamidinium Iodide
Pb	Lead
I	Iodine
Cl	Chlorine
Br	Bromine
SRH	Shokley-Read-Hall
SBJ	Small Bell jar

ACKNOWLEDGMENTS

First and foremost, I am thankful to my advisor Professor. Vikram Dalal for providing me the opportunity of being his student and in preparing me for the real world. He has been always been generous, trust worthy, encouraging, inspirational and supportive during this eventful journey. I extend my thanks to my committee members Prof. Kristen P. Constant, Prof. Joseph Shinar, Prof. Rana Biswas and Prof. Mani Mina for their support.

Special thanks to Max Noack for being a great mentor. Also, like to thank Dr. Ranjith Kottokkaran for his contribution to my work. I am thankful to Dr. Balaji Ganapathy, Dr. Wei Leung, Dr. Mehran Samiee, Dr. Pranav Joshi, Dr. Siva Konduri, Istiaque Hossain, Satvik Shah, Liang Zhang, Behrang Bagheri, Andrew Kitahara, Dr. Mahendra Dhaka, Sabrina Stark and Nishtha Bhatnagar for their help and support.

Finally, and most importantly, I am extremely thankful to my mom Saira, brother Nihal, sister Misbah, Uncle Nizar & Haneef, Aunt Sameera, Anand, Beena and rest of my family members and friends for always being there for me through thick and thin. They are my true strength.

ABSTRACT

Perovskite solar cells has been the fastest growing solar cell material till date with verified efficiencies of over 22%. Most groups in the world focuses their research on solution based devices that has residual solvent in the material bulk. This work focuses extensively on the fabrication and properties of vapor based perovskite devices that is devoid of solvents.

The initial part of my work focuses on the detailed fabrication of high efficiency consistent sequential vapor NIP devices made using P3HT as P-type Type II heterojunction. The sequential vapor devices experiences device anomalies like voltage evolution and IV hysteresis owing to charge trapping in TiO_2. Hence, sequential PIN devices were fabricated using doped Type-II heterojunctions that had no device anomalies.

The sequential PIN devices has processing restriction, as organic Type-II heterojunction materials cannot withstand high processing temperature, hence limiting device efficiency. Thereby bringing the need of co-evaporation for fabricating high efficiency consistent PIN devices, the approach has no-restriction on substrates and offers stoichiometric control. A comprehensive description of the fabrication, Co-evaporator setup and how to build it is described. The results of Co-evaporated devices clearly show that grain size, stoichiometry and doped transport layers are all critical for eliminating device anomalies and in fabricating high efficiency devices.

Finally, Formamidinium based perovskite were fabricated using sequential approach. A thermal degradation study was conducted on Methyl Ammonium Vs. Formamidinium based perovskite films, Formamidinium based perovskites were found to be more stable. Lastly, inorganic films such as CdS and NiO_x were developed in this work.

CHAPTER I

NEED FOR ENERGY AND PHOTOVOLTAICS

1.1. Energy

Energy is essential for a functioning society and its resources are critical for human survival. The scale of energy use is correlated with the class of life, capabilities of a land and development of nations into technological advanced society. Differences in opulence, well-being and political supremacy are thus evident between nations based on its energy usage. United States of America and China together consume about 42% of the world's energy in 2015. However, United States of America which accounts for only 4% of the World population consumes about 18% of the world's energy production. Fig 1.1 shows annual growth in energy consumption.

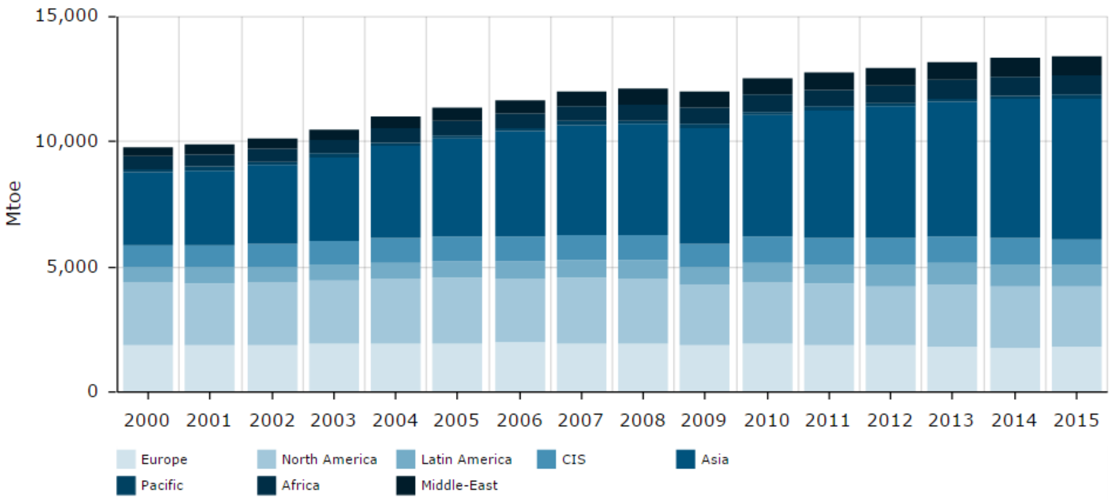

Fig 1.1: World energy consumption by year[1]

Developing and developed nations alike would continue to consume and demand for more energy, it's unfair and impossible to curb the energy needs of growing nations. Hence there arises a need for producing energy without damaging environment and causing social instability. The solution to the dilemma is producing sustainable energy resources.

1.1.1. Sustainable energy

Energy consumption and creation is entwined with use of valuable natural resources like minerals, forests, water, food and land. Furthermore, energy use can hurt earth's environment and human well-being over extensive length and time scale. Developing nations like India and China are drastically increasing their energy consumption for growing their economic and non-renewable energy sources are available to them at affordable prices causing a concern as there would an increase in the emission of fossil derived CO_2 and CH_4 into the atmosphere.

Sustainability responsiveness meets a phalanx of global forces such as prevalent human impact, economic health, environmental degradation and geopolitical fairness. Sustainable energy is a living harmony between the equitable availability of energy services to all people and the preservation of earth for future generation. For energy to be considered Sustainable it needs to satisfy two key conditions: replenish (short time) and no carbon footprints. Five energy sources meet the requirement for Renewable energy sources they are the follows: Solar, Geothermal, Wind, Hydropower and Biomass. Fig 1.2 shows the main renewable energy sources.

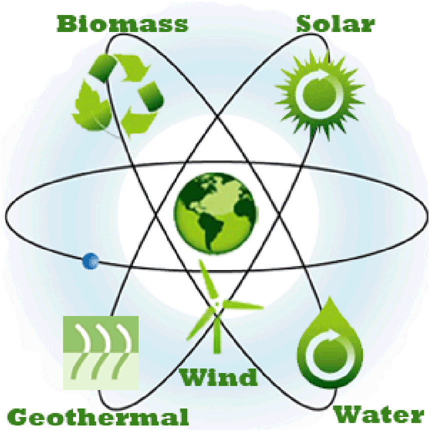

Fig 1.2: Renewable Energy Sources [2]

There was an argument in regards to nuclear energy being considered renewable as it does not produce carbon footprints, however uranium the fuel for nuclear energy cannot be refilled. The worlds existing cost effective uranium would last for ~1000 years if the world uses only nuclear energy and until an efficient way comes to extract the existing uranium or finding newer sources nuclear energy is not renewable. Also, the capita for nuclear plant setup is substantially higher in comparison to any renewable energy sources.

When all the five energy sources are examined, one would realize that they all draw their energy from sun except for Geothermal which draws energy from earth's magma (some of its energy is from sun too). In using other renewable energy sources like wind, hydropower and bio-mass we are indirectly using solar energy, so why cannot we directly harvest solar energy? The solar power that generated on earths land mass is about 120000 TW-yr per year while earths energy consumption is only about 16 TW-yr per year, which comprises of only 0.013% of the solar produced energy. If we lay 20% efficient Solar cell panels across Sahara desert (>9,000,000+ km^2), we can produce about 630 Tera Watt of energy, which is approx. 46 times the earths energy requirement [3] and these are pretty conservative numbers.

Fig 1.3 shows recoverable finite and renewable energy sources, it can be clearly seen that solar energy reserves is greater than all others energy sources put together by orders of magnitude. Hence, it's just common sense to tap a very small portion of the over abundant and predictable solar power for meeting the future energy requirements. Obviously, there are challenges that need to be systematically overcome for efficiently tapping, storing and utilizing solar power, however if done properly the pros will far outweigh the cons.

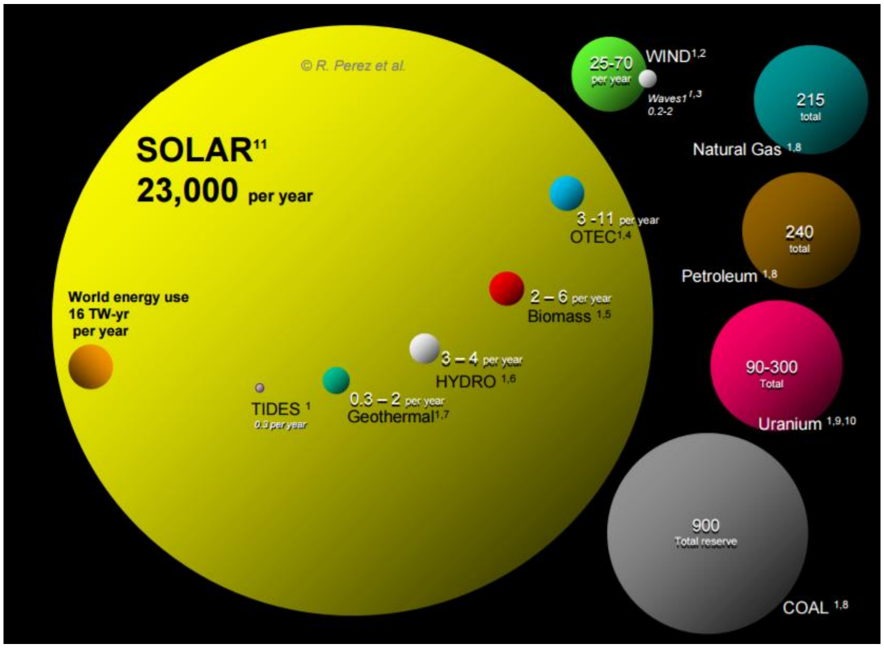

Fig 1.3: Comparing finite and renewable planetary energy reserves (Tera watt years). [4]

1.1.2. Comparison of sustainable energy sources in USA

Fig 1.4 shows the renewable energy capacity by source and it is noticeable that the sustainable energy production has been steadily increasing over the last decade.

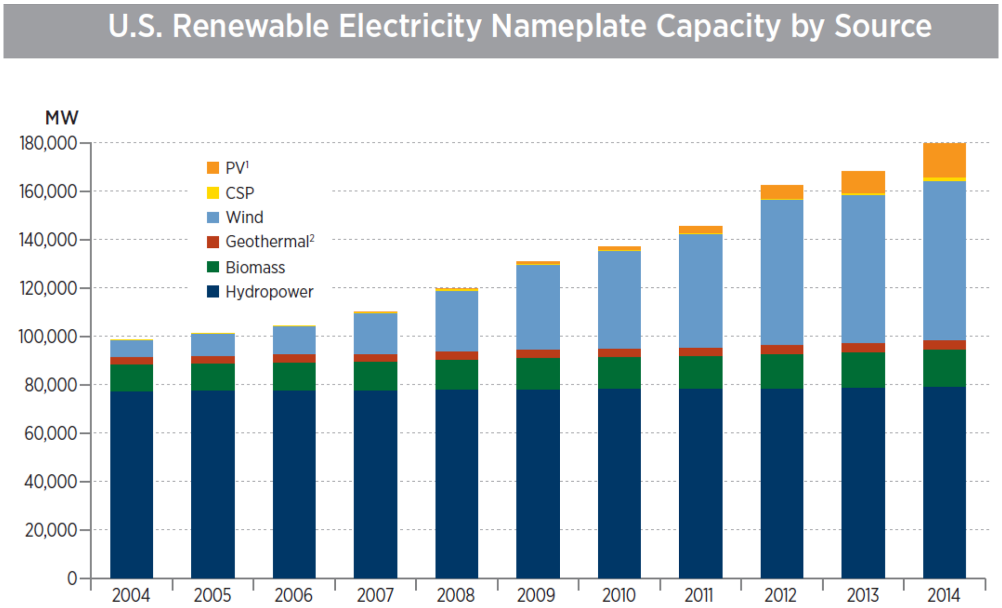

Fig 1.4: U.S. Renewable electricity nameplate capacity by source [5]

The increase in renewable energy can be attributed to the growing energy needs, the advancement in technology, growing population and global warming concerns. However, when the different renewable energy sources are compared, one can perceive that the growth of solar energy has been the greatest. Figure 1.5 shows the growth of renewable energy sources by year over the last decade.

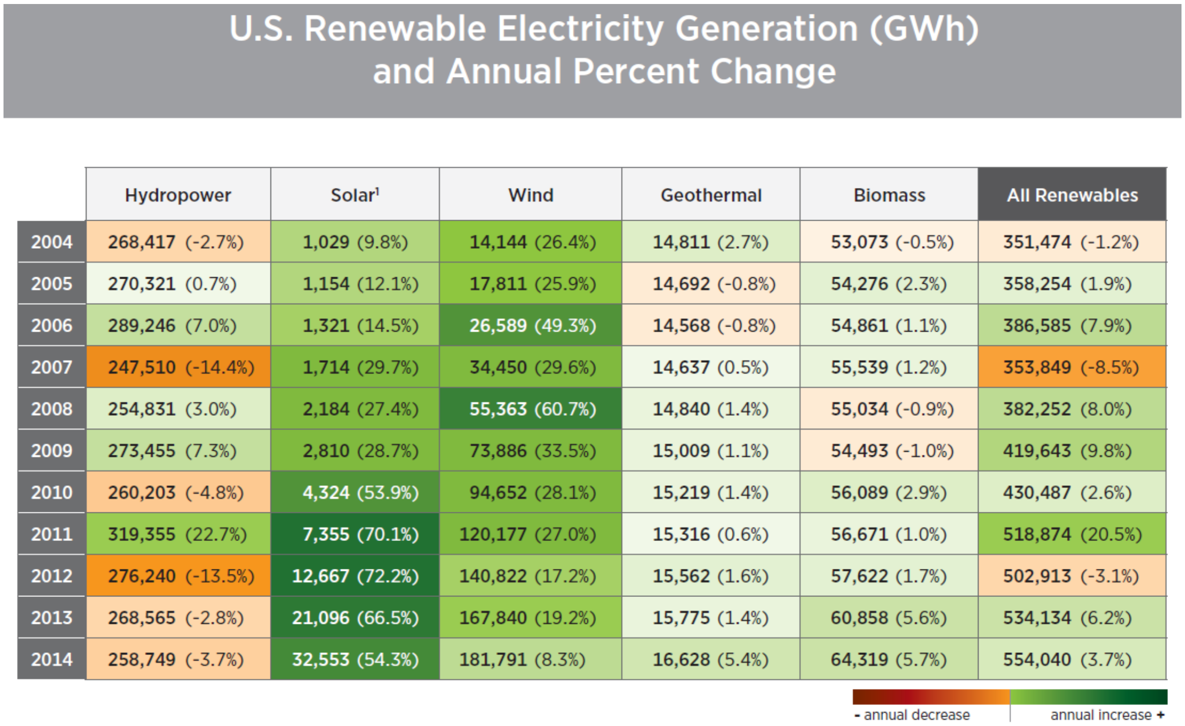

U.S. Renewable Electricity Generation (GWh)
and Annual Percent Change

	Hydropower	Solar[1]	Wind	Geothermal	Biomass	All Renewables
2004	268,417 (-2.7%)	1,029 (9.8%)	14,144 (26.4%)	14,811 (2.7%)	53,073 (-0.5%)	351,474 (-1.2%)
2005	270,321 (0.7%)	1,154 (12.1%)	17,811 (25.9%)	14,692 (-0.8%)	54,276 (2.3%)	358,254 (1.9%)
2006	289,246 (7.0%)	1,321 (14.5%)	26,589 (49.3%)	14,568 (-0.8%)	54,861 (1.1%)	386,585 (7.9%)
2007	247,510 (-14.4%)	1,714 (29.7%)	34,450 (29.6%)	14,637 (0.5%)	55,539 (1.2%)	353,849 (-8.5%)
2008	254,831 (3.0%)	2,184 (27.4%)	55,363 (60.7%)	14,840 (1.4%)	55,034 (-0.9%)	382,252 (8.0%)
2009	273,455 (7.3%)	2,810 (28.7%)	73,886 (33.5%)	15,009 (1.1%)	54,493 (-1.0%)	419,643 (9.8%)
2010	260,203 (-4.8%)	4,324 (53.9%)	94,652 (28.1%)	15,219 (1.4%)	56,089 (2.9%)	430,487 (2.6%)
2011	319,355 (22.7%)	7,355 (70.1%)	120,177 (27.0%)	15,316 (0.6%)	56,671 (1.0%)	518,874 (20.5%)
2012	276,240 (-13.5%)	12,667 (72.2%)	140,822 (17.2%)	15,562 (1.6%)	57,622 (1.7%)	502,913 (-3.1%)
2013	268,565 (-2.8%)	21,096 (66.5%)	167,840 (19.2%)	15,775 (1.4%)	60,858 (5.6%)	534,134 (6.2%)
2014	258,749 (-3.7%)	32,553 (54.3%)	181,791 (8.3%)	16,628 (5.4%)	64,319 (5.7%)	554,040 (3.7%)

Figure 1.5: U.S. Renewable Electricity Annual Growth Percentage [5]

1.2. Growth of Silicon Photovoltaic Industry

The growth of Solar can be attributed to drop in price of poly-silicon, rise in efficiency of Solar panels, advancements in manufacturing technology and increasing competition between companies. A close look at the solar output shows that it has been increasing steadily since 2004 in comparison to other renewable energy, there was a small drop in solar output in 2008 owing to the increase in price of poly-Silicon, however polysilicon prices dropped drastically in the following years resulting in increase in solar power production. Fig 1.6 shows the price of Silicon solar cells which started off at $76 per watt (1977) down to $0.30 per watt in 2015, with module price costing as low as $0.57[6] in 2015.

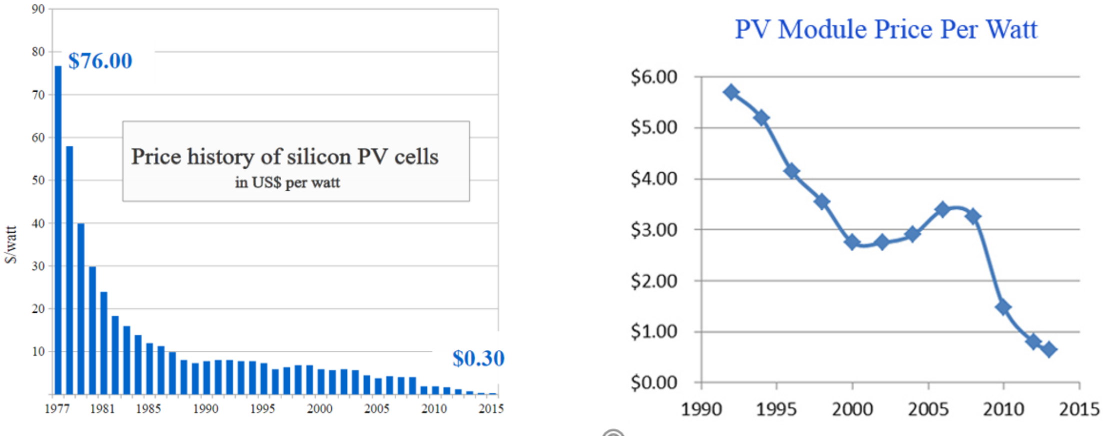

Fig 1.6: Silicon price history [6]

Silicon solar cells dominate 90 percent of the existing global photovoltaic market today [7] yet the record efficiency for silicon has increased merely from 25% to 25.6% over the last 15 years. The photovoltaic industry is thus looking for other alternatives that can use the existing technology of silicon by making Tandem cells on Silicon or even possibly replacing silicon with other inexpensive alternatives, however the latter is less likely considering Silicon market share and dominance.

A detailed breakdown of the price of silicon solar cell as mounted by utility system is shown in Fig 1.7, projections are made that by 2020 price will drop down to 99 cents/Watt. On reviewing the breakdown price of PV system, it’s evident that even in 2020 most of the expense (57 cents) would go towards the PV module, hence there is a need to develop inexpensive photovoltaic material that is easy to fabricate and mass produce which would eventually reduce the cost of PV systems.

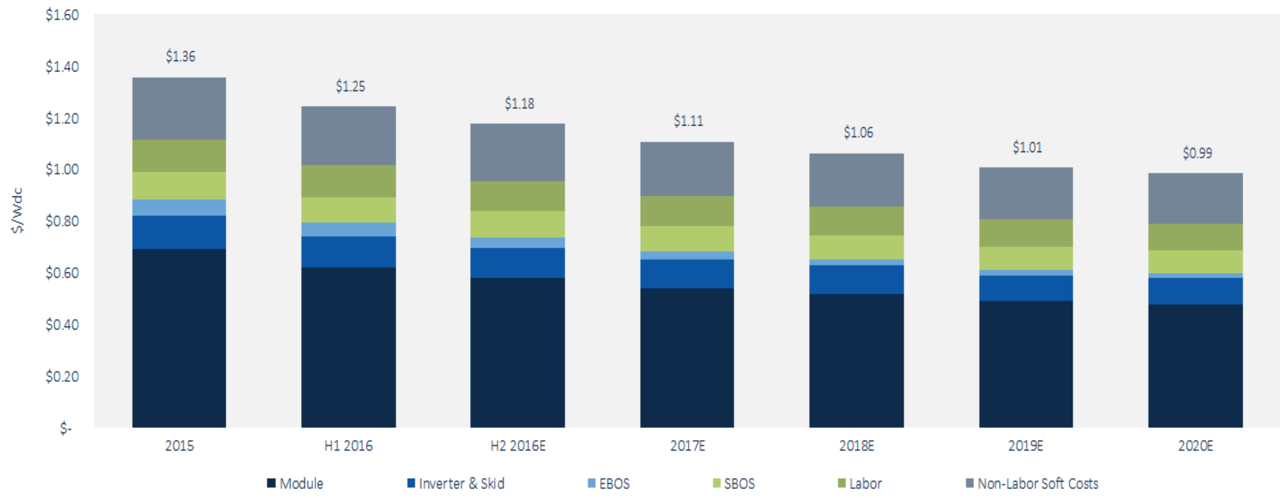

Fig 1.7: Utility Fixed-Tilt PV Systems Pricing by Cost Category [8]

1.2.1. Thin film photovoltaic

An alternative to silicon solar cells is Thin film photovoltaic which uses material like Amorphous Silicon, Organic Photovoltaic, Cadmium Telluride (CdTe) & Copper Indium Gallium Arsenide and depending on the thin film module preferred the efficiency can range from 7%-22.1%. Advantage of thin film solar panels over C-Si are follows: mass production is simple making them potentially cheaper to manufacture, can be made flexible which opens a wide range of applications, higher bandgap material can perform better at places which has warmer temperature and if space is not an issue thin film solar cell might be more logical. First Solar concentrates more on the utility sector than on roof-top installation which is dominated by C-Si modules. They have established some of the largest solar farms like the Topaz and Desert sunlight project each having a capacity of 550 megawatts [9]

Driving ahead in the thin film technology race is CdTe PV systems which has theoretical efficiency of above 30% [10] and is manufactured by First solar, they announced a record efficiency of 22.1% in February 2016 and have a 5.1% worldwide market share [9]. First Solar has suggested that they can match the average efficiency of crystalline silicon and produce modules with efficiency of 19.5% by 2017 [11]. For the last few decades the Open Circuit Voltage (Voc) in CdTe solar cells hasn't exceeded 0.9V, however in February 2016 significant milestone was hit by making processing changes that helped Voc exceed 1V [12]. First Solar the firm believes that 25% efficiency is a realistic likelihood and are working towards it [11]. Fig 1.8 shows the efficiency evolution of various Thin film photovoltaic technologies.

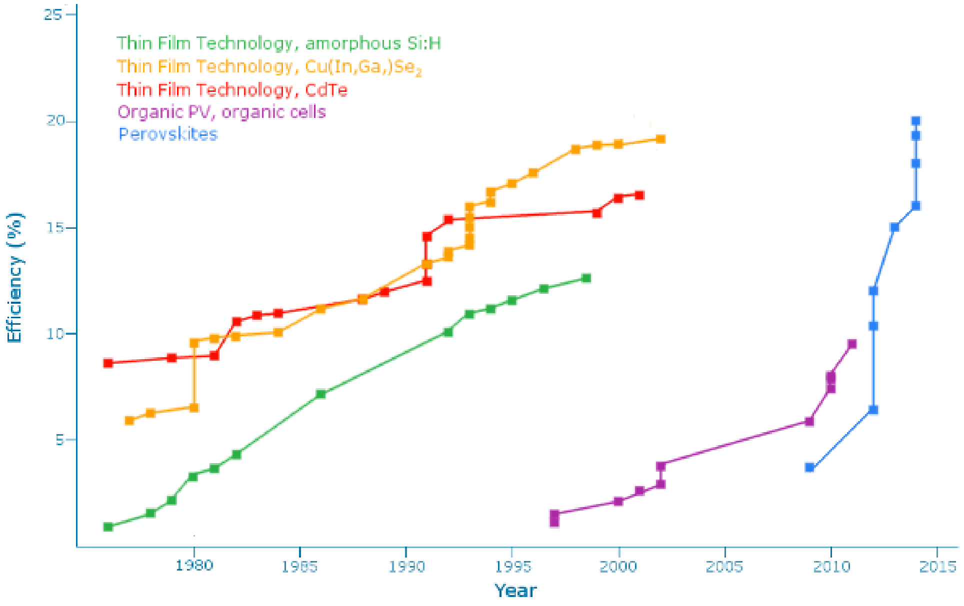

Fig 1.8: Thin film PV efficiency evolution [13]

1.3. Rise of Perovskite

Towards the beginning of 2013, a new breed of PV material called Perovskite caught the attention of everyone in the PV community primarily due to the work done by Michael Gratzel [14] and Henry Snaith[15], both fabricated devices with 15% efficiency catching the attention of everyone working in solar cells. As of today, perovskite solar cells have a verified efficiency of 22.1% [13] making them the fastest growing solar cell material till date. Fig 1.8 shows the efficiency of all PV technologies and it is evident that Perovskite have the fastest growth till date.

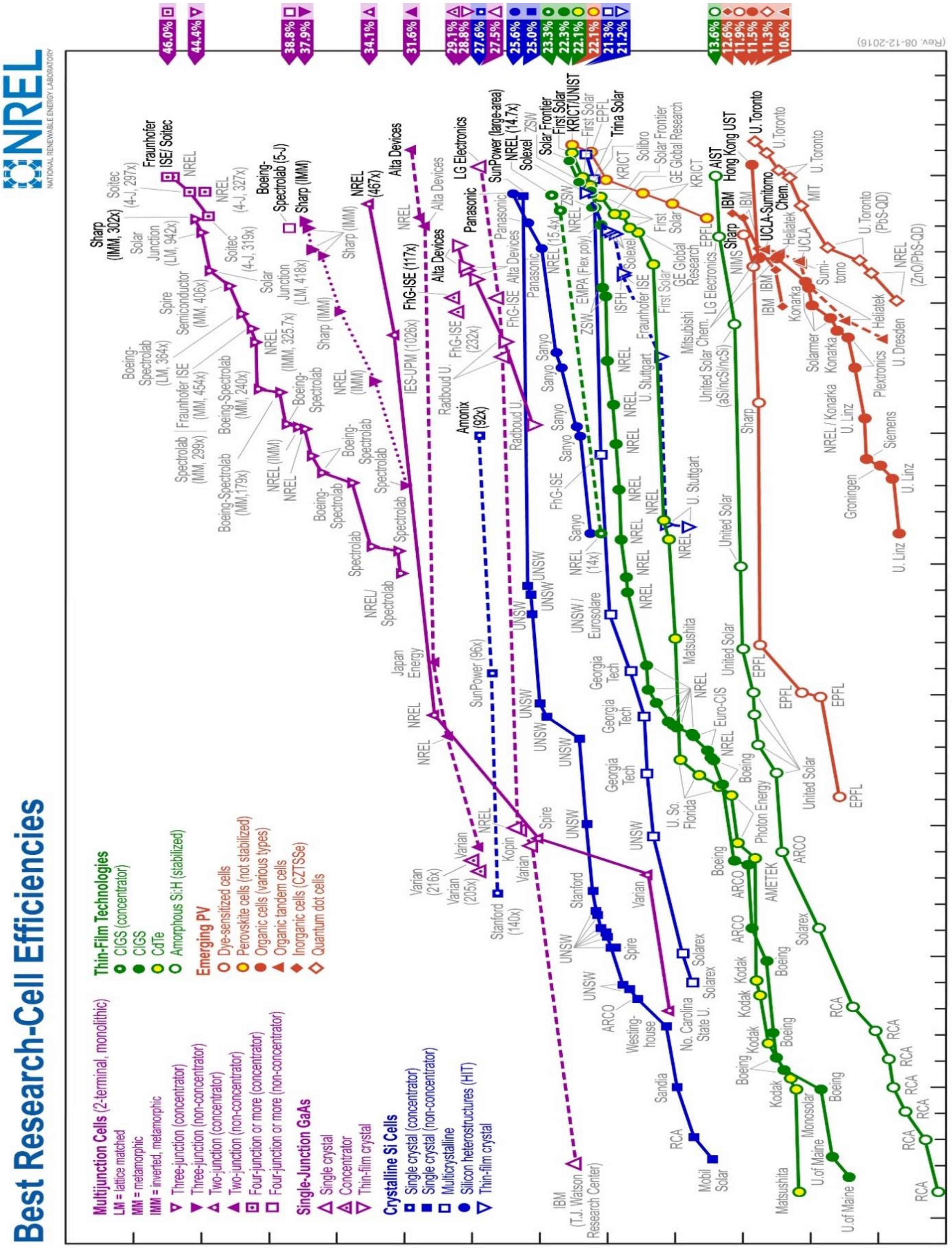

Fig 1.9: NREL efficiency chart [13]

1.3.1. Perovskite crystal structure

Any material with the crystal structure of $CaTiO_3$ commonly known as Perovskite structure [16] is identified as Perovskite and is named after Russian mineralogist Lev Perovski [1792-1856] The mineral Calcium Titanate was first discovered in the Ural Mountains of Russia by Gustav Rose in 1839 and oxides with chemical formula ABO_3 adopt this structure. Fig 1.9 shows the crystal structure of Perovskite material.

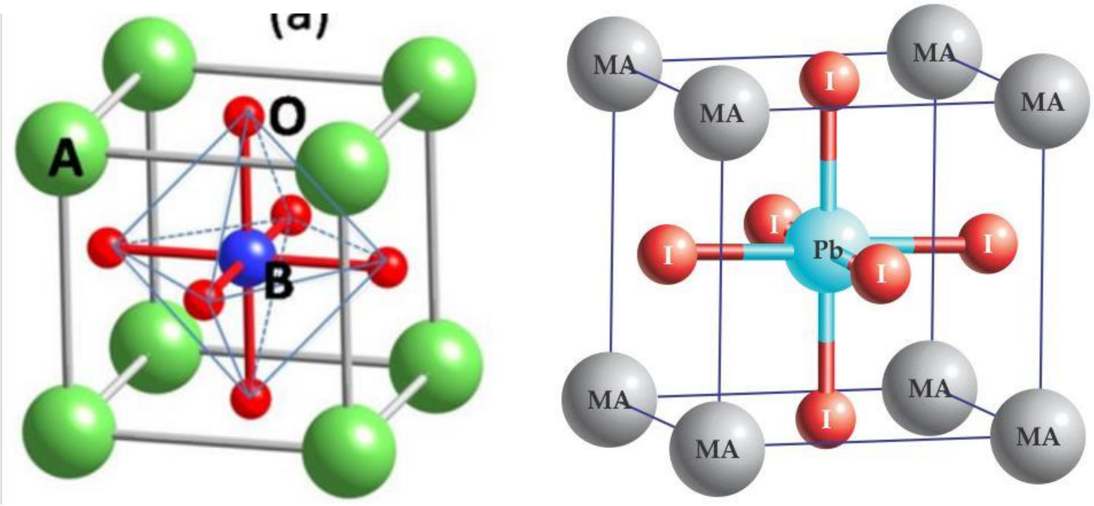

Fig 1.10: Crystal structure Oxide perovskite (right) and PV (right) Perovskite [17, 18]

The general chemical formula of perovskite is ABX_3, where A and B are cation of different size (A is larger than B) and X is the anion bonding to both cations. If the perovskite has ideal cubic structure, A has a coordination number of 12 and B has a coordination number of 6. Nevertheless, comparative size of ions that is required for stability of a crystal structure are quite severe and given by the Goldschmidt Tolerance factor $'t'$ [19-21] and octahedral factor $'\mu'$ [20, 21].

$$\text{Where, } t = \frac{(R_A+R_X)}{\sqrt{2}(R_B+R_X)} \quad (1)$$

$$\text{and } \mu = \frac{R_B}{R_X} \quad (2)$$

R_A, R_B & R_X are the radii of A cation, B cation and X anion respectively.

For halide based perovskite, A cation can be either Methyl Ammonium/ $CH_3NH_3{}^+$ (MA), Formamidinium / $NH_2CH = NH_2{}^+$(FA) [22] or Cesium [23], B cation can be Lead (Pb) or Tin (Sn) [24] and C anion can be Iodide (I), Chloride (Cl) [25], Bromide (Br) [26] , Nitrate or Thiocyanide [27]. Slight buckling, alteration and degradation of the structure could lead to distortion of the high symmetry structure to lower symmetries. When t=0.9 to 1.0, cubic structure is expected, however slightly lower or greater ‘t’ can form tetragonal, rhombohedral and orthorhombic structures. Based on the tolerance and octahedral factor several possible materials can form the perovskite structure. Fig 1.10 shows the material that can possibly be used.

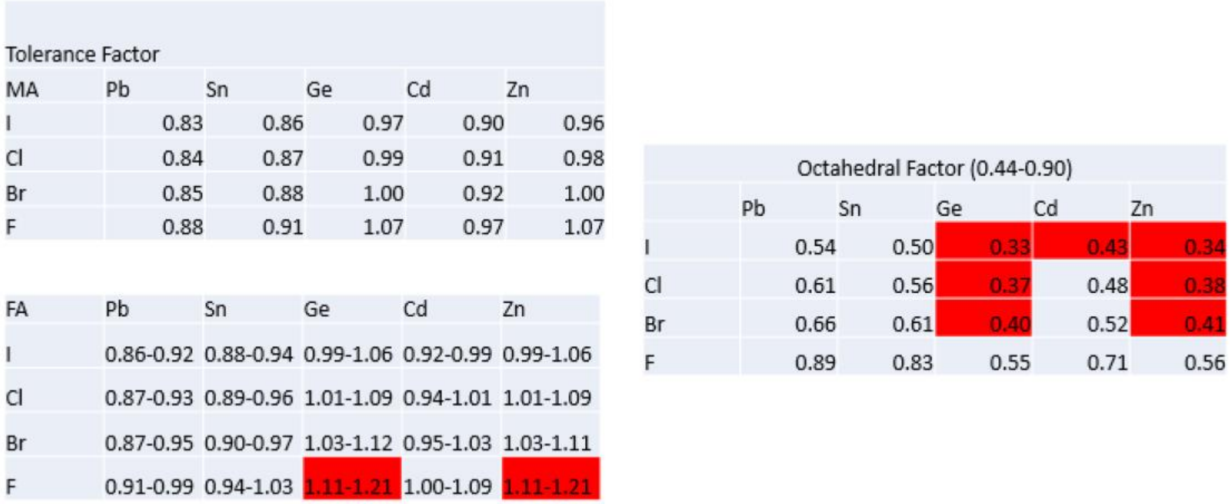

Tolerance Factor

MA	Pb	Sn	Ge	Cd	Zn
I	0.83	0.86	0.97	0.90	0.96
Cl	0.84	0.87	0.99	0.91	0.98
Br	0.85	0.88	1.00	0.92	1.00
F	0.88	0.91	1.07	0.97	1.07

FA	Pb	Sn	Ge	Cd	Zn
I	0.86-0.92	0.88-0.94	0.99-1.06	0.92-0.99	0.99-1.06
Cl	0.87-0.93	0.89-0.96	1.01-1.09	0.94-1.01	1.01-1.09
Br	0.87-0.95	0.90-0.97	1.03-1.12	0.95-1.03	1.03-1.11
F	0.91-0.99	0.94-1.03	1.11-1.21	1.00-1.09	1.11-1.21

Octahedral Factor (0.44-0.90)

	Pb	Sn	Ge	Cd	Zn
I	0.54	0.50	0.33	0.43	0.34
Cl	0.61	0.56	0.37	0.48	0.38
Br	0.66	0.61	0.40	0.52	0.41
F	0.89	0.83	0.55	0.71	0.56

Fig 1.11: Tolerance and Octahedral factor[28]

Couple of research groups have shown temperature based transition and fabrication dependent crystal structure, however a trend is seen i.e. at higher temperature perovskite takes a cubic structure [29-32], as temperature decreases perovskite undergoes distortion to form tetragonal [29-32], rhombohedral and orthorhombic structures [29, 33]. In the case of $APbI_3$ perovskite, the A cation can range from 2.12 A^o (t=0.9) to 2.6 A^o (t=1.0) for cubic structure. However, since MA cation has an ionic radius of 2.7 A^o, MAPbI3 perovskite (the most studied halide perovskite) should theoretically form a tetragonal perovskite, but due to distortion, fabrication variation and differences in measurement ambience there could be different structures too.

1.3.2. Perovskite evolution

The first documented interest in Organic-Inorganic halide perovskite was over a century ago [34], however the material's interest was lit up again following thin film transistor and LED work by Mitzi and team[35, 36]. Since LED materials can exhibit good PV properties the transition to solar cell was anticipated. Tsutomu Miyasaka's team first reported PV results for Perovskite on 2006 [37], they initially made a MAPbBr perovskite with an efficiency of 2.2% and later the replaced Bromine with Iodine and reported an efficiency of 3.8% [38]. Next, Park and his team deposited Perovskite as 2.5nm diameter nanoparticles on TiO_2(Titanium dioxide) and got an efficiency of 6.5% in 2011[39]. Fig 1.11 shows pictographically the evolution of Perovskite architecture.

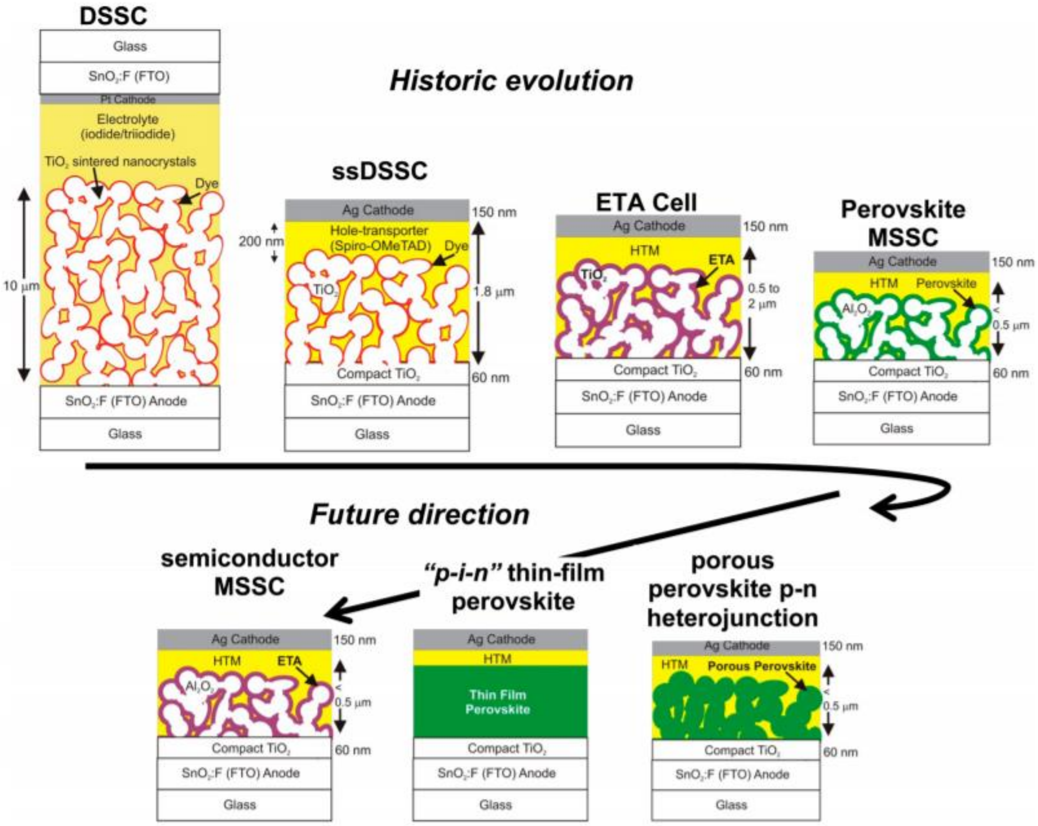

Fig 1.12: Historic evolution of Perovskite[40]

Subsequently, Gratzel and Park worked together and used spiro-MeOTAD (2,2’,7,7’-tetrakis(N,N-di-p-methoxyphenylamine)-9,9’-spirobifluorene) as Hole collecting Type-II heterojunction and achieved an efficiency of 10.9% [41, 42]. (Snaith also showed similar results using Spiro) Following this, Seok joined Gratzel and they capped the scaffold (mesoporous- Electron collecting Type II Heterojunction) with a overlaying layer of perovskite and this increased the efficiency to 12.3% [43, 44]. Finally, the big jump came when Gratzel via sequential solution deposition [14] and Snaith via co-evaporation [15] both independently reported devices with 15% efficiency.

1.3.3. What makes Perovskite attractive?

Perovskite is a direct bandgap material [45, 46] with high absorption co-efficient $\alpha \sim 10^5 cm^{-1}$ [21] [47-49] making them ideal for thin film application. High absorption and direct bandgap implies that the thickness required for absorbing photons is less, hence less raw material. Fig 1.12 shows the absorption coefficient of perovskite in comparison to other PV materials.

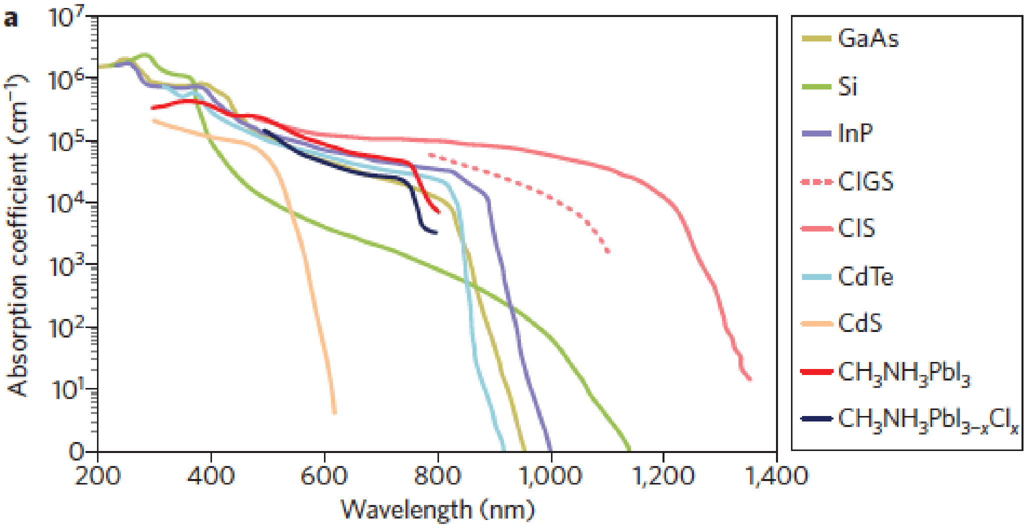

Fig 1.13: Absorption coefficient of Perovskite [21]

Using equation (3), we can calculate the thickness of film required for absorption most of the photons,

$$I_{Transmitted} = I_0 e^{-abs\,coeff\,*thickness} \quad (3)$$

For absorbing 98% incident photons, a thickness of only ~390nm is necessary. The band structure of perovskite is calculated using Density function theory and is shown in Fig 1.13. On observing the structure, it can be evident that irrespective of the halide used, the conduction band minima and the valence band maxima are at the same crystal momentum (k-vector) in the Brillouin zone, therefore it’s a direct bandgap semiconductor.

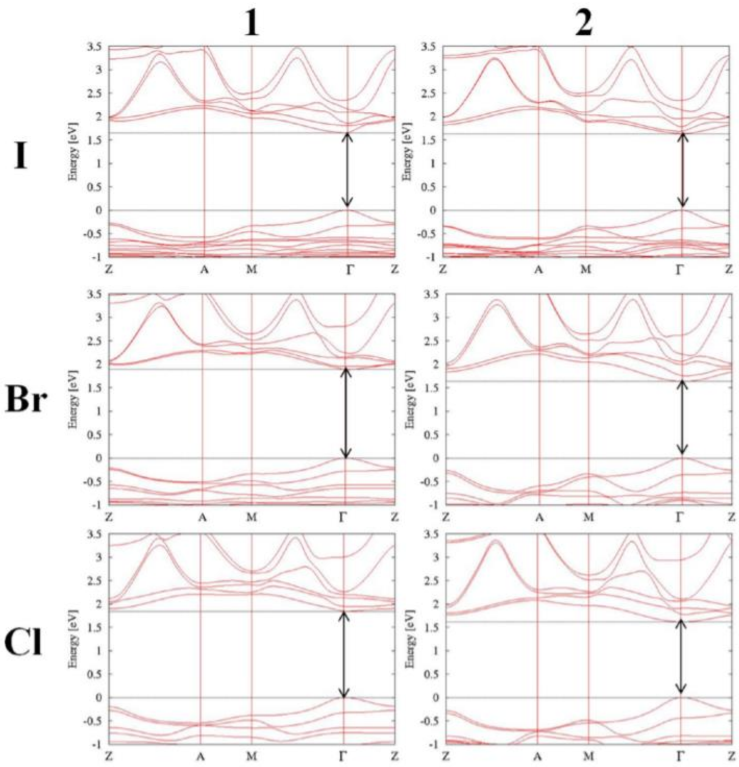

Fig 1.14: Band Structure of Perovskite[46]

Perovskite has a bandgap of ~1.57 eV[42, 49, 50] and this is not too far away from 1.34 eV (the bandgap for maximum possible theoretical efficiency of 33.7% of single p-n junction as per Shockley-Queisser limit [51]). The maximum possible theoretical efficiency for perovskite is ~30% [52]. Fig 1.4 shows the calculated bandgap of Perovskite found using Tauc plot [53, 54]

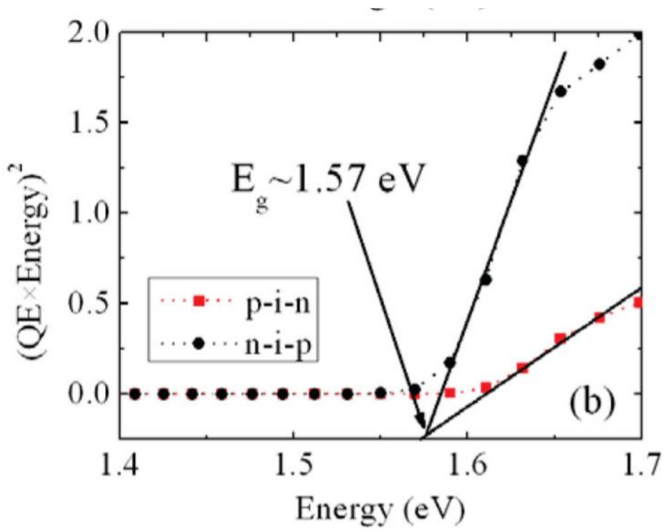

Fig 1.15: Bandgap of Perovskite[50]

Perovskite has a large dielectric constant 18-70 [50, 55-57] and therefore a small exciton binding energy of 2-50 meV [55, 58-62]. Therefore, the charge transport mechanism is non-excitonic and there is minimal bi-molecular recombination, hence good charge collection. Perovskite thin films have diffusion length in the micrometer range [42, 48, 63-66], while single crystals have diffusion length 175um-10mm range [67] [68].

Long diffusion length suggests good charge collection as carriers do not recombine with each other, in addition Perovskite has low defect density [50, 69], so there not much trap assisted recombination which further improves the collection of carriers, therefore improving the generated current. However, the need for highly doped Type-II heterojunction for electron and hole collection brings in debate in regards to the charge transport mechanism of perovskite.

The conduction band (~3.8 eV) and valence band (~5.4 eV) edges of Perovskite matches with a wide range of materials, allowing research groups across the world to work with different materials as Type II n-type and p-type heterojunction. Fig 1.15 shows the band edges of Perovskite and some of the more commonly used type heterojunctions. Other materials like Molybdenum oxide, Vanadium oxide, Rhenium oxide, Ruthenium oxide and Tungsten oxide can also be used as p-type Type II heterojunction [70] for perovskite.

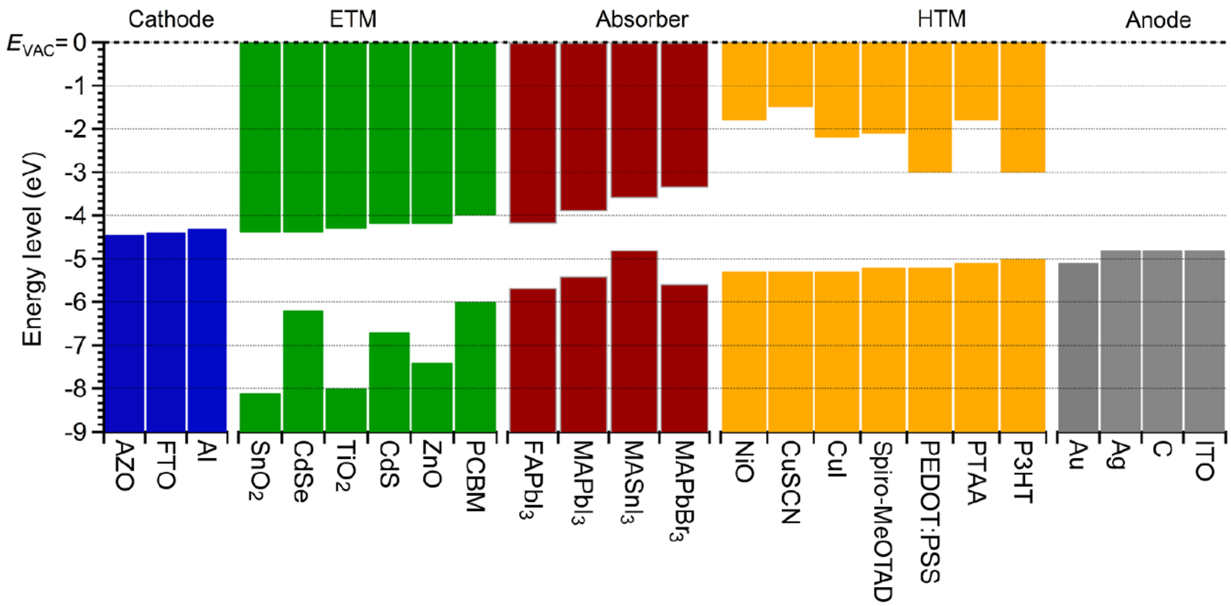

Fig 1.16: Band edge of materials [71]

The bandgap of perovskite is tunable [72-74] as visible in Fig 1.16, this is specifically advantageous for Tandem cell application. Perovskite with bandgap of 1.74 eV was engineered and tandem cell will >25% efficiency have already been made[75].

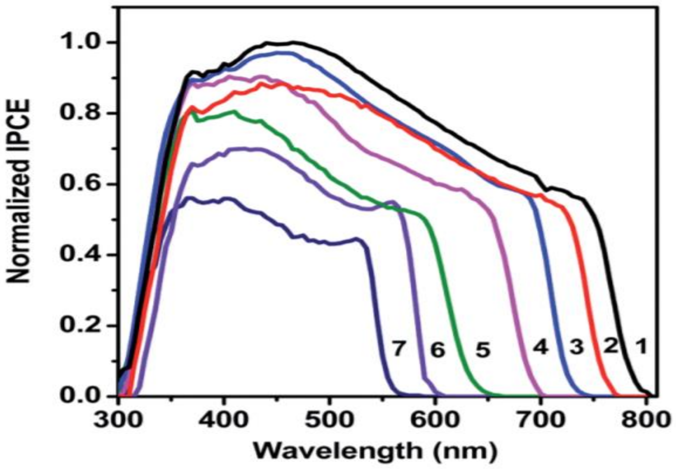

Fig 1.17: Tunable bandgap of Perovskite[72]

Fig 1.17 shows that the maximum possible theoretical efficiency for a 2 junction Tandem of Perovskite (1.74 eV bandgap) and Si/CIGS (1.1 eV bandgap) is ~ 45%, this very is exciting as perovskite can be incorporated into the existing and established Silicon PV technology.

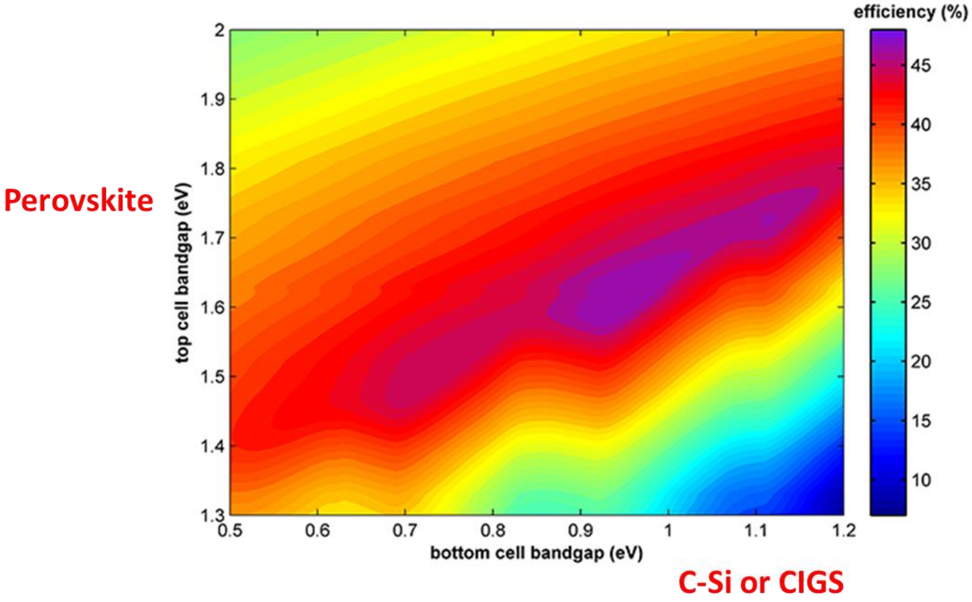

Fig 1.18: Maximum efficiency 2-junction Tandem [13]

In addition, to the above advantages Perovskite has economical and fabrication/manufacturing benefits which make it so easily available and affordable to research groups. The material required for making perovskite solar cell such as Lead Iodide, Lead Chloride, Lead Bromide, Methyl ammonium Iodide, Formamidine Iodide etc. are relatively inexpensive [76-80] and easily accessible. In addition, there are some numerous ways of making the Thin film via both solution and vapor approach, which will be discussed more elaborately later in Chapter 3.

Nevertheless, Perovskite has its share of disadvantages. It consists of Lead halide (water soluble) which is a big environmental hazard[81-83], millions of dollars have been spend over the last decade to remove lead[84-86], it’s unlikely the EPA is going to allow its reintroduction. Also, its naturally unstable unless encapsulated from moisture[87-90]. However, initial studies by groups have shown the material to be Photostable.[91-93]

1.4. Outline of Thesis

The first chapter talks briefly on the need for renewable energy especially Photovoltaic, its steady growth and the evolution and advantages of Perovskite Thin film solar cell. Second chapter, goes over the underlying Device physics and the characterization essential for making good electrical and PV grade thin films. In the third chapter, we will learn details of fabrication and talk elaborately on Co-evaporator build-up. We assembled an in-house vacuum deposition chamber for ~$50K (cost of man hours not included), which it had bought commercially would have cost us ~$400K [94] and using the chamber we made high quality devices. Fourth chapter analyzes the results of sequentially made NIP (MAI based), PIN (MAI based) and NIP (FAI device) and the voltage evolution studies. Fifth chapter converses the thermal stability of Perovskite and the structural advantages of FAI over MAI based devices. Lastly, sixth chapter discusses the results of Co-evaporated PIN (MAI), NIP(MAI) and FAI (PIN) devices. To conclude, the Seventh chapter summarizes the work done in this Thesis and suggestions for future work.

CHAPTER 2

DEVICE PHYSICS AND CHARACTERIZATION

Solar cell transforms the energy from the sun into electrical energy. When light is absorbed by matter, the photons lose its energy to excite an electron to a higher energy state within the material, and the excited electron relaxes back to ground state dissipating energy as either heat or a photon. However, in photovoltaic material there is an internal field which extracts and collects the excited electrons. The separation and collection of the excess carriers causes charge build up and a resulting potential difference that is used to drive electrons for electromotive work. The solar cell is just a simple PN junction with no voltage applied across but one that generates voltage and current.

To be a good photovoltaic material, the material needs to fulfill the following conditions: -

- The material needs to have an energy gap that separates states that are full with electrons from the empty states.
- The photons incident on material needs to be completely absorbed.
- Each absorbed photon must generate an electron-hole pair.
- The electron hole-pair must not recombine.
- The generated charges should be separated.
- Finally, charges need to be transported to an external circuit without any losses.

All the above listed criteria's i.e. absorption, electron-hole pair creation, no recombination, charge separation and transportation of charges can be met using a PN junction. Let us consider each of these phenomena in further detail.

2.1. Generation

Generation is the process of increasing the number of free carriers available to carry charge. The process requires an energy input that could be given in different ways, i.e. via kinetic energy of carriers (impact ionization), phonons (vibration energy of lattice) or photons (light). We know that at absolute zero, no electrons are present in the conduction band but as temperature increases the lattice gains vibrational energy and provides part of the energy to electrons, thereby exciting it to conduction band. This process is known as thermal generation. In general, we refer to the excitation of electron from valence band to conduction band as generation, nevertheless creation of individual charges i.e. only electron or hole is also generation. When carrier is excited from a defect site to conduction band, an electron is created and not a hole and this is also generation. Similarly, excitation a carrier from valence band to a defect state creates a hole and no electron and is also a generation event.

Photogeneration is the principal generation process for Photovoltaics and makes movable electron and hole via absorption of photon. However, there are other optical process that can occur due to photons, such as absorption of photons by carriers increasing its kinetic energy (occurs at higher carrier concentration) or absorption of photons by crystal lattice to generate phonons. These events occur at photon energy <100ev and results in enhancing the thermal generation of carriers.

2.2. Absorption

One of the most powerful and easiest methods for studying the band structure of a semiconductor material is to measure its absorption spectrum. When semiconductor is illuminated with light, photons may be absorbed or pass through the semiconductor as though it is transparent depending on photon energy and bandgap of semiconductor. In absorption process, a photon of known energy or wavelength excites an electron from lower energy to higher energy state, hence if light from a monochromator is passed through a block of semiconductor and changes in transmission is analyzed, one can deduce the possible transition an electron makes and find the distribution of states in the material.

There are several transition an electron can make such as band to band, between subbands, bands and impurities, transition of free carrier in a band, exciton, resonance of impurities, vibrations of crystal lattice and chemical bonds.

2.2.1. Band to band transition

Absorption is expressed in terms of its coefficient $\alpha(h\upsilon)$, which is defined as the relative rate of decrease in light intensity $L(h\upsilon)$ along its propagation path[95]:

$$\alpha(h\upsilon) = \frac{1}{L(h\upsilon)} \frac{d[L(h\upsilon)]}{dx}$$

The fundamental absorption refers to the transition of an electron from the valence to the conduction band. If the energy of the photon$(h\upsilon)$ is less than bandgap energy (E_g) it passes through the material, however if photon energy is equal to or greater than bandgap energy the electron is excited from the valence to the conduction band. For the case when $(h\upsilon) > E_g$, the excess energy provides additional kinetic energy to electron and its dissipated thermally via collision with the crystal lattice. Fig 2.1 shows the basic absorption process.

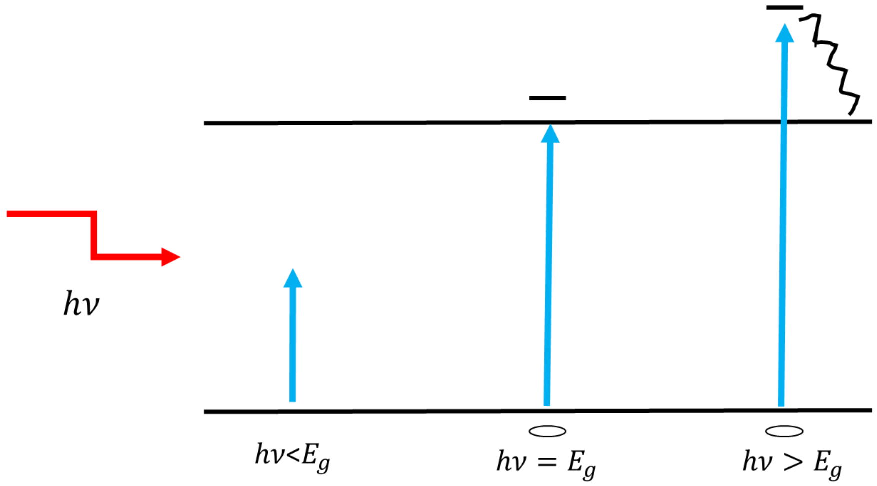

Fig 2.1 Optical generated electron-hole pair

Absorption coefficient $\alpha(h\upsilon)$ for a material is proportional to the probability of transition between initial to final state (P_{if}), density of initial state (n_i) and density of final state (n_f) and can be written as

$$\alpha(h\upsilon) \propto \sum P_{if}\, n_i n_f$$

Since the photons momentum, h/λ (λ is the wavelength of light, few thousand angstroms), is significantly lesser than the crystal momentum (k) h/a (a is the lattice constant, few angstroms), the photon cannot provide electrons with momentum i.e. if incase there is a momentum mismatch. If all momentum conserving transitions are permissible, P_{if} is photon energy independent. However, in some materials quantum selection rules prohibits direct transition at k=0 [95], in this case P_{if} increases with photon energy.

In indirect bandgap semiconductor, transitions require change in both energy and momentum. And as photons cannot give the necessary momentum, the momentum conservation is given by phonons (lattice vibration) interaction, in general it's the acoustic phonons. Fig 2.2 shows the two-step process.

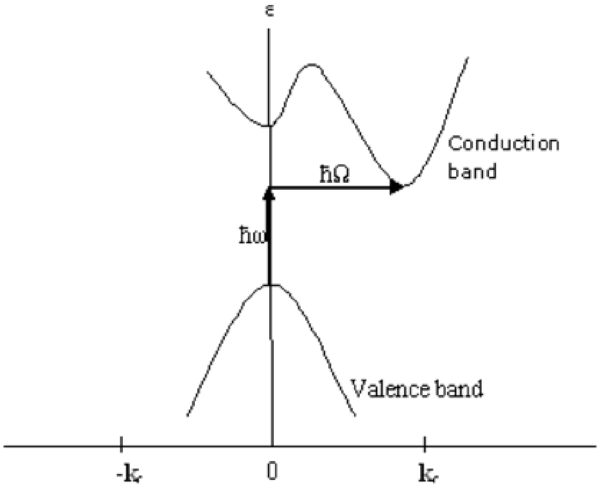

Fig 2.2: Phonon assisted transition [96]

Though broad spectrums of phonons are available, only the phonons with the necessary momentum fluctuations are usable. As temperature decreases, phonon density decreases diminishing the probability for 2 step process, resulting in a drop of $\alpha(h\upsilon)$.

2.2.2. Band tail and deep defect transition

For photon energies, less than bandgap energy $(h\nu < E_g)$ one would expect that there is no absorption but this is seldom the case. An exponentially increasing absorption edge is seen [97-99], and it is found that

$$\frac{d(\ln \alpha)}{d(h\nu)} = \frac{1}{KT}$$

and is known by Urbach's rule [100]. The absorption occurs due to subgap transitions namely from band tail and deep tracks. Fig 2.3 shows a visual representation of the possible subgap transitions.

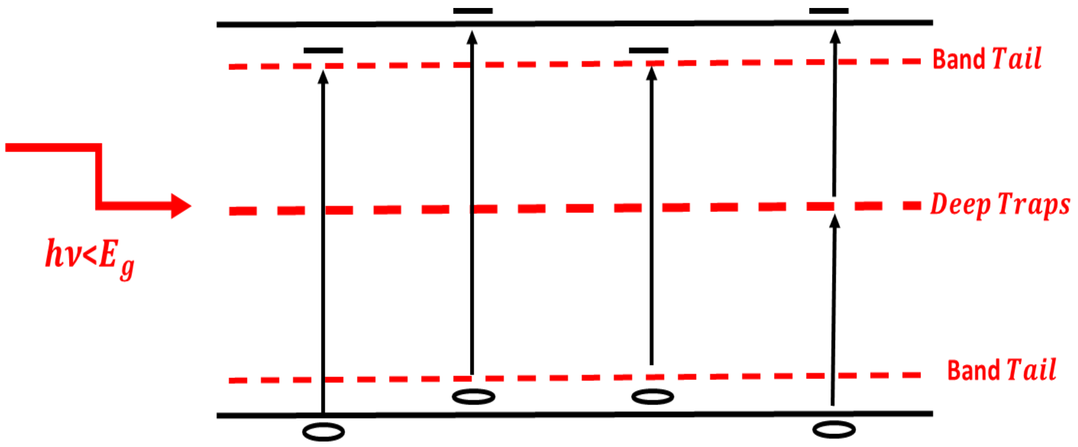

Fig 2.3: Band tail and Deep trap transition

These transitions are significantly smaller in comparison to band-band transition as the density of tails traps and deep traps are less in comparison to the density of states available in the valence and conduction band. However, they provide valuable information of the materials band structure especially distribution of the tail states and deep states [101-104]. For example, by plotting photon energy vs absorption coefficient[105], one can determine Urbach energy (empirical parameter with units of energy that describe the distribution of states).

2.2.3. Exciton absorption

Excitons are electron-hole pairs that are bound by columbic attractive forces. Exciton moves through the crystal and transfers energy but not electronic charge as they are neutral. The exciton formation is observed both in direct bandgap semiconductor and indirect bandgap semiconductors. In direct bandgap semiconductor, the transitions occurs as pronounced peaks in the absorption spectrum at very low temperatures but the peaks broadens out at higher temperatures[98]. In indirect semiconductor, exciton absorptions are observed as steps in absorption spectrum[106, 107] and requires a phonon participation for conservation of momentum. Fig 2.3 shows the exciton absorption process.

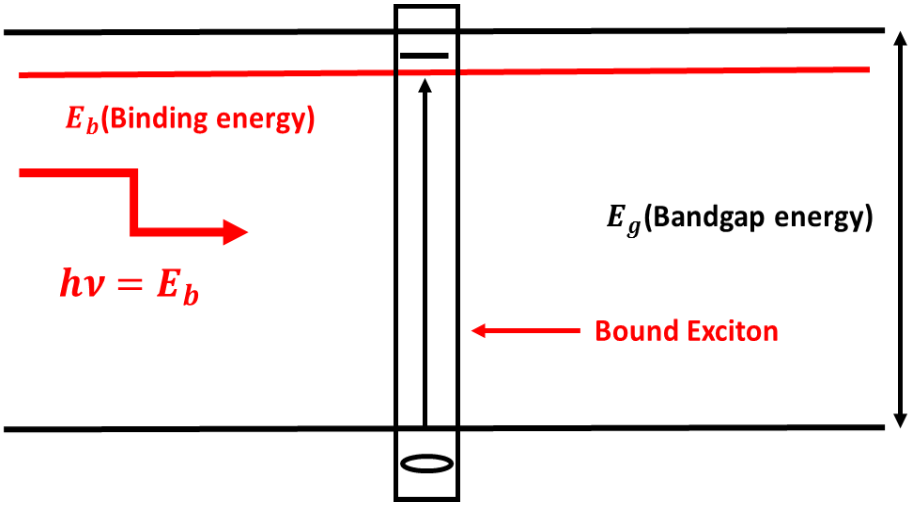

Fig 2.4: Exciton Absorption

2.3. Recombination

Recombination is a relaxation event of excited mobile charge carriers that results in the release of energy. The excess energy can be given off as photons or phonons or even as kinetic energy to an existing charge. Generation-Recombination is nature's way of restoring order i.e. excess carrier in a material is eliminated. So, for every generation there is and there will be an equivalent recombination process. There are multiple ways that a recombination might occur and accordingly electrons or hole or both as a couple could be annihilated. For example, if an electron in the conduction bands drops to a hole in valence bond, then both the electron and hole is lost. However, if electrons drop from conduction band to trap state only electrons are lost or in the contrary electron drops from trap state to valence band, a hole is lost.

The above specified recombination's can be distinguished into avoidable and un-avoidable. Unavoidable are due to essential physical processes while avoidable are due to traps state or defect in the material. The unavoidable recombination is mostly Band-to-Band, while all other recombination's such as exciton, Auger, Trap assisted, Surface and Grain boundary recombination could in theory be avoided.

2.3.1. Band to band recombination

Theoretically the simplest of recombination processes is band-to-band recombination, and is also referred to as thermal recombination or bimolecular recombination. It's the direct extinction of conduction band electron and valence band hole, the electron drops from an allowed conduction band state to an unfilled valence band state with the release of energy that is typically radiative in the form of photons, which corresponds to the material bandgap. Fig 2.5 represents band to band recombination.

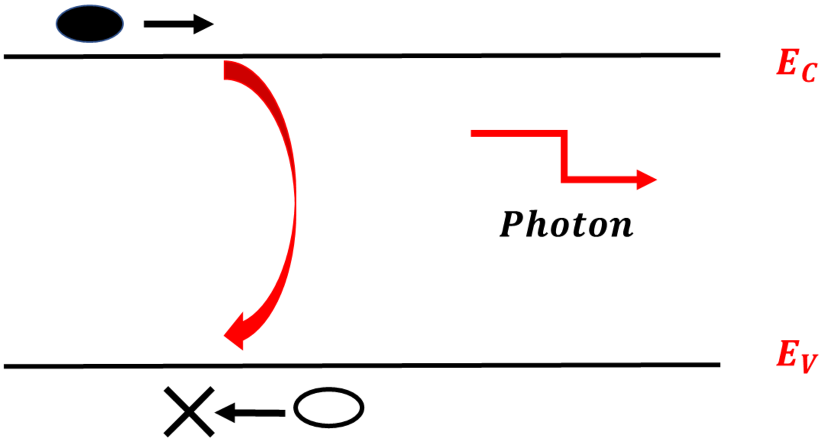

Fig 2.5: Band to band recombination

The recombination equation can be represented by the following expression:

$$R = C(np - {n_i}^2)$$

Where C is the band to band recombination constant ($\frac{cm^3}{sec}$). n, p and n_i are the electron, hole and intrinsic carrier concentration (cm^{-3}). The above equation can be simplified for small signal condition. For n- type semiconductor,

$$R \cong C.\Delta p.N_D = \frac{\Delta p}{\tau_p}$$

$$\tau_p = \frac{1}{CN_D}$$

τ_p is the minority carrier hole lifetime, N_D is the donor concentration and Δp is the excess carrier concentration. Hence, for n-type material, lifetime of minority hole electron is inversely proportional to donor concentration. Similarly, for p-type material, lifetime of minority carrier electron is inversely proportional to acceptor concentration [108-112].

2.3.2. Trap assisted recombination

We envision semiconductors as ideal crystals with perfect periodic functions, having no energy states within the bandgap, however this is seldom the case. In real crystal, defects can arise due to unwanted impurities, broken bonds and strain. The lattice strain induces shallow traps while broken bonds and unwanted impurities induces deep traps which acts as recombination centers. There is subtle difference between trap and recombination center. Fig 2.6 shows a very simple portrayal of a shallow trap.

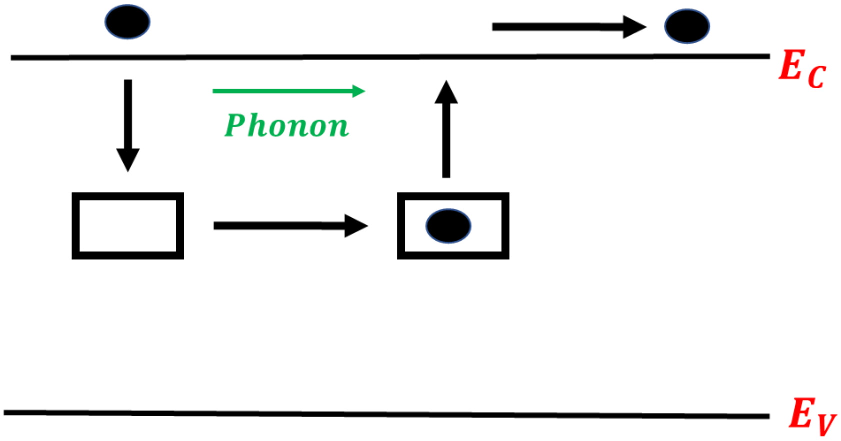

Fig 2.6: Shallow trap recombination

Localizes states within the bandgap that captures carriers of one type are often referred to as shallow traps. The electron is captured by the trap state and sub sequentially via thermal excitation the electron can excited back into the conduction band. So, the electron is not lost but captured and released, thus influencing the mobility of free carriers. Note that when electrons fall from conduction band to trap state extra energy is released as phonons.

Now let us consider recombination center also known as deep traps. Fig 2.7 shows a very simple pictorial representation of deep trap. The empty trap is occupied by conduction band electron and with the extra energy being released as phonons. This is followed by a valence band hole combining with the electron in the trap with a phonon release. Since, the trap as annihilated a conduction band electron and valence band hole, we refer to these as recombination centers or deep traps. One can also visualize the hole combining with electron in the trap state, as just electron dropping from trap state to valence band free state. However, what is important to distinguish is that the deep trap has emptied itself and available again from annihilation of mobile carriers. The recombination via trap levels is referred to as Shockley -Read-Hall (SRH) recombination.

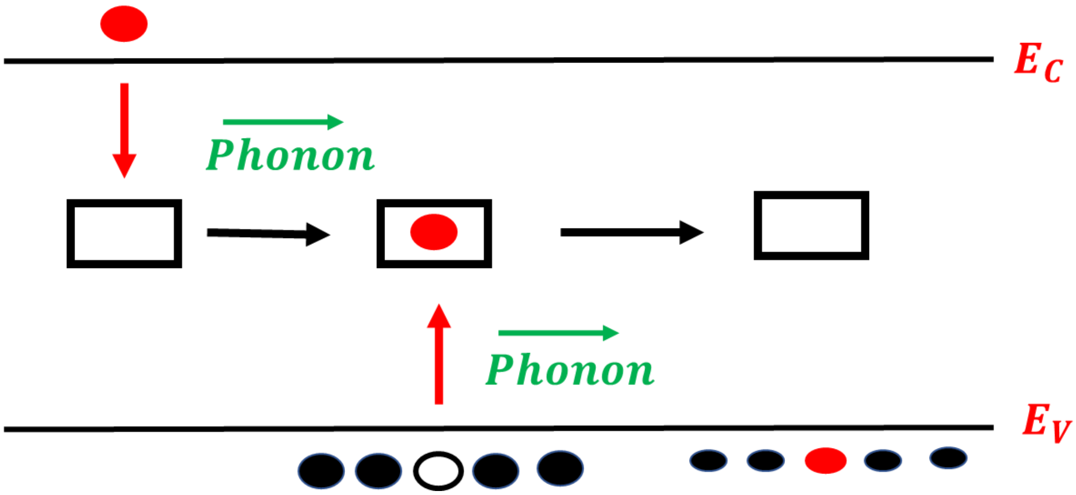

Fig 2.7: Deep trap recombination

SRH recombination can be represented by the following equation [108],

$$R_n = R_p = \frac{C_n C_p N_t (np - {n_i}^2)}{C_n(n + n') + C_p(p + p')} \equiv R$$

Where C_n & C_p are the electron and hole capture cross section, and N_t is the total concentration of trap centers, and n_i , n & p are intrinsic carrier concentration, conduction band electron concentration and valence band hole concentration, and n'& p' are quantifiable constants equal to electron and hole concentration if fermi level is at trap level.

For n-type semiconductor under small signal condition, the equation simplifies as follows:

$$R \cong C_p.\Delta p.N_t = \frac{\Delta p}{\tau_p}$$

Where

$$\tau_p = \frac{1}{C_p N_T}$$

Thus, the minority carrier hole lifetime is inversely proportional to the density of traps. Similarly, for a p-type material, minority carrier electron lifetime is inversely proportional to density of trap[108].

2.3.3. Auger recombination

Auger recombination is a 3-body or 3 carrier process (2 electron+1 hole or 2 hole+1 electron). The collision of 2 like carriers (electron-electron or hole-hole), results in one of the carrier gaining kinetic energy and the other losing an equivalent energy. The extinct carrier loses energy and recombines with the valence band hole or trap state, while the one that gains kinetic energy goes to a higher energy state and slowly loses the extra energy via thermalization (i.e. collision with the lattice) and drops back to the conduction band. Fig 2.8 shows pictographically the Auger recombination process, the steps seen in the picture is a representation of the thermalizing loss experienced by the higher energy electron.

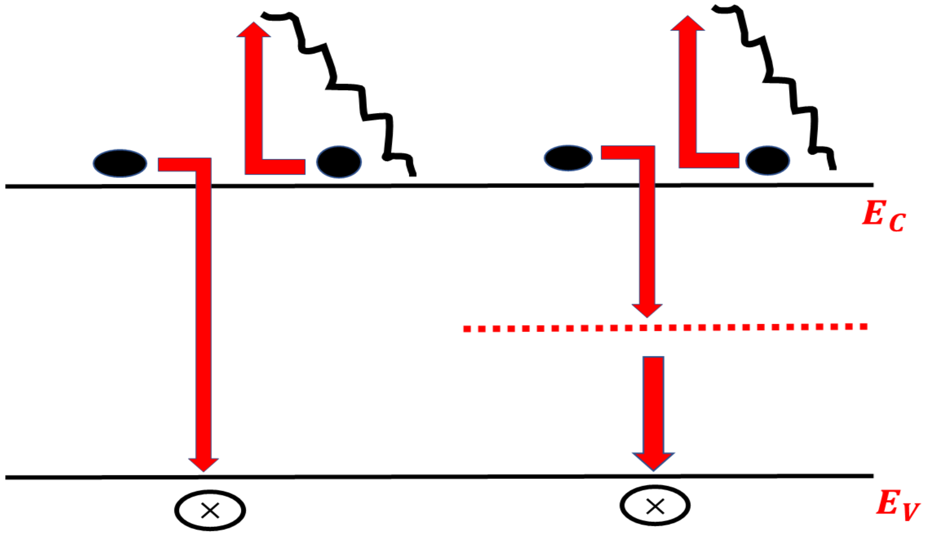

Fig 2.8: Auger recombination

The probability of carrier-carrier collision increases with carrier concentration, so the possibility of Auger recombination also increases with carrier concentration. Auger recombination occurs in the degenerately doped region of the device, such as n^+& p^+regions of the solar cell. Auger recombination for highly doped n-type semiconductor can be represented by the following equation [110, 111],

$$R = C(n^2p - n.{n_i}^2)$$

Where c is the recombination constant, and n, p & n_i are the electron, hole and intrinsic carrier concentration respectively. For small signal condition, the above equation reduces as follows:

$$R \cong C\Delta p.{N_D}^2 = \frac{\Delta p}{\tau_p}$$

Where

$$\tau_p = \frac{1}{C{N_D}^2}$$

τ_p is the minority carrier lifetime & N_D is the donor density. Therefore, for highly doped semiconductor the lifetime of minority carrier is inversely proportional to the square of doping concentration. Hence, Auger recombination becomes the dominant mechanism for degenerately or highly doped regions of the device.

The bulk lifetime of carrier comprises of band-to-band lifetime, SRH lifetime and Auger lifetime and can be represented as follows [113, 114]

$$\frac{1}{\tau} = \frac{1}{\tau_{b-b}} + \frac{1}{\tau_{SRH}} + \frac{1}{\tau_{Auger}}$$

Where τ_{b-b}, τ_{SRH} & τ_{Auger} are the band-to-band, SRH and Auger lifetime respectively.

2.3.4. Excitonic recombination

Typically, the electron and hole are envisioned as separate charged particles that react to applied field independently, nevertheless there is a possibility that they are coupled together in a hydrogen atom like arrangement and move as a unit due to the Columbic attraction between unlike charges. The electron-hole pair is referred as exciton pair and if one of the elements are trapped at a shallow-level site, the resulting formation is known as bound exciton. The energy required for exciton formation is slightly less than the bandgap energy and is imagined as introducing an energy level slightly below the conduction band, or above the valence band or both [95, 110] as shown in Fig 4.9. The recombination of the exciton electron-hole pair results in sub-bandgap radiation especially at low temperature and is the major light producing mechanism is LED's.

The exciton binding energy for n^{th} level is given by [112, 115]

$$E_b = -\frac{\mu}{m_0} \times \frac{R_H}{n^2} \times \frac{1}{\epsilon_r}$$

Where µ is the reduced mass, m_o is the electron mass, $R_H$is the Rydberg constant and ϵ_r is the material dielectric constant.

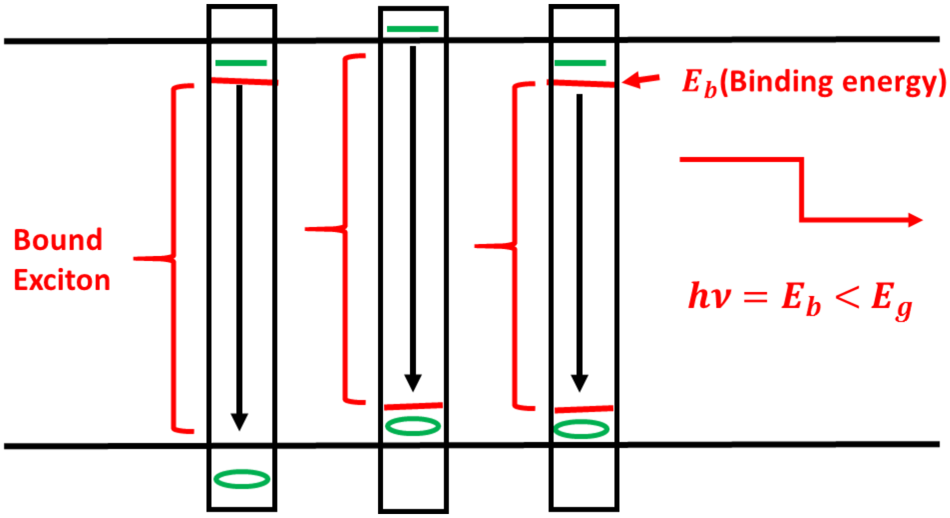

Fig 2.9: Exciton recombination

In the case of inorganic semiconductor such as silicon ($\in_r = 11.9$) the exciton binding energy is 15 meV [116, 117] and since this energy is less than kT (25 meV), the exciton dissociates itself at room temperature, however for organic semiconductor $\in_r \sim 2 - 5$Error! Bookmark not defined. [118] and the exciton binding energy is in between 0.2 eV-1 eV [118-120], resulting in significant exciton recombination.

2.3.5. Surface and grain boundary recombination

We have implicitly assumed the semiconductor to be infinite in extent and we not concerned about boundary conditions, however in reality this is not the case. The material is finite in range, with boundaries at surface terminating the periodic nature of crystal, in addition, if the devices have interfaces with heterostructures, then this would also abrupt the perfect periodic potential. In addition, the surfaces and interfaces between material may acquire impurities from surrounding and have broken bonds. All these results in the interfaces have a distribution of traps throughout the bandgap, acting as good recombination centers. Fig 2.10 (left) shows pictographically the recombination at surfaces.

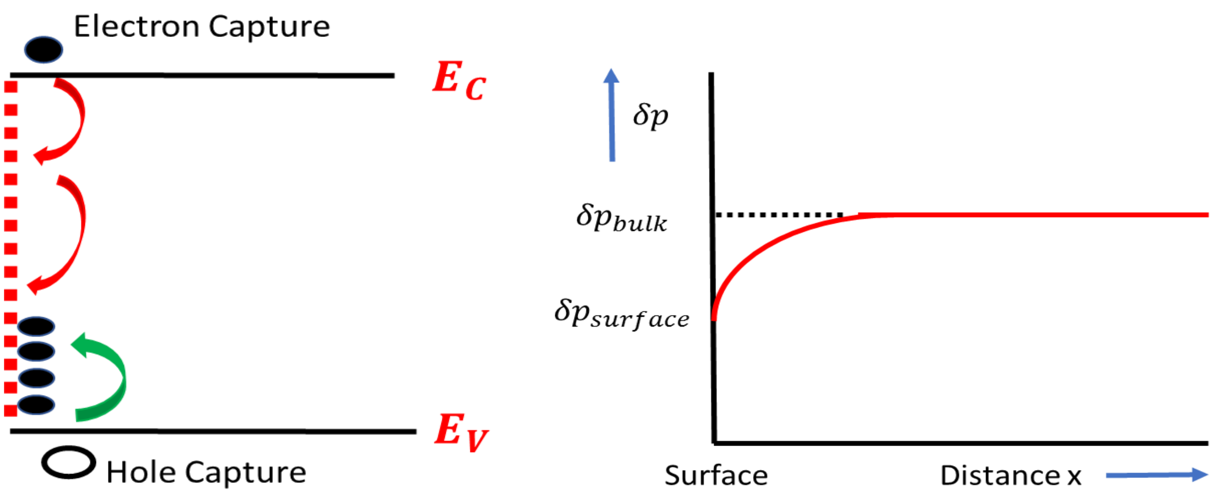

Fig 2.10: Surface Recombination(left) and surface carrier concentration(right)

Also, from the earlier SRH recombination we learnt that recombination life time is inversely proportional to the inverse of the trap density. As we can see from Fig 2.10 (left), the surface trap densities are throughout the bandgap and hence they are greater than the bulk density. From SRH recombination (for n-type semiconductor) we know,

$$R_{bulk} \cong C_p.\Delta p_{bulk}.N_t = \frac{\Delta p_{bulk}}{\tau_{p0}}$$

Where minority carrier hole lifetime $\tau_p = \frac{1}{CN_t}$, N_t is the trap density and Δp_{bulk} is the bulk carrier concentration. From SRH, recombination at surface can be written as[108]

$$R_{surface} = \frac{\Delta p_{surface}}{\tau_{surface}}$$

We know that trap density at surface is more in comparison to the bulk, therefore $\tau_{surface} < \tau_{bulk}$. Under steady state, carriers are generated and recombine at the same rate throughout the semiconductor, therefore $R_{surface} = R_{bulk}$. Under this argument, we get $(\Delta p_{surface} < \Delta p_{bulk})$, so the carrier concentration should decrease at the surface and this is shown in Fig 2.10 (right).

In adding to boundary condition at the physical edges of semiconductor that disturb the perfect periodic potential, there are termination of boundary conditions inside the material between crystal regions[111] i.e. between grains of polycrystalline films. This can be critical recombination mechanism in devices that use polycrystalline films. Fig 2.11 shows the grain boundary recombination of n-type semiconductor as defined by Seager [121]

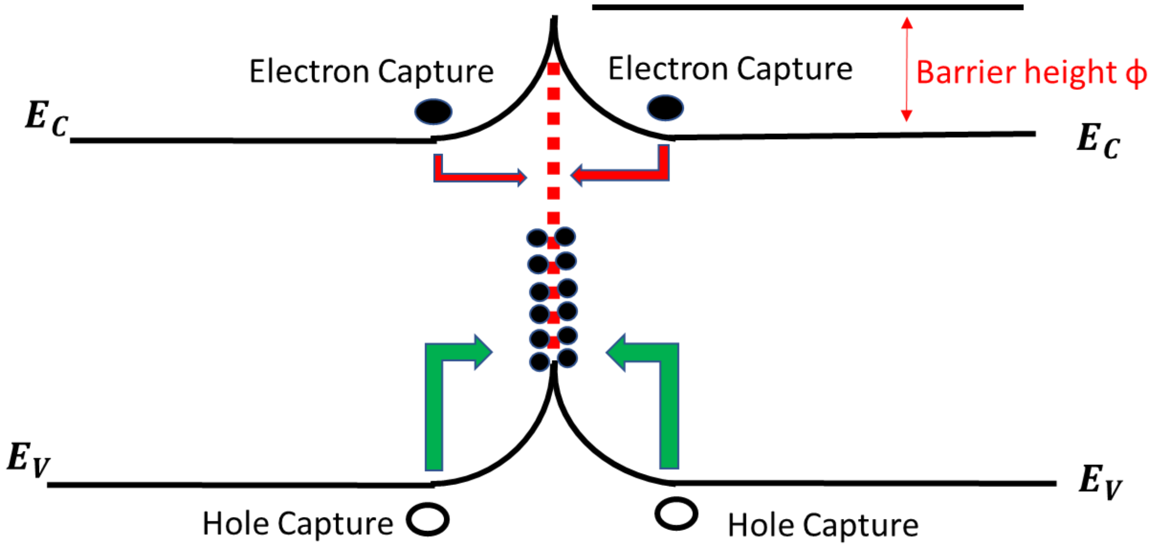

Fig 2.11: Grain boundary Recombination (n-type semiconductor)

Like surface recombination, grain boundary recombination also suffers from increased recombination and decreased carrier concentration at boundaries of grain. In addition, there is also a localized increase in potential at grain edges that influence the mobility of both electron and holes[121-123] as seen in Fig 2.11. To large extent, both grain boundary and surface recombination can be largely controlled by fine tuning processing condition. For polycrystalline films, grain boundary recombination can be reduced by increasing the grain size, this diminishes the surface area of grain boundaries and improves carrier collection.

Surface recombination, is bit more challenging, but intelligent and careful processing steps could mitigate it. If possible one could passivate the surface states, however this is material dependent and involves material explorations and could be a tedious approach. However, in the case of perovskite films, small attention to details like driving away the moisture before depositing each material type (as perovskite has different heterostructures sandwiched together) has helped achieve good charge collection.

2.4. Carrier Transport

Once the carriers are generated, it is important to know the movements of these excess carriers in space and time, and in the presence of electric field and charge density gradients. The behavior of these excess carriers can be described by ambipolar transport equation, and may be written as [108]

$$D' \frac{\partial^2(\delta n)}{\partial x^2} + \mu' E \frac{\partial(\delta n)}{\partial x} + g - R = \frac{\partial(\delta n)}{\partial t}$$

The parameter D' is the ambipolar diffusion coefficient, μ' is the ambipolar mobility, δn is the excess carrier concentration, g is the generation and R is the recombination rate. D' & μ' are related by Einstein's relation. Using the Einstein relation, the ambipolar diffusion coefficient and mobility can be written as

$$D' = \frac{D_n D_p (n + p)}{D_n n + D_p p}$$

$$\mu' = \frac{\mu_n \mu_p (p - n)}{\mu_n n + \mu_p p}$$

D_n & D_p are the electron & hole ambipolar diffusion coefficient, μ_n & μ_p are the electron & hole mobility, p & n are the thermal equilibrium electron and hole concentration.

For Low injection and extrinsic doping, the ambipolar transport equation simplifies as follows

For p-type semiconductor

$$D_n \frac{\partial^2(\delta n)}{\partial x^2} + \mu_n E \frac{\partial(\delta n)}{\partial x} + g - \frac{\delta n}{\tau_{no}} = \frac{\partial(\delta n)}{\partial t}$$

And for n-type semiconductor

$$D_p \frac{\partial^2(\delta n)}{\partial x^2} + \mu_p E \frac{\partial(\delta n)}{\partial x} + g - \frac{\delta n}{\tau_{po}} = \frac{\partial(\delta n)}{\partial t}$$

Where τ_{no} & τ_{po} are minority carrier electron lifetime.

It's important to recognize from ambipolar transport equation that the diffusion, drift and recombination of excess carriers are that of the minority carrier. Also, from the transport equation, we know that two mechanisms namely diffusion and drift regulate carrier transport. Accordingly, two collection types namely Diffusion based collection & Field based collection occurs in devices. Material properties such as crystallinity, diffusion length etc. determine them.

2.4.1. Diffusion based collection

Let us consider a p-type semiconductor in which excess carriers are generated at $x = 0$ ($g = 0\ for\ x \neq 0$)with zero applied bias (E=0) and let us assume the semiconductor is at steady state ($\frac{\partial(\delta n)}{\partial t} = 0$), the ambipolar transport equation simplifies and can be written as

$$D_n \frac{\partial^2(\delta n)}{\partial x^2} - \frac{\delta n}{\tau_{no}} = 0$$

The generated excess minority carrier will diffuse and concentration will vary as a function of x. The above equation, gives the following minority carrier concentration

$$\delta n(x) = \delta n(0) e^{-\frac{x}{L_n}}$$

$L_n = \sqrt{D_n \tau_{no}}$ is the diffusion length of minority carrier and is the average length a carrier travels between generation and recombination. As the diffusion length increases the distance travelled by minority carrier increases [108]. The maximum thickness of the bulk for a solar cell will be determined by its diffusion length.

In general, we like to have thicknesses of bulk in micrometers to absorb all photons, but if the diffusion is not in the micrometer range we need to reduce the thickness. In general, it's a good to have device thickness (t) less than diffusion length (t<L_n) to ensure good collection. Since, Crystalline Silicon have minority carrier diffusion lengths in the 100's of micrometer range, the solar cells are made on wafers of comparable thicknesses. Fig 2.12 shows the structure of HIT solar cell made on p-type substrate, all excess carriers generated in the bulk is collected by diffusion.

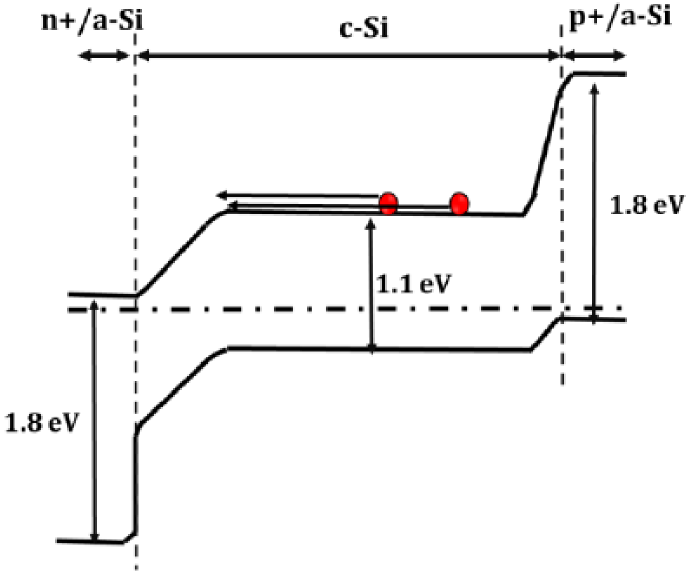

Fig 2.12: Diffusion assisted transport HIT solar cell [112]

2.4.2. Field based collection

Let us consider a p-type semiconductor with negligible diffusion coefficient ($D_n \frac{\partial^2(\delta n)}{\partial x^2} = 0$), an internal field E, no generation ($g = 0$), at steady state ($\frac{\partial(\delta n)}{\partial t} = 0$), the ambipolar transport equation for this can be written as

$$\mu_n E \frac{\partial(\delta n)}{\partial x} - \frac{\delta n}{\tau_{no}} = 0$$

The distribution of carriers can be written as

$$\delta n(x) = \delta n(0)e^{-\frac{x}{L_{nDrift}}}$$

$L_{nDrift} = \mu_n \tau_{no} E$, is the carrier drift length or Range, the distance travelled by minority carrier owing to the internal field before it recombines [124, 125]. For good collection, thickness of device should be lesser than drift length (L_{nDrift}). For example, amorphous silicon has very low diffusion length[126-128], hence it's not possible to have 100 micrometer thick films. Nevertheless amorphous silicon has high absorption coefficient and thin film solar cells with thickness ~ 1um can be made using PIN structures. Note that the intrinsic region of these cells is completely depleted and carrier collection is field assisted. Fig 2.13 shows the band structure of P^+iN^+amorphous Thin film solar cell.

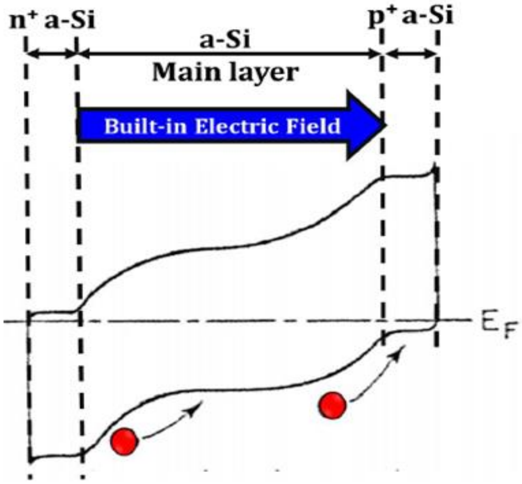

Fig 2.13: Drift assisted transport in Amorphous Silicon solar cell [129]

2.5. Carrier Separation

Photovoltaic energy conversion is a result of generation, separation and transport. Charge separation requires a driving force that needs to be inbuilt in the device. The essential force for charge separation can be provided by creating a gradient in one of the quasi-fermi levels during the photogeneration process. Looking at it differently if an external circuit provides low resistance path to one carrier type that could also induce a charge gradient. There are many other ways of attaining charge separation, the most common approach is by creating a spatially varying electrostatic field within the material.

A junction between two electrically dissimilar material creates a non-zero electric field producing a drift current. Correspondingly, a gradient in carrier concentration causes diffusion current. Charge selective contacts can produce the necessary concentration gradient across the film thickness. Carrier density gradient is an outcome of difference in generation and recombination rate and this can result in a net current only if the electron and hole diffusion constants are different, as if they are the same, electron and hole current will cancel each other.

Dember potential, the potential arising due to difference in diffusion constants is not large enough in crystalline material for effective charge separation. However, large diffusive current can be generated by an added mechanism that creates an asymmetry and selectively removes electron or holes. As mentioned before, this could be carrier selective contact. For example, by creating a low resistive path to electrons, the contact will now act as an electron sink and start driving an electron diffusive current. As no holes were collected, electron and hole current do not cancel out. In the same way, there could be second contact to selectively remove holes and drive a hole diffusion current.

Charge separation can also be inbuilt in the material by creating an internal field. There are four ways to create a field within a semiconductor material.

1. Gradient in electron affinity in material.
2. Gradient in work function in material.
3. Gradient in bandgap
4. Gradient in band density of states

1,2 & 3 are exploited in PV research, and can be realized at the interface of two semiconductor material using heterojunctions and rightly so, this was used by us for efficient charge separation. There are three types of hetero-junction: Type I, Type II & Type III.

In Type I heterojunction (Straddling) the bandgap of one material completely overlaps the bandgap of second material. Type II (staggered) both the conduction band and valence band of one material is lower than the corresponding band edges of second material. Type III (broken gap) the band edges do not overlap at all, the conduction band of one material is below the valance band of second material. Fig 2.14 shows the schematic of different types of heterojunctions.

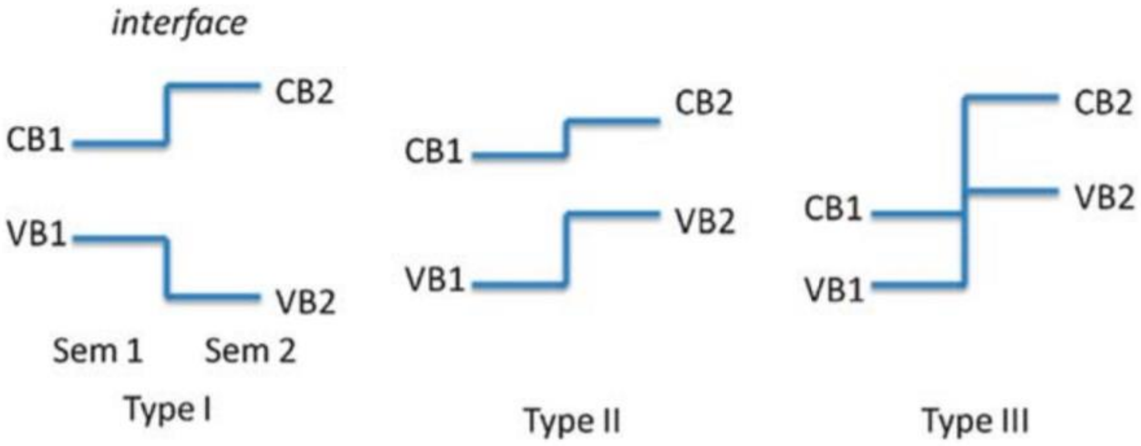

Fig 2.14: Types of heterojunction[130]

2.6. Equivalent Circuit of a Solar Cell

The equivalent circuit of a solar cell is shown in Figure 2.15. The circuit has current source I_L, two diodes D_1 & D_2, a series resistance R_S and a shunt resistance R_{SH}. The two diodes D_1 & D_2 each represent a recombination mechanism, I_L is a constant current generator that represents the photogeneration process and is proportional to light intensity, R_S signifies the series resistance across the bulk and contacts (series resistance needs to be as low as possible, high series resistance can reduce the short circuit current), R_{SH} the shunt resistance or parallel resistance represents the resistance of alternate paths that prevents the photo current from reaching the load (Examples are pin holes, crystal edge, grain boundaries in polycrystalline films etc.) The shunt resistance needs to high as possible, low shunt resistance will diminish open circuit voltage.

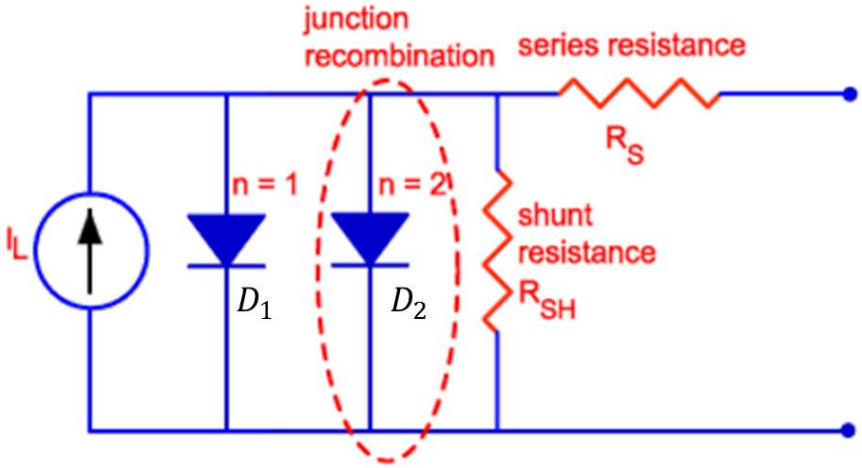

Fig 2.15: 2-Diode model solar cell equivalent circuit[131]

In an ideal diode, the ideality factor is 1. This entails that all the recombination is occurring in the bulk and at the surface, however, there is recombination in the depletion region too and this is denoted by ideality factor 2. The probability of carriers recombining in the junction, increases with the width of depletion region, the width is a function of voltages across the diode. Therefore, ideality factor is also a function of voltage across the device. The net current can be written as

$$I = I_L - I_{D1} - I_{D2} - I_{sh}$$

$$I = I_L - I_{01}\left[\exp\left(\frac{q(V+IR_s)}{KT}\right) - 1\right] - I_{02}\left[\exp\left(\frac{q(V+IR_s)}{2KT}\right) - 1\right] - \frac{(V+IR_s)}{R_{SH}}$$

I_{01} is the reverse saturation current density & I_{02} is the generation current density respectively. The different current regions of a diode can be seen by plotting the dark IV curve of a diode in Semilog plot.

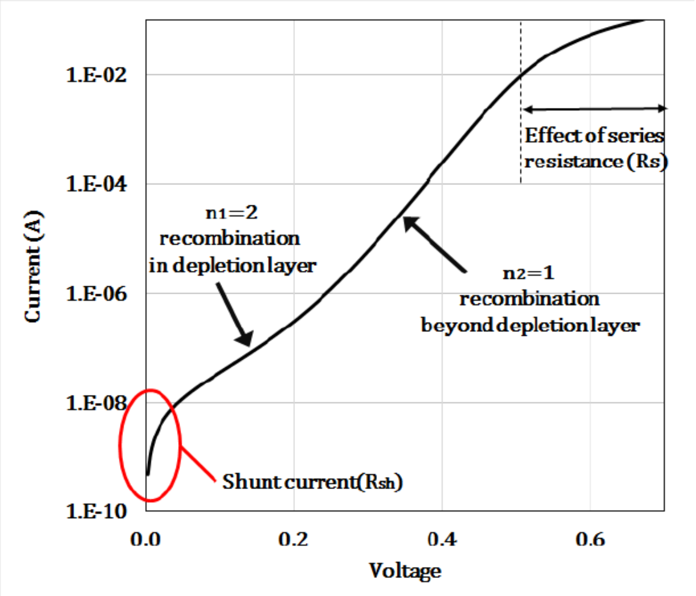

Fig 2.16: Dark IV curve[112]

At very low voltage, shunt current through R_{SH} is dominant, then as voltage increases, current increases exponentially in 2 different regimes (Ideality factor 1 for higher voltage & Ideality factor 2 for lower voltage) due to the different recombination mechanisms which is a function of voltage. As current increases, further, voltage drop across the series resistance starts to become important, thus limiting the current and causing the IV curvw to deviate from exponential behavior. Also, at higher current regime we get into high level injection and ideality factor becomes 2.

2.7. IV Curve of a Solar Cell

The light IV curve is simply the superposition of the dark IV curve with the light generated current[132], the photovoltaic effect has the ability to shift the IV curve into the 4th quadrant where power can be extracted from the solar cell. For mere visual convenience, we flip the IV in the first quadrant. Fig 2.17 shows a visual representation of current generation and the resulting IV curve[133].

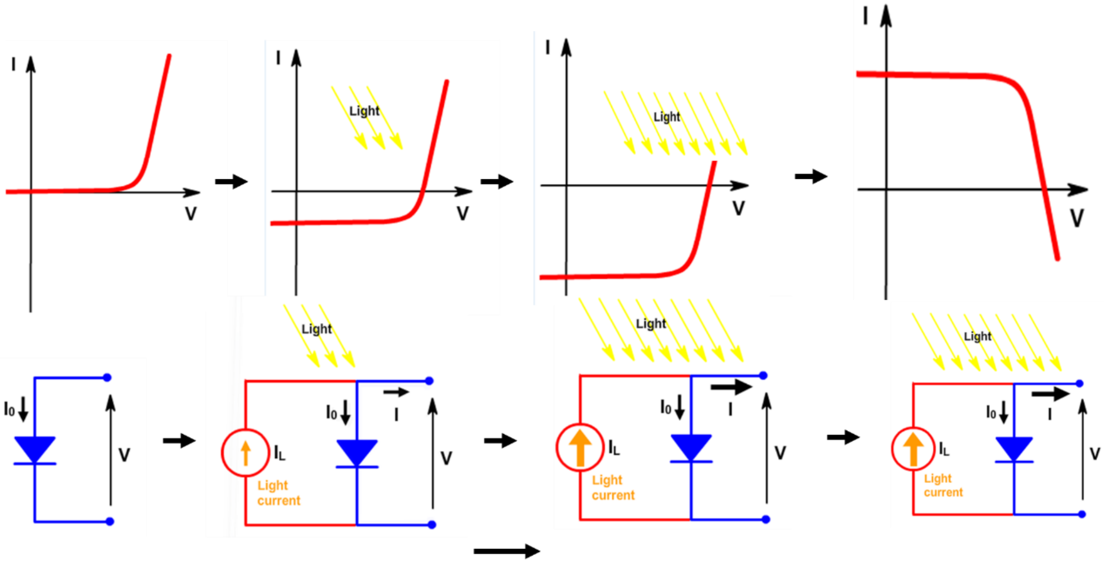

Fig 2.17: Light IV curve

2.7.1. Short circuit current

The short circuit current is the maximum conceivable current from a solar cell and it occurs when the voltage across the solar cell is zero. The short circuit commonly denoted by I_{SC} is a resultant of generation and collection of photo generated carriers and for moderate resistive losses photo-generated current is equal to short circuit current. The short circuit current depends on collection probability, optical properties of material (absorption & reflection), spectrum of light, number of photons and area of solar cell (to eliminate effect of area it is denoted as Short circuit current density J_{SC} in $\frac{mA}{cm^2}$). The short circuit current has a strong dependence on generation and diffusion length and can be approximated by the following equation.

$$J_{SC} = qG[L_n + L_p]$$

G is the generation rate, L_n & L_p are the electron and hole diffusion length respectively. The short circuit current of solar cell is shown in Fig 2.18.

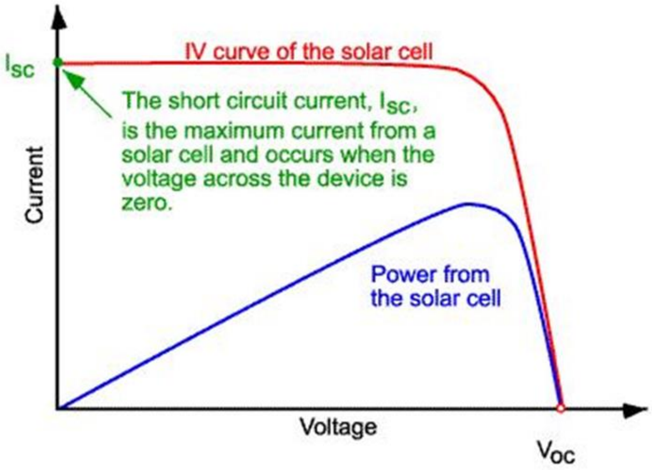

Fig 2.18: Short circuit current[134]

2.7.2. Open circuit voltage

The open circuit voltage symbolized by V_{OC} is the maximum voltage available from a solar cell occurring at current zero and signifies the forward bias on the solar cell junction due to photo-current. Fig 2.19 shows the open circuit voltage in the IV curve. The V_{OC} of a solar cell can be written as

$$V_{OC} = \frac{nkT}{q} ln\left[\frac{I_L}{I_0} + 1\right]$$

I_L & I_0 are the photo-generated and reverse saturation current respectively. I_L has a small influence on V_{OC}, while I_0 has a large influence of open circuit voltage, as I_0 changes in orders of magnitude in correspondence to the recombination in the device. Therefore, if recombination increase, V_{OC} decreases. Since I_0 is a strong function of intrinsic carrier concentration, which is a function of bandgap of the semiconductor, as bandgap increases I_0 decreases causing the V_{OC} to increase (the quasi-fermi level splits more for wider bandgap materials). Also, since I_0 is function of temperature, V_{OC} is also a function of temperature. The equation for I_0 and n_i (intrinsic carrier concentration) are given below.

$$I_0 = q.n_i{}^2\left[\frac{D_h}{L_h N_d} + \frac{D_n}{L_n N_a}\right]$$

D_h & D_n is the hole and electron diffusion coefficient, L_h & L_n is hole & electron diffusion length and N_d & N_a are donor and acceptor concentration.

$$n_i{}^2 = N_c N_v exp\left[-\frac{E_g}{K_B T}\right]$$

N_c & N_v are the conduction band and valence band states and E_g is the bandgap of the semiconductor.

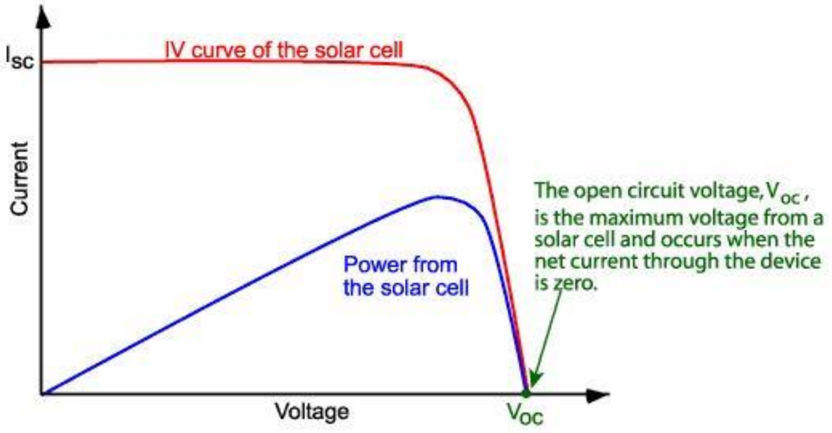

Fig 2.19: Open circuit Voltage [135]

2.7.3. Fill factor

Fig 2.20 represents the Fill factor (FF) representation of a solar cell. As one can envision, even though V_{OC} and I_{SC} are the maximum attainable voltage and current, the achievable power at these points are zero. FF helps determine the maximum power from the solar and is defined as the ratio of maximum obtainable power to the product of V_{OC} & I_{SC} and be written as

$$Fill\ factor = \frac{V_{MP} \times I_{MP}}{V_{OC} \times I_{SC}}$$

FF is the 'squareness' or measure of largest rectangle that can be drawn inside the IV curve Graphically it can be visualized that the rounded part of IV curve takes lesser area with increasing open circuit voltage (i.e. bandgap of semiconductor). For example, best Silicon lab devices have a fill factor of 0.85 while best GaAs device has a FF approaching 0.89[136]. Fig 2.20 shows Fill factor representation of a solar cell.

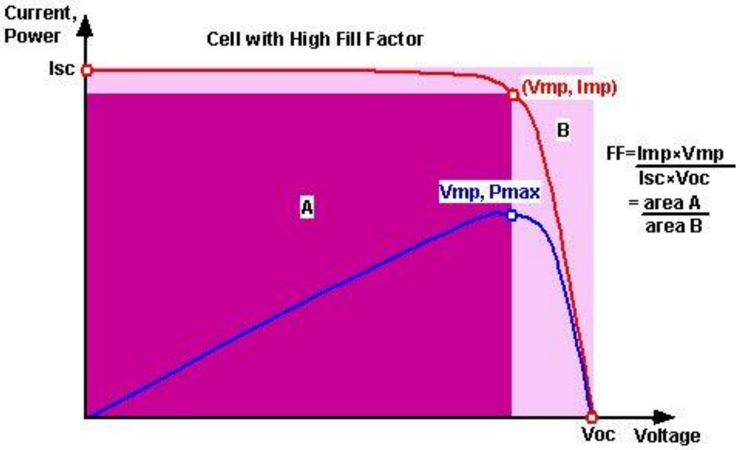

Fig 2.20: Fill factor [136]

The factor that influence the solar cell from achieving maximum fill factor are series resistance (needs to be minimum), shunt resistance (needs to be maximum) and recombination (Ideality factor n=1). As the carrier collection increases, the fill factor will improve.

2.7.4. Efficiency

Efficiency (η) is the parameter use to measure the performance of a solar cell and is defined as the ratio of output power to input power (P_{in}). It can be written as

$$\eta = \frac{P_{max}}{P_{in}} = \frac{V_{OC} I_{SC} FF}{P_{in}}$$

Since V_{OC} is a function of temperature & I_{SC} is a function of spectrum and intensity. The condition for efficiency measurement is standardized, for terrestrial solar cells efficiency is measured under AM1.5 condition at a temperature of 25^0C (room temperature). The input power for solar cell calculation is taken as 100 $\frac{mW}{cm^2}$.

An ABET 105000 solar simulator (uses a Xenon lamp) with a AM1.5G filter from ABET technologies was used to produce the full solar spectrum. Fig 2.21 shows the solar spectrum generated from ABET 105000, as one can see the ABET 105000 has additional photons in IR spectrum, these photons are not absorbed by Perovskite due to its larger bandgap. However, they need to be removed and are cutoff using the AM1.5G filter because the ABET 105000 are calibrated using Silicon solar cells and Si absorbs in the IR spectrum.

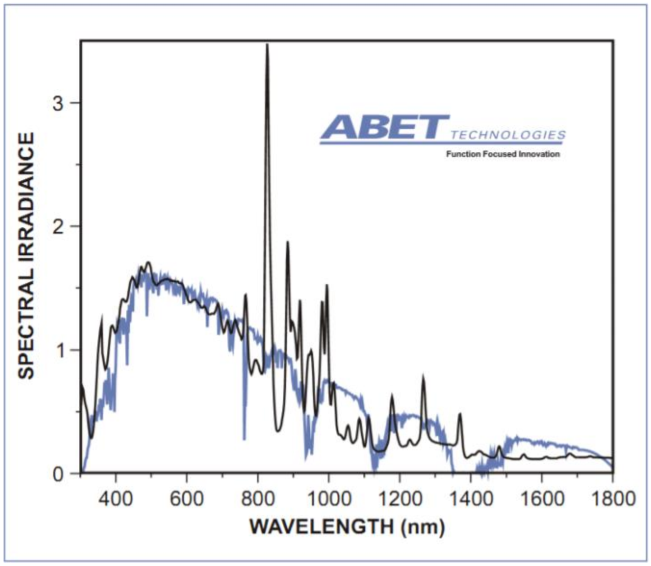

Fig 2.21: Solar spectrum ABET 105000[137]

A Keithley 236 source-measure unit run using a LabVIEW program was used to measure the IV curve. In Perovskite solar cells, direction of measurement and light soaking has a significant impact on the IV curve. Therefore, as a standard IV measurements were done from high bias voltage to low bias condition, and for hysteresis measurements it is quickly followed by an immediate sweep from low bias to high bias. The LABVIEW programs measures the open circuit voltage and short circuit current before the sweep. It starts the sweep at voltage 15% above the measured V_{OC} to a low bias of -1 Volt. Lot of information can be extracted from just the IV curve, if the current continues to increase at lower bias, then we know that there is a collection problem.

Also, if the IV curve has a double diode, we know there is a Ohmic contact issue at either the front or back contact.

2.8. External Quantum Efficiency

The external quantum efficiency (EQE) [138-141] of a solar cell is the ratio of number of carriers generated by the solar cell to the number of photons of corresponding wavelength incident on the it. If all the carriers for a given wavelength are collected then the EQE for that wavelength should be 1, however the EQE can never be 1, because even if there is no recombination and say that all photons are absorbed, there is still reflection from the film and substrate. Hence, EQE cannot be one (unless higher energy photons can excite 2 carriers). The EQE of a typical Silicon solar cell is shown in Fig 2.21.

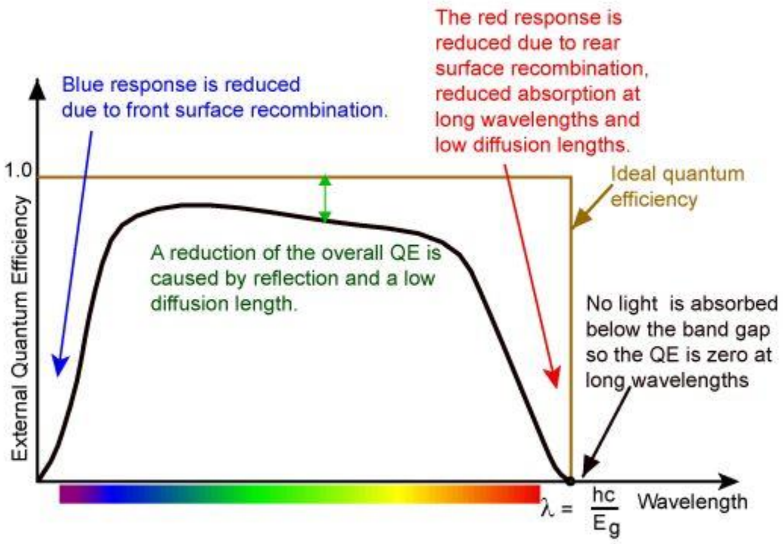

Fig 2.22: Quantum efficiency [142]

EQE can be written as

$$EQE = \frac{\#\ of\ collected\ carriers\ (\lambda)}{\#\ of\ incident\ photons\ (\lambda)}$$

The EQE is very powerful analysis tool and lot of information can be collected from its detailed analysis. EQE can be used to determine the bandgap, as EQE for photons below the bandgap of material is zero. Mainly it gives us information of carrier collection, hence diffusion length can be directly determined. Also, if one is designing Heterostructures for carrier collection, then surface recombination either front/back service can be known from EQE. Also, the thickness of the device required for optimum carrier collection can be experimentally determined using EQE.

In addition to above, EQE has been used for obtaining information on $\mu\tau$ product, band-tail and mid-gap defects, mechanisms of degradation, optimizing tandem-junction and graded junctions cells by V.L. Dalal et al [1986][138].

A schematic of the QE measurement set up is shown in Fig 2.23

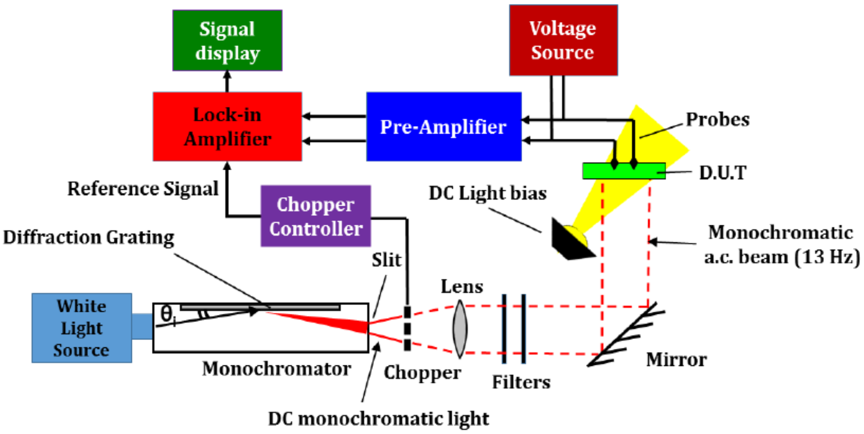

Fig 2.23: QE measurement set up[112]

A halogen lamp generates white light which is monochromatized, the incident lights photon flux is known using a reference solar cell (Silicon) whose EQE at different λ is known. Following this the sample solar cells signal is measured and EQE is obtained by comparing the sample's signal with that of reference using the following equation:

$$EQE = \frac{Signal\ from\ sample(\lambda)}{Area\ of\ sample} \times \frac{Area\ of\ reference}{Signal\ of\ reference(\lambda)} \times QE\ of\ reference(\lambda)$$

Higher order harmonics from the monochromator is cutoff using necessary filters, also unwanted signal such as external lights in the measurement room or from unknown interfering electromagnetic noise is isolated using a lock-amplifier.

2.9. X-ray Diffraction [143]

To observe objects, a source of rays and detector is required. However, atoms whose atomic radii are from few tenths of an angstrom to few angstroms are too small to be distinguished using normal light sources. X-rays have wavelength ranging from $\sim 0.1\text{Å}\ to\ \sim 100\text{Å}$. The X-rays sources used in crystallography range from $\sim 0.5\text{Å}\ to\ \sim 2.5\text{Å}$, as they correspond to the shortest interatomic distance of all observed inorganic and organic compounds, also, they can be easily generated in laboratories.

When X-rays propagate trough a substance, the following processes occur:

1. Coherent scattering, produces photons of same wavelength as incident beam (no loss of energy)
2. Incoherent scattering, produces photon of longer wavelength due to partial loss of photon energy in collisions with core electrons (Crompton effect).
3. Absorption, photons are dissipated due to random direction scattering, also loss of photon energy due to photoelectric effect.

Only coherent scattering results in diffraction. It’s know that when waves interact with point object, the outcome is a new wave that scatters in all direction, with origin of wave coinciding with object. If no energy loss occurs, the resulting wave has same frequency of incident wave and we refer to the process has elastic scattering. If two or more-point sources are involved in the elastic scattering process, they all produce spherical waves which interact with one another.

If two scattered waves are propagating parallelly, in complete phase, their amplitude is doubled (constructive interference) and if they are completely out of phase they distinguish one another (destructive interference).

Constructive interference that occurs between periodic array of points, increases the amplitude of resultant wave by many orders of magnitude and this phenomenon is the corner stone of powder diffraction. In 1913-1914, W.H. Bragg and his son W.L. Bragg formulated Bragg’s law that related diffraction angle, wavelength and interplanar spacing, the crystal structure can be determined from Bragg’s law and it is written as follows

$$n\lambda = 2dsin\theta$$

Fig 2.24 shows a schematic Bragg-Brentano diffractometer and elastic scattering of incident waves.

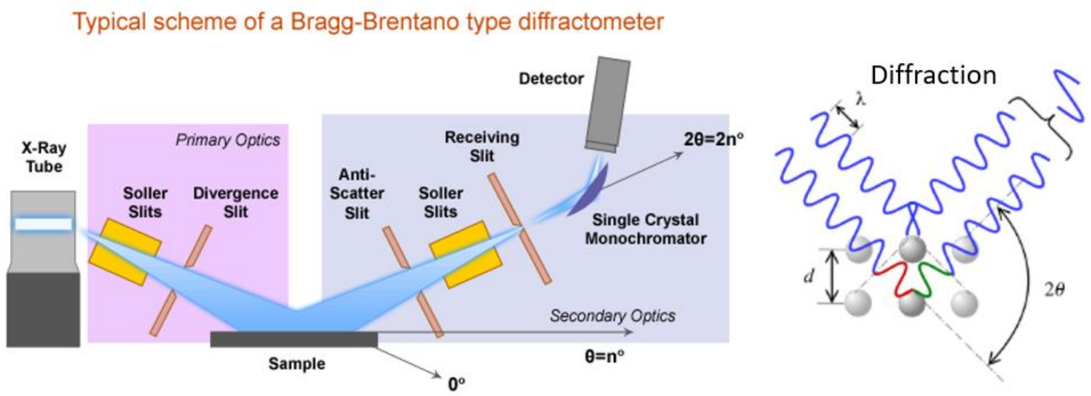

Fig 2.24: X-ray Diffractometer [144]

It is important to note that X-rays scatters from electrons, more precisely the electron density which is distributed periodically in the crystal lattice. Other types of radiation like neutron and electron beam can also diffract from crystals and produce diffraction pattern and give crystal structural information. Unlike X-rays, neutrons are scattered from nuclei and do not suffer from atomic scattering factor, while electrons interact with electrostatic potential. Since, nuclei (for neutron diffraction), electron density (for X-ray diffraction) and electrostatic potential (for electron scattering) are distributed equally in the same crystal, Neutron, X-ray or Electron diffraction can all be used for obtaining information on crystal structure. The key difference in them is the comparative differences in the intensity of the diffracted signal.

2.10. Scanning Electron Microscopy[145]

The Scanning electron microscope (SEM) uses a high-energy focused electron beam to scan a sample and produce an image. Electron beam is produced via thermal or field emission using an electron gun. The beam is focused using electromagnetic lenses and rastered across the sample using scanning coils. The primary electron beam interacts with the electrons present in the sample and generates different kinds of signal, such as Secondary electrons (SE), Backscattered electrons (BSE), Auger electrons, Cathodoluminescence, Phonons, Plasmons and Characteristic X-rays. These signals provide information on samples surface topology, chemical composition, crystallography etc. in accordance to the application. Most SEM's are mainly used for Secondary electron imaging, Backscattered imaging and for EDS purposes.

Secondary electrons (SE) are generated by the interaction of the electron beam with the electrons in the conduction band of the sample. On interaction, the conduction band electrons gain kinetic energy and are ejected and mostly have energy in the range of 5-10eV. 50eV is considered the cut-off for secondary electrons. Since they are low energy electrons they do not have energy to propagate through the surface of the material, therefore they are restricted to the surface i.e. 100 nm of the surface. These electrons help produce topographical information of the surface. Increasing the tilt can increase the SE generation, as it increases surface volume interaction of the electron beam. SE imaging is ideal for rough imaging rough samples.

Back scattered electrons (BSE) are generated due to elastic scattering of the electron beam and increases with increase in atomic number of material. High Z material has high BSE coefficient. Change in tits also increase BSE generation, however the increase is not much as in comparison with how much it increases with Atomic number. BSE image produces an atomic contrast image of the sample, therefore are useful for imaging samples that are flat, polished with varying Z contrast.

When high energy electrons strike a sample, the collision can cause the tightly bound inner shell electrons to be ejected, leaving the atom in an excited state. This leads to a transition of electrons from higher energy shells to lower energy shells and the excess energy of the higher energy shells are released as characteristic X-ray photons. The energy of the X-ray photon is characteristic of the material and used for quantitative and qualitative analysis in EDS. Fig 2.25 shows a schematic of SEM.

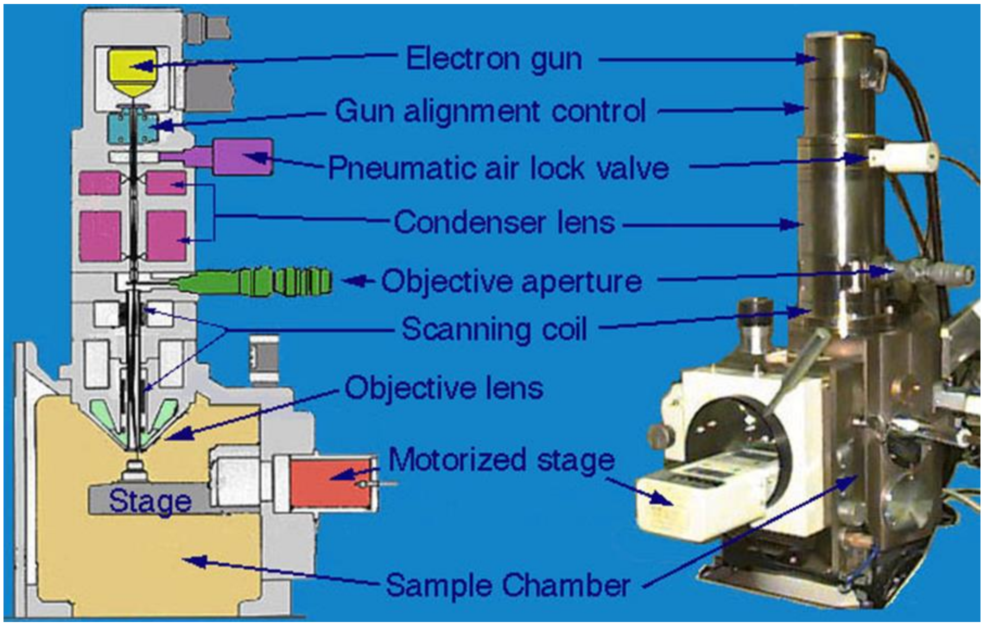

Fig 2.25: Scanning Electron Microscope[146]

2.11. Basic Device Terminologies

The supporting structure that we grow thin films on is called a substrate and based on thin film solar cell designs we can distinguish them further into substrate and superstrate. If the substrate acts as only a supporting structure we call them as substrate, however when they act as both as supporting structure and window to the incident light, they are known as superstrates. Superstrates solar cells are comparatively cheaper as we save on encapsulation cost, also, they act as UV filters. Perovskites solar cells in this work are all based on superstrate design.

In Perovskite structure, we use both n-type Type & p-type Type II heterojunction for corresponding carrier extractions. If light is incident on the solar cell through n-type Type II heterojunction, by convention we refer to this device architecture as NIP. In the contrary if light enters through the p-type Type II heterojunction, we refer to this architecture as PIN. Fig 2.26 shows the two superstrate architectures.

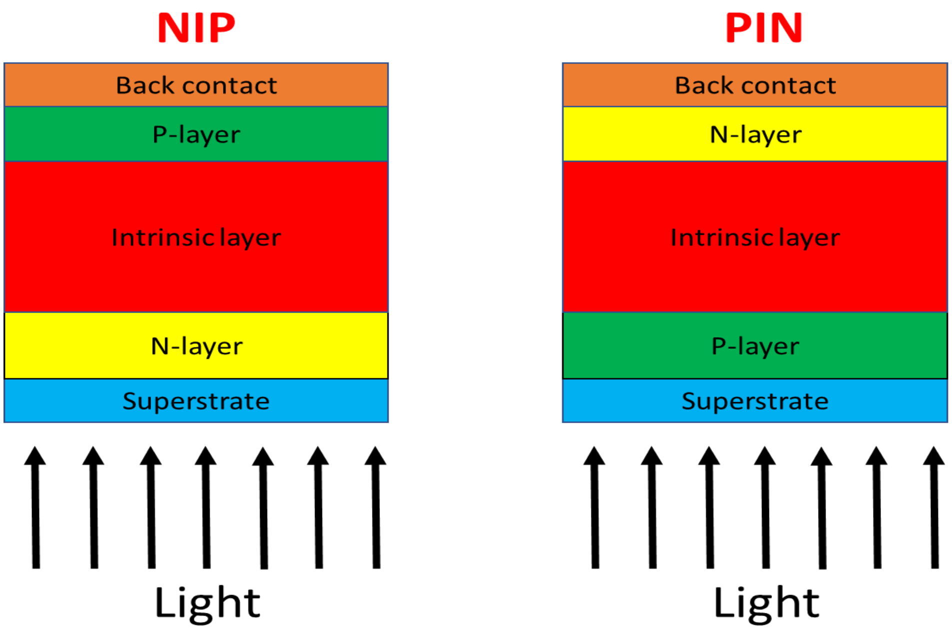

Fig 2.26: PIN vs NIP

CHAPTER 3

PROCESS DEVELOPMENT AND SYSTEM DUILDING

A striking advantage of Perovskites solar cells is the different ways one can fabricate it. A variety of solution and vapor based approaches have been reported till date that includes one step spin coating[147-149], two step techniques[14, 150], solvent-solvent extraction[150], vapor assisted solution process[26, 151, 152], Co-evaporation[55, 153-158], hybrid deposition[159-161], hybrid chemical vapor deposition[162, 163], sequential vapor deposition[164, 165], flash evaporation [166]etc. The multiple ways of film depositions and ability to have low temperature process has given researchers the ability to coat and process on flexible substrates too. Fig 3.1 shows the multiple ways of Perovskite film deposition.

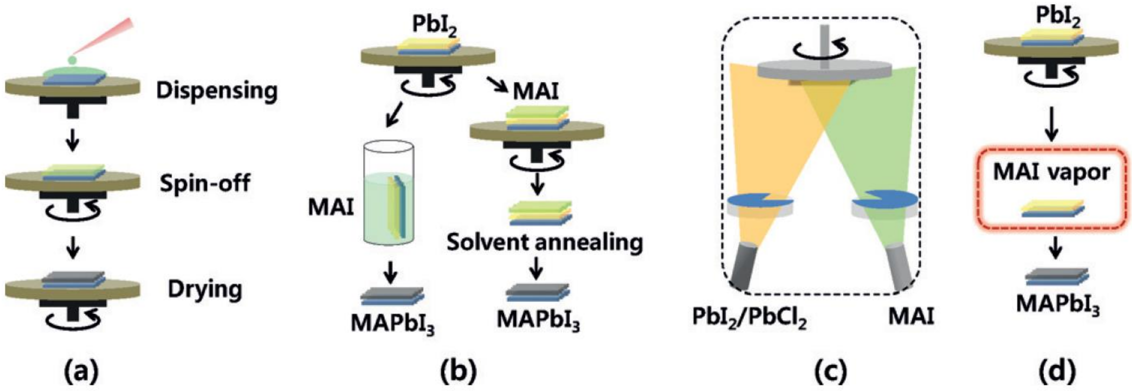

Fig 3.1: Film deposition techniques[167]

Solution and vapor approach, both show potential in regards to scalability. Solution could work out cheaper, however the remnant solvent in the material brings a query on the stability of solution device over vapor. As we know, stability is one of the biggest concerns with respect to perovskite material. Vapor deposition is a mature technique and is presently being used in Thin film solar cell industry, Liquid-crystal display industry, glazing industry etc. In addition, vapor deposition technique is process compatible with the methods of both Silicon based and Thin film based solar cells for Tandem applications. In the future, if stable higher efficiency vapor devices are possible, we might already have the infrastructure required in place to scale up this technology. Vapor processing has numerous advantages over solution processing.

1. High purity films will be formed by sublimating the powder precursors after extensive outgassing under a vacuum environment
2. Precise stoichiometry can be obtained irrespective of the precursor using vapor approach. This is complex via solution method due to solubility limits, for example, if one wants to make mixed halide perovskite ($MAI_{3-x}Cl_x$) perovskite using solution approach, the precursors will not dissolve in DMF for higher $PbCl_2$ ratio, the highest mixable concentration in DMF for $PbCl_2 : MAI$ is 1:3.
3. The commonly used solvents in solution devices such as DMF (Boiling point~153^0C), DMSO (Boiling point~189^0C), Water (Boiling point~100^0C), Chlorobenzene (Boiling point~131^0C) etc. have relatively high boiling points in comparison to degradation temperature of perovskite film as we will see in Chapter 5. Most, solution processed devices are annealed at a mere temperature of around 70~120^0C [168-170], at these temperatures it is unlikely that the solvents are completely driven away and there is a high likelihood that solvents are intercalated between grains or crystallites.
4. With vapor deposition it is possible to make several stacks of films for multilayered structure[165], this is not possible via solution approach. Since, the solvents will wash away the underlying structure.

5. Vapor Perovskites films can be evaporated on any substrates, the wettability issues is not a concern (Fig 3.21) when it comes to vapor evaporated Perovskites. This is somewhat of problem when it comes to solution devices, as DMF solvents will not wet most polymer transport layers (Poly-TPD, PCDTBT, P3HT, PTAA etc.) other than Pedot-PSS.
6. Contrary to popular belief Perovskite is a field controlled device [171], precise thicknesses ~300nm is vital for good charge collection. Optimizing the concentration and spin speed of solution for obtaining exact thickness is tedious and exhaustive. Vapor approach gives you precise device thicknesses easily.

In this thesis, we will consider different vapor based fabrication approaches, study their advantages and disadvantages, and modifications that we had to impart on deposition tool and discuss tool building. The tools designed and modified by us had to make systematic changes based on issues faced and practicality for making highly efficiency consistent vapor based devices. There are two primary approaches for making vapor devices:

1. Sequential evaporation
2. Co-evaporation.

3.1 Sequential Evaporation

Sequential vapor approach was first proposed Yang Yang et al, and is shown in Fig 3.2. The approach takes advantage of kinetic reactivity of MAI.

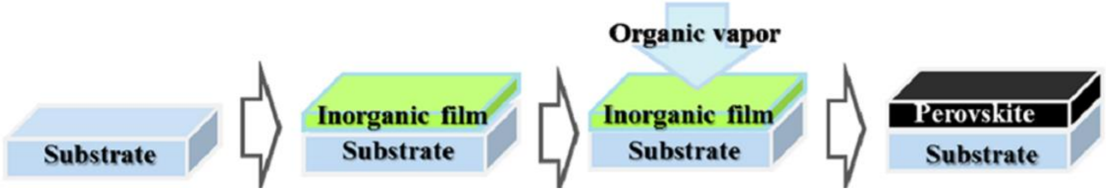

Fig 3.2: Vapor assisted solution process[172]

Yang Yang et al used a NIP architecture: FTO/TiO_2/Perovskite/Spiro meotad/Silver. The steps suggested in the original paper was as follows: PbI_2 (0.87 Molar solution) was spin coated on FTO/TiO_2 following which it was annealed in a petri-dish with MAI at $150^0\ C$ for 4 hours. However, there were many issues with this approach.

Our goal has always been to make consistent and reproducible high efficiency devices and this was not possible using the original recipe, so we decided to use the above idea but change the processing methods. Numerous studies were conducted by us to understand the mechanisms involved and in optimizing each layer of our architecture and by using results from IV, QE, SEM, EDS, XRD & optical imaging (pin holes), we attained our goals. The processing modifications we applied will be discussed in detail. Recipes also had to be modified corresponding to device architecture (NIP or PIN) and precursor used (MAI or FAI). We will start the discussion with NIP (MAI), followed by PIN (MAI) and finally NIP(FAI).

3.1.1. NIP sequential devices

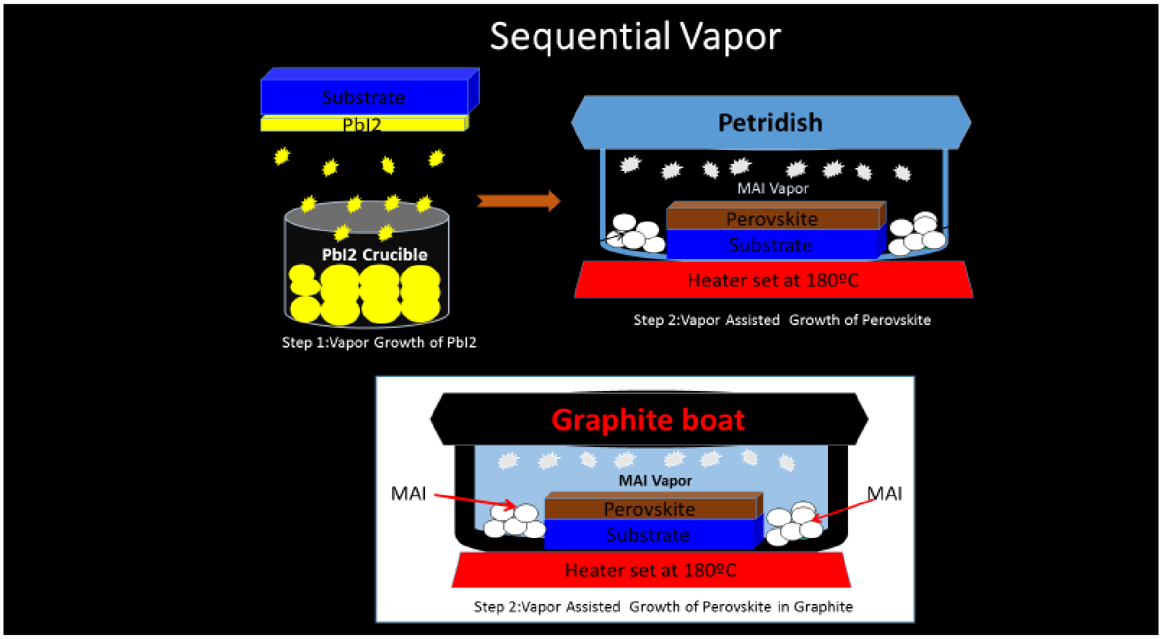

Fig 3.3: Sequential Vapor using Graphite

Fig 3.3 shows the NIP sequential vapor deposition process PbI_2 is vapor deposited followed by MAI vaporization. Instead of petri-dish, we used a Graphite boat. The fabrication steps are follows:

3.1.1.1. Transport layers

Titanium dioxide is used as our n-type Type II heterojunction, it has a wide bandgap of ~ 3.5eV[173] [174], its conduction band edge lies at ~ 4.0eV (Fig 1.16) and valence band edge lies ~7.5 eV (Fig 1.16), making it a good n-type Type II heterojunction for perovskite whose conduction band edge is at ~3.85 eV & valence band edge at ~5.4eV (Fig 1.16). Therefore, allowing collection of electrons while blocking holes, the TiO_2 film was deposited using spin coating and its recipe is given below.

The TiO_2 film was spun coated and its recipe is follows: 0.15 M and 0.3M titanium Diisopropoxide Bis(acetylacetonate) (Sigma Aldrich) is spun coated at 6000 rpm for 30 s subsequently. Post drying at 125°C for 10 min, they are sintered at 550°C for 15 min in air. The substrate is then immersed in 50 mM TiCl4 (Aldrich) aqueous solutions for 30 min at 70 °C and washed with distilled water and isopropanol, followed by annealing at 550 °C for 30 min in air to form a compact n-type layer of TiO_2. Fig 3.4 shows the transmission of TiO_2, it has 90% transmission.

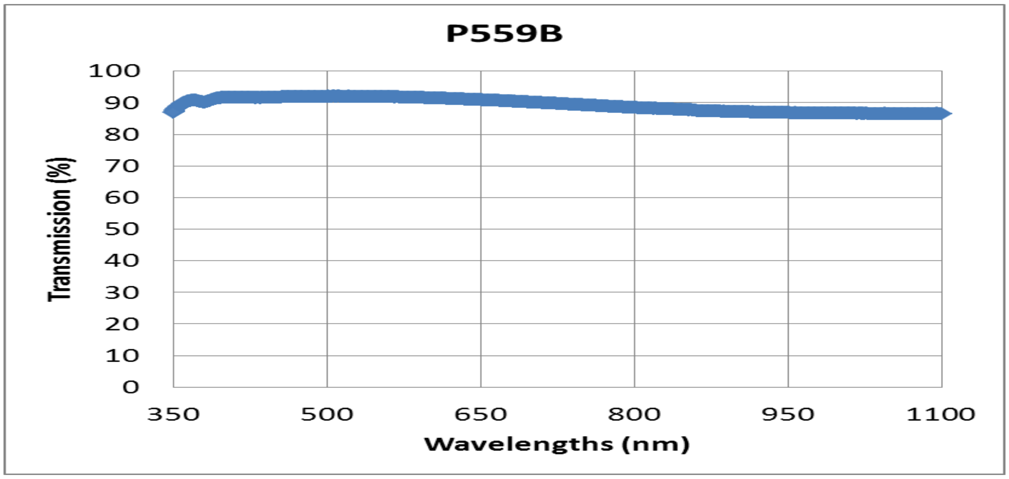

Fig 3.4: Titanium Dioxide transmission

Before, the p-type Type II heterojunction is mentioned, we need to go back to the timeline of this work. This work was performed in the beginning of 2014, at that time the material was still new to everyone. The highest efficiency at that point for NIP vapor and solution was only 15% [14, 15] and all groups used TiO_2 and Spiro-meotad as n-type and p-type Type II heterojunction respectively. However, we chose a different path and the reason being for Spiro to work Lithium salt had to be added as a dopant, that bothered us a Lithium is known to diffuse[175-178] through in materials and not much was known about Spiro either, it was also novel to PV applications [41, 42].

Hence, P3HT (1-Material) is used as our p-type Type II heterojunction. As one knows, P3HT is crystalline for polymers [179] , and most studied in regards to organic polymers and we had experience with this polymer. Its conduction band edge is at 2.9 eV and valence band edge is at 5.1 eV [180], thus, making it a good candidate for p-type Type II heterojunction. The optimized recipe for P3HT was found is given and it corresponded to a thickness of 30nm. The results will be discussed in Chapter 4 and this work was published [181].

P3HT concentration: 12mg/ml in Chlorobenzene

Spin speed: 4000 rpm

Annealing condition post spin coat: 110^0C/15mins in Glove box [Nitrogen Ambient]

3.1.1.2. Metal contacts

Pure gold with a work function of ~5.3-5.4 eV[182] makes a good contact with P3HT and hence used as our back contact (hole extraction). 80-90nm of gold (Ames lab) was deposited using Thermal evaporation on P3HT at a rate of 15-20 $Å/s$ and typically 1 gm of gold was used per run.

FTO coated glass (Pilkington), the transparent conducting film with a work function is ~4.2-4.4 eV [183] makes a good contact with TiO_2 and hence, used as our front contact.

3.1.1.3. Thermally evaporated lead iodide

The key reason for evaporating Lead iodide is so that the active layer is devoid of any solvent and groups have shown that perovskites form complexes with solvents like DMF[184], DMSO [168] and H_2O [185]. Hence, it was important to move away from spin coating of Lead iodide. Another problem we encountered spin coating PbI_2 was that it was inconsistent from one film to the next and this will be highlighted using both SEM and Optical images of lead iodide films. Fig 3.5 shows variation in the morphology and grain size of spin coated PbI_2 on FTO/TiO_2, also some of the films are porous which could create significant differences in the eventual grain size.

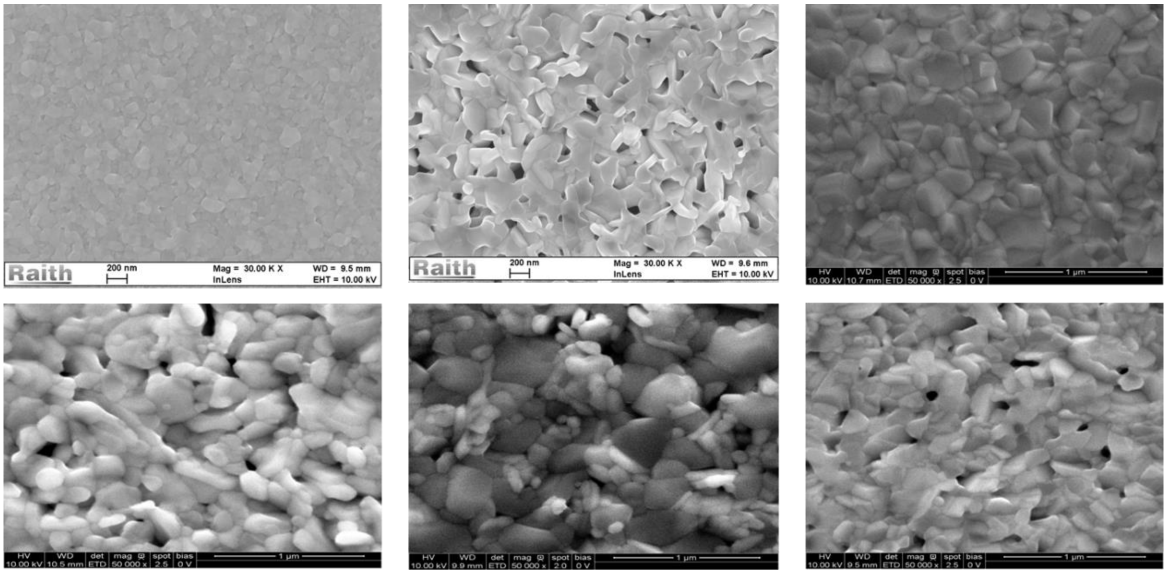

Fig 3.5: SEM images Spin coated PbI_2

These variations arise from reasons as simple as the order in which one spin coats substrates to age of solution. The solution [DMF+PbI_2] is stirred overnight in hotplate at 80^0C for spin coating next day morning, for the first spin coating the temperature of PbI_2/DMF solution is say ~ 80^0C, however for the successive spin coating the solution temperature is different as PbI_2 takes time to attain the same temperature, spin coating cold solution is not an option, as PbI_2 will start to crystallize if the DMF solvent is not at hot temperature. Also, every time you open the bottle for spin coating the concentration is increasing considering that DMF's flash point is 58^0C.

In regards to the age of solution, it's not practically possible to do experiments at exact time every single time. And thus, keeping for 12hrs to 18hrs might bring about changes in the concentration and miscibility of solutions, also the solution is stirred in glass vial's which are not conflat flange sealed, so concentration will change in regards to how long the solution is stirred. Fig 3.5 shows the differences in grain size of hybrid Perovskite (PbI_2 is solution and MAI is vapor) because of varying morphology of PbI_2 on FTO/TiO_2 superstrate.

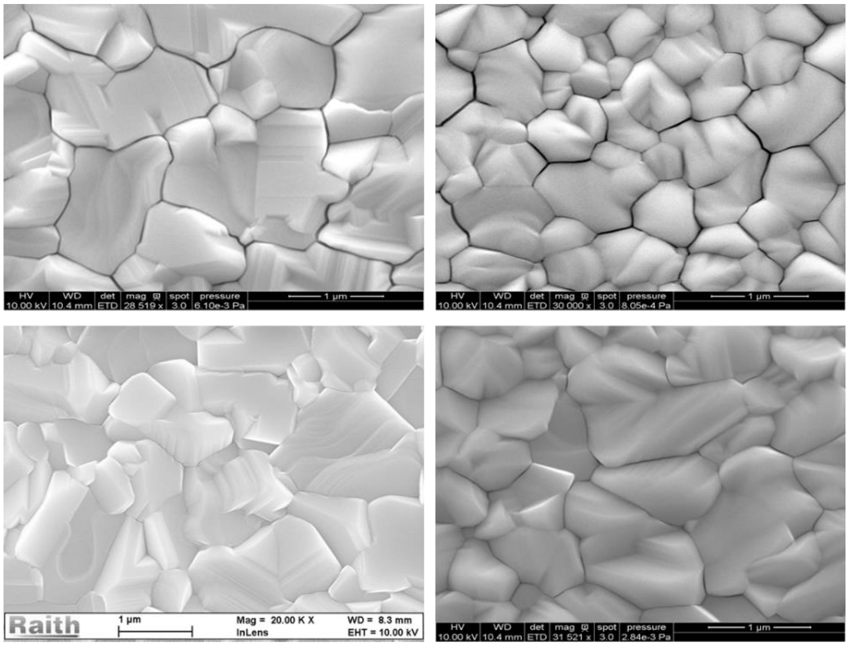

Fig 3.6: SEM images Hybrid Perovskite

Though, from a device point of view grain morphology of PbI_2 is unimportant, nevertheless it influences grain size of perovskite and thus, is a serious concern. We require as large a grain as possible to counteract the effect of grain boundary recombination and enhance carrier collection and if there is variation in grain size's, device performances will differ. Hence, we vaporized PbI_2. Fig 3.7 shows the morphology of evaporated PbI_2 on different sample's, they have the same grain structure and packing density.

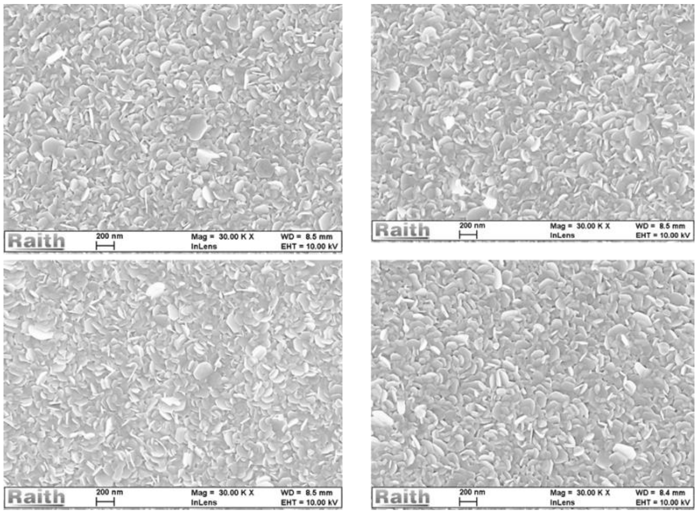

Fig 3.7: SEM images Vapor PbI_2

In addition, to have consistent morphology, the PbI_2 films were pin-hole and consistent from run to run. Fig 3.8 shows optical images of PbI_2 film with light shining from bottom.

Fig 3.8: Optical images PbI_2

PbI_2 was evaporated thermally using Radak furnaces[186] from Luxel, Fig 3.9 shows an image of the thermal evaporator with the Radak furnace installed and PbI_2 crucible.

Fig 3.9: Thermal evaporator- Radak furnace

3.1.1.4. Graphite boat Perovskite formation

Device to device consistency is crucial and the MAI vaporization procedure in the petri-dish was highly inconsistent. Not just in mere device performance, but in perovskite formation itself. The procedure as described by Yang Yang was to keep the PbI_2 coated substrate in a petri-dish surrounded by MAI followed by heating the dish to 150^0C in glovebox. And on doing so the film will turn from yellow to black, signifying the formation of Perovskite. Fig 3.10, shows an image of substrate in the petri-dish before and after perovskite formation (ideal case).

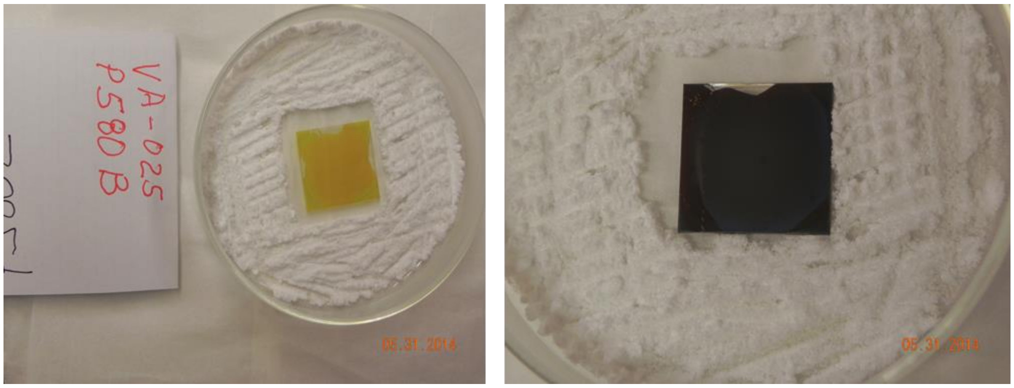

Fig 3.10: Ideal perovskite formation Petri-dish

However, this does happen always, often the perovskite is incomplete and films look different, creating a device to device variance. Fig 3.11, shows images of 16 perovskite films, each one looks different.

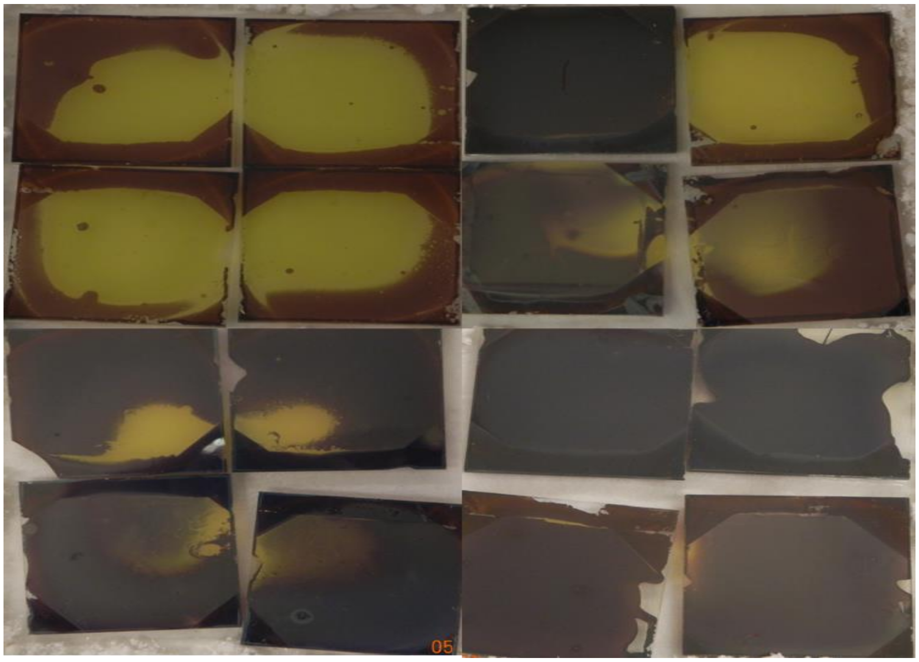

Fig 3.11: Incomplete perovskite formation Petri-dish

The reason for incomplete perovskite formation is that the petri-dish does not seal the MAI vapor efficiently, hence there is no build of MAI vapor inside the dish leading to insufficient concentration of MAI for both nucleation and grain formation and can be explained using Lamer-

Dinegar model. Fig 3.12 describes the model that is based on classical nucleation theory [187, 188].

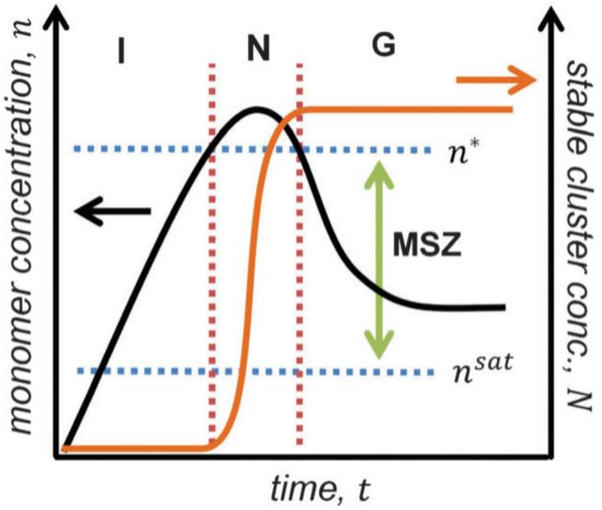

Fig 3.12: Lamer Dinegar model [188]

In fig 3.12, ‘I’ represent the induction regime, ‘N’ is the nucleation regime, ‘G’ is grain growth regime, n^* is the minimum concentration required for nucleation and n^{sat} is the minimum concentration for grain enhancement i.e. grain enhancement will take place when concentration (n) is between concentrations i.e. $n^{sat} < n < n^*$. This is represented by MSZ, the metastable zone where growth of existing grains, absent nucleation, occurs. Below n^{sat} nothing happens, concentration is insufficient for both grain growth and nucleation.

The black line in Fig 3.12 represents the changing concentration, while orange line represents nucleation and grain growth. This model will be used for future explanations. The model describes that a minimum MAI concentration is required for nucleation to start and once it starts, MAI concentration decreases as the precursor is being used up for creating perovskite nucleation site followed by grain growth. But, as MAI pressure does not build effectively in petri-dish to sustain MAI flow, both nucleation and grain growth is incomplete in petri-dishes.

In addition, the petri-dish had lot of static charge, causing MAI to stick on the lid while closing the dish and these particles eventually fall onto the PbI_2 coated films creating pin holes in the perovskite, hence shorting the device. Hence, we decided not to proceed further using petri-dish. The new material had to have the following properties:

- Conductor (to avoid static build-up)
- Non-metal (as MAI etches metals-will be discussed)
- Heavy or screw able lid (to build vapor pressure)

A material that satisfies all these requirements was high density Graphite. Fig 3.13 shows images of the graphite set up, and the films pre-and post-Perovskite formation. The films made using graphite was pin-hole free and very consistent, device results will be discussed in Chapter 4.

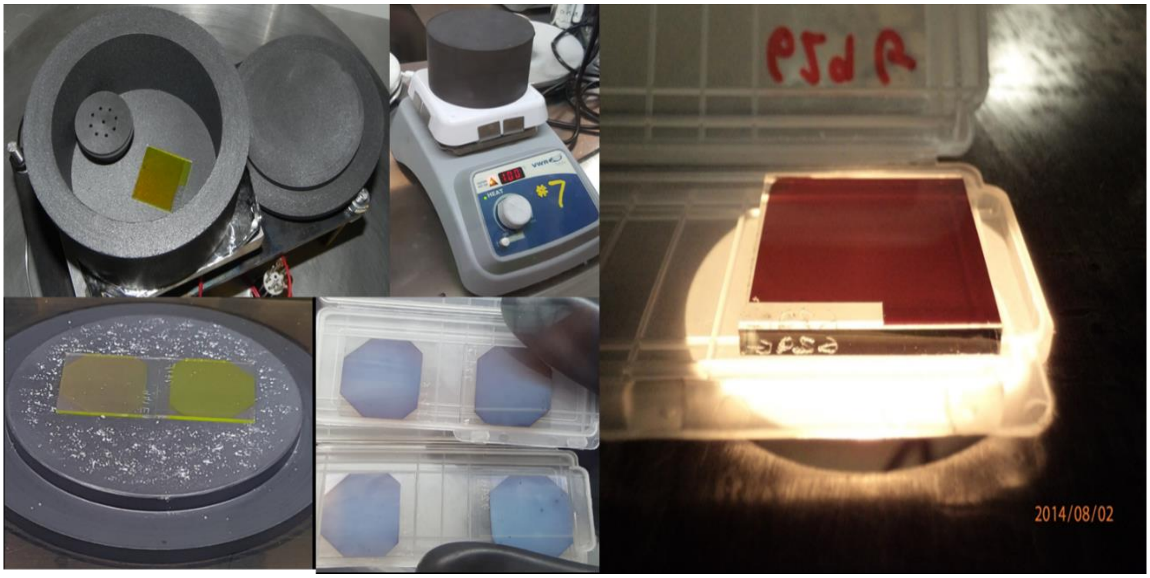

Fig 3.13: Graphite set up & film

The temperature for MAI vaporization in the glovebox was set at 180^0C and duration was 3hrs (though the films form in ~2hrs) for grain enhancement purposes as per Ostwalds ripening [189, 190]. Since large grains are thermodynamically more stable grow, if annealed for longer durations the larger ones will grow at the expense of less stable smaller grains. The thicknesses of film formed ~350nm (for $PbI_2\ thickness{\sim}160nm$).

Also, the MAI temperature was ramped up in steps to form lesser nucleation sites i.e. instead of increasing the temperature rapidly to 180^0C, it was increased in steps of 10^0C starting from 130^0C to final temperature of 180^0C. Figure 3.14 shows image of rapid increase (left) and step increased (right) perovskite film, clearly step increased film has larger grains. This can be explained using the model of nucleation shown earlier in Fig 3.12, when concentration increases above n^*nucleation starts, however if concentration increase above n^* is not rapid, then the number of nucleation sites is reduced and the subsequent MAI flow goes towards grain enhancement.

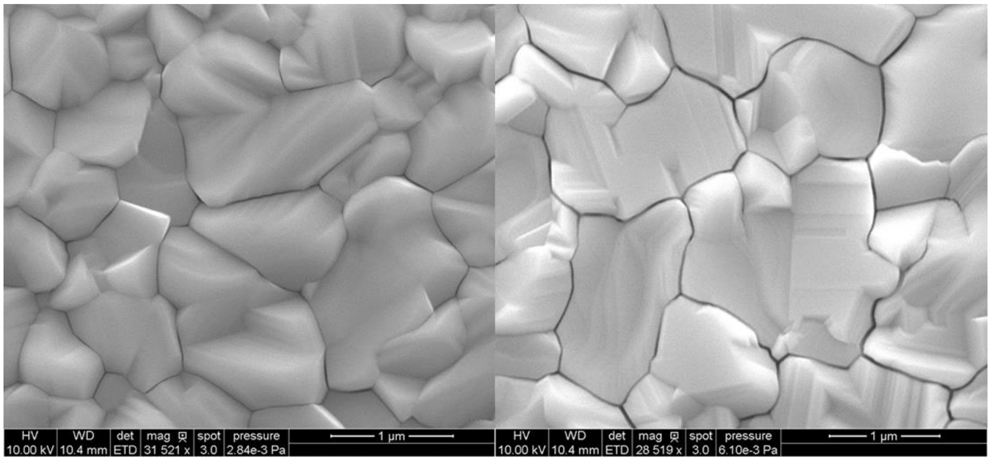

Fig 3.14: Grain size (NIP): Rapid increase (L) vs Step increase (R)

3.1.1.5. Vacuum annealing

Even though we were making high quality pin-hole free films, we were encountering other issues that was affecting device performances and required our attention. The main problem we were facing is that excess MAI is now being deposited on top of the film, this caused series resistance to increase and the fill factor we were getting was in the 0.48-0.52 range (Chapter 4 will discuss results), and if one observes Fig 3.13 and looks at the image of the 4 films, all films appear whitish in the top, this is due to the excess MAI and it needs to removed. So, we founded this new technique to remove the excess MAI and termed it Vacuum annealing(VA).

Vacuum Annealing is a simple technique which takes advantage of high vapor pressure of MAI [160, 191]. MAI has very high vapor pressure and any vacuum deposition system exposed to MAI, will outgas MAI till is scrubbed or cleaned with Isopropanol(IPA). For now, to just to get a feel of vapor pressure of MAI, let us look at vapor PbI_2 films (Fig 3.14) that was evaporated in the co-evaporation chamber (will be discussed in next section) before and after chamber clean-up, the film in left looks like perovskite though it was intended to be only PbI_2. What happened during the run is that MAI in chamber outgassed and caused perovskite to form (at room temperature). But, the film on the right is yellow, since the chamber was scrubbed and cleaned with IPA. The whole point of showing the films (Fig 3.15) was to visually explain that MAI has high vapor pressure.

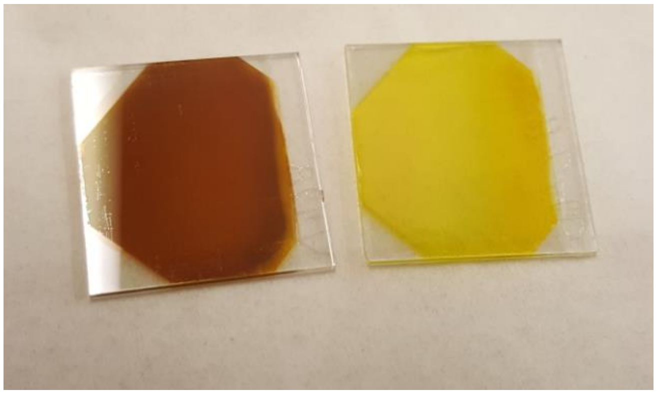

Fig 3.15: PbI_2 films Co-evaporator

Since we knew that MAI has high vapor pressure, we came up with a new idea to take advantage of this property. So, we took the as the deposited Perovskite films and annealed at 100^0C (indicated temperature) for 1 hour in vacuum chamber that was specially built for this purpose. On doing so, the excess MAI from the film was detached, thus decreasing the series resistance and improving device performance. As it is difficult to capture the differences in the white-tinge at the surface using a camera, we came up with an experiment to capture it. We put metal contact masks on the film and carried out the vacuum annealing procedure, the film appears different at the contact locations. Fig 3.15 shows the differences in film quality and one can visually observe that excess MAI is removed by our new technique.

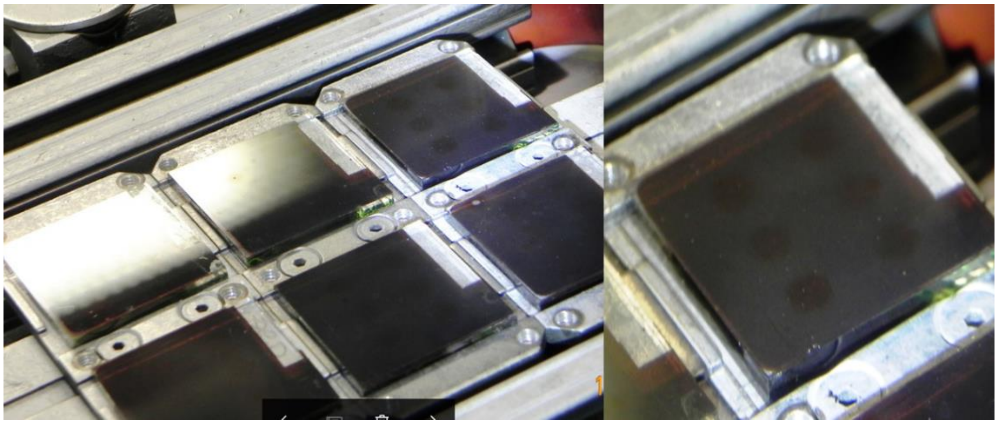

Fig 3.16: Vacuum Annealed films

The vacuum annealing was done in a system which we refer to as the Small Bell Jar (SBJ). The system has a rotary pump and a turbo pump that pumps it down to ~ $4\times10^{-6}\ Torr$, it has stage with heating capabilities powered by a Variac variable transformer. It is important to recognize that vacuum annealing is a technique for fine tuning performance and must be used appropriately. Fig 3.16, shows images of the film kept on the heating plate and the Vacuum anneal system.

Fig 3.17: Vacuum Anneal set up

3.1.1.6. Sequential vapor limitations: FTO vs ITO

If one looks up the literature of sequential vapor devices, one would notice that all devices made till date are on FTO, there is not a single device that is made on ITO and the reason is very intriguing. It is due to the acidic and etching nature of MAI. Before Dysol [192] sold MAI, all group including we made our own MAI. MAI is made from methylamine and hydroiodic acid [HI] [193], HI is very strong acid and etches anything that is metallic and there arises the fabrication dilemma. It also etches through some of sensor's, pumps, value's etc. and we will talk about in co-evaporator section. Now if we consider, FTO (Fluorine doped Tin Oxide) and ITO (Indium doped Tin oxide), FTO is doped with fluorine, a halide dopant while ITO is doped with Indium, a transition metal. As explained earlier, when MAI is heated, it breaks up into methylamine and HI, and the HI attacks (etches) ITO. On heating an ITO substrate in MAI ambient at $150^0\ C$, it resistivity changed from $10^{-4}\ \Omega - cm$ before heating to $10^8\ \Omega - cm$ after heating. Fig 3.17 shows images of ITO substrates that were used for sequential vapor process, as one can see the substrate looks disoriented.

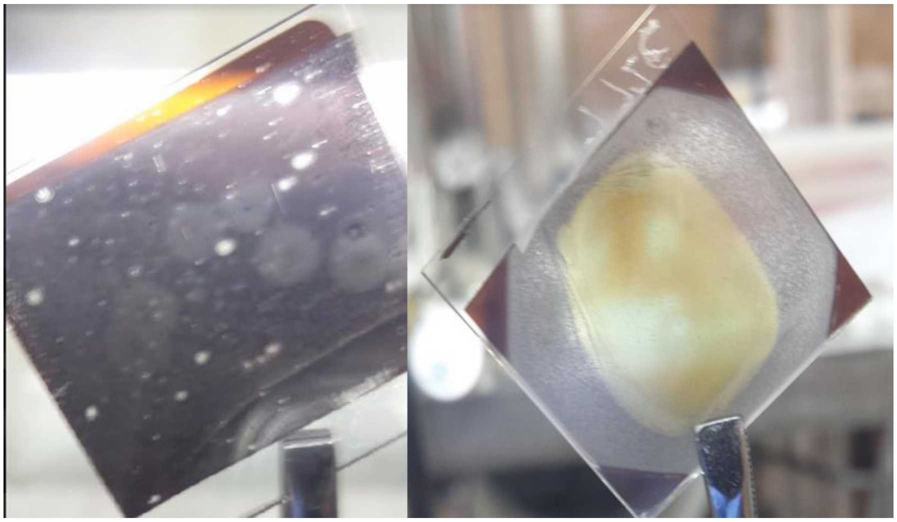

Fig 3.18: ITO substrates attacked by MAI

Fig 3.19 is a supplementary image to show the reactivity of MAI. One of the vacuum systems that had exposure to MAI has a gold-plated electrode as part of its internal wiring. The MAI in the system in due course etched through the gold plating. The image also shows how the electrode (right) would have looked if not attacked. Hence, sequential vapor can only be performed on FTO substrate and this is of concern as for making PIN devices ITO is required, as it has better band matching (band diagrams on device architecture for PIN's will be shown in Chapter 4 & 6).

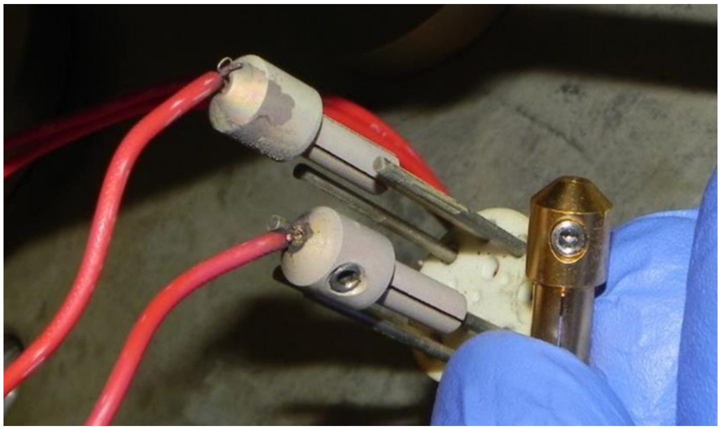

Fig 3.19: Gold plated electrodes etched my MAI(left)

3.1.2. PIN sequential devices

For PIN architecture, ITO is ideal for band matching, however ITO cannot be used for reasons explained above. FTO can be used if there is tunnel junction, i.e. the Type II heterojunction matched with FTO should be highly doped, else you won't have an ohmic contact. NiO_x is a good option for p-type Type II heterojunction and works well on FTO for solution devices, however it is attacked by MAI at higher temperature and patterns can be seen on the films when heated in MAI ambience as seen in Fig 3.20

~

Fig 3.20: Nickel oxide based Sequential Vapor Perovskite.

As, we ran out of options in the inorganic side, we decided to use Organic materials for making p-type Type-II heterojunction. Though there are many organic materials with a valence band of ~5.3 eV (Fig 1.16). Nevertheless, the organic material needs to be highly doped else it cannot make a tunnel junction with FTO. Pedot provides good band matching (~5.4 eV) and is highly doped, however studies have shown that Pedot starts degrading at temperature > 150^0C, and the rate of material change gets rapid as temperature increases[194, 195]. So, for PIN sequential vapor the growth temperature was dropped to 150^0C and slow ramping approach (explained using the nucleation model in Fig 3.14) was used for grain enhancement. We also found that when P3HT was used as an interface layer, the device performance improved (results discussed in chapter 4). Others Polymers like PTAA, PCDTBT, Poly-TPD etc. were also tried however they could not withstand the high temperature. Hence, Pedot/P3HT was preferred for sequential PIN process. Fortunately, we evaporated PbI_2, because solution PbI_2 has wetting issues with all polymer transport layers (except Pedot) as one can see in Fig 3.21. Fig 3.21 show spin coated PbI_2(left) on Pedot/P3HT and evaporated PbI_2(right) on Pedot/P3HT, clearly spin coated PbI_2 has wetting issues and does not stick.

Fig 3.21: PbI_2 film on P3HT

The difference in PIN processing conditions in comparison to NIP is that PIN was processed at lower temperature as polymers cannot take high temperature, also slower ramping was used. Otherwise, like in NIP sequential vapor, for PIN the PbI_2 was evaporated, MAI processing was carried out using graphite in glovebox and post vacuum annealing was carried out.

3.1.3. FAI sequential devices [NIP architecture]

Finally, in the sequence of sequential vapor devices is Formamidinium Iodide (FAI) based Perovskite. FAI based perovskites requires a high temperature for phase transition and subsequent perovskite formation [22] and initial studies showed signs of thermal stability. Thermal degradation results for FAI and MAI perovskites will be discussed in chapter 5. However, fabricating FAI(NIP) devices in the glove box was not possible using MAI(NIP) conditions, because FAI has a higher a sublimation temperature in comparison to MAI. We conducted a TGS analysis on FAI and MAI, and the results are shown in Fig 3.22.

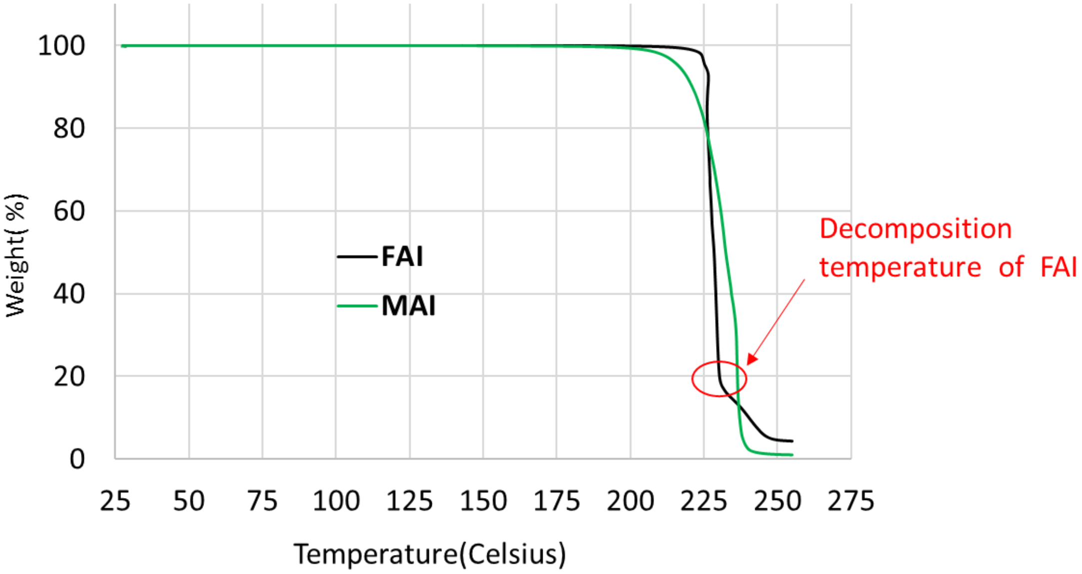

Fig 3.22: TGA analysis

As one can see from Fig 3.22, FAI requires a higher temperature to sublime (~25^0C more), so our standard NIP(MAI) condition of 180^0C, does not provide sufficient FAI flow for nucleation to start (Fig 3.12 – Lamer Dinegar Model) or for the subsequent grain growth. On analyzing the TGA (Fig 3.22) data, we understand that at ~230^0C FAI starts to decompose; hence the temperature was increased to a maximum of 220^0C for FAI vapor process in the glovebox and started to see perovskite growth. Nonetheless, the films were incomplete and inconsistent like observed earlier in the petri-dish NIP (MAI) process. Fig 3.23 shows the FAI (NIP) that was grown in the glovebox, also the FAI perovskite had a characteristic reddish color to it as reported by other groups.

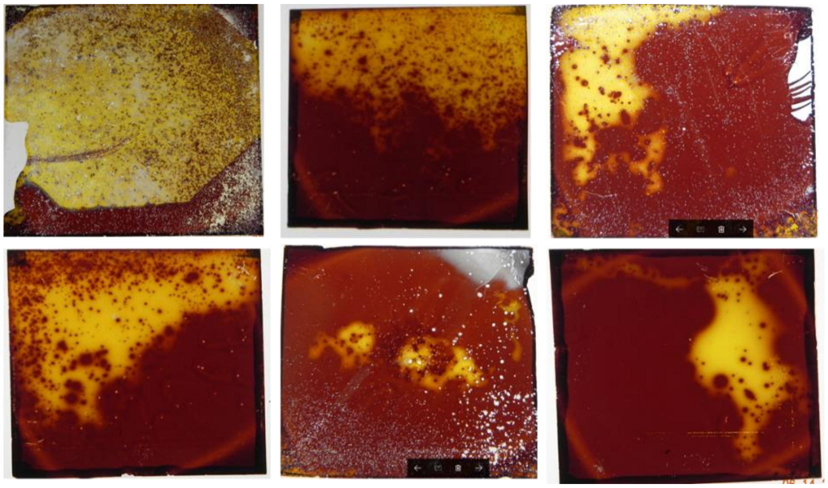

Fig 3.23: Incomplete FAI film (glove box)

As growing FAI perovskite in the glove box was not likely, we found a new approach for growing FAI vapor perovskite. We carried the sequential FAI vapor process in vacuum conditions using SBJ (Fig 3.17), the system that was built for vacuum annealing. We know FAI has a lower vapor pressure at 760 Torr, but its vaporization will increase if pressure decreases. Hence, the graphite boat was heated in vacuum conditions for enhancing the FAI vapor process. Fig 3.24 shows the graphite boat in SBJ and the resulting film. (FAI results will be discussed in Chapter 4)

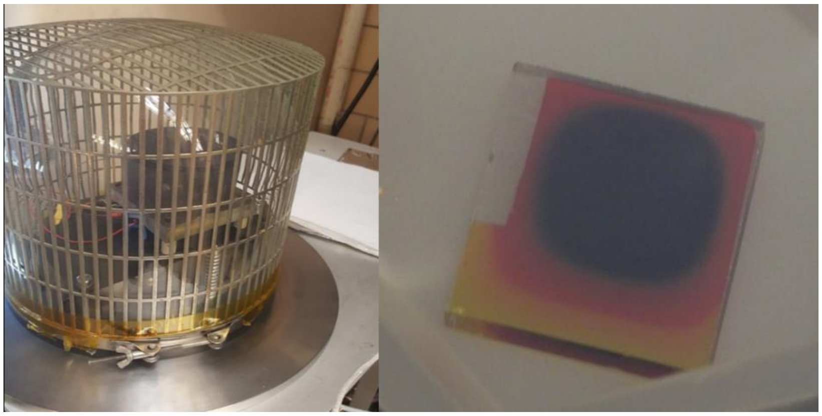

Fig 3.24: FAI setup and resulting film

After loading the graphite in SBJ, the system was pumped down to ~ $5\times10^{-6}\,Torr$ to keep moisture low. Next, the gate valve is closed and N_2 is flown into the chamber till pressure reaches 1 Torr, following which the graphite is heated to an indicated temperature of ~230^0C. The chamber was filled with N_2 for consistency and better heat transfer, as one knows if chamber is in high vacuum then heat transfer will only be through radiation, thus filling with N_2 will bring in convection.

3.2. Co-Evaporation

A lot of time and effort went into optimizing the process design of sequential vapor and in achieving high efficiency devices. Though, it was simple technique to implement, it has its limitations such as:

1. Sequential MAI vaporization is more of a diffusion process than evaporation, hence there is going to be a stoichiometric variation in the film causing material properties to vary spatially. So, properties like diffusion length, lifetime etc. would be different than what it could have been i.e. if stoichiometry is ideal.
2. A literature review shows that the fill factor for sequential vapor devices are in the ~0.55-0.68 range, while solution devices have FF in the 0.8 range. One reason for the comparatively lower fill factor could be the extra MAI on the surface of these perovskite films that increases its series resistance. In diffusive processes the surface of the film will have higher concentration, so for attaining high FF co-evaporation might be the better technique.
3. Sequential vapor works only on FTO substrates and for PIN architecture ITO is more apt. Unfortunately, sequential does not work on ITO substrates.
4. Sequential works best on FTO/TiO_2, however TiO_2 is intrinsic and has a lot of empty states that causes charge trapping (will be discussed in Chapter). To avoid charge trapping,

transport layers needs to doped but as far as we know other than FTO most other oxides are doped using metal dopants and they are attacked by MAI.

5. Sequential does not allow the use of polymer as bottom transport layer or interfacial layers, since they cannot withstand high temperature.
6. High open circuit voltage in hetero-structures solar cells necessitates using materials with proper band matching, and sequential vapor limits the use of materials that we can use.

Hence for solving the problems related to charge trapping, low fill factor, and to achieve higher open circuit voltage, we move towards co-evaporation of precursors. Also, co-evaporation will help produce films with tunable stoichiometry (for example: 1:1 ratio of MAI:PbI_2). The co-evaporator system was build bottom up. Though few groups have done co-evaporation[15, 55, 153, 154, 158, 159], we are the only group to have successfully build a co-evaporator outside the glove box in ambient environment till date, and currently we have the highest efficient (17.4%) co-evaporated PIN perovskite solar. To counter the volatile and erratic nature several systematic modifications were made, however this section will go over the important changes and if others need to build a system, then these recommendations will be helpful and handy.

3.2.1. Chamber parts

The Co-evaporation chamber comprises of the following parts: -

1. 3 furnaces (Radak-Luxel)
2. 2 DC power supplies
3. 2 Rotary pumps [Roughing & backing] with N_2 purge (to prevent oil backstreaming)
4. Turbo pump & Gate valve
5. 2 Ion gauges [one for Chamber and other to check leaks & functioning of Turbo)
6. 2 Pirani gauges [one for chamber and other for backing]

7. Two water cooled Trap (one for Turbo & second for Ion guage)
8. Copper mesh filter to protect Turbo
9. Variac transformer for heating substrate holder
10. Thermocouple’s for measuring temperature of furnace’s and substrate holder.

In addition, the chamber was encircled by blower motor (fans) for cooling the walls during the run and was also wrapped with heating pads for degassing MAI (post run). The chamber and all its parts were made using stainless steel.

3.2.2. Chamber modifications

The furnaces are mounted on the base plate at equidistance and accurate angles from the substrate holder. Fig 3.25 shows furnace installation (left) and the same post deposition(right).

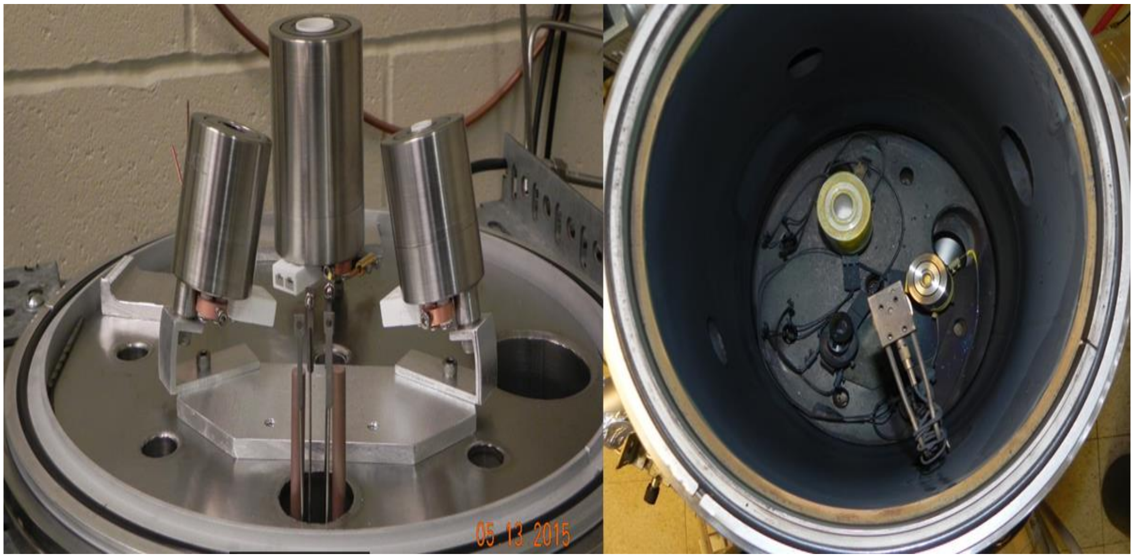

Fig 3.25: Luxel furnaces

The first design of the system is shown in Figure 3.26.

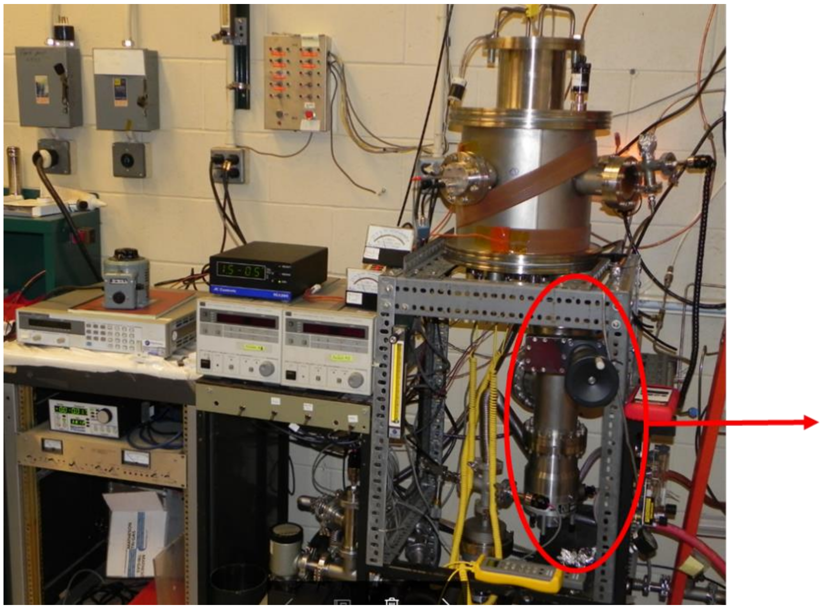

No trap & filter before gate valve and Turbo

Fig 3.26: First Design Co-evaporator.

The original design of the system did not include traps or filters as we did not foresee the damage MAI could cause us and we lost about 2 gate-value’s, 3 Turbo pumps, 2 rotary pumps etc. As one can imagine not all parts fail together, it was one at a time so changes were made accordingly. Fig 3.27 shows images of one of the corroded gate valves.

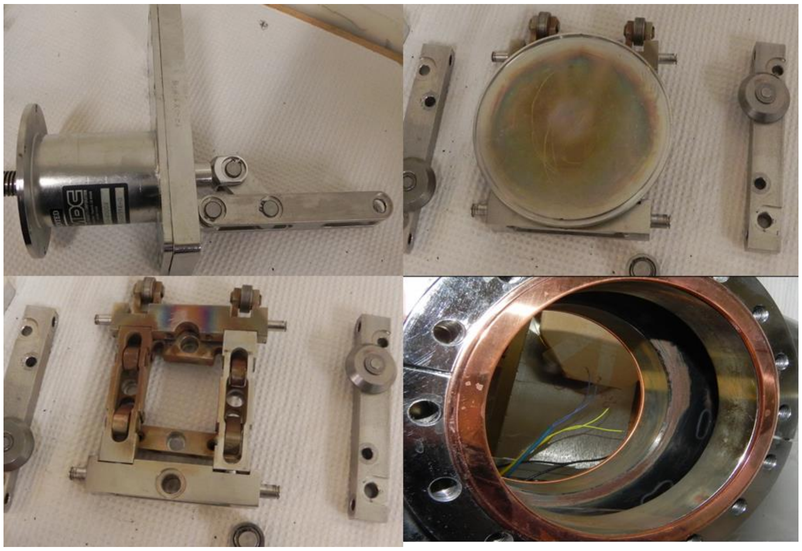

Fig 3.27: Corroded Parts-Gate valve

So, to protect the gate valve a water-cooled trap was introduced before the value and a picture of it is show in Fig 3.27.

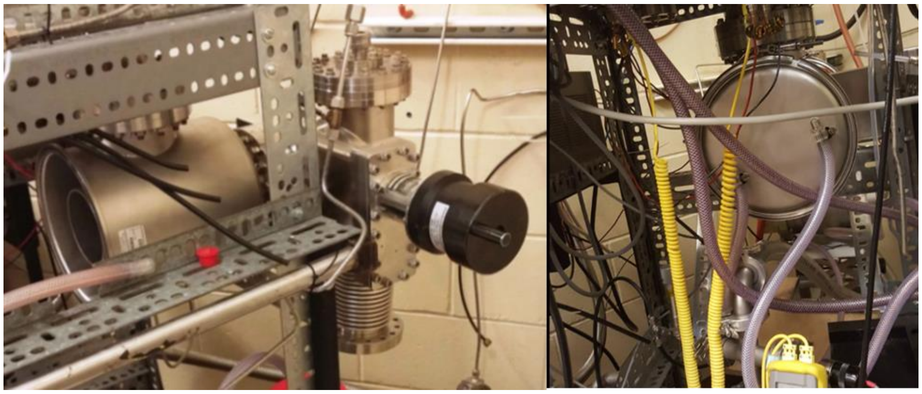

Fig 3.28: Water-cooled Trap

The water-cooled trap is cleaned every week to remove MAI. We thought the trap was adequate for guarding the turbo pump from MAI, but it proved insufficient as the turbo was damaged. So, we introduced a copper filter in between the gate-valve and turbo to trap MAI. Fig 3.29 (left) shows an image of the filter included in the system design, also an ion gauge is directly attached above the turbo pump to monitor its operation and will serve as an indicator when to change the filter. Fig 3.29 (right) shows image of a filter that was included in SBJ, as you can see MAI will also attack the copper mesh and the filter needs to be periodically replaced for system maintenance.

Fig 3.29: Filter

3.2.3. Sensors in chamber.

Before we go into the sensors used, an understanding of sensors and its importance for film deposition is critical. The most common way of measuring thicknesses of film is using Quartz crystal thickness monitor (QCM), it uses density and acoustic impedance of the deposited film to eventually calculate it thickness by detecting the change in resonance frequency of quartz crystal. However, if the QCM is taken apart, one will notice that it has gold plated electrodes for delivering electrical signals and these electrodes are etched by MAI. Hence, the QCM is unreliable for MAI related systems.

However, for material like perovskite whose carrier collection is field assisted[171], the thickness of film is critical, as it determines carrier collection. Since, QCM doesn't work, an alternative approach is doing calibration runs, knowing rate and depositing for 300nm. However, even for this method the precursor's rate need to be individually monitored and since we are forming a compound, their individual rates need to be precise.

PbI_2 rate is monitored primarily using the furnace temperature, the secondary check for it is the DC power to the furnace. Next is MAI, but since it has high vapor pressure and outgasses a lot, it is difficult to in control it using furnace temperature. However, its high vapor pressure makes it omnipresent and as we are forming a compound by chemical reaction on the substrate surface, so we just need to set a constant MAI pressure during deposition. hence MAI can be monitored using Ion-gauge. Fig 3.30(left) shows an image of trap fitted ion-gauge used to measure MAI pressure.

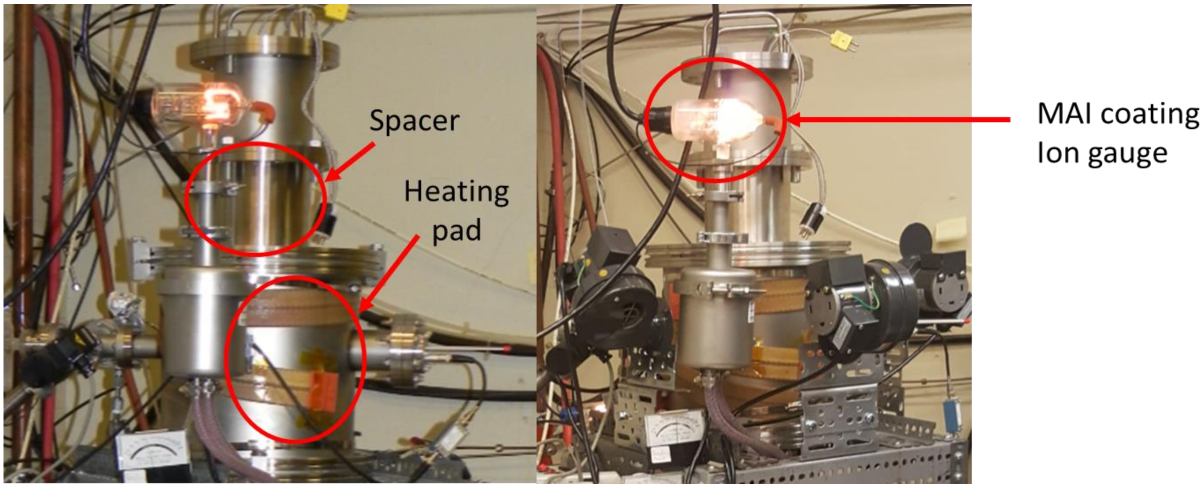

Fig3.30: Trap fitted Ion gauge

The ion gauge filament is made from iridium metal, which can be strongly degraded by organic contaminant, thus giving false readings. Though, we cannot isolate it from MAI we can still prolong its lifetime by have a water-cooled trap to lessen the influence of MAI. However, MAI still makes it through and we change the Ion gauge as soon as we see the white coating as seen in Fig 3.30 (right), else we are reading incorrect value. We use up ~3 ion gauges per week for functioning of the system.

3.2.4. System maintenance

MAI is hygroscopic material and absorbs moisture. As we know, higher the moisture content in a vacuum system the more difficult it is to bring the pressure down, hence every week the chamber walls are scrubbed and cleaned with Isopropanol, followed by bake-out for a day to drive away all the solvents. All the traps are also cleaned weekly to remove MAI and on doing so, we will prolong the life of gate-valve and turbo pump. In Fig 3.30 we can see of chamber strapped with heating pad to help in bake out.

3.2.5. Film deposition

Initially the films grown using co-evaporation had high series resistance. However, we knew from the sequential experience that it was from MAI. The base pressure before we ramp up the furnace is ~$9\times10^{-6} Torr$ and the shutter for film depostion is open only when the MAI pressure reaches 9×10^{-5} $Torr$ and this takes about ~ 1hr. Still, MAI will deposit on the substrate even if the shutter is closed as it does not follow line of sight deposition. Thereby, increasing the series resistance and creating erratic behavior.

To counter the problem of MAI depositing on substrate, 10 nm of pre-PbI_2 is deposited on the substrate i.e. even before MAI temperature is increased. Since, MAI is very reactive in vacuum, the initial vapors of MAI will react with the pre-PbI_2, forming perovskite while the chamber is being ramped up to achieve required MAI pressure. The chamber must be ramped to the required pressure no later than ~60-70min. The co-evaporated devices were grown on PIN & NIP architecture, the structure and results will be discussed in chapter 6.

The best results for room temperature deposition are follows: -

MAI chamber pressures: 9×10^{-5} $Torr$

PbI_2 temp: 315^0C

Run time: 75 mins

Thickness ~300nm

Growth rate (Perovskite)~ 0.67 A/s

Also, a spacer (Fig 3.30) was inserted in between the substrate holder and chamber to increase the distance between the substrate and furnace, thereby minimizing the thickness variation across sample. In addition, perovskites were also grown at substrate temperature of 50^0C & 75^0C, the growth conditions of the same and results will be discussed in Chapter 6.

CHAPTER 4

METHYL AMMONIUM IODIDE PEROVSKITES

4.1. NIP Sequential Devices

The band structure of NIP(MAI) device is shown in Fig 4.1.

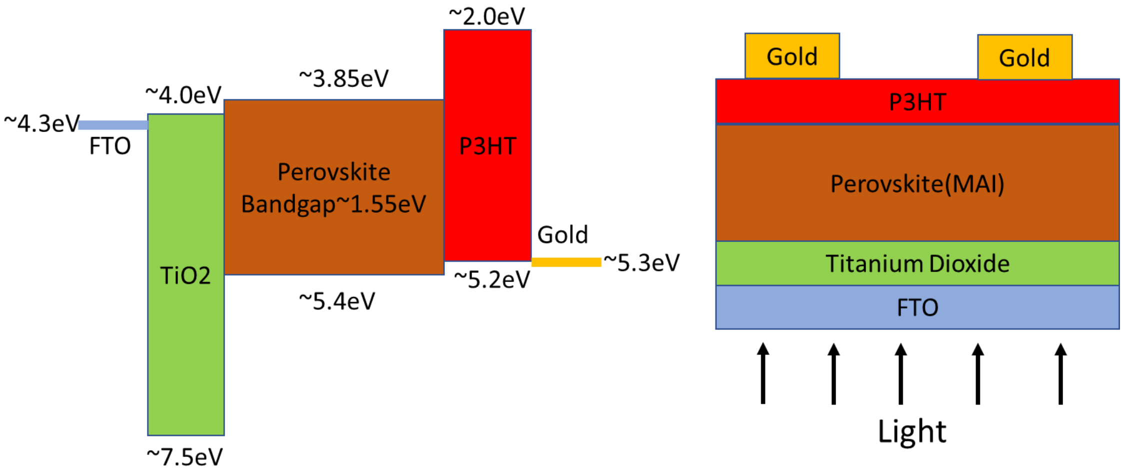

Fig 4.1: NIP sequential architecture

The NIP architecture was slightly altered from previous NIP vapor architecture's. We were the first group to use un-doped P3HT as Hole Transport layer (HTL) to fabricate high efficiency (13.7%) NIP devices [181], the polymer used most commonly at the time of our work was Spiro-meotad[14, 15]. P3HT doped with Lithium had been reported prior to our work [196] with efficiency of ~10% but we wanted to stay away from mobile dopants (the reason will become obvious by the end of this chapter).

Even though our work was on sequential vapor process, we made hybrid devices [i.e. PbI_2 (solution) & MAI (Vapor)] before making Sequential vapor devices. The IV [Fig 4.2] and Quantum efficiency [Fig 4.3] of our best hybrid device is shown in figures below. The cell had an efficiency of 12.3% with a $J_{sc} = 20.1mA/cm^2$, $V_{oc} = 0.93V$ and Fill factor=0.65.

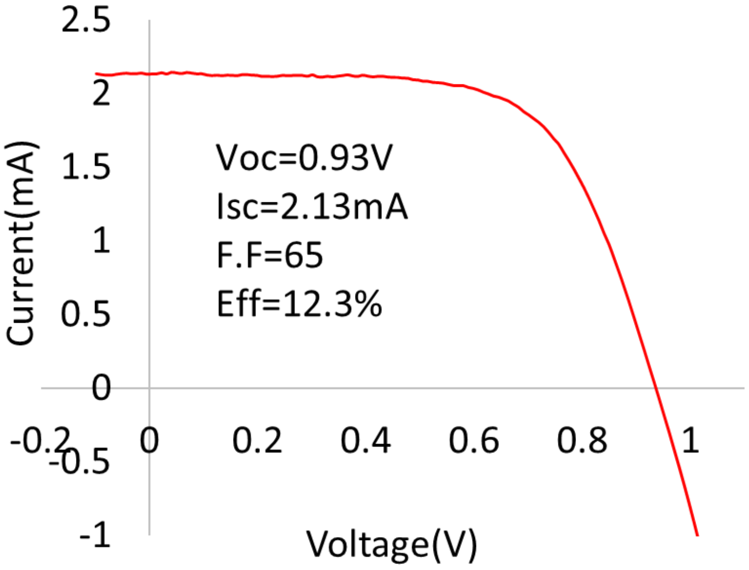

Fig 4.2: IV Hybrid NIP

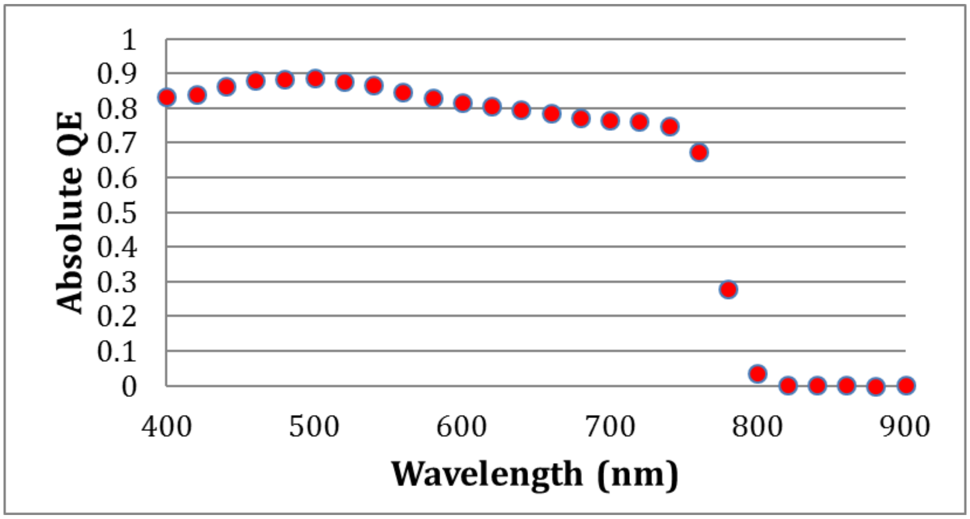

Fig 4.3: QE Hybrid NIP

The results of our hybrid device is comparable to the work done by Yang Yang [172] whose efficiency was 12.1%, however Yang Yang had used Spiro while we used the inexpensive P3HT. Still, the hybrid approach had disadvantages, the morphology of spin coated PbI_2 varied from sample to sample [Fig 3.5], resulting in differences in Perovskite grain size [Fig 3.6]. Hence, we moved towards sequential vapor and used a high-density graphite boat. The PbI_2 morphology was consistent [Fig 3.7], and thru grain enhancement [Fig 3.14] and vacuum annealing [Fig 3.17] we made high efficiency NIP devices [181]. The IV & QE of the device is shown in Fig 4.4 and SEM image & XRD peaks are shown in Fig 4.5. XRD shows that PbI_2 has completely changed into perovskite and SEM shows that the film has an average grain size of ~ 1um.

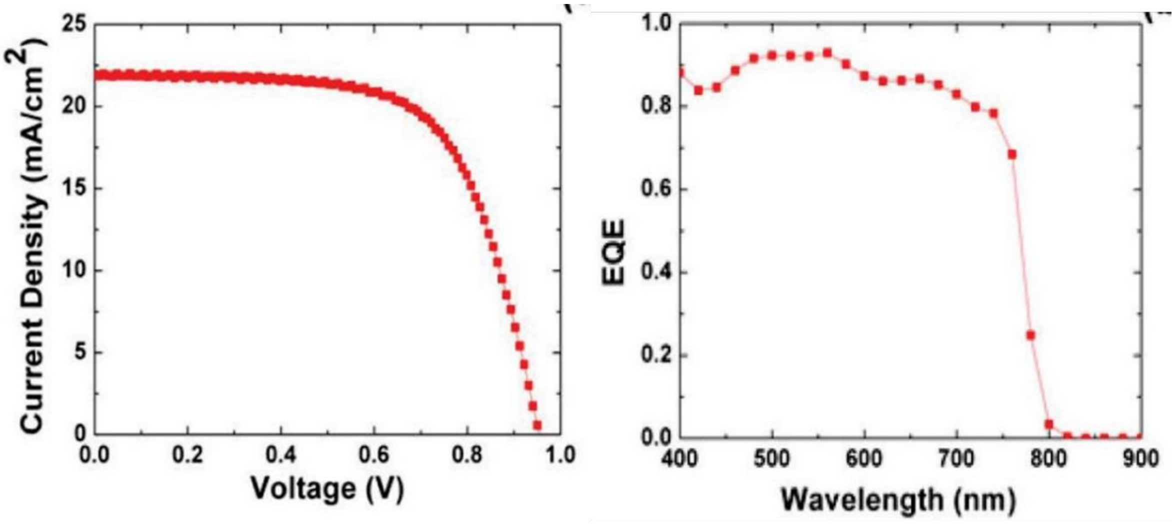

Fig 4.4: IV & QE Sequential NIP vapor [181]

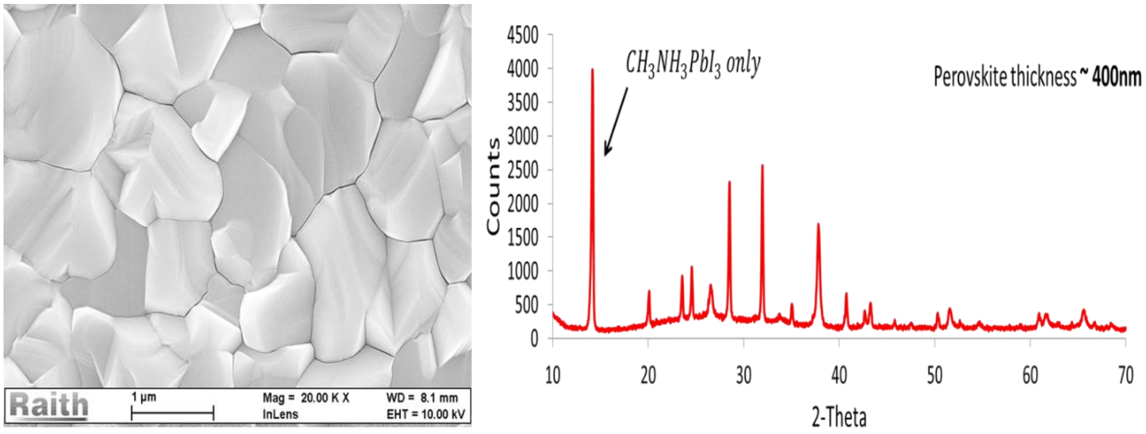

Fig 4.5: SEM & XRD of NIP vapor film [181]

The best device had an efficiency of 13.7% with a $J_{sc} = 21.8 mA/cm^2$, $V_{oc} = 0.96V$ and Fill factor=0.65. The device parameters such as short circuit current, open Circuit Voltage, fill factor and efficiency are very consistent for successive devices fabricated via the Sequential vapor approach and the histogram (Fig 4.6) and summary of 28 devices shown below (Fig 4.7) represents the same.

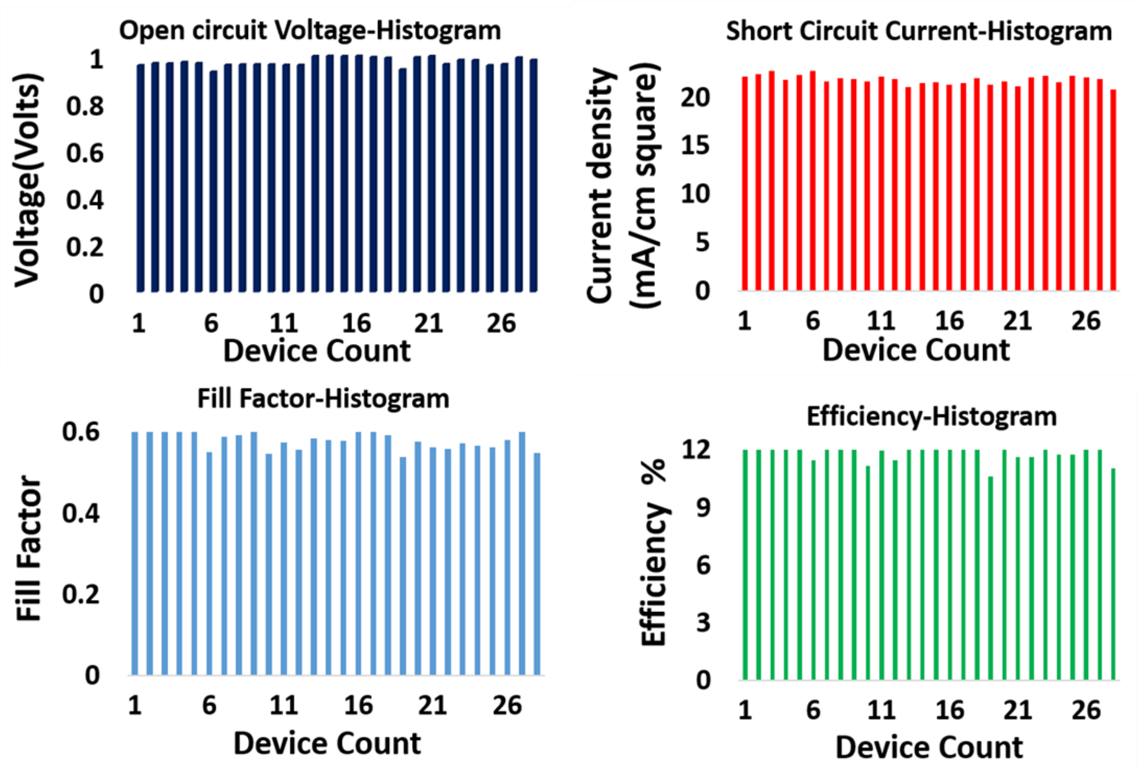

Fig 4.6: Histogram [181]

Parameters	Mean	Std Dev
Efficiency (%)	12.19	0.688
Voltage (V)	0.975	0.018
Current Density (mA/cm^2)	21.82	0.466
Fill Factor	0.584	0.026

Fig 4.7: Summary of results [181]

The summary made known are the results of 5 consecutive devices, each having 6 contacts. The mean efficiency= 12.2%, mean Current= 21.8mA/cm^2, mean Fill factor= 0.58 and mean Open circuit voltage~ 0.98 V, with some contacts have voltage of up to 1 Volt. The previous highest open circuit voltage that had been reported using P3HT as HTL for Perovskite solar cells was 0.92V [196], and the reason we believe for us to have achieved significantly higher open circuit (1

Volt) is that the bulk perovskite layer is vapor made and devoid of solvents, hence minimalizing shunt paths.

Another important optimization study done was the thickness variation of P3HT. We discovered that the thickness of the P3HT layer was a critical parameter that determined the fill factor. The reason being P3HT has high resistivity ($\sim 10^{-4}\ \Omega$ cm). This means that the resistance of the layer and space charge limited current becomes a factor in determining the fill factor i.e. if the thickness is too high. If the thickness is too low, then the entire layer is depleted, and then, the work function of the electrode plays a role in determining the voltage. Fig 4.8 shows the device performance as a function of thickness.

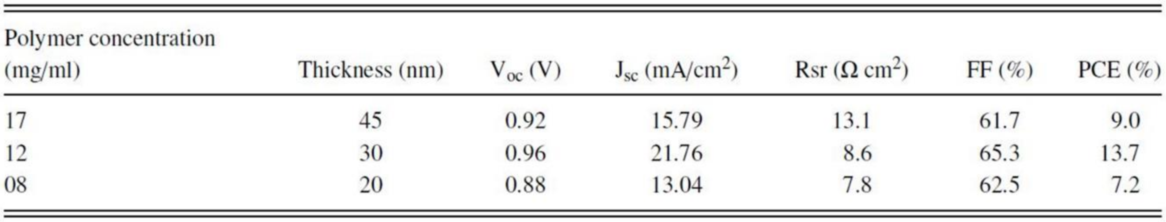

Polymer concentration (mg/ml)	Thickness (nm)	V_{oc} (V)	J_{sc} (mA/cm^2)	Rsr (Ω cm^2)	FF (%)	PCE (%)
17	45	0.92	15.79	13.1	61.7	9.0
12	30	0.96	21.76	8.6	65.3	13.7
08	20	0.88	13.04	7.8	62.5	7.2

Fig 4.8: P3HT concentration study

From the above table, we can see how a very thin P3HT layer leads to a loss in voltage, whereas a too thick layer leads to a loss due to increasing series resistance. Note how the series resistance for the two thicker P3HT films scales with the thickness of the film. For the thinnest film, since the film is totally depleted, as indicated by the precipitous voltage drop, the current is carried by space charge limited current, and the linear scaling factor does not apply. The best device performance was obtained with the intermediate thickness of the P3HT film. The thicknesses were measured using a surface profilometer.

Despite having good and consistent device parameters, the above fabrication process and chosen transport layers (Type II Heterojunction) creates anomalies in device behavior (Hysteresis and Voltage evolution- Data is shown in Fig 4.11 & 4.12 & also explained). Hysteresis in IV is a device behavior where the device exhibits different device performance depending on direction of voltage scan, this behavior influences all performance parameters (fill factor, voltage, current and efficiency). The other anomaly of concern is voltage evolution, the open circuit voltage and fill factor increases with time when device is measured under open circuit condition (or by applying a forward bias), subsequently changing the device characteristics. The reasons for these anomalies and the necessary fabrication modification and preferred device architecture essential to lessen this effect will be discussed.

4.1.1. Anomalies from carrier trapping and mobile Ions.

The phenomenon of IV hysteresis has been reported by numerous groups working on Perovskite solar cells. Based on literature, hysteresis in IV is dependent on sweep direction [197] , sweep rate [198], pre-biasing [198] and starting scanning voltage [199]. However, there are groups who have not observed any hysteresis, mostly all groups working on PIN architecture do not observe any hysteresis [200], also studies have shown that increase in grain size decreases the hysteresis in IV [201]. Hysteresis in IV has been observed typically in NIP architecture that uses TiO_2, however groups have shown that when TiO_2 is coated with PCBM [202, 203]or replaced by C60 hysteresis almost vanishes [204].

On observing the data from our own group (we work on both NIP & PIN, also we work with different transport layers for each architecture) and literature data, a clear similarity in data arose in devices that have hysteresis, reduced hysteresis and no-hysteresis. We see that devices that use doped transport layer have no hysteresis, while devices that possess larger grains have reduced hysteresis. However, devices that use un-doped transport layers' like TiO_2, Al_2O_3 etc. have significant hysteresis.

Hysteresis is observed commonly in NIP structure that explicitly use TiO_2 [205-208] but is absent in NIP[209] & PIN architecture[155, 200, 210, 211] using doped transport layers indicating the presence of interface states in un-doped TiO_2 that might be acting as potential trap states for charged carriers. These trapped carriers (electrons & holes) could bring about a change in the internal electric field of the bulk material, thus causing hysteresis. Though hysteresis can be explained by the charge trapping phenomena for our results and majority of the literature data, results also indicate an added mechanism.

For example, an interface layer of PCBM on TiO_2 reduces hysteresis [202, 203], thus supporting charge trapping in TiO_2, also replacing TiO_2 with C60 reduces hysteresis [204] but doesn’t eliminate it, despite C60 being doped. Likewise, the results of grain size enhancement decreasing hysteresis [201] indicate an second phenomena. The above explained and the results of poling effect, where PIP devices [212-215] with no charge selective contacts displaying photovoltaic behavior on exposure to light indicates excess mobile ions in the bulk that accumulate at the material interface, hence reducing the internal field. A detailed study of ion migration and it influence on electrical characteristic is shown by Joshi et al[28, 91, 216].

4.1.2. Source of ions

The subject of hysteresis and its origin brought about quite a debate, some groups claimed it was due to ferroelectric effect, while others claiming it was due to Ion migration throughout the bulk. But the results of Leijtens et al [214], revealed field-induced poling is significant at room temperature and decreased at lower temperatures and this is contrary to the ferroelectric nature; as ferroelectric behavior is anticipated to increase at lower temperatures when thermal disorder is lesser.

Even before the advent of Perovskites in photovoltaics, ionic conductivity studies on halide perovskites have reported low activation energy for ionic conduction[217-219]. Numerous studies were once again carried out on perovskite and like earlier, they also reported low activation energy for ion conduction. A summary of activation energy (E_a) calculated for $CH_3NH_3PbI_3$ perovskite by different groups [28] is given below.

I^-[$E_a(eV)$]	$CH_3NH_3{}^+$[$E_a(eV)$]	Pb^{2+}[$E_a(eV)$]	Reference
0.08	0.46	0.80	[220]
0.28	0.7	1.39	[221]
0.32	0.57	-	[222]
0.58	0.84	2.31	[223]

As one can see there are differences in the reported values of activation energy, it is possible that these discrepancies could be a result of different theoretical assumptions made during calculations. Interstitial migration is seldom considered as mode of ion motion in halide perovskites due to lack of spacing [223]. Commonly, all reports consider vacancy mediated migration as the dominant ion transfer mechanism. Walsh et al[224] calculated the activation energy for Schottky defect in perovskite is 140 meV that corresponds to ~10^{19} vacancies at room temperature.

Also, from the reported values of activation energies, I^- has the lowest activation energy and is the ion that associated with migration via vacancies in the structure. Also, based on activation energies, it is probable that $CH_3NH_3{}^+$can also migrate[225]. However, the activation energy of Pb^{2+} vacancies is relatively high and is improbable for ionic motion. The calculations above only consider vacancies as mean of ion transport, however experimental results suggest there are other pathways for ionic motion. For example dependence on hysteresis [201] and field induced poling [213] on grain size suggest that grain boundaries are also effective pathways for ion motion. A schematic of the different ion motion pathways is shown in Fig 4.9.

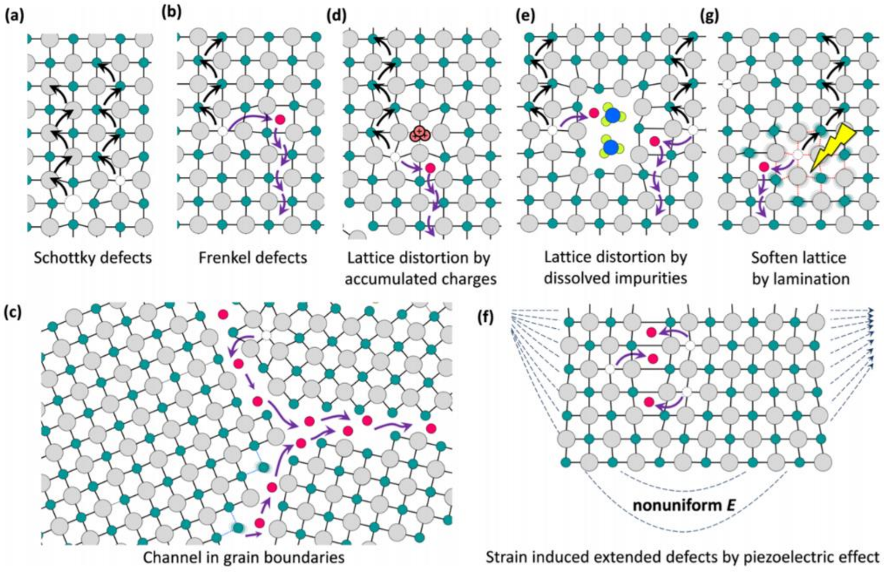

Fig 4.9: Ionic motion pathways [226]

4.1.3. Influence of ionic motion on device performance

The above briefing on conditions when hysteresis is observed (scanning direction, rate etc.), the cause of hysteresis (carrier trapping in un-doped transport layers & excess ions in bulk), ions responsible for hysteresis ($I^{-}, CH_3NH_3{}^{+}$), ionic pathways etc. was to help understand the IV hysteresis and Voltage evolution. Let us consider Fig 4.10, to better understand how trapped charges and excess ions influence the device performance in NIP architecture with un-doped transport layers.

As explained in Chapter 2 (Page 39), an internal electric field is created in the bulk of the material if there is difference in work function or electron affinity in between the electron and hole transport layers. The NIP structure is bandgap engineered using selective Type-II heterojunction to collect electron and holes using an internal field as can be seen in Fig 4.12, hence the internal field is not only felt by carriers (electrons/holes) but also by the ions in the bulk. From table above (section 4.1.3-Page 95), we know that the activation energy required to break bonds and create mobile ions is relatively low in perovskite.

Hence, negative ions (I^-) are driven to the N type interface (TiO_2) and positive ions ($CH_3NH_3{}^+$) are driven to the p-type interface (P3HT). The mobility of the moveable ions depends on both available pathways and on diffusion coefficient of individual ions. It is important to realize that ions unlike electrons/holes migrate via grain boundaries and vacancies (Fig 4.9). Owing to the low activation energy of ions, just the internal electric field in the bulk can create ions (I^- & $CH_3NH_3{}^+$) and any non-stoichiometry, for example excess MAI in the bulk (as in the case of sequential vapor devices), can contribute to additional ions being generated, this would lead to further accumulation of ions at the interface that would oppose the internal field.

Further, in polycrystalline material we have grain boundaries, that primarily serve as pathways for ion migration but they can also be a source of ions, since grain boundaries imply broken bonds. The ions from bulk and grain boundaries continue to accumulate at the interface till the electric field forces are balanced by the opposing diffusive force.

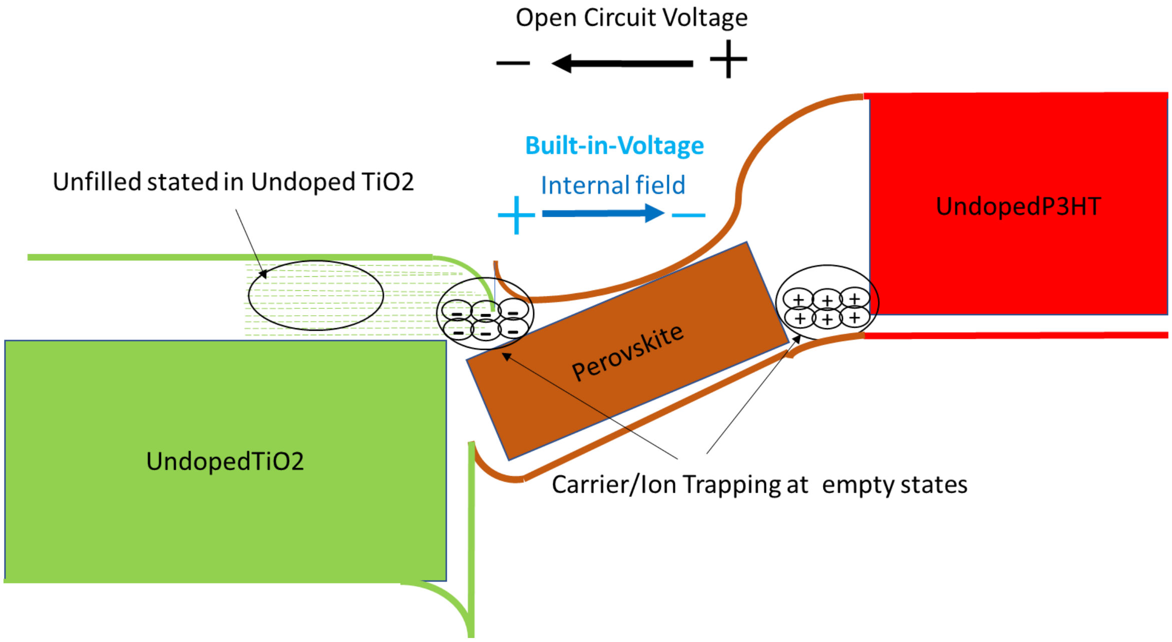

Fig 4.10: Ion Trapping in NIP architecture

The ions accumulating at the interface, reduces the internal electric field (V_{OC} dependent of field) and built-in-voltage, thereby reducing the Open circuit voltage and carrier collection. Carrier collection, because perovskite is a field controlled device as experimentally shown by Dalal et al [171]. In addition, there is a decrease in collected carriers due to the increased recombination in the bulk owing to the broken bonds that arises owing to the ions migrating from the bulk to the interface, thus increasing I_0 and reducing the V_{OC}. This is the explanation behind the phenomena of both voltage evolution (Fig 4.11) and IV hysteresis (Fig 4.13) that will be seen in detail.

First, the results of voltage evolution (Fig 4.11) is explained. The device is light exposed under open circuit conditions and IV is scanned at 0mins, 2mins, 5mins, 10mins, 15mins and 20 mins in the reverse direction (i.e. form high bias to low bias). The results clearly show an increase in voltage and fill factor with increasing light exposure. The ions collecting at the interface opposes the internal field of the bulk decreasing the built-in-voltage and thereby, the open circuit voltage (V_{OC}). So, at 0mins, we have decreased V_{OC} and reduced carrier collection. Also, the relative number of broken bonds in the bulk is at its maximum at 0mins, causing added recombination that further decreases both carrier collection (fill factor) and V_{OC}.

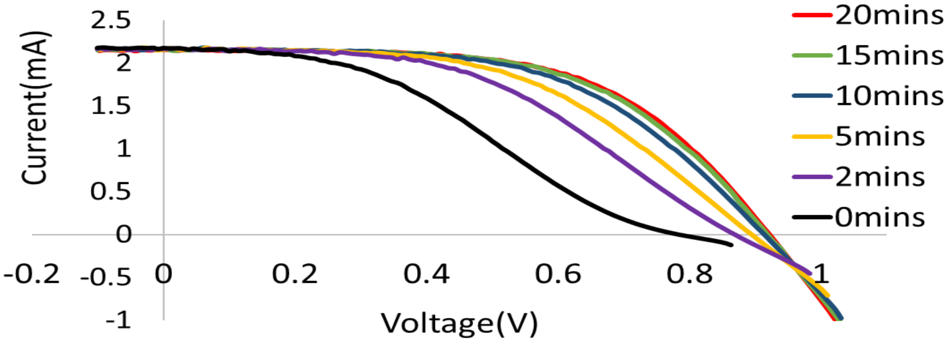

Voltage (Volts)	Current (mA)	Fill Factor	Efficiency %	Wait time [mins]
0.79	2.17	37	6.0	0
0.87	2.17	47	8.4	2
0.89	2.16	52	9.4	5
0.91	2.16	55	10.3	10
0.92	2.17	57	10.7	15
0.92	2.15	58	10.9	20

Fig 4.11: Voltage evolution

In the voltage evolution study, the device is light exposed under open circuit condition (forward bias ($or\ V_{OC}$)). In forward bias (V_{OC}) condition the internal field is reduced, changing the balance of the forces experienced by the ions i.e. electric field forces causing the ions to migrate to the interface decreases and diffusive forces that initiates the ions migration back to the bulk increases. Thus, ions diffuse back to the bulk till an equilibrium between field and diffusive force is re-established. Hence, the forward bias (V_{OC}) causes ions to migrate back to the bulk resulting in an increase in V_{OC}(forward bias), the increase in V_{OC} is accompanied by additional diffusion of ions to the bulk further increasing the V_{OC} and so on. Therefore, as we measure at different times we continue to observe an increase in V_{OC} (Fig 4.11, V_{OC} increases from 0.79V to 0.92V).

When ions migrate to the interface, it creates broken bonds i.e. deep states (recombination centers) in the bulk, creating a collection problem. Hence, at 0mins the fill factor is reduced. In open circuit condition (forward bias), the ions diffuse back into to the bulk, the ions that migrate back in the bulk might reform the bonds it broke, thus reducing the deep states and thereby increasing carrier collection (fill factor). An increase in fill factor is clearly seen with increasing exposure time in open circuit conditions from the voltage evolution curves in Fig 4.11, the $fill\ factor$ increases from 0.37 to 0.58.

Ions generated due to the internal field migrates to the interface. The ion generation and migration will continue until the internal field forces and diffusive forces of ion cancel one another. Consequently, when the device is under forward bias, the internal field declines resulting in an unbalance of the counter acting forces. Hence, the ions accumulated at the interface diffuse back to the bulk. However, not all accumulated ions can diffuse back to the bulk, owing to the always existing internal field, so some ions will diffuse back but only till the opposing forces balance out. For the above reason, the true V_{OC} might never ever be achieved.

This re-emphasis the importance of doped transport layers, as un-doped or intrinsic transport layer will have empty states, that might trap ions and decrease the V_{OC}. Also, depending on the energy level of the trap states, increasing voltage (energy) might be required for releasing the trapped ions. This implies slower voltage evolution, as a longer time is taken for ions to diffuse back to the bulk and for the V_{OC} to build up. The biasing voltage required for diffusing the ions back to the bulk depends on ion density (source of ions i.e. MAI content and grain boundaries), pathways for ion to migrate (grain boundaries) and trapping of ions at interface (undoped transport layers). Hence, it is both device architecture and processing dependent.

The S shape or double diode characteristic at 0mins can also be explained from visualization of the band diagram in Fig 4.10. The band diagram is drawn basing perovskite as a n-type material, we know that perovskite is an n-type type material from the CV data of Samiee et al [50] measured on NIP device [Fig 4.12 (left)] and P. Joshi[28] measured on PIN device [Fig 4.12 (right)], in both devices independent of the architecture, the capacitance depletes at negative bias, therefore we can conclusively say it is n-type material.

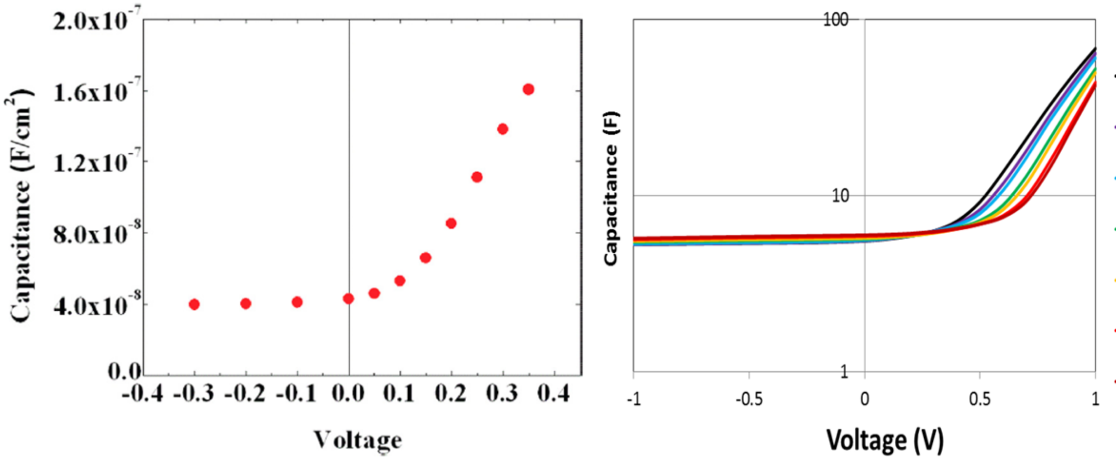

Fig 4.12: CV: NIP(left) and PIN(right) [28, 50]

Since Perovskite in an n-type material and TiO_2 is undoped, a barrier for electrons that current from perovskite to TiO_2 interface will form as can be seen from the band diagram in Fig 4.10, electron can hurdle across the barrier thermally or tunnel through it. The tunneling current (J_T) can be given by the following equation:

$$J_T \propto exp\left(\frac{-e\varphi_{BN}}{E}\right)$$

φ_{BN} is the barrier height and E is the electric field. At 0mins, the ions are accumulated at TiO_2 interface, causing the internal field to decrease, thus diminishing the tunneling probability across the barrier, under this circumstance if the electron does not have the necessary thermal energy to hurdle across, then there would be an electron accumulation at the barrier. However, under forward bias, the ions diffuse to the bulk and the relative electric field and tunneling probability increases, thus causing the electrons to tunnel through. At 0mins, we see a double diode or S shaped curve but as the ions are repelled, the built-in field increases resulting in carriers being tunneled across the barrier and the S shape disappears.

For explaining IV hysteresis (Fig 4.13), the terms ‘Reverse scan’ and ‘Forward scan’ is going to be used repeatedly. As explained earlier in Chapter 2 (Page 47) section 2.7.4, the IV is typically scanned from high bias to low bias, this we term as Reverse scan. In the contrary, scanning from low bias to high bias is referred to as Forward scan. In the voltage evolution study (Fig 4.11) on continued exposure of the contact in open circuit condition, post 15mins we experimentally realized that there is not any further significant increase in V_{OC} indicating that the ions have attained a local equilibrium. Hence, the final IV measurement is scanned at 20mins as follows: IV is scanned in reverse direction followed by immediately scanning it in forward direction.

In the final reverse scan (Fig 4.13), the device prior to scanning is light exposed under open circuit (V_{OC}) i.e. forward bias condition, so most ions would have diffused back to the bulk and re-bonded with the broken bonds reducing deep states, and reverse saturation current and increasing the electric field. Thus, the device has its maximum V_{OC} and fill factor. Following the reverse scan, we instantaneously scan in the forward direction i.e. from low bias to high bias. The scan is started from -0.1V to 15% above V_{OC}, at -0.1V due to maximum electric field in the bulk, all carriers are collected.

Nevertheless, the ions will also experience this field and migrate to the interface. This results in broken bonds in the bulk that will increase the recombination $[I_O]$, resulting in decrease of V_{OC} and fill factor and the following is clearly seen from the results (Fig 4.13). This phenomenon of change of change in Fill factor and V_{OC} based on scanning direction is referred to as IV hysteresis. The results in Fig 4.13, shows the difference in V_{OC} (0.95V to 0.91V), Fill factor (0.61 to 0.50) and resulting efficiency change (11.6% to 9.2%), just by changing scanning direction.

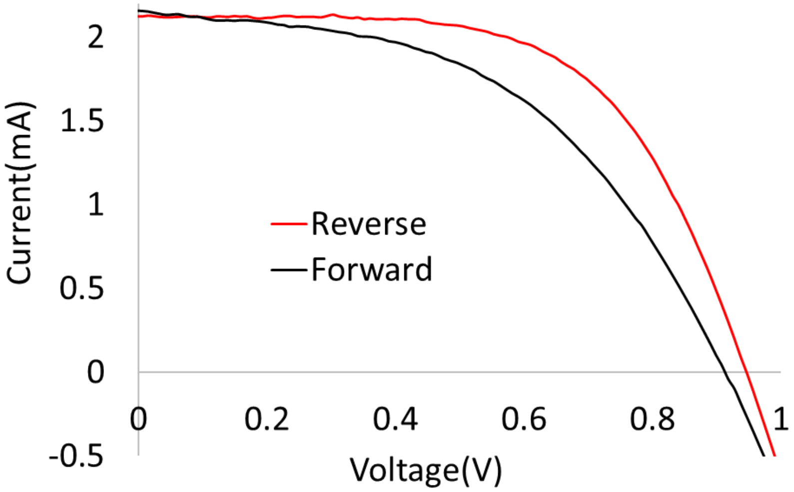

Scan Direction	Current(mA)	Voltage(V)	Fill Factor	Efficiency %
Reverse	**2.13**	**0.95**	**0.61**	**11.6**
Forward	**2.15**	**0.91**	**0.50**	**9.2**

Fig 4.13: IV hysteresis

4.1.4. Reducing voltage evolution

Voltage evolution and hysteresis are both due to ions accumulating at the interface, so if ion motion to the interface is eliminated, then there would be no voltage evolution or hysteresis. The factors that control voltage evolution and hysteresis are grain size, ion density and doping of transport layers (TiO_2 & $P3HT$). Large grains decrease the possible pathways for ion motions, perfect stoichiometric or apt precursor (MAI) concentration reduces the generated ion density in the bulk and doped transport layers prevents charge trapping at the interface.

The dopants for transport layers needs to be immobile, else the dopants themselves can contribute to ion accumulation at the interface. A good example for mobile dopants is Lithium which is commonly used in organic transport layers like Spiro-meotad and this could possibly worsen both hysteresis & voltage evolution effects. Even though doped metal oxides should theoretically work perfectly, it cannot be used as metal rich interface layers are attacked by MAI. As per literature

TiO_2 can be doped using metal dopants[227] but we cannot take that route as it is not suitable for vapor process for the reason just mentioned.

The doped transport layers' route for minimizing device irregularities isn't too promising, hence for solving anomalies, we tried to minimize the ion density and increase grain size. The ion density can be controlled by varying the MAI concentration in the film, as MAI is the source of ions. This can be accomplished by decreasing the MAI diffusion (reaction) time and by reducing the quantity of MAI used in the graphite boat. So, the first experiment was to lessen the MAI diffusion time. The standard recipe for MAI diffusion (explained in chapter 3 in detail) is spread 40 mg of MAI around substrate, ramp temperature of graphite starting from 130^0C to 180^0C in 10 minutes' interval, and set graphite to a final temperature of 180^0C for 3hrs.

In the constant source (MAI) diffusion model, the distribution of source is given by complimentary error function,

$$n(x,t) = n_O erfc\left(\frac{x}{2\sqrt{Dt}}\right)$$

n_O is the concentration at surface, D is the diffusivity of MAI, x is the distance along the film and t is the time ($\sqrt{Dt}$ is the diffusion length of MAI). Diffusion has an exponential relation with temperature, and varying temperature is a better way to control concentration in the bulk. However, we chose not to take that path, as large grains were critical for device performance and from past experimentations we know that decreasing temperature decreases grain size. Hence, the approaches taken to decrease concentration in the bulk are: -

- Decrease MAI diffusion time
- Decrease MAI amount

4.1.4.1. Decrease diffusion time

By lessening the MAI distribution in the bulk, we will decrease the density of mobile ions generated in the bulk, thus controlling the ions accumulating at the interface. From constant source diffusion model, MAI concentration in the bulk is a function of diffusion time, so by decreasing diffusion duration we can reduce the concentration of MAI and thereby, the generated mobile ions that would eventually collect at the interface. The standard condition is 3 hours, so we decided to reduce the diffusion time to 2 Hours and 1.5 hours.

The consequence of shortening the diffusion time is that perovskite film can be incompletely formed, also by reducing the time we are not assisting grain enhancement. Though an improvement in voltage evolution is sort after, decreasing time would also decrease grain size. Grain size influences both diffusion length and recombination current, thus affecting both carrier collection (fill factor) and V_{OC}.

Smaller grains increase the ionic pathways, leading to a greater number of ions accumulating at the interface. Correspondingly, smaller grains imply larger number of broken bonds that could eventually contribute to additional free ions. So, using this approach, we know a compromise had to be made between grain size and final MAI concentration in the bulk. Fig 4.14 shows the voltage evolution curve and Fig 4.15 shows the corresponding device parameter comparisons for diffusion time study.

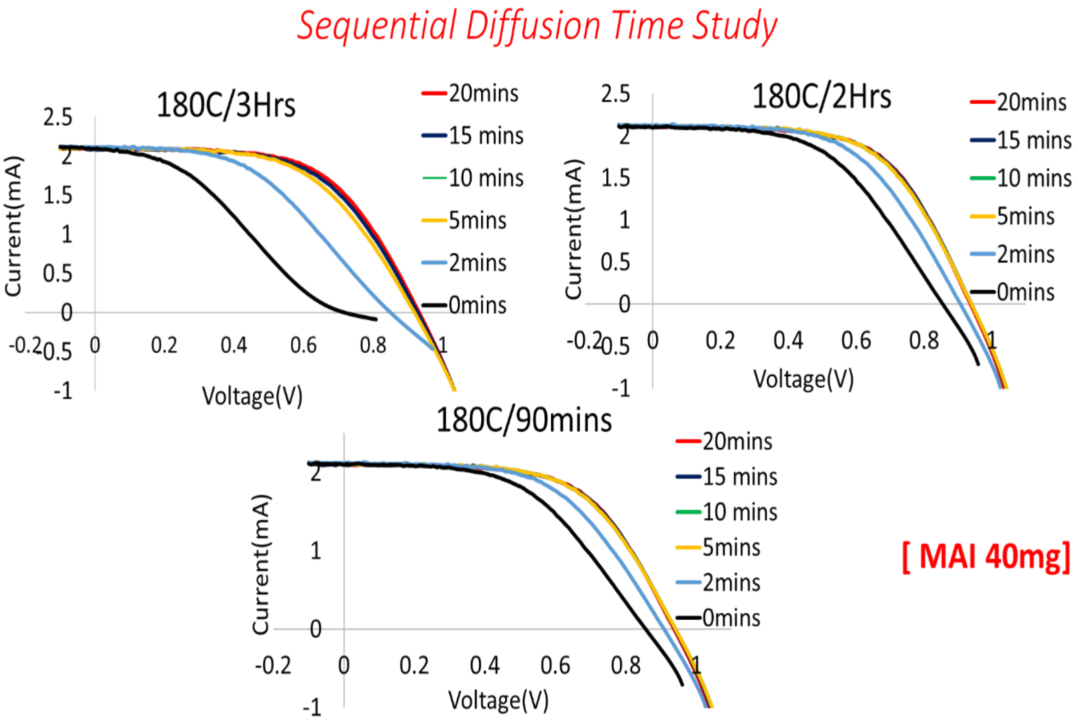

Fig 4.14: IV Diffusion time study

The results from Figure 4.14 shows that by reducing the diffusion time, the voltage evolution effect improves because we are reducing the MAI concentration in the bulk, thus lessening ion accumulation at interface. From the voltage evolution curves in Fig 4.14, we can observe that 180C/ 3hr as a S curve, which is absent for 180C/2hr and 180C/90mins indicating reduced ion accumulation at the interface for the decreased diffusion durations. As explained earlier, greater ion accumulation at interface, lesser the in-built electric field, there decreasing the tunneling probability of carriers across the barrier (Fig 4.10).

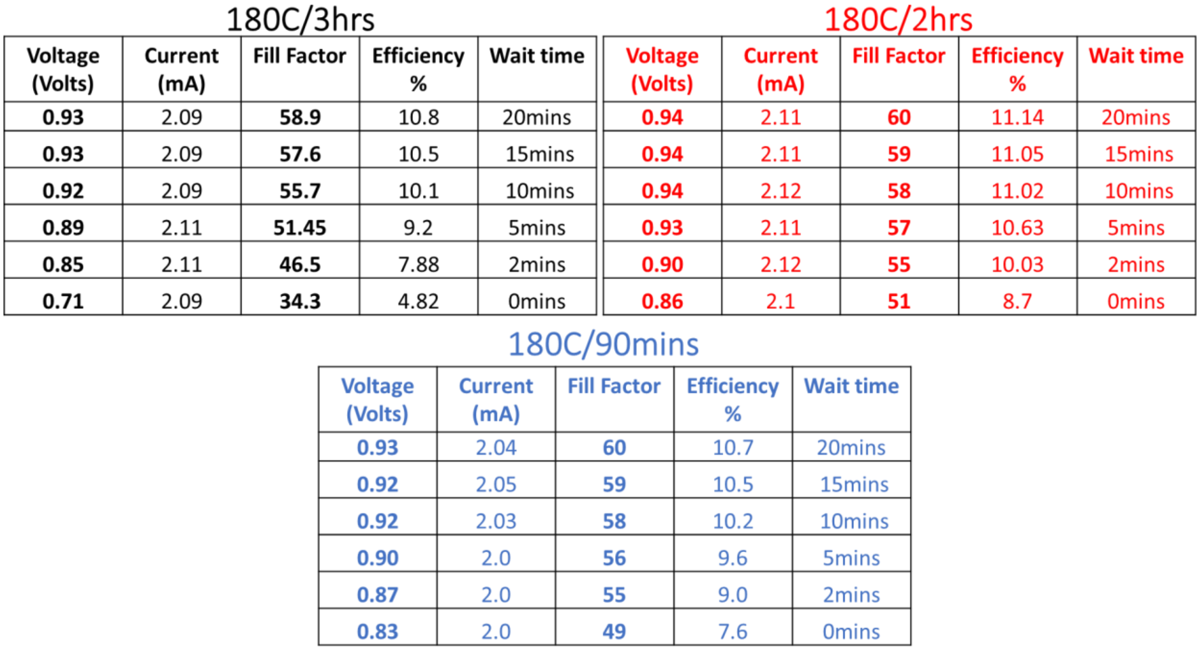

180C/3hrs

Voltage (Volts)	Current (mA)	Fill Factor	Efficiency %	Wait time
0.93	2.09	**58.9**	10.8	20mins
0.93	2.09	**57.6**	10.5	15mins
0.92	2.09	**55.7**	10.1	10mins
0.89	2.11	**51.45**	9.2	5mins
0.85	2.11	**46.5**	7.88	2mins
0.71	2.09	**34.3**	4.82	0mins

180C/2hrs

Voltage (Volts)	Current (mA)	Fill Factor	Efficiency %	Wait time
0.94	2.11	**60**	11.14	20mins
0.94	2.11	**59**	11.05	15mins
0.94	2.12	**58**	11.02	10mins
0.93	2.11	**57**	10.63	5mins
0.90	2.12	**55**	10.03	2mins
0.86	2.1	**51**	8.7	0mins

180C/90mins

Voltage (Volts)	Current (mA)	Fill Factor	Efficiency %	Wait time
0.93	2.04	**60**	10.7	20mins
0.92	2.05	**59**	10.5	15mins
0.92	2.03	**58**	10.2	10mins
0.90	2.0	**56**	9.6	5mins
0.87	2.0	**55**	9.0	2mins
0.83	2.0	**49**	7.6	0mins

Fig 4.15: Device parameters voltage evolution study

Also, from Fig 4.15 we can see that for 180C/3Hr condition, the V_{OC} onsets at a lower voltage of 0.71V at 0mins and increases to a maximum 0.93V in 15mins, while for 180C/2Hr the V_{OC} starts at a higher voltage of 0.86V at 0mins and increases to a maximum 0.94V in just10mins, signifying lesser ion density at interface for 180C/2Hr. A similar faster rise is also seen for 180C/90mins, but its current is slightly lower in comparison to 180C/3hour and 180C/2hour indicating incomplete film formation and smaller grain size. The QE and SEM images will help confirm the same. Figure 4.16 & 4.17 shows the QE and SEM comparison for the respective conditions.

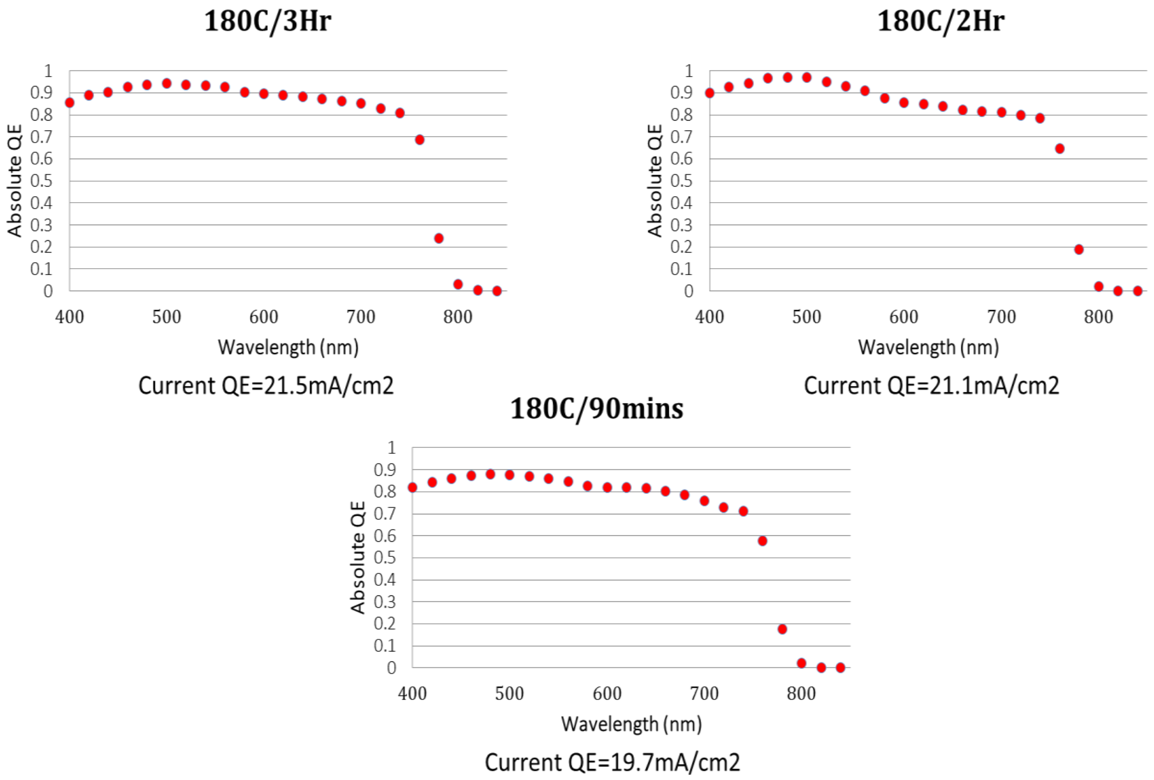

Fig 4.16: QE diffusion time study

The QE (Fig 4.16) and SEM images (Fig 4.17) agrees with each other, the QE current decreases with decrease in diffusion time. Also, there is a drop-in QE in the longer wavelength for the 90mins diffusion time condition indicating incompletely formed perovskite and looking at the SEM images, 90mins deposition has a larger distribution of smaller grains. The grain size distribution increases as we move towards longer diffusion times, due to grain enhancement that occurs with longer reaction time and this is reflected in the current too. Even though, 180C/180mins possesses larger grains and has higher current, the ion density is also greater due to the excess MAI in the surface and bulk. However, 180C/2hr’s current and grain size distribution isn’t too dissimilar from 180C/3Hr, but it has significantly better voltage evolution, so for that reason for the future study, we used 180C/2Hours as our apt condition.

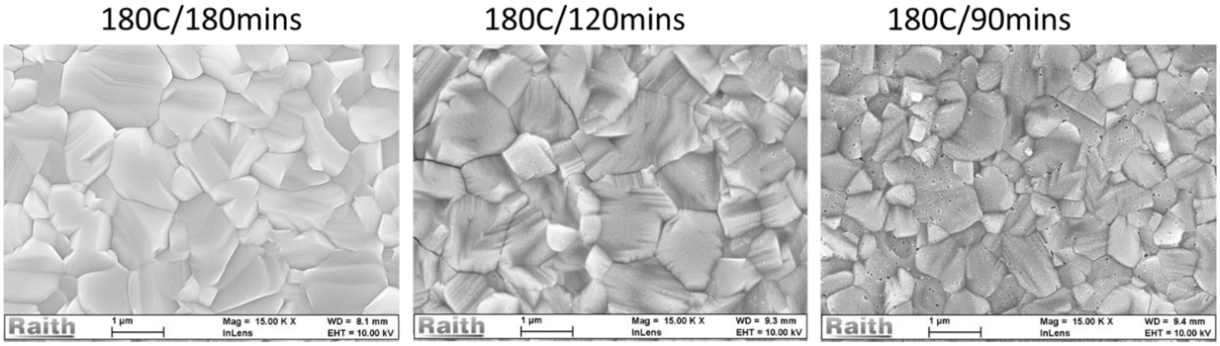

Fig 4.17: SEM diffusion time study

4.1.4.2. Reduce MAI amount

Like previous study, the goal of this study is to reduce the ion density at interface but by decreasing the quantity of MAI used in the graphite boat. From constant source diffusion model, by decreasing the constant source of MAI at the surface n_O, it is possible to decrease the amount of MAI in the surface and bulk. The earlier study used 40mg of MAI, so we decided to study the variation in voltage evolution by using 20mg, 30mg and 60mg for the 180C/2hr diffusion condition. Also, from Lamer-Dinegar model (page 66), an increase in grain size is probable, i.e. if concentration increase above n^* (nucleation concentration) is not rapid, then the number of nucleation sites is reduced and the subsequent MAI flow goes towards grain enhancement. The IV results of the decreased MAI amount-Voltage evolution study is shown in Fig 4.18 and the corresponding device parameters are shown in Fig 4.19.

The results of the study show that by decreasing MAI amount, the voltage evolution decreases (Fig 4.19). For the 60mg case, we see a S shaped curve that is absent for 40mg, 30mg and 20mg case, indicating that 60mg has a larger accumulation of ion at the interface. The voltage evolution trend for the 40mg, 30mg and 20mg are hard to differentiate and voltage saturates in ~10mins (Fig 4.18 & 4.19). Nevertheless, the 20 mg has better current. The higher current for 20mg case corresponds to its larger distribution of grain size (Fig 4.20). The larger grain distribution for the 20mg case can be explained using the Lamer-Dinegar model (Page 66), the MAI vapor concentration for the 20mg case is less than the 30mg case. Hence, the concentration does not exceed too much above the minimum nucleation concentration (n^*), thereby reducing the number of nucleation site, also the future MAI concentration made available goes towards grain enhancement rather than towards creating newer nucleation sites. Consequently, when the grain grows it achieves large size, as it is unrestricted by the surrounding smaller grains that would have formed if new nucleation sites were created.

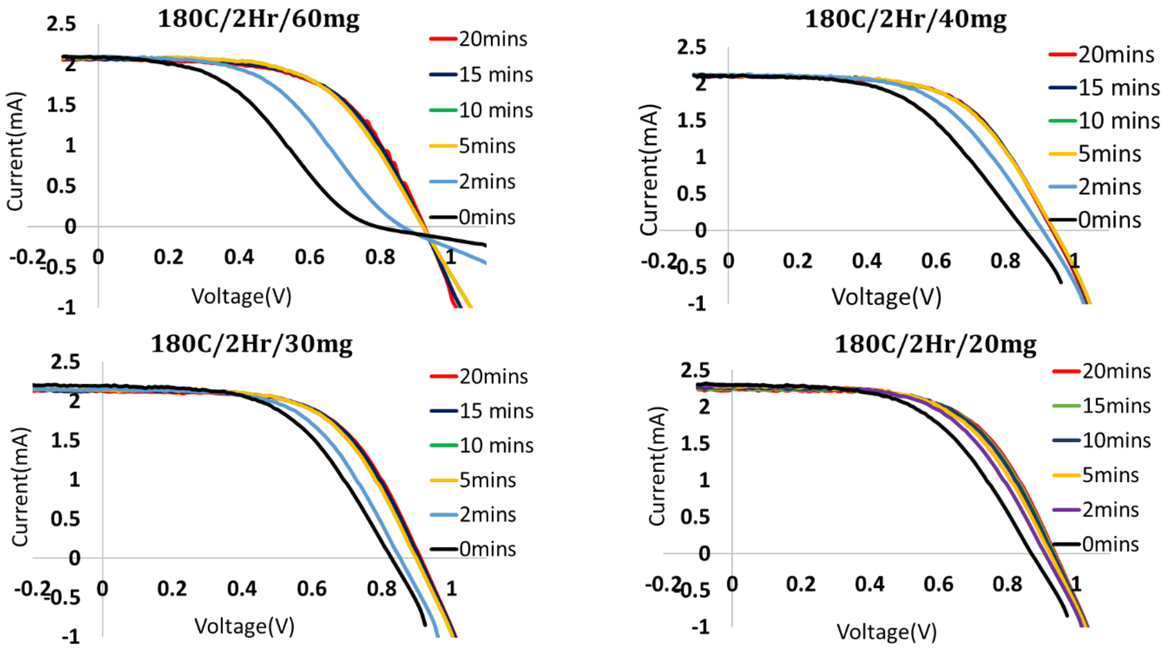

Fig 4.18: IV MAI amount study

180C/2Hr/60mg

Voltage (Volts)	Current (mA)	Fill Factor	Efficiency %	Wait time [mins]
0.93	2.06	**57.5**	10.39	20
0.92	2.07	**58.4**	10.46	15
0.92	2.08	**57.4**	10.34	10
0.90	2.08	**53.8**	9.50	5
0.86	2.09	**47.8**	8.15	2
0.79	2.08	**39.9**	6.23	0

180C/2Hr/40mg

Voltage (Volts)	Current (mA)	Fill Factor	Efficiency %	Wait time
0.94	2.11	**60**	11.14	20mins
0.94	2.11	**59**	11.05	15mins
0.94	2.12	**58**	11.02	10mins
0.93	2.11	**57**	10.63	5mins
0.90	2.12	**55**	10.03	2mins
0.86	2.1	**51**	8.7	0mins

180C/2Hr/30mg

Voltage (Volts)	Current (mA)	Fill Factor	Efficiency %	Wait time [mins]
0.91	2.13	**60**	10.95	20
0.91	2.13	**60**	10.90	15
0.9	2.14	**59**	10.78	10
0.88	2.14	**58**	10.35	5
0.85	2.17	**56**	9.78	2
0.83	2.20	**53**	9.07	0

180C/2Hr/20mg

Voltage (Volts)	Current (mA)	Fill Factor	Efficiency %	Wait time [mins]
0.94	2.25	**59**	11.87	20
0.94	2.25	**60**	11.86	15
0.94	2.28	**59**	11.85	10
0.93	2.28	**58**	11.45	5
0.91	2.28	**57**	11.11	2
0.87	2.3	**54**	10.10	0

Fig 4.19: Voltage evolution MAI amount study

Fig 2.20 shows that 20mg has a larger grain distribution in comparison to 30mg case. Also, the QE current as shown in Fig 2.21 agrees with the SEM data, the QE current for 20mg is $\sim 1 mA/cm^2$ higher than the 30mg case due to its larger grains.

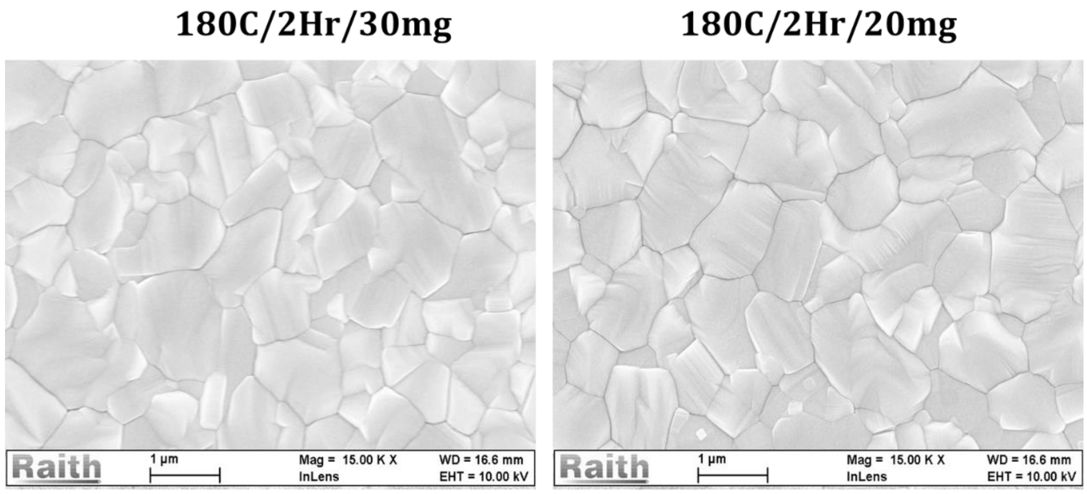

180C/2Hr/30mg **180C/2Hr/20mg**

Fig 4.20: SEM: 20mg vs 30mg

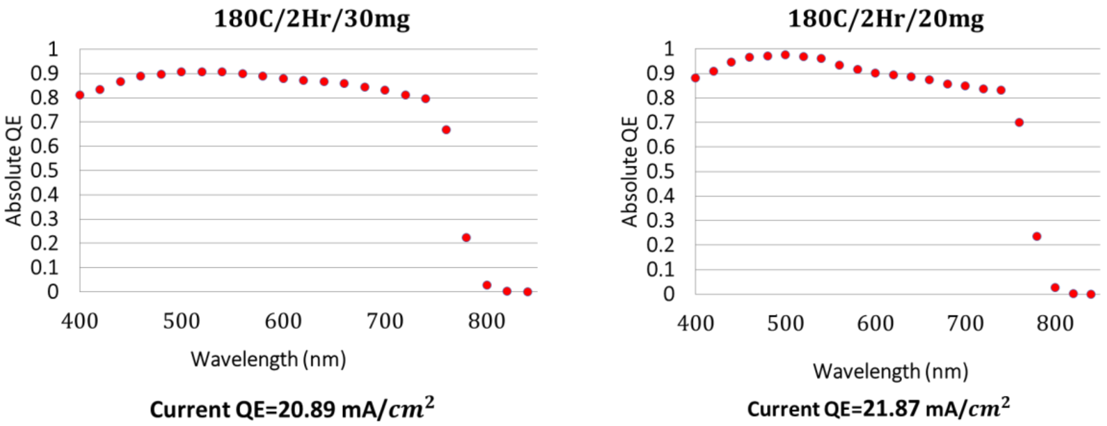

Fig 4.21: QE: 20mg vs 30mg

Even though voltage evolution showed improvement by decreasing diffusion time and MAI quantity, it is important to understand that MAI concentration is going to follow a erfc function across the film thickness, therefore there is always going to excess ions in the surface of the film. In addition, TiO_2 is un-doped transport layer and suffers charge trapping that worsens the voltage evolution and hysteresis phenomenon. Fig 4.22 shows the hysteresis curve for the 20mg-2Hr diffusion condition and clearly the device has hysteresis. The hysteresis is due to the charge trapping in the transport layers.

The hysteresis IV measurements are taken by scanning a reverse scan followed by an immediate forward scan. We must understand that post reverse scan and pre-forward scan, the device is under short circuit condition (maximum electric field), hence ions along with carriers will be attracted back to the interface. However, as the forward scan is taken, the device's forward bias gradually increases, thus deflecting ions back to the bulk. However, if the transport layers are un-doped, the device will experience charge trapping and this decreases both fill factor and V_{OC} especially when the device is forward scanned.

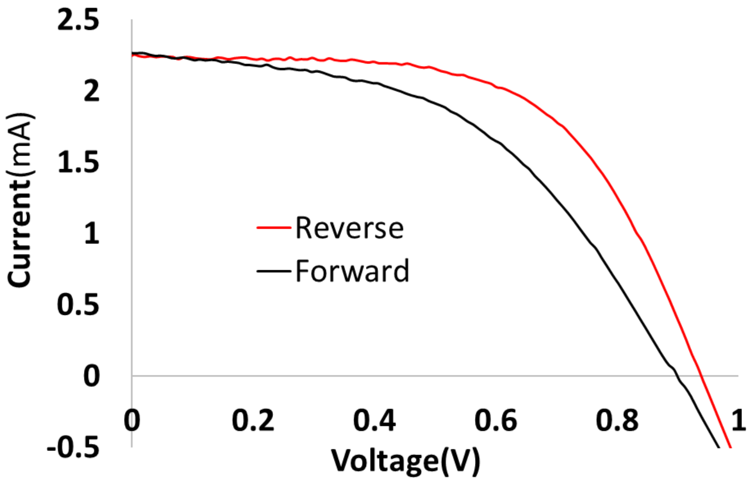

Scan Direction	Current(mA)	Voltage(V)	Fill Factor	Efficiency %
Reverse	**2.25**	**0.94**	**0.59**	**11.9**
Forward	**2.26**	**0.90**	**0.49**	**9.4**

Fig 4.22: 20mg MAI-2 Hour diffusion IV Hysteresis

4.1.4.3. Voltage soaking

Until now all IV measurements were carried out by exposing the device to light exposed under open circuit conditions i.e. the devices were all forward biased with the open circuit voltage before scanning and the applied bias helped deflected the ions back to the bulk. However, the applied forward bias is inconsistent and totally device dependent i.e. if the device has larger accumulation of ions at the interface, the V_{OC} build up is slow, as seen earlier from the results of the Voltage Evolution study and it may take a longer time to deflect the ions from the interface.

So, a better approach to the do the same is to give a constant forward bias of 1 V while keeping the device in dark. On doing so, the device performed much better because a fixed bias of 1V is applied for a 10-15mins to deflect the ions, in contrast to the changing V_{OC} that's build up with time. Fig 4.23 shows a comparison of two devices that was light soaked and voltage soaked, and the same device had better fill factor, V_{OC} and efficiency, when voltage soaked. This study was done to further support the deflection of ions by applying bias, but in all future studies we continued to measure devices under light exposure in Open circuit condition, as it is a more realistic condition.

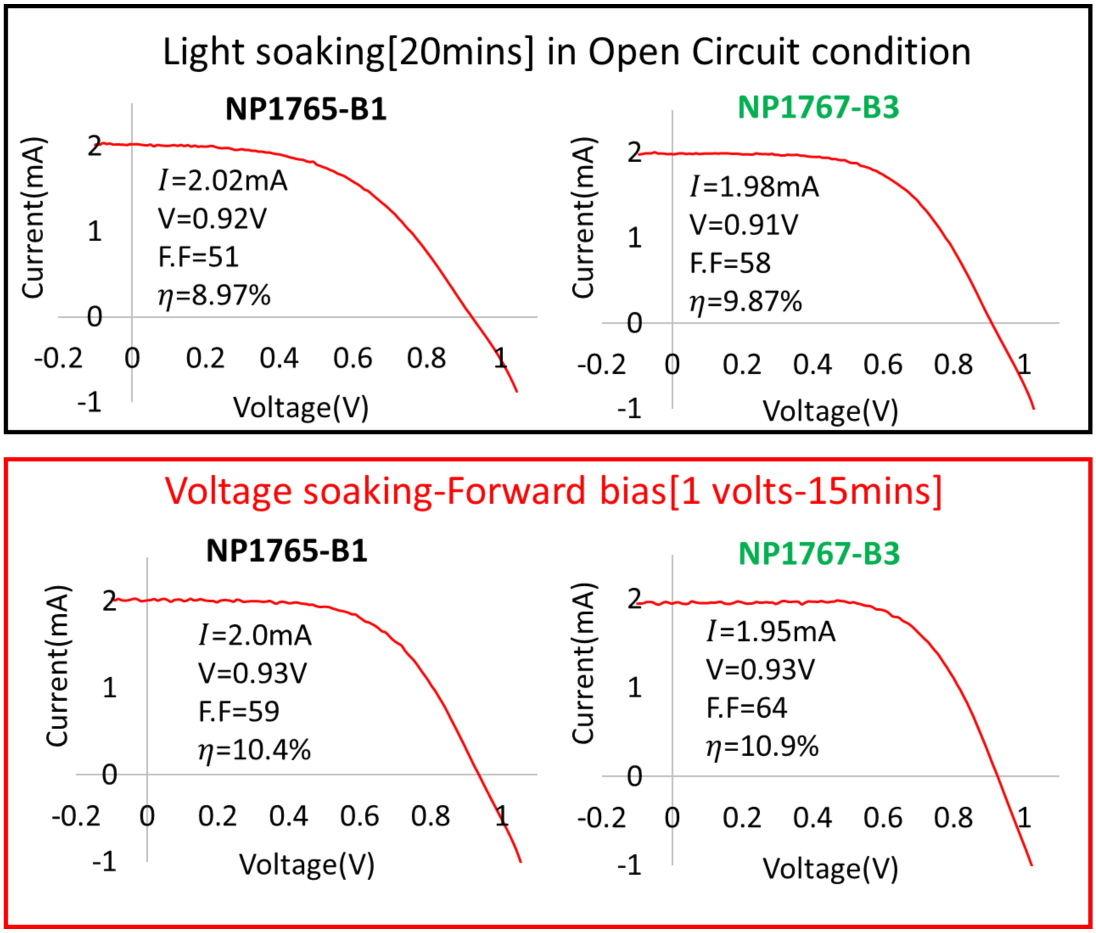

Fig 4.23: Voltage soaking

From the results (Fig 4.23), device NP1765-B1 under light soaking in open circuit condition had an efficiency of 8.97% with a fill factor of 0.51 and V_{OC} of 0.92V, while under voltage soaking its efficiency increased to 10.4% with a fill factor of 0.59 and V_{OC} of 0.93V. Similarly, NP1767-B3 had an efficiency of 9.87% with a fill factor of 0.58 and V_{OC} of 0.91V under light exposure in open circuit condition and its efficiency increased to 10.9% with a fill factor of 0.64 and V_{OC} of 0.93V. The parameter that improved in both cases was the fill factor and V_{OC} , we associate this to the constant and stronger field of the applied bias that helps in ions migrating back to the bulk and rebonding with the broken bonds, thus reducing recombination and I_O. Thereby improving fill factor and V_{OC}.

4.1.4.4. Critical thickness

In the earlier QE's (Fig 4.16), we saw that the QE is approximately in the 0.9 range across the whole spectrum. As mentioned in the fabrication section, the optimal thickness is in the ~350nm range. In our previous work, we published that perovskite is a field controlled device [171], so if thickness is greater than the range of the field, carrier collection would decrease. To show this, we made a ~500nm perovskite device and measured the QE for the same with and without a bias. Fig 4.24 shows the results of the experiment, one can see clearly that by applying a negative bias the carrier collection across the whole spectrum improved emphasizing that perovskite if field controlled, hence thickness of device needs to be carefully monitored. If perovskite is made too thin, we don't have enough photon absorption whereas if made too thick we have collection issues.

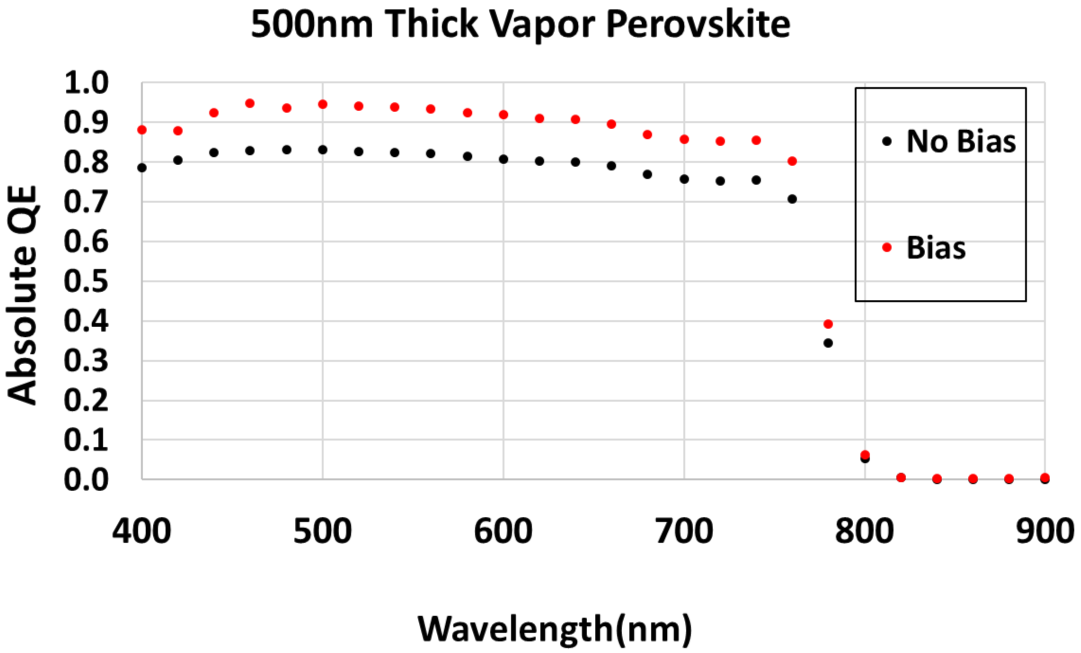

Fig 4.24: QE with Bias

4.2. PIN Sequential Devices

Voltage evolution and hysteresis arises from a combination of charge trapping from un-doped transport layers, stoichiometry (excess MAI) and grain size. The electron transport layer in NIP devices namely TiO_2 is un-doped and causes charge trapping. Almost all inorganic transport layers that align with the band edges of perovskite are doped using metal dopants, for example TiO_2 is doped with Yttrium, ZnO is doped with Al, NiO is doped with Cu etc. and they are all attacked by MAI during the diffusion process. So, an alternate is to use doped organic layers as electron and hole transport layers.

PEDOT and PCBM are doped organic layers that align well with the band edges of Perovskite. PEDOT has its valence band edge at ~5.2eV and conduction band edge at ~2.0eV, while PCBM has its conduction band edge at ~4.0eV and valence band edge at ~6.4eV. Hence, aligning as good Type-II heterojunction for hole and electron extraction respectively. FTO was used as a bottom contact and not ITO, as ITO will attacked be MAI as shown earlier in Chapter 3. The band structure of the PIN sequential architecture is shown in Figure 4.25.

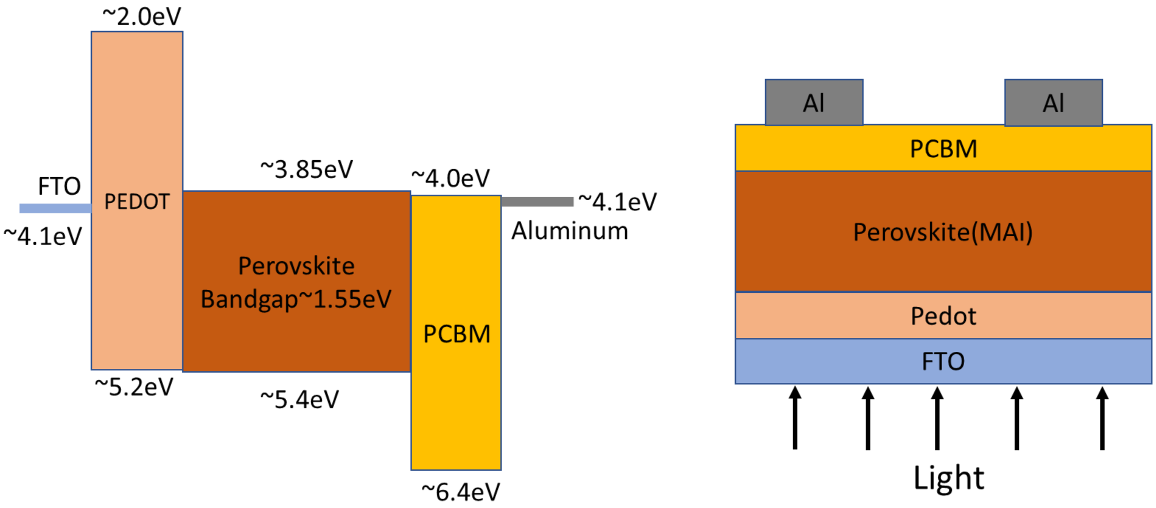

Fig 4.25: PIN sequential architecture PEDOT

Even though the bands align, from experiments we realized that adding an interfacial layer of P3HT improved carrier collection. So, the modified architecture is shown in Figure 4.26.

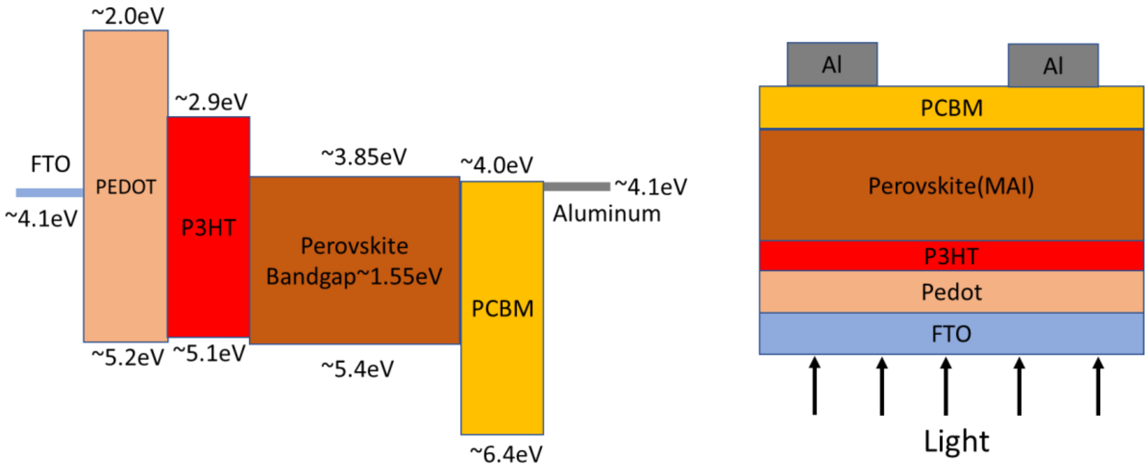

Fig 4.26: PIN sequential architecture Pedot/P3HT

The comparisons of PEDOT vs PEDOT/P3HT is shown in Figure 4.27. PEDOT/P3HT devices has higher current and voltage in comparison to PEDOT only devices.

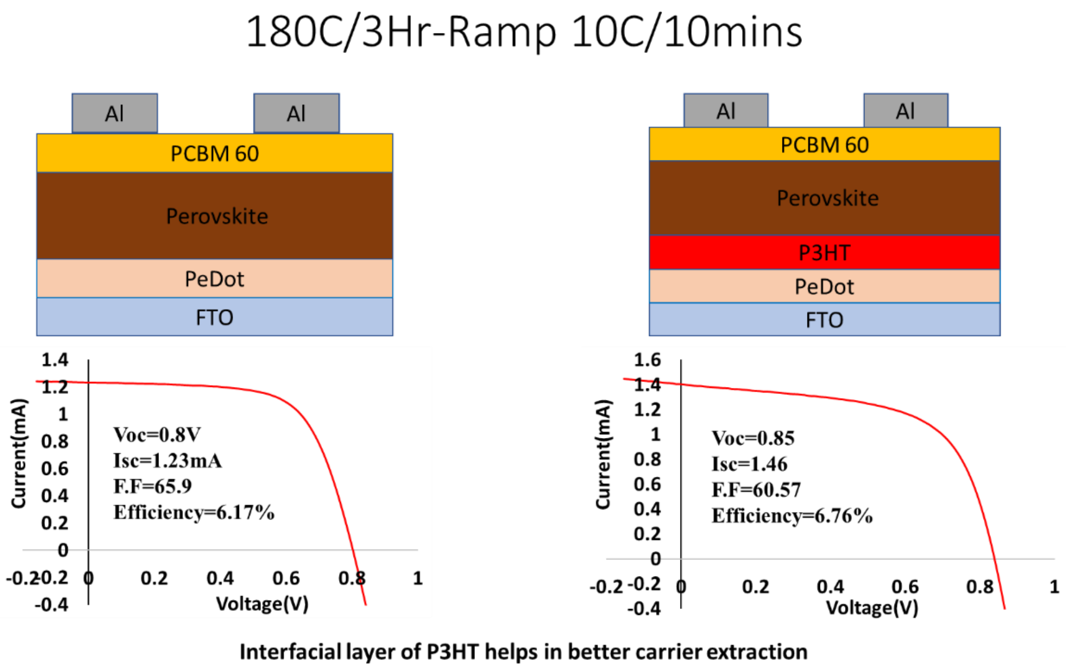
180C/3Hr-Ramp 10C/10mins

Interfacial layer of P3HT helps in better carrier extraction

Fig 4.27: PEDOT vs PEDOT/P3HT

Another issue using organic transport layers is that they cannot withstand high temperature of $180^{O}C$ for 3 hours (diffusion time of Perovskite formation). So, we had to lower the temperature to 150^0 C and used slower temperature ramp up for grain enhancement. Fig 4.28 shows the results of grain enhancement study. The temperature of graphite was ramped from 100^0C to 150^0C in steps of 10^0C. The best results were obtained for 10^0C/1Hr condition with grain size ranging from ~ 300nm-600nm. The grains are smaller than NIP grains and we associate this to lower growth temperature and changed substrate surface.

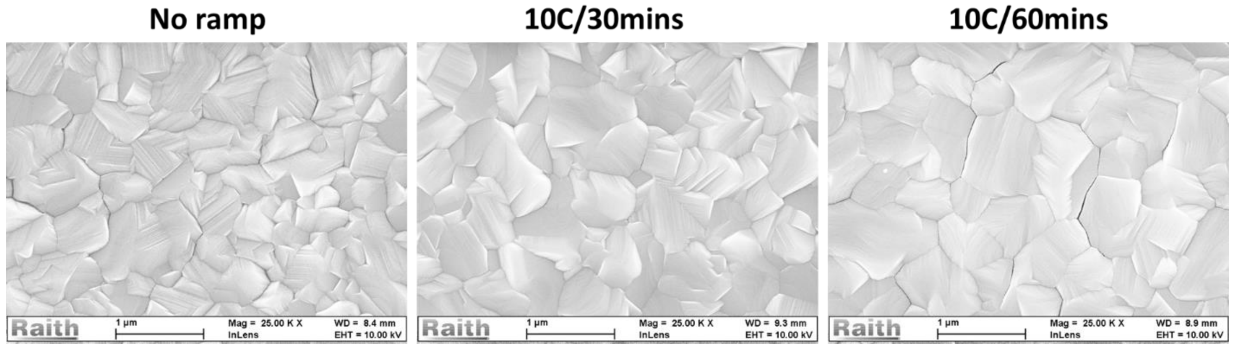
No ramp
10C/30mins
10C/60mins

Fig 4.28: Grain enhancement PIN

The film thickness was ~350nm, and it took 6hrs to form the film at 150^0C. The film wasn't kept for longer duration to minimalize the degradation of the organic transport layers. The results of 10^0C/0.5Hr & 10^0C/1Hr is shown in Figure 4.29.

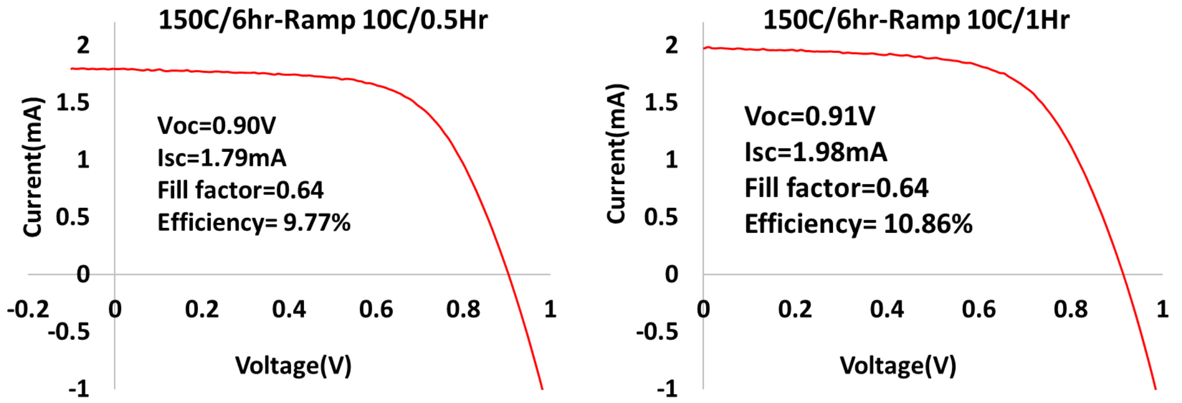
150C/6hr-Ramp 10C/0.5Hr
150C/6hr-Ramp 10C/1Hr

Fig 4.29: IV results- Sequential PIN

From the IV results, we can see that $10^0 C/60mins$ has higher current in comparison to $10^0 C/30mins$ and we associate it to the larger grain size for $10^0 C/60mins$ ramping condition [Fig 4.28]. The QE comparison for the same study is shown in Fig 4.30.

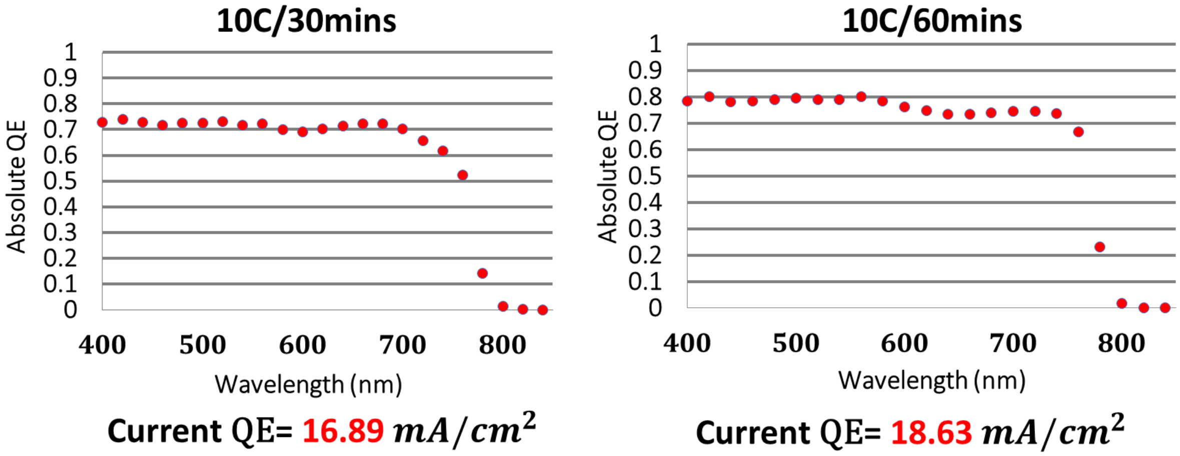

Figure 4.30: QE results- Sequential PIN

The QE results agree with the SEM results. The QE current for the $10^0 C/60mins$ ramping is $\sim 1.7 mA/cm^2$ greater than the $10^0 C/30mins$ condition and we associate this to the larger grains. Yet, high current as seen in NIP devices ($22mA/cm^2$) cannot be attained in sequential PIN owing to the constraint in diffusion temperature of organic transport layers that cannot be processed at high temperature. This is the main limitation of making sequential devices on organic transport layers.

Nevertheless, these devices have no hysteresis and negligible voltage evolution, as its transport layers are doped and the bulk had reduced MAI content owing to the reduced growth temperature. Also, the grains are of respectable size in 0.5um range. The IV hysteresis results are shown in Figure 4.31. From the results, we do see a small change in the fill factor and this could be due to non-stoichiometry in the surface (erfc function) that generates additional ions which accumulate at the interface at zero bias or when slight negative bias is applied before the forward scan.

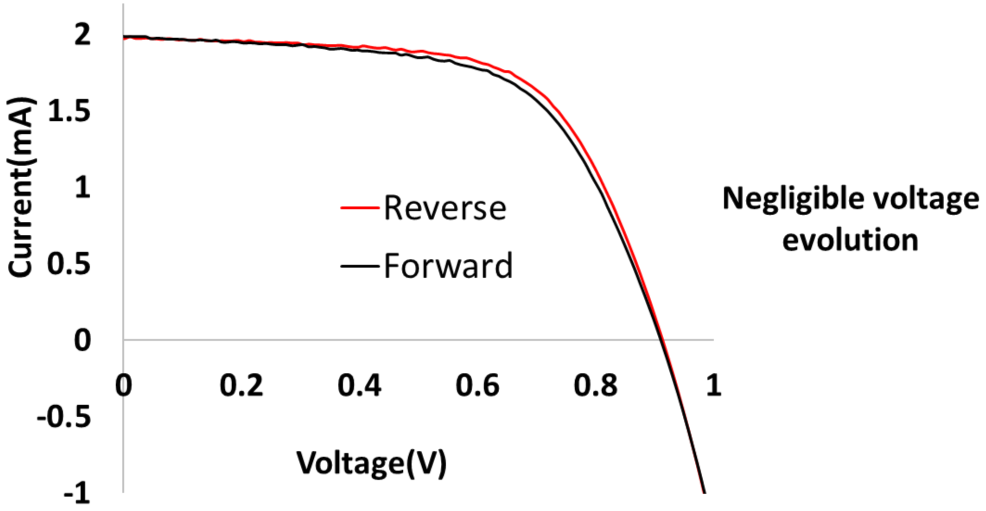

Scan Direction	Current(mA)	Voltage(V)	Fill Factor	Efficiency %
Reverse	1.98	0.91	0.64	10.86
Forward	1.99	0.91	0.61	10.47

Fig 4.31: IV Hysteresis-PIN sequential device.

The above study shows that when doped transport layer are used, there is no hysteresis and insignificant voltage evolution. Since, the transport layers are doped, there is no charge trapping at the end of reverse scan and beginning of forward scan (as explained for Fig 4.22), thus we see no hysteresis. However, organic transport layer which is used in the above architecture is not suitable for high temperature processing, thereby bringing the need for co-evaporation, a room temperature process.

4.3. PIN Co-Evaporated Devices

Though sequential vapor processing produced respectable high efficiency devices, the technique has its limitations. The process is not suitable for organic transport layers due to processing limitations, ITO substrates or metal doped transport layers as it is attacked by MAI, and stoichiometry is intrinsically nonuniform across thickness owing to erfc function MAI distribution. Thus, a better approach to fabricating vapor devices is co-evaporation as it has no restriction on the materials used as transport layers and contacts, it enables stoichiometric control and it is a room temperature process.

As we made co-evaporated devices numerous challenges were overcome, the co-evaporator was constantly modified to meet the processing requirements and to establish control, chapter 3 goes over this in detail. We are still working on our system, in the future we plan to use ceramic based capacitance monometers to monitor the chamber pressure, as they will not be affected by MAI. Also, we modified the PIN architecture.

4.3.1. FTO/PEDOT/PTAA/Perovskite/PCBM/Aluminum

A small modification to our earlier Sequential PIN architecture was made before we proceeded with co-evaporated devices, we replaced P3HT with PTAA (Poly (triaryl amine)). PTAA has a larger bandgap (~3.2 eV) than P3HT (~2.2 eV), thereby enabling more transmission of light across the spectrum. PTAA is amorphous doped p-type semiconductor polymer and is commonly used as hole transport material in OLED’s [228]. Figure 4.32 shows the transmission of PTAA. At 2.0 mg/ml (solvent is Toluene), the transmission is nearly 100% across the spectrum as can be seen in the Figure 4.32.

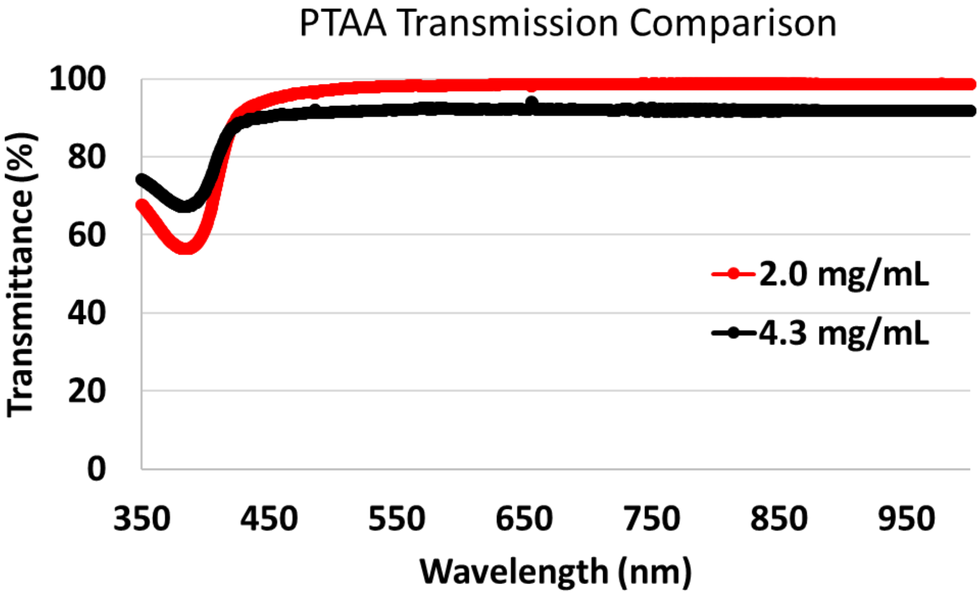

Fig 4.32: PTAA Transmission

The band structure of PIN architecture is shown in Figure 4.33, the PTAA-Perovskite valence band edges align better than P3HT-Perovskite band edge, thus enabling lesser band offset and higher V_{OC}. Also, the literature review on PTAA demonstrates that group using PTAA as hole transport layer have attained V_{OC} in the 1.0V-1.1V [43, 168, 229-231] range indicating that its valence band edge is approximately in the 5.3eV-5.4ev range.

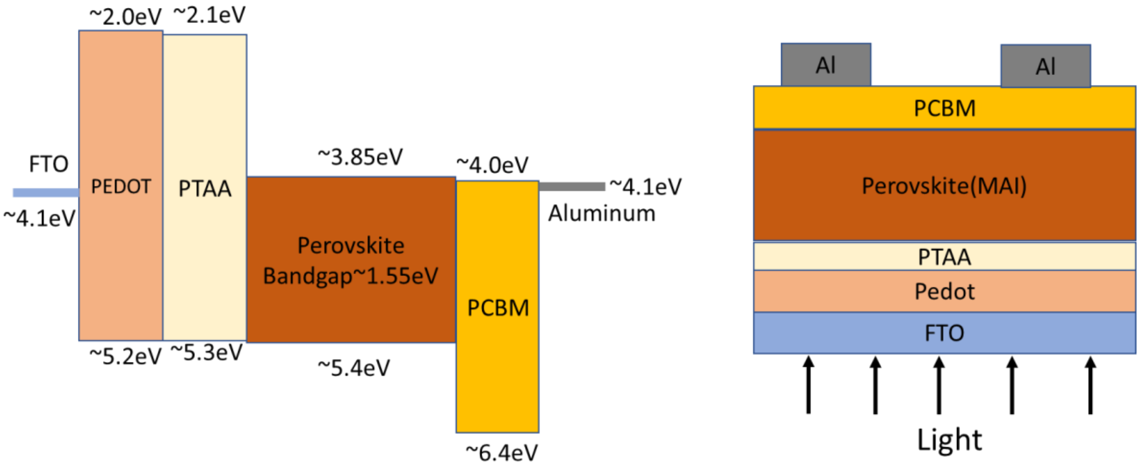

Fig 4.33: PIN architecture-FTO/PEDOT/PTAA

From the Hysteresis and voltage evolution studies, we know that MAI at the interface can create double diode (S shaped curve), voltage evolution and hysteresis. As explained elaborately in Chapter 3, MAI has high vapor pressure and will deposit on any cold surface including the substrate. To ensure that no excess MAI is on the substrate, ~10nm of PbI2 is deposited on the substrate before ramping up MAI crucible. That way while establishing PbI_2 rate and MAI chamber pressure for the run, excess MAI is not deposited in the substrate but on PbI_2 film which will convert to perovskite. We found that for ~10nm PbI_2, the stabilization of PbI_2 and MAI has to be carried forth in ~60mins-70mins for best results.

The $PbI_2 - MAI$ stoichiometry optimization study was carried out by keeping the PbI_2 rate (crucible temperature) constant at $315^O C$[~0.6 $Å/s$] and varying the MAI pressure. Also, the PTAA concentration and spin coating conditions was 2mg/ml PTAA in Toluene, spin coated at 6000rpm/40sec and post annealed at 150°C/10mins in glovebox. The results of the experiment are shown below in Fig 4.34-4.36.

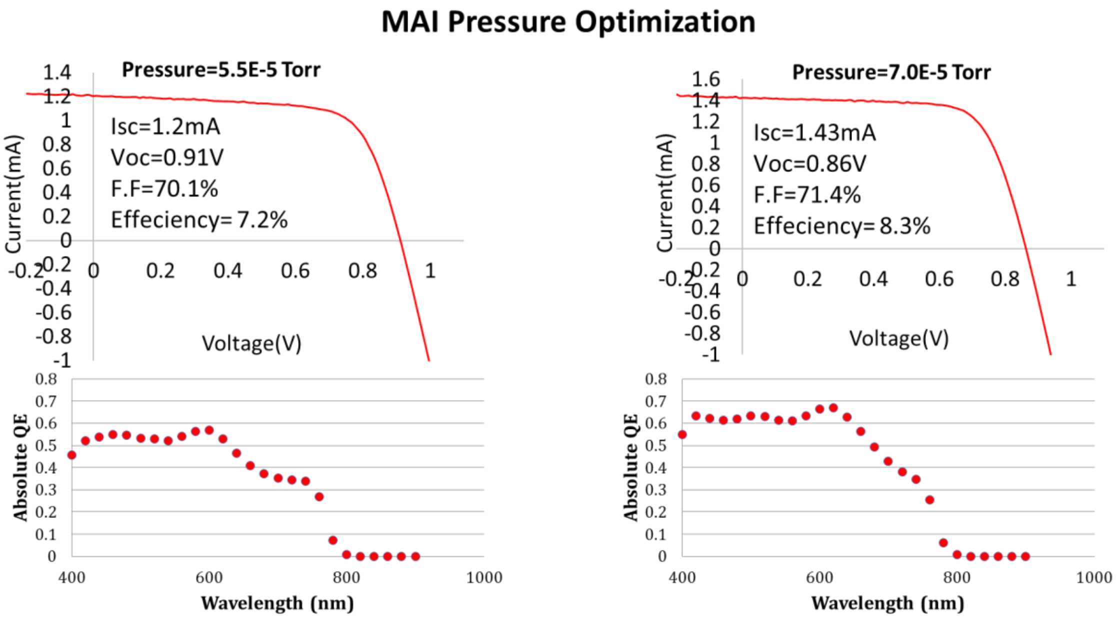

Fig 4.34: MAI pressure optimization Study 1

From the IV and QE results, we can see that increasing the MAI pressure increases the current. Therefore, we continued to increase the pressure and the results are shown in Fig 4.35. From the results of IV and QE, the current increased on increasing the MAI pressure, however increasing MAI pressure to the $10^{-4}\,Torr$ range, offset the stoichiometry. Hence, we did further fine tuning in the $9.5\times10^{-5}\,Torr$ range.

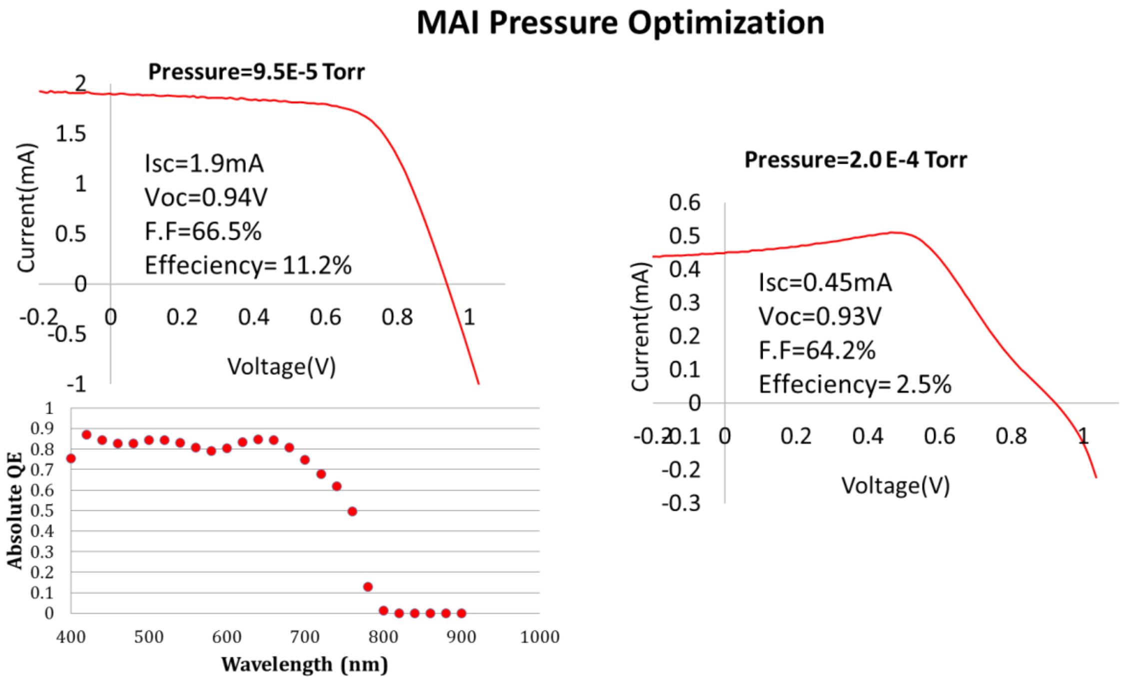

Fig 4.35: MAI pressure optimization Study 2

Since PTAA is an amorphous polymer, its thickness is decreased for reducing the series resistance. The ideal concentration was found to be 0.75mg/ml for the same spin coating conditions. Also, we further fine-tuned the MAI pressure to $9.0\times10^{-5}\,Torr$, doing so improved the fill factor, voltage and current. The results of the best cell on FTO/PEDOT/PTAA is shown in Fig 4.36. The device had an efficiency of 15%, $V_{OC} = 1.01V$, Current=19.1 mA/cm^2 and Fill factor=0.78. The current as seen from QE needs more improvement, nevertheless our fill factor was excellent better than any other group in literature.

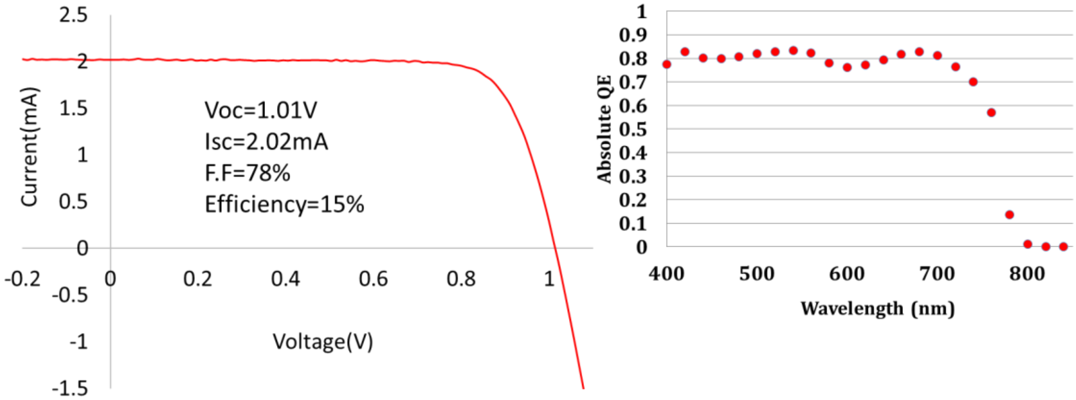

Fig 4.36: Best Device- FTO/PEDOT/PTAA

Figure 4.37 shows the hysteresis and voltage evolution for the FTO/Pedot/PTAA device, both the transport layers i.e. PTAA and PCBM are doped, so there is no charge trapping, hence no hysteresis is observed. However, there is a minor voltage evolution i.e. its takes the device 2 minutes to stabilize to the final voltage. The reasons for voltage evolution will be explained later (section 4.3.4).

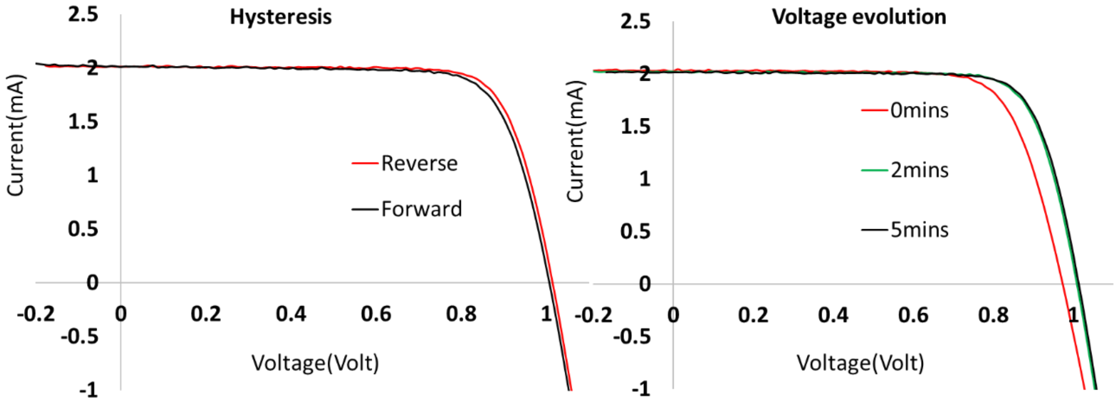

Fig 4.37: IV Hysteresis & Voltage evolution-FTO/PEDOT/PTAA

4.3.2. ITO/PTAA/Perovskite/PCBM/Aluminum

Driving away moisture from the surface of the PTAA films before co-evaporation is important as moisture at the interface could lead to recombination center or surface states. Even though FTO/PEDOT/PTAA produced good devices, we decided to modify the architecture because

PEDOT is strongly hygroscopic [232] polymer. Under normal circumstance, it is spin coated outside the glovebox and then transferred into the glovebox, following which it is annealed at 150℃ /10mins i.e. to drive away the moisture before spin coating the active layers.

But our co-evaporator is not in the glovebox, so the film is briefly exposed to atmosphere before loading it in the co-evaporator, hence there is a high probability of moisture retention in PEDOT films considering its hygroscopic nature. Also, PTAA is doped polymer and can make good ohmic contact on FTO and ITO. As PEDOT isn't required in our architecture, we removed it. Also, FTO was replaced by ITO, as it's a better band match for PTAA. The band structure of the new architecture is shown in Figure 4.38.

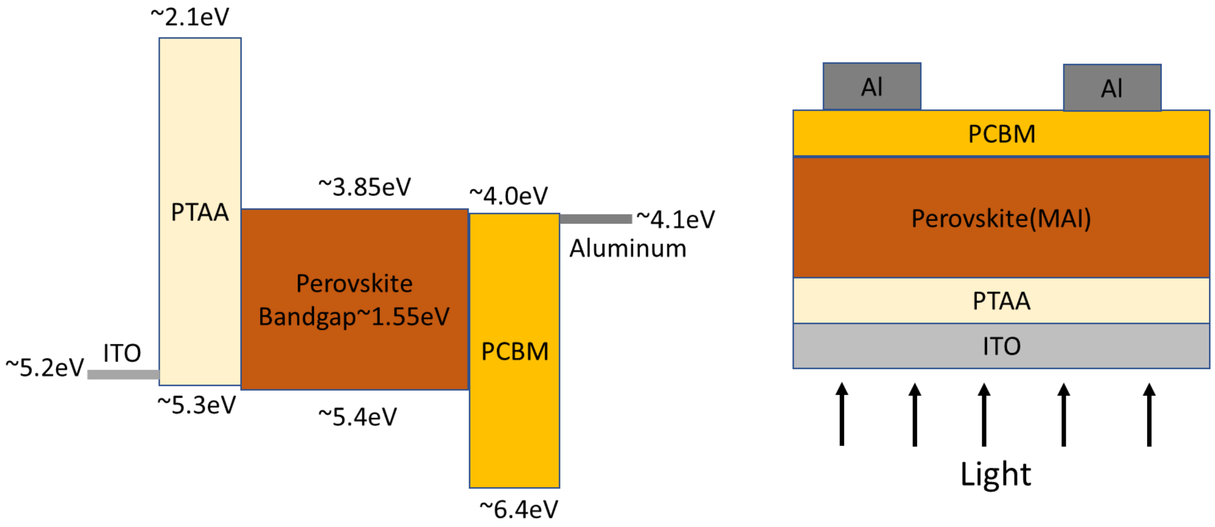

Fig 4.38: PIN architecture-ITO/PTAA

In the earlier FTO/PEDOT/PTAA devices, substrate temperature was kept at room temperature. But, for the ITO/PTAA based devices, the substrate temperature was increased for two reasons, namely to increase grain size and drive away moisture. However, it is important to recognize that MAI has high vapor pressure, so the substrate temperature cannot be increased beyond a point else the compound wont form.

The disadvantage is that high temperature is important for grain growth. From experiments, we found that if substrate temperature is increased beyond 100°C, MAI reevaporates and does not form perovskite, so the maximum substrate temperature was set to $75^{O}C$. Fig 4.39 shows grain size of perovskite crystals grown by co-evaporation at room temperature, 50°C and 75°C.

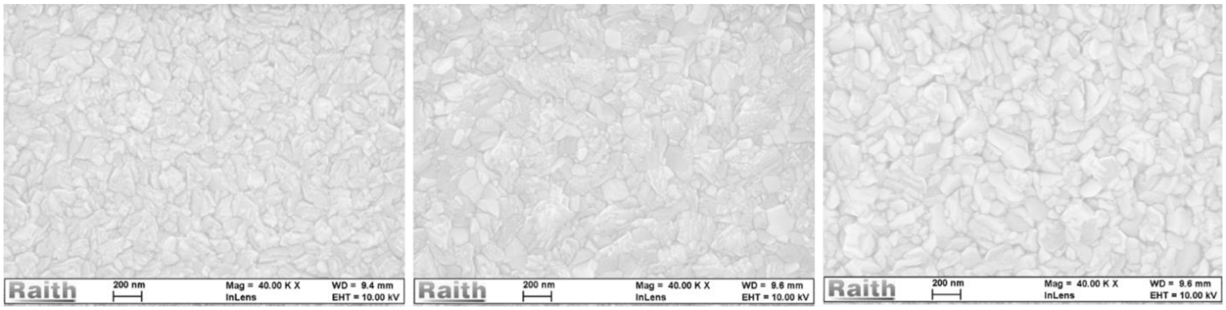

Room Temperature **50 Celsius** **75 Celsius**

Fig 4.39: Grain size- ITO/PTAA

Though, not a large difference, we can still see that the grain size distribution increases with increasing temperature i.e. 75°C grown films appears to have larger grain size distribution in comparison to the room temperature grown films. Fig 4.40 shows the results of the room temperature vs 50°C grown films.

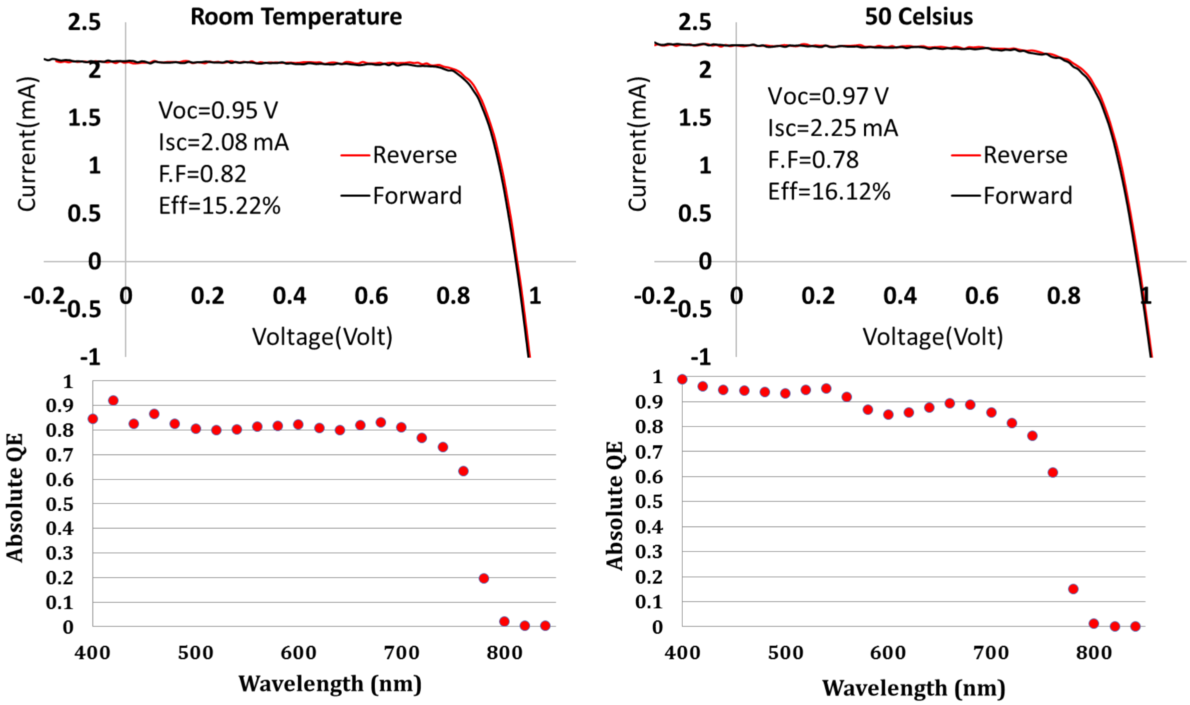

Fig 4.40: IV & QE-Room Temperature vs 50°C [ITO/PTAA]

For the 50°C substrate temperature grown perovskite, the growth rate had to be slowed down for perovskite formation owing to the high vapor pressure of MAI. The MAI pressure was kept constant at $9\times10^{-5}\ Torr$, however the PbI_2 crucible temperature was decreased to 295°C that corresponds to a growth rate of $0.26\ Å/s$. From the IV and QE results [Figure 4.40], we can see that 50°C had better carrier collection and higher current, we attribute the better current to mainly larger grains and no moisture at the interface.

Also, like in the earlier architecture there is no hysteresis for both room temperature and 50°C grown perovskite films as can be seen in the IV curves [Figure 4.40], thus emphasizing the importance of doped transport layers. Figure 4.41 shows the results for 75°C substrate temperature grown perovskite.

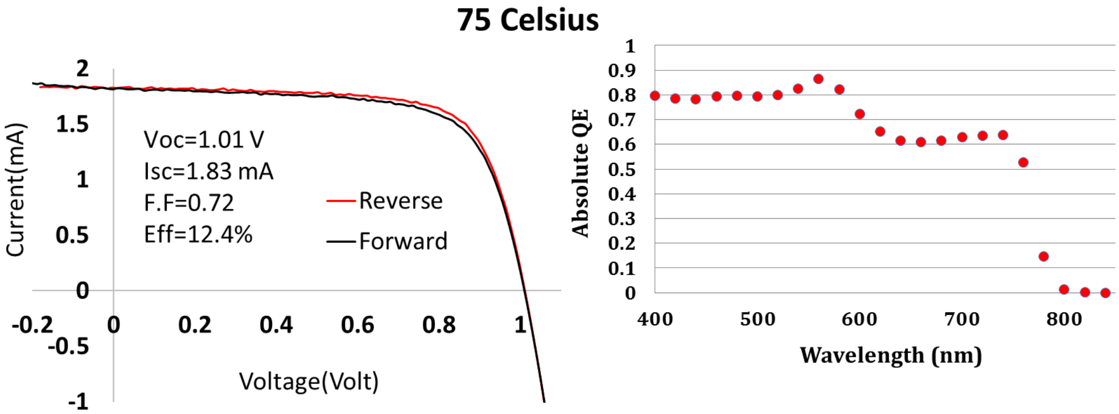

Fig 4.41: IV- 75℃ [ITO/PTAA]

For the 75℃ substrate temperature grown perovskites, no perovskite film formed when the MAI pressure was kept in the $9\times10^{-5}\,Torr$ range. Therefore, the pressure was increased to $1.0-2.0\times10^{-4}\,Torr$ range, keeping the PbI_2 growth rate constant at $0.26Å/s$. However, this condition was difficult to control owing to MAI's high vapor pressure, the pressure often surpassed above the $2\times10^{-4}\,Torr$ range and stabilizing the chamber pressure post overshoot is problematic.

To simply things, we increased the growth rate back to $0.6Å/s$ keeping the pressure in the $(2-4)\times10^{-4}\,Torr$ range. But, again keeping the substrate at 75℃ and increasing the MAI pressure introduced another problem, MAI started attacking the ITO. The results of the 75℃ run (Fig 4.41) shown above is a shortened run, with perovskite thickness of ~200nm, as can be seen from the QE. Longer runs gave us bad devices as ITO was attacked by MAI.

The IV shows no hysteresis, however the current is less. Though ITO is a better architecture, FTO is more suitable for the substrate temperature study as it will not be attacked by MAI. Figure 4.42 shows the results of voltage evolution study for ITO/PTA based devices. As can be clearly seen, ITO/PTAA has voltage evolution with the voltage stabilizing in 6mins. The explanation for this will be given in section 4.3.4.

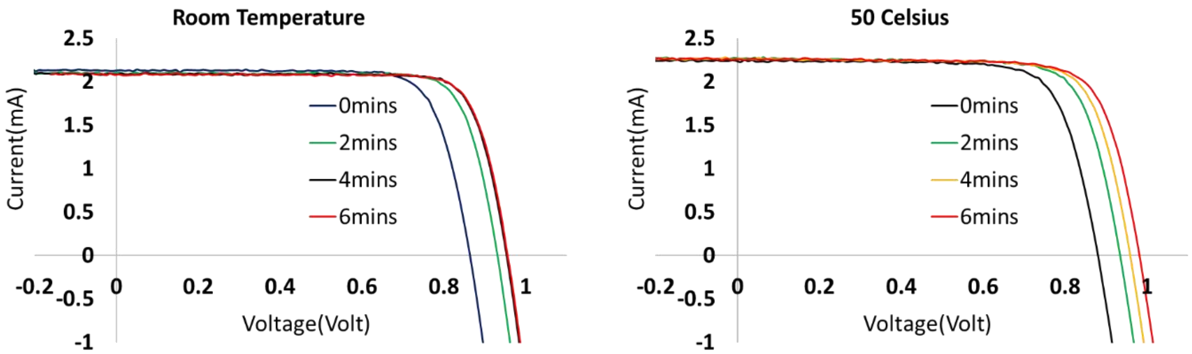

Voltage (Volts)	Current (mA)	Fill Factor	Efficiency %	Wait time
0.953	2.08	0.82	15.24	6mins
0.949	2.08	0.82	15.23	4mins
0.93	2.10	0.80	14.85	2mins
0.86	2.12	0.79	13.68	0mins

Voltage (Volts)	Current (mA)	Fill Factor	Efficiency %	Wait time
0.97	2.25	0.78	16.11	6mins
0.96	2.26	0.77	15.81	4mins
0.93	2.27	0.77	15.38	2mins
0.88	2.24	0.76	14.18	0mins

Fig 4.42: Room Temperature vs 50℃ -Voltage evolution

4.3.3. FTO/PTAA/Perovskite/PCBM/Aluminum

As ITO substrates, cannot withstand MAI at elevated temperature, we revert to FTO based substrate. FTO unlike ITO does not get attacked by MAI, thereby allowing for processing flexibility at higher pressure and temperature. Also, since PTAA is a doped organic transport layer, it makes good ohmic contact with FTO, so there is no problem on replacing ITO with FTO. Figure 4.43 shows the band structure of the FTO/PTAA device architecture.

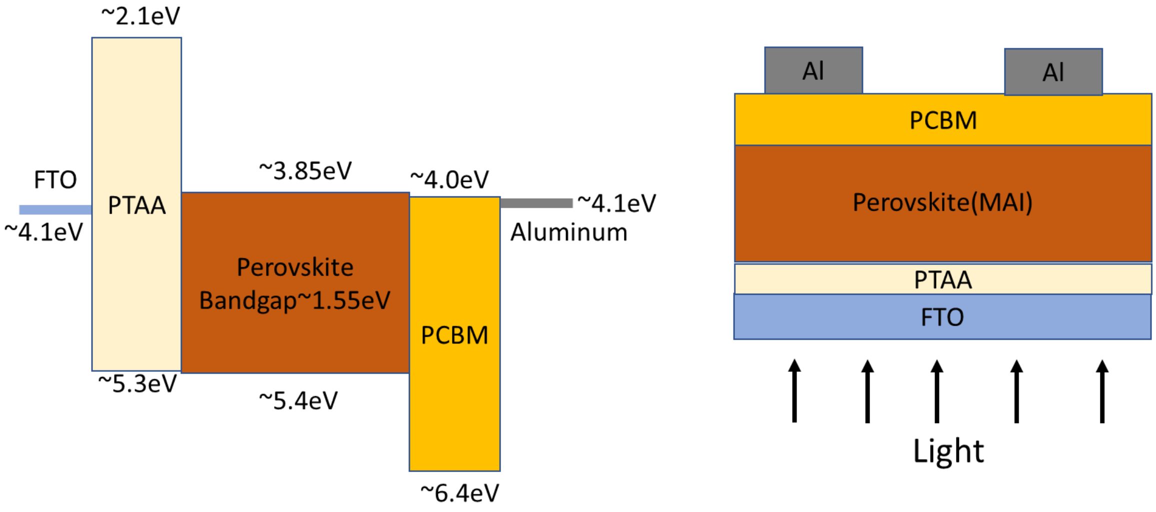

Fig 4.43: PIN architecture-FTO/PTAA

A similar study to the one concluded on ITO/PTAA (Fig 4.39) devices is carried out on FTO/PTAA based devices. Figure 4.44 shows the grain size comparison of perovskite grown on FTO/PTAA at different temperatures (room temperature vs 50℃ vs 75℃). As one can see from the images [Figure 4.44], the grain size grows slightly as the substrate temperature is increased from room temperature to 75℃. The processing conditions for the different temperature conditions are same as carried out earlier on ITO/PTAA devices.

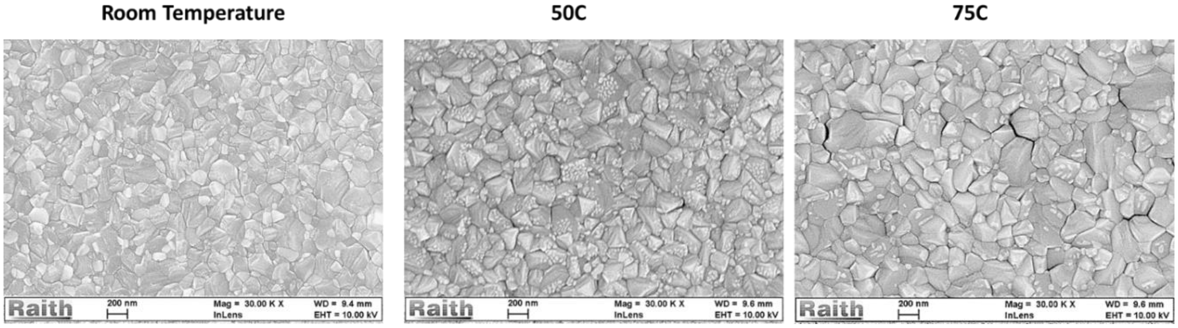

Fig 4.44: Grain size- FTO/PTAA

The IV and QE results of the room temperature vs 50℃ vs 75℃ are shown in Figure 4.45-4.47 respectively. The results are similar, with I_{SC} $\sim 2.3mA$ [$J_{SC}\sim 21.7mA/cm^2$], V_{OC} $\sim 1V$, Fill Factor~0.75 % and Efficiency ~16%. For degradation studies [Istiaque Hossian's PhD work], we expect 75℃ to show better results owing to the larger grain size and lack of moisture. The QE of the FTO/PTAA devices is 0.9 across the spectrum [Figure 4.45-4.47] clearly showing good carrier collection. Also, the devices have no hysteresis emphasizing the importance of doped transport layers.

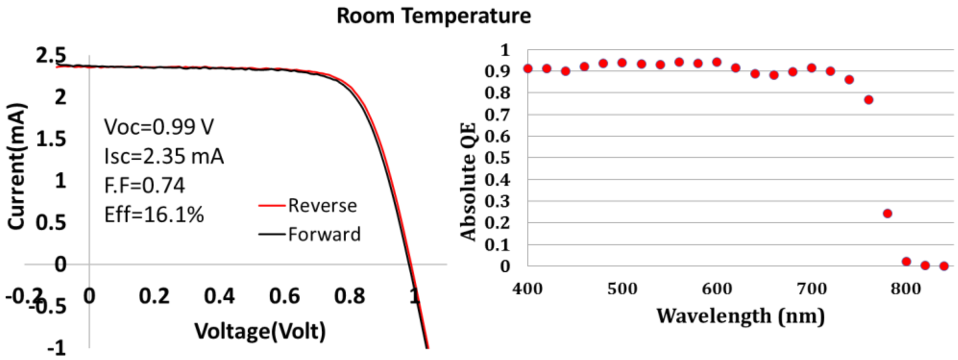

Fig 4.45: IV Room Temperature -FTO/PTAA

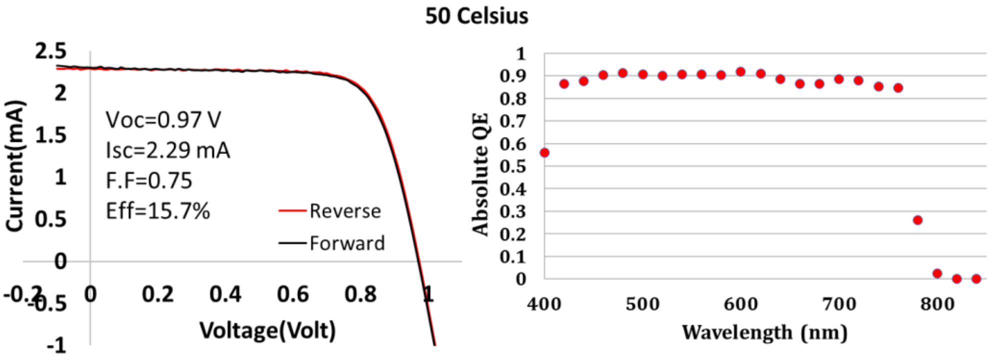

Fig 4.46: IV 50℃ -FTO/PTAA

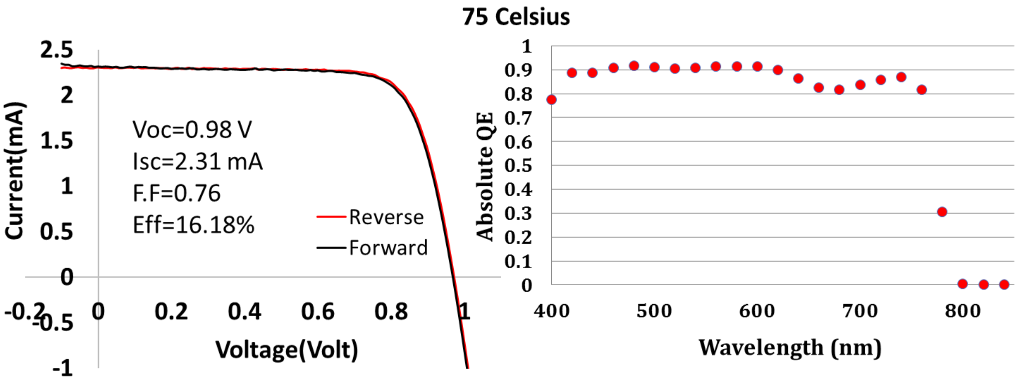

Fig 4.47: IV 75℃ -FTO/PTAA

Nonetheless FTO/PTAA devices also has voltage evolution. It takes 2 minutes for the device to stabilize buts its voltage evolution is faster than that observed in ITO/PTAA devices. We will compare the voltage evolution of the ITO vs FTO based devices in the next section.

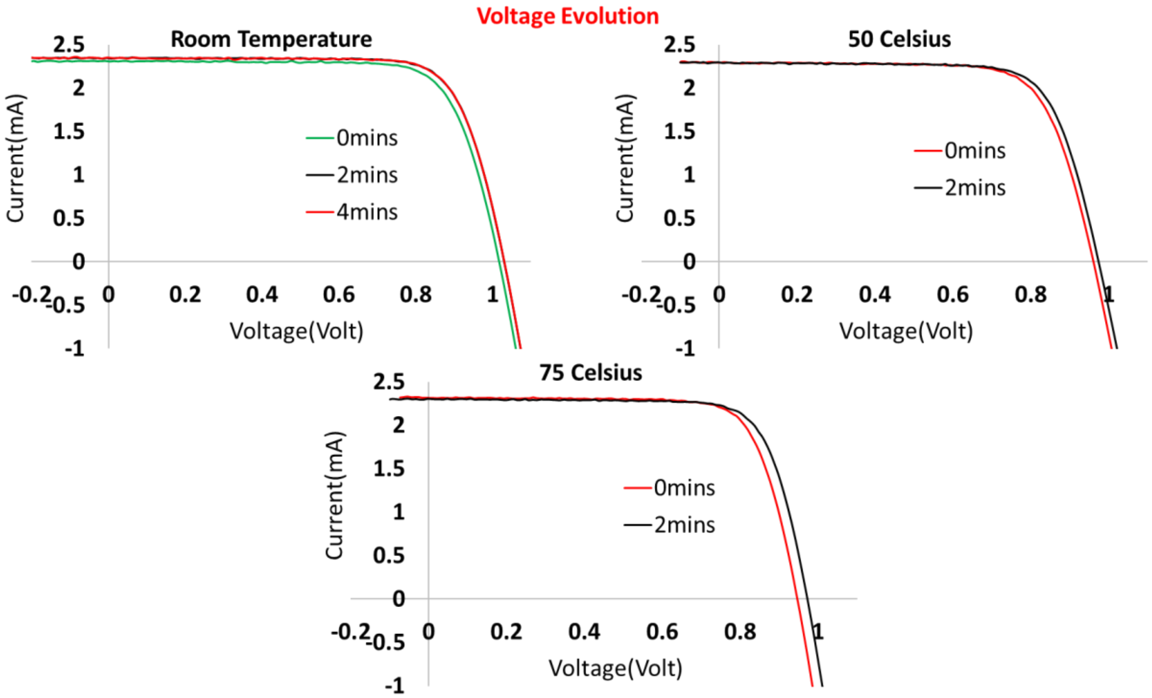

Fig 4.48: Voltage evolution-FTO/PTAA devices

4.3.4. Voltage evolution: ITO/PTAA vs FTO/PTAA

The voltage evolution on co-evaporated devices can be explained from the grain size of the films. We have already seen the importance MAI amount (stoichiometry) and doped transport layers, this section will emphasize the importance of grain size on device anomalies. Figure 4.49 shows the grain size of perovskite grown on ITO/PTAA vs FTO/PTAA devices. The grain size of perovskites grown on FTO/PTAA is naturally larger, perhaps owing to difference in surface energy of FTO/PTAA vs ITO/PTAA surface. As we know, large grains have several advantages such as higher current, lesser recombination, better fill factor and high voltage. In addition, we will see that larger grains also minimizes voltage evolution.

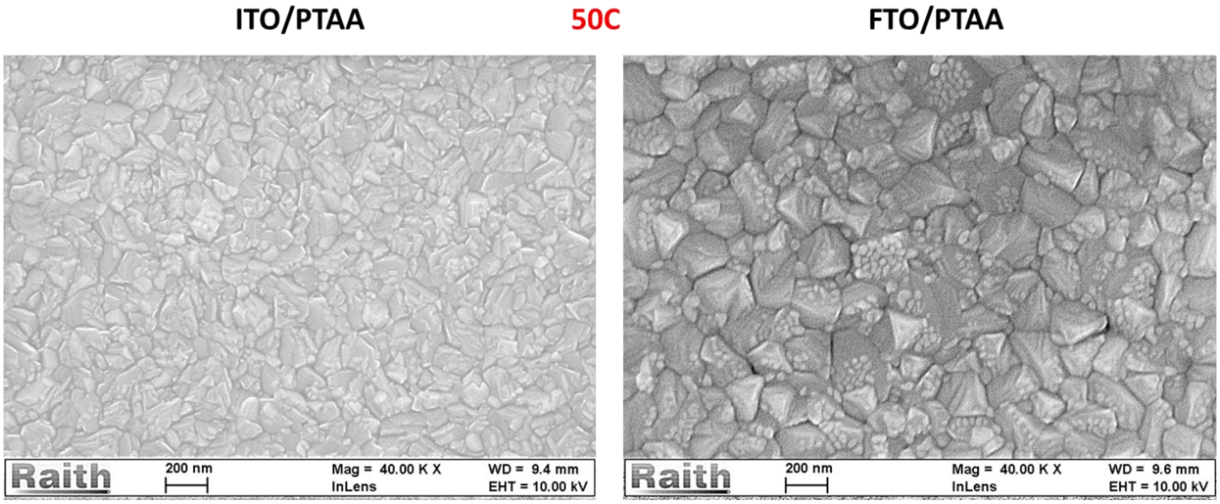

Fig 4.49: Grain size: ITO/PTAA vs FTO/PTAA

Figure 4.50 shows the voltage evolution comparison for the ITO/PTAA vs FTO/PTAA devices, the ITO/PTAA devices takes ~6mins to stabilize while the FTO/PTAA devices takes 2 mins to stabilize.

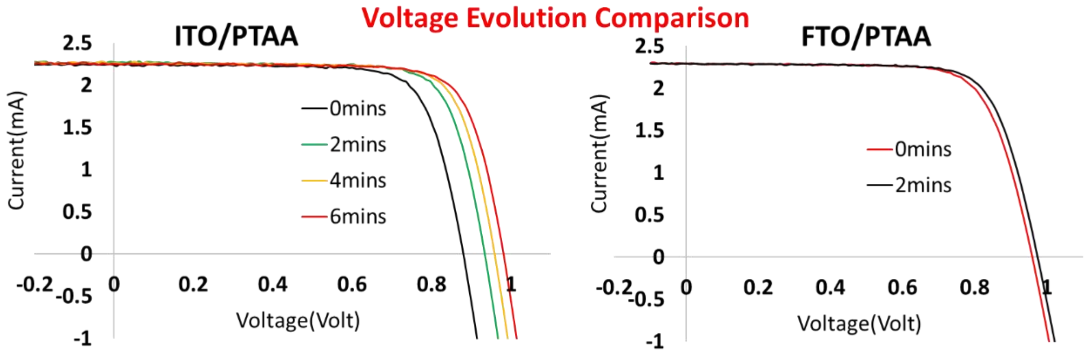

Voltage (Volts)	Current (mA)	Fill Factor	Efficiency %	Wait time
0.97	2.25	0.78	16.11	6mins
0.96	2.26	0.77	15.81	4mins
0.93	2.27	0.77	15.38	2mins
0.88	2.24	0.76	14.18	0mins

Voltage (Volts)	Current (mA)	Fill Factor	Efficiency %	Wait time
0.97	2.29	0.75	15.71	2mins
0.96	2.29	0.74	15.16	0mins

Fig 4.50: Voltage evolution: ITO/PTAA vs FTO/PTAA

We know that smaller the grain size, larger the grain boundaries surface. Also, these grain boundaries have broken bonds, that can generate ions, thus increasing the ion density. Therefore, grain boundaries offer pathways and is a source of ions. Consequently, ITO/PTAA owing to its smaller grain films has more ion accumulation at the interface and a slower voltage evolution in comparison to FTO/PTAA that has larger grain. However, there is no hysteresis in both ITO/PTAA/Perovskite/PCBM/AL and FTO/PTAA/Perovskite/PCBM/AL architecture as the transport layers namely PTAA and PCBM are doped, thereby having no charge trapping of carriers/ions at the interface during the revere and instant forward scan.

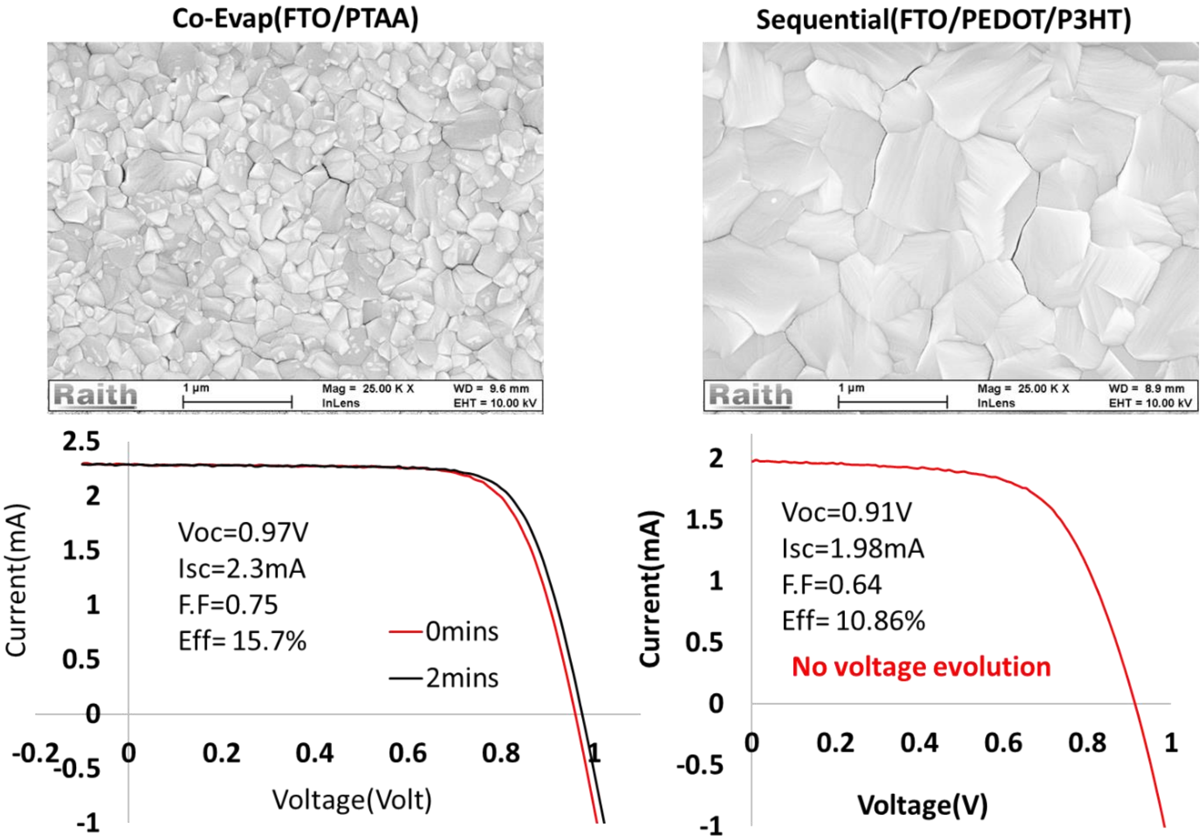

Fig 4.51: Voltage evolution: FTO/PTAA vs FTO/PEDOT/P3HT

Figure 4.51 compares the Grain size & Voltage evolution of the Co-Evaporated FTO/PTAA and sequentially evaporated FTO/PEDOT/P3HT device. The sequentially evaporated device owing to $150°C/6hr$ MAI diffusion has large grains in comparison to the FTO/PTAA device. Therefore, there is no voltage evolution because large grain have less pathways for ionic migration, also diminished grain boundaries generate lesser ions. The 6-hour duration was the exact time required for complete perovskite formation, so we assume excess MAI in the bulk is significantly reduced. Even though sequentially grown devices have no voltage evolution and hysteresis, its performance is sub-par in comparison to the co-evaporated devices.

The lone disadvantage of co-evaporated device is the voltage evolution and it is minimalized to an extent using FTO/PTAA architecture. Techniques like solvent annealing, a proven technique for grain enhancement could be utilized, however the whole purpose of vapor devices is to make the active layer solvent free, so solvent annealing defeats the purpose especially in vapor devices. So, in the future, novel grain enhancement approaches need to be devised for grain enhancement.

4.3.5. Record efficiency PIN cell.

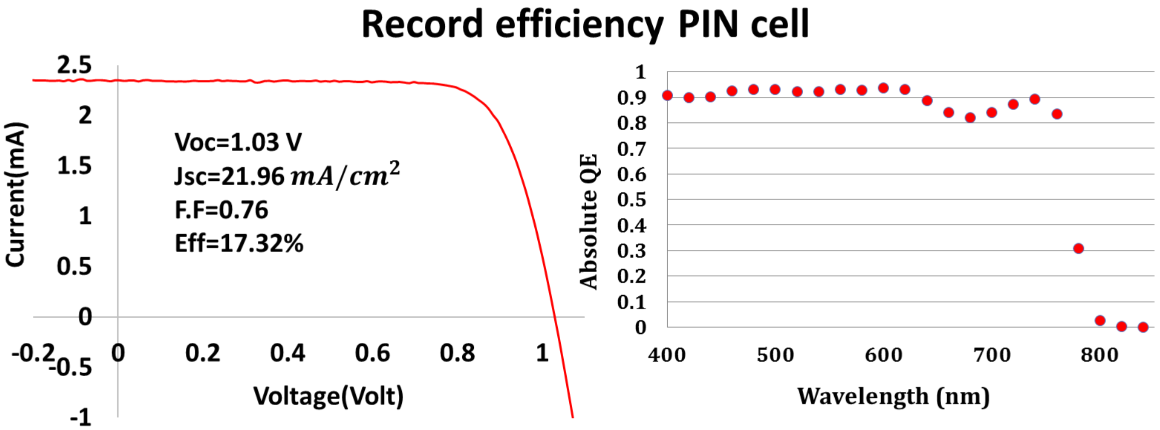

Fig 4.52: Record efficiency-PIN cell

The champion PIN cell made by us has an efficiency of 17.3% with current density of 21.96 mA/cm^2, $V_{OC} = 1.03V$ & F. F=0.76, the device was grown on FTO/PTAA at room temperature. 17.3% is the highest ever recorded efficiency till date for Co-evaporated PIN devices surpassing the PIN cell made by Meredith et al[55]. Figure 4.53 shows a histogram of co-evaporated PIN devices. The average Efficiency~15.4%, average V_{OC}~0.99V, average Fill factor~0.76 and average J_{sc}~20.6 mA/cm^2.

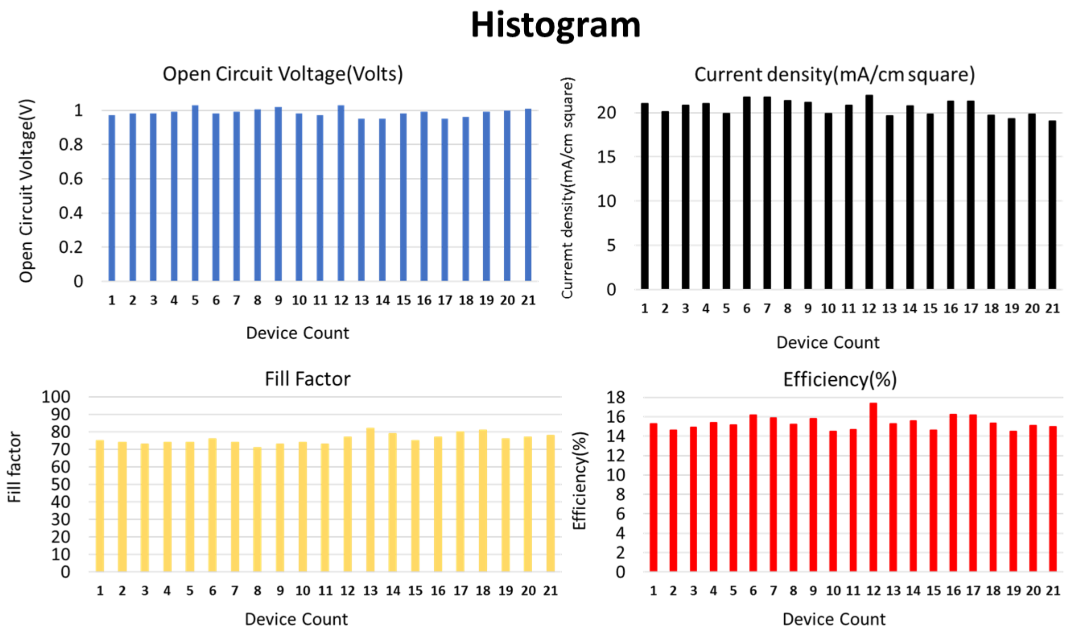

Parameters	Mean	Std Dev
Efficiency (%)	15.38	0.72
Voltage (V)	0.986	0.02
Current (mA/cm^2)	20.59	0.87
Fill Factor	0.76	2.88

Fig 4.53: Histogram Co-evaporated PIN cell.

4.4. NIP Co-Evaporated Devices

Lastly, we made co-evaporated NIP devices on FTO/TiO_2, the device architecture is shown in Figure 4.54. We tweaked our co-evaporation fabrication and added an additional step. Post co-evaporation, we annealed the as-deposited film in the glove-box in the presence of MAI (20mg) at $180℃/60mins$ (no ramping) for post-deposition grain enhancement. Grain enhancement as seen earlier in ITO/PTAA vs FTO/PTAA devices, helps reduce voltage evolution. In PIN architecture, post deposition grain enhancement wasn't an option due to temperature limitation of organic layers.

TiO_2 is an un-doped transport layer, so it is impossible to eliminate voltage evolution and hysteresis owing to charge trapping. Even though hysteresis and voltage evolution cannot be completely evaded, it can be minimized to an extent by decreasing the excess ion density (stoichiometry control & large grains) and ionic pathways (grain boundaries). So, we decided to post anneal in the presence of MAI at high temperature to grow the grains, if annealing is done without MAI, perovskite will disintegrate to PbI_2 as will be seen in chapter 5.

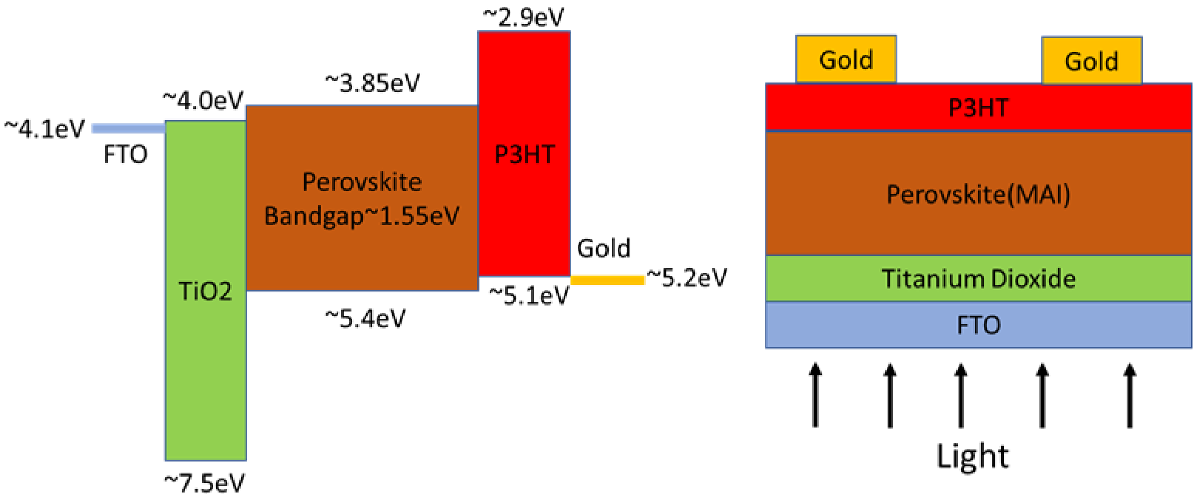

Fig 4.54: Co-evaporated NIP architecture

Fig 4.55 shows the grain size comparison of Co-evaporated PIN on FTO/PTAA vs Grain enhanced Co-evaporated NIP (grain enhanced) vs Sequential NIP.

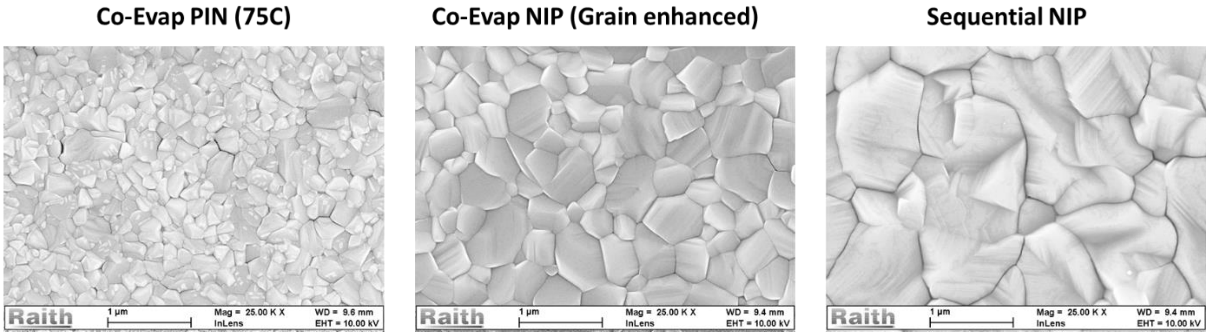
Co-Evap PIN (75C) **Co-Evap NIP (Grain enhanced)** **Sequential NIP**

Fig 4.55: Co-Evap [PIN vs NIP] vs Sequential NIP

The grain size of co-evaporated NIP is significantly larger than co-evaporated PIN owing to grain enhancement. Similar grain enhancement technique for coevaporated-PIN devices is not possible as organic layers cannot withstand high temperature of $180^{\circ}C$. Yet, the grain size of sequential device will be larger, as the fabrication procedure involves slow ramp up $(10^{\circ}C/10mins)$ and $180^{\circ}C/2Hrs$ diffusion that helps in producing large grain.

But the drawback of sequential devices is that these films have excess ion density at the interface of perovskite/P3HT owing to the erfc function. For architectures with un-doped transport layers, large grain is critical as it minimizes ion density at the interface. Figure 4.56 shows the results of grain enhanced co-evaporated NIP device.

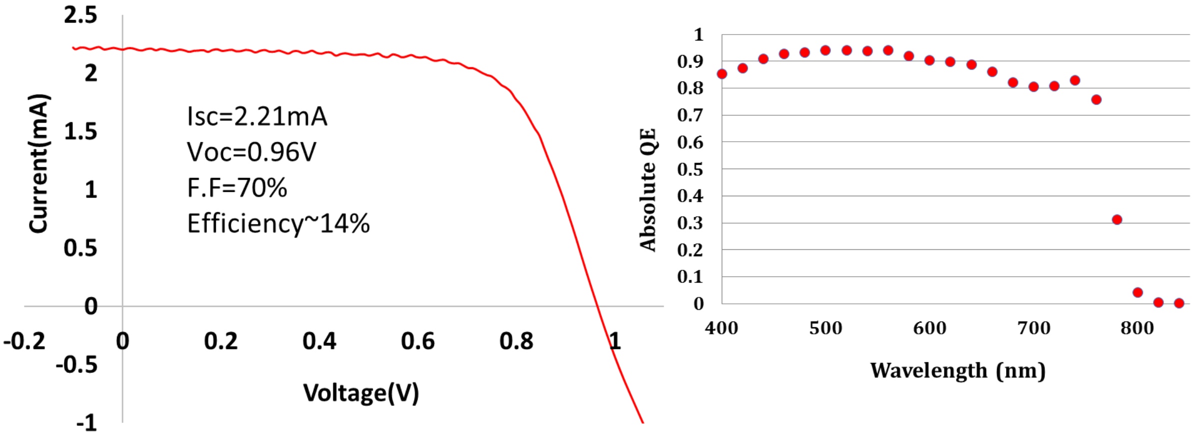

Fig 4.56: Co-Evaporated NIP results

The devices efficiency is comparable to our best sequential device (13.7%). The device has Efficiency~14%, V_{OC}=0.96V, $J_{sc} = 20.9mA/cm^2$ and Fill factor= 0.70. The QE current agrees, also from QE we know that the current can be improved with thickness optimization.

4.4.1. Sequential NIP vs co-evaporated NIP

Even though the sequential NIP devices have large grains, its ion accumulation at interface will be larger owing to stoichiometry variations across the bulk (erfc function). Co-evaporated device offers stoichiometry control, and with grain enhancement we expect better voltage evolution. The hysteresis comparison of Co-evaporated NIP vs Sequential NIP is shown in Figure 4.57.

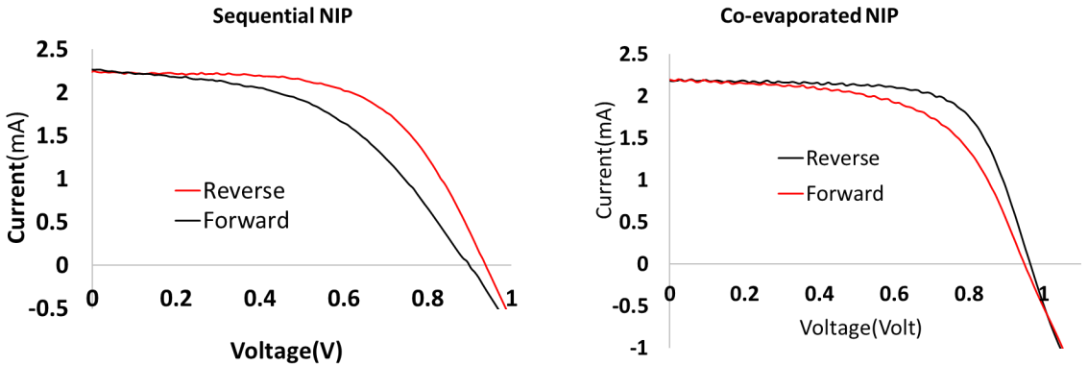

Scan Direction	Current(mA)	Voltage(V)	Fill Factor	Efficiency %
Reverse	2.25	0.94	0.59	11.9
Forward	2.26	0.90	0.49	9.4

Scan Direction	Current(mA)	Voltage(V)	Fill Factor	Efficiency %
Reverse	2.19	0.96	0.69	13.8
Forward	2.19	0.945	0.59	11.6

Fig 4.57: NIP IV Hysteresis: Sequential vs Co-Evaporated

From the hysteresis comparison (Fig 4.57), the co-evaporated devices have less hysteresis and we associate this to better stoichiometry control in the film which leads to reduced ion density at the interface. However, unlike PIN device that has doped transport layers, the NIP device has an un-doped transport layer (TiO_2) that traps charges, hence hysteresis isn't eliminated.

As explained before, when the IV is scanned in the reverse direction (high bias to low bias), the inbuilt field gradually increases resulting in migration of ions back to the interface and some of the charges are trapped at the interface, reducing the electric field and V_{OC}. Also, a negative bias is applied before the forward scan (low bias to high bias), resulting in ions being attracted back to the interface. Consequently, the forward scan has a lesser V_{OC} and Fill factor. However, the hysteresis response has improved using co-evaporation. Next, Figure 4.58 shows the voltage evolution comparison of Sequential vs Co-evaporated device.

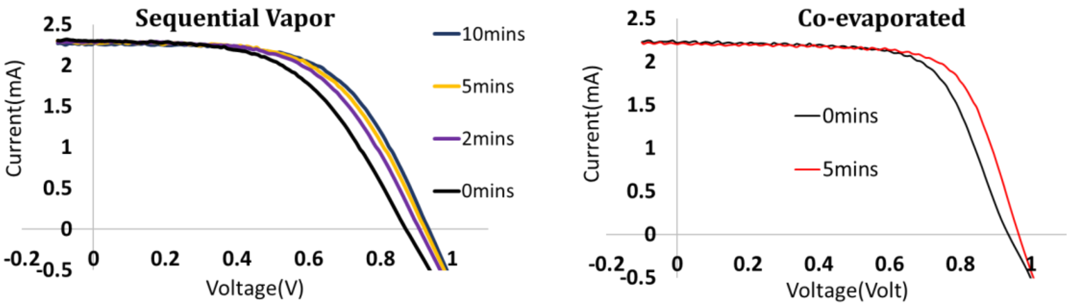

Voltage (Volts)	Current (mA)	Fill Factor	Efficiency %	Wait time [mins]
0.94	2.28	59	11.85	10
0.93	2.28	58	11.45	5
0.91	2.28	57	11.11	2
0.87	2.3	54	10.10	0

Voltage (Volts)	Current (mA)	Fill Factor	Efficiency %	Wait time [mins]
0.96	2.2	0.7	13.95	5
0.935	2.2	0.67	13.01	0

Fig 4.58: NIP Voltage evolution: Sequential vs Co-Evaporated

From the voltage evolution comparison (Fig 4.58), we can clearly see that co-evaporated NIP devices have a faster voltage evolution or stabilization in comparison to the sequential NIP devices. The co-evaporated device’s voltage onsets at ~0.94V [0mins] and stabilizes at 0.96V [5mins], while the sequential device’s V_{OC} onsets at 0.87V [0mins] and stabilizes at 0.94V [10mins]. The higher starting V_{OC} of co-evaporated devices indicates that it has lesser ion accumulation at the interface owing to the techniques stoichiometry control.

In the contrary, sequential device has a significantly lower onset voltage of 0.87V implying that it has greater ion accumulation which reduces its in-built field, thus decreasing the V_{OC} and fill factor. Also, comparing the voltage evolution FTO/PTA-PIN co-evaporated device [Fig 4.48] with Co-evaporated NIP device [Fig 4.58], the voltage of the co-evaporated NIP device takes 5mins to stabilize in comparison to PIN device that takes 2mins, even though NIP device has larger grains [Figure 4.55]. We associate this anomaly to charge trapping that occurs in TiO_2 and not in PTAA, as it is doped, thereby resulting in faster voltage stabilization. This result again re-emphasizes the importance of doped transport layers.

CHAPTER 5

FAI PEROVSKITES & TRANSPORT LAYERS

Perovskites materials have a general formula of ABX_3 and wide variety of elemental combinations can be used to be form the perovskite structure. In general, A is Methyl Ammonium $(CH_3NH_3{}^+)$ [MA] or Formamidinium $(HC(NH_2)_2{}^+)$ [FA] or Cesium, while B is metal like Lead (Pb) or Tin (Sn) and X is a halide like Chlorine (Cl) or Bromine (Br) or Iodine (I). If we consider the three A cations, Cs has a smaller effective ionic radius than MA, while FA has a larger organic cation than MA [233]. Replacing MA with smaller cation Cs will increase the bandgap to ~1.73eV, while substituting with the larger cation will decrease the bandgap to ~1.47 eV[22].

Hence, FA based perovskites has a greater absorption spectrum and its bandgap is closer to maximum theoretical efficiencies derived for a single junction from the Shockley−Queisser limit [51]. FA Lead iodide based perovskite's have reported diffusion length of $6.6\mu m$, whereas FA lead bromide have longer diffusion lengths in the range of 19um [234]. Also, $FAPbI_3$ single crystal have shown long carrier lifetime of 484 ns, high carrier mobility of $4.4\, cm^2V^{-1}s^{-1}$ and a conductivity of $1.1\times10^{-7}(\Omega cm)^{-1}$ [235]. The reported properties of this material in literature illustrates that it is favorable for photovoltaic applications.

5.1. Degradation Studies

Solar cells need to be able to handle high temperature especially if they are going to be mounted in developing nations in Africa or in the Indian subcontinent. It's not uncommon for the desert temperature in Saudi Arabia to reach 54℃ on a summer day. Photovoltaic (PV) modules typically come with 20 year warranties that guarantee that the panels will produce at least 80% of the rated power after 20 years of use. The general rule of thumb is that panels will degrade by about 1% each year. So, thermal-stability and photo-stability of PV materials are critical. In this chapter, we are going to study the thermal stability of the organic cation based Perovskites. Figure 5.1 compares the XRD spectra of the two organo-cation i.e. MAI and FAI sequentially grown perovskites.

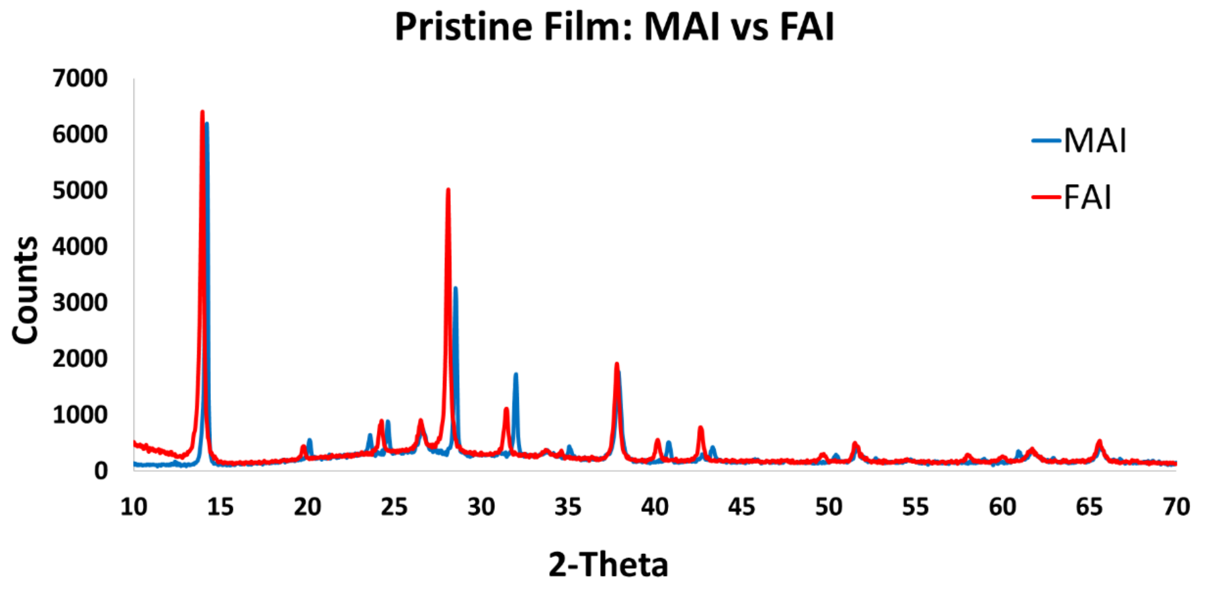

Fig 5.1: XRD: FAI vs MAI

As can be observed from Figure 5.1, the peaks of the FAI based perovskite shifts to the left of MAI perovskite, this is because FAI is larger cation and as per Bragg's law $[n\lambda = 2dsin\theta]$, d is inversely proportional to θ, so as d increase for larger cation, the θ for the peaks will shift to the left. Next, we took these pristine films and annealed them in a glove box (filled with N_2) for 24hrs in calibrated hotplate at $100℃$ to study the thermal stability of the perovskite material. Figure 5.2 shows the XRD spectra for the 24-hour annealed MAI based perovskites.

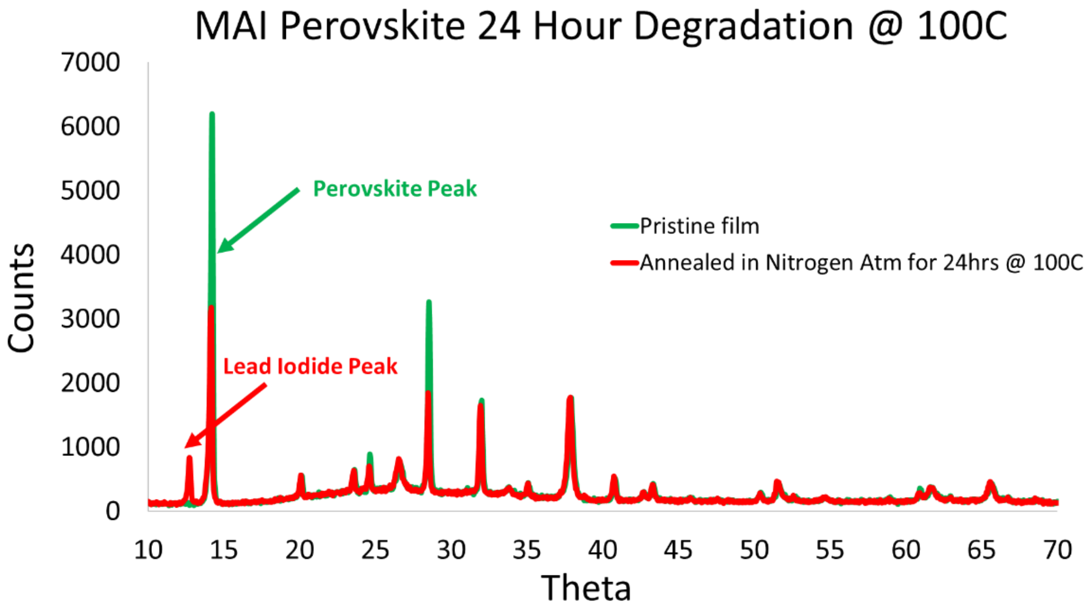

Fig 5.2: XRD: MAI Perovskite degradation [100℃]

The peak at 2θ value of 14.1^0 corresponds to Perovskite, and by post annealing at 100℃ for 24 hours, a peak arises at 2θ value of 12.7^0 that corresponds to the precursor PbI_2, thus signifying that perovskite has degraded. Similar experiment was conducted for FAI perovskite and XRD spectra of the same is shown in Figure 5.3.

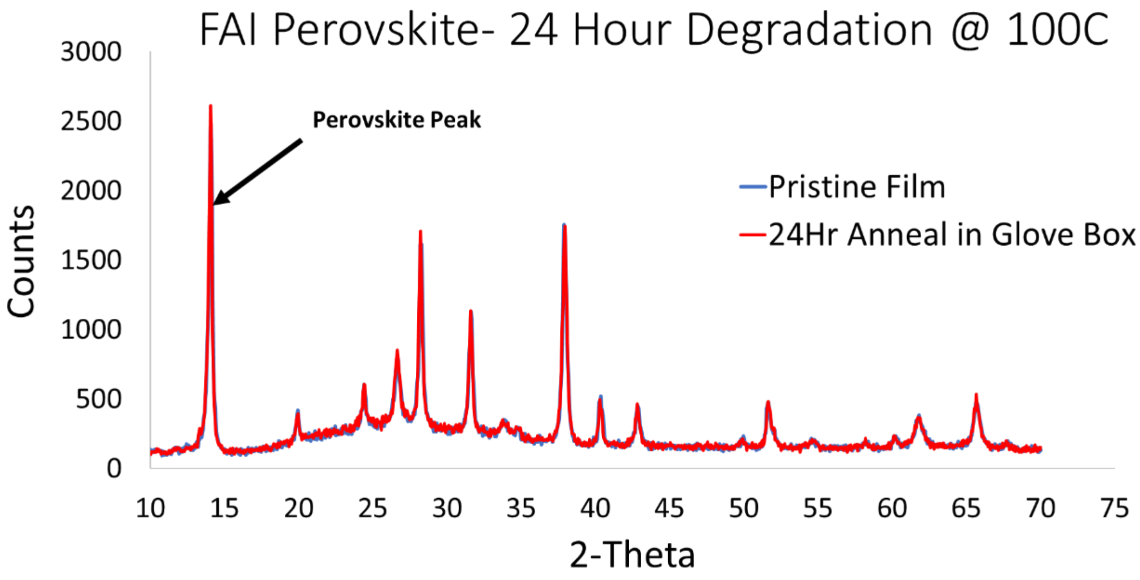

Fig 5.3: XRD: FAI Perovskite degradation [100℃]

Unlike, the MAI perovskite the FAI perovskite post annealing for 24 hours at 100℃ did not degrade as observed from the XRD spectra in Figure 5.3. Thus, showing that FAI perovskite in addition to absorbing wider spectrum of photon is also thermally more stable. We continued to study the stability of FAI perovskite by annealing the pristine film at 125℃ for 24 hours in a N_2 filled glove box. The results of the study are shown in Figure 5.4.

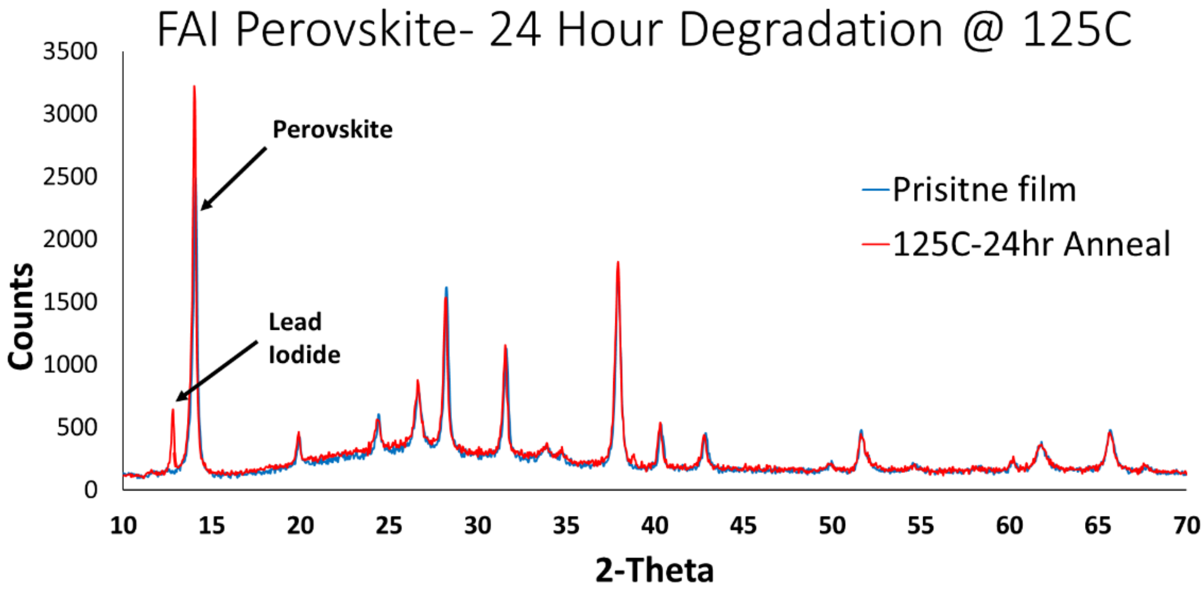

Fig 5.4: XRD: FAI Perovskite degradation [125℃]

On annealing at 125℃ for 24 hours, the PbI_2 peak at 2θ value of 12.7^0 appears showing that FAI perovskite also degrades like MAI perovskite but at temperature of 125℃. Therefore, using FAI as substitute to MAI perovskite, produces a thermally more stable alternative. We decided to repeat the 125℃/24 Hour experiment but by sealing the film using Poly (methyl methacrylate) (PMMA), a clear colorless polymer i.e. resistant to chemicals and weather [236]. The results of the study are shown in Figure 5.5. The results show that sealing the film, the FAI perovskite does not degrade (the PbI_2 peak at 2θ value of 12.7^0 did not appear).

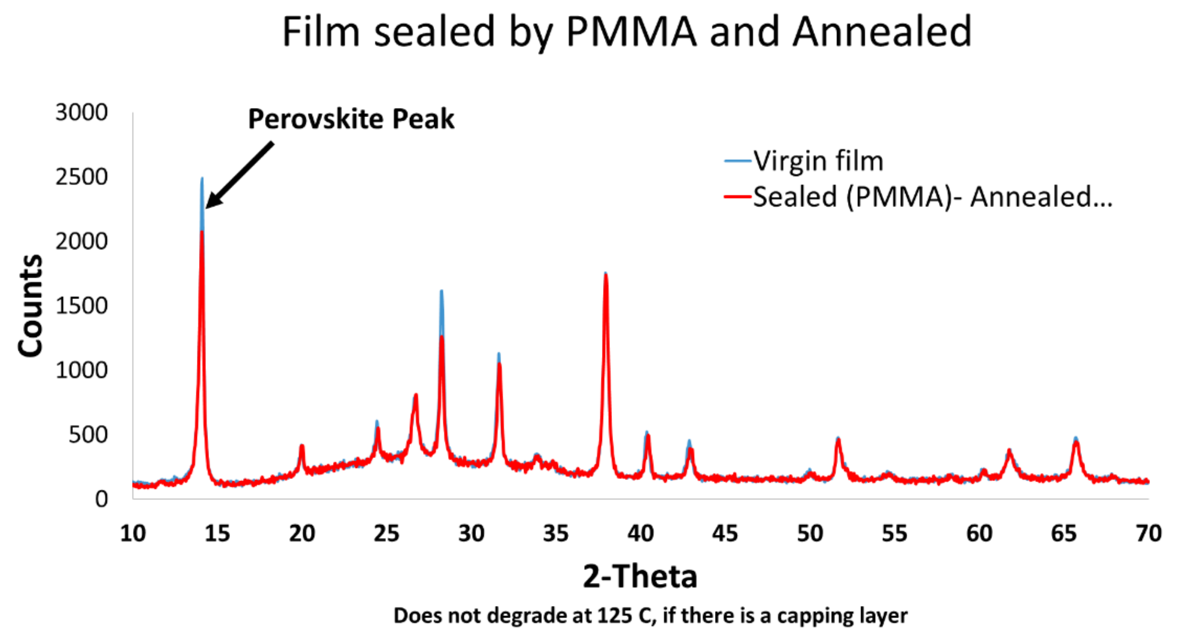

Fig 5.5: XRD: FAI Perovskite capped degradation [125℃]

The stability of the FAI perovskite in comparison to MAI perovskite can be associated to ion migration. F. H. Alharbi et al [237] showed that by replacing Methyl Amine organic cation with other organic cation's, the structural stability improves owing to the electron coupling between the organic cation and PbI_6 octahedral. Also, Kai Zhu et al [238] showed that at high temperature, the composition of material varied at grain boundaries indicating migration of mobile of ions at grain boundaries that start's degradation. Finally, the work by Venkataraman el al [239] shows that the predominant mechanism of device degradation was thermally activated fast ion. They calculated the diffusion coefficient and activation energy for MA and FA at 45℃, the values are given below.

Organic Cation	Diffusion coefficient $(cm^2 s^{-1})$	Activation energy (eV)
Methyl Ammonium	$\sim 3.6 \times 10^{-12}$	0.227
Formamidinium	$\sim 3.0 \times 10^{-13}$	0.787

As methyl ammonium has a higher diffusion coefficient and lower activation energy, the ions are more mobile in Methyl amine based perovskite inducing faster degradation, hence MAI perovskite degrades faster in comparison to FAI perovskite.

5.2. FAI Sequential Vapor Devices

In addition, we also fabricated Sequential FAI devices using the NIP architecture, the band structure, IV and QE results of the FAI devices is shown in Figure 5.6 & 5.7. The fabrication steps of the sequential FAI devices are mentioned in detail in Chapter 3.

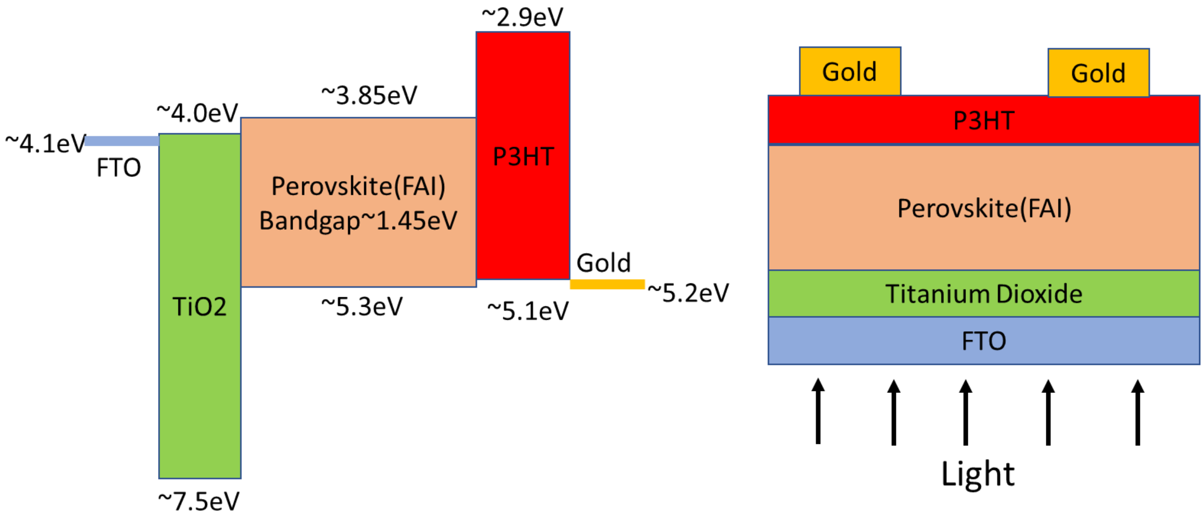

Fig 5.6: FAI device NIP architecture

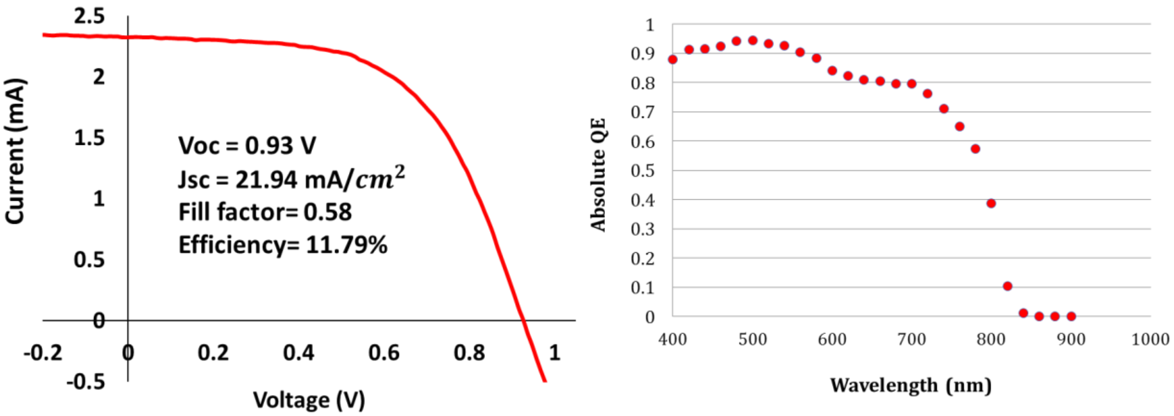

Fig 5.7: FAI device IV & QE

The best FAI device had an efficiency~11.8%, $V_{OC}\sim 0.93V$, Fill factor~0.58 & Efficiency~11.8%. From the QE results, we recognize that higher current can easily be achieved by optimization of the device thickness. Figure 5.8 shows a histogram of the FAI device parameters.

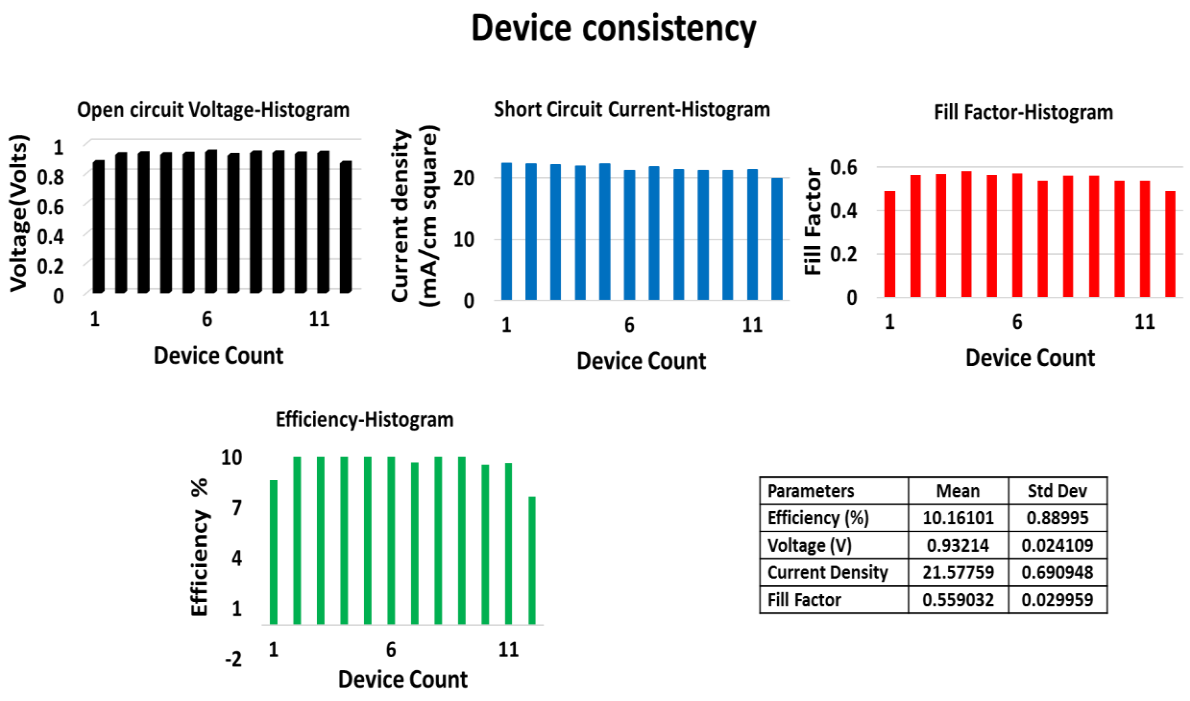

Parameters	Mean	Std Dev
Efficiency (%)	10.16101	0.88995
Voltage (V)	0.93214	0.024109
Current Density	21.57759	0.690948
Fill Factor	0.559032	0.029959

Fig 5.8: FAI device Histogram

Till date, we are the only group to make FAI devices using the sequential vapor approach. The device parameters of the FAI devices are as follows: mean $Efficiency\sim 10.2\%$, mean $V_{OC} = 0.93V$, mean $Fill\,factor\sim 0.56$ & mean $Current\sim 21.6mA/cm^2$. As can be seen from the histogram, the devices were very consistent.

Finally, a QE comparison of the MAI and FAI device is shown in Figure 5.9, the results clearly show that FAI perovskite has a smaller bandgap to MAI perovskite. FAI perovskite's bandgap is ~1.45eV whereas MAI perovskite bandgap is ~ 1.55eV. Therefore, FAI perovskite has a broader absorption spectrum in comparison to MAI perovskite. With grain enhancement techniques and slight thickness optimization higher current can be obtained for FAI devices.

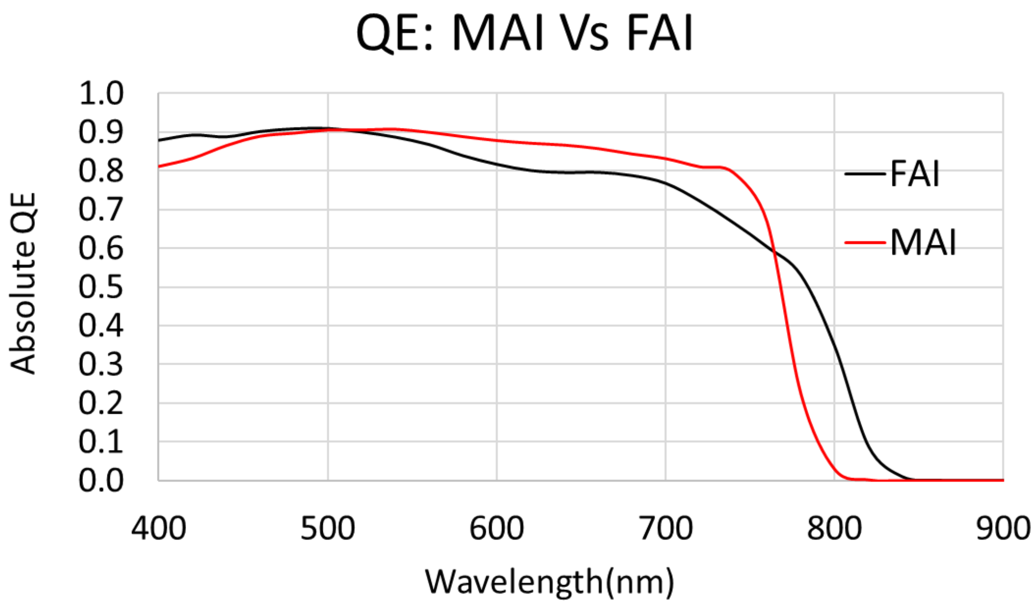

Fig 5.9: QE: FAI vs MAI

5.3. Transport Layer Development

In addition to developing Perovskite solar cells, some of my work also involved development of transport layers namely Nickel oxide (NiO_x) and Cadmium sulphide (CdS). Nickel oxide is one of few p-type oxides that has it valence band matching perfectly with Perovskite. It's valence band edge is at ~5.4eV and conduction band edge is at ~ 2.2 eV making it a very good Type-II heterojunction for collecting holes and blocking electrons. Likewise, Cadmium sulphide has its conduction band edge at ~ 4.1eV and valence band edge at ~ 6.52eV making it a very good Type-II heterojunction for extracting electrons and blocking holes.

The cadmium sulphide film development was for futuristic needs i.e. to make multijunction or tandem solar cell. To make tandem solar cells using perovskite as large bandgap material and crystalline silicon as the low bandgap material, light must come from the top, thus entailing use of conductive oxide like sputtered Aluminum Doped Zinc oxide as top contact. However, perovskite and PCBM, both cannot endure plasma and will degrade. So, depositing a thin layer of CdS on top of PCBM will protect both perovskite and PCBM from plasma. Also, since PCBM makes ohmic contact with Perovskite and doped ZnO, there is no collection issues. Both, NiO_x and CdS recipes were developed using E-Beam evaporator, by depositing it at a rate of 1.0 A/s and post deposition NiO_x was annealed at 200/60mins. The transmission of NiO_x and CdS is shown in Figure 5.10 & 5.11 respectively.

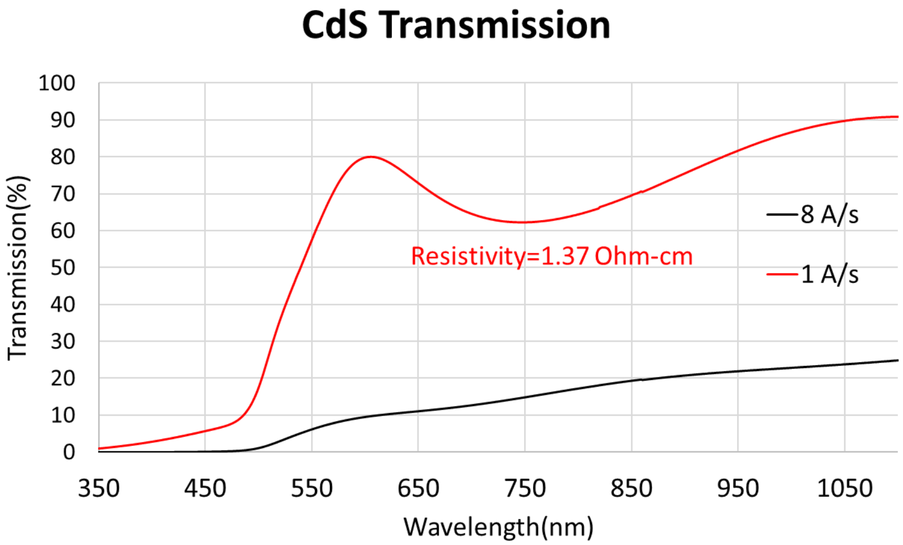

Fig 5.10: CdS Transmission

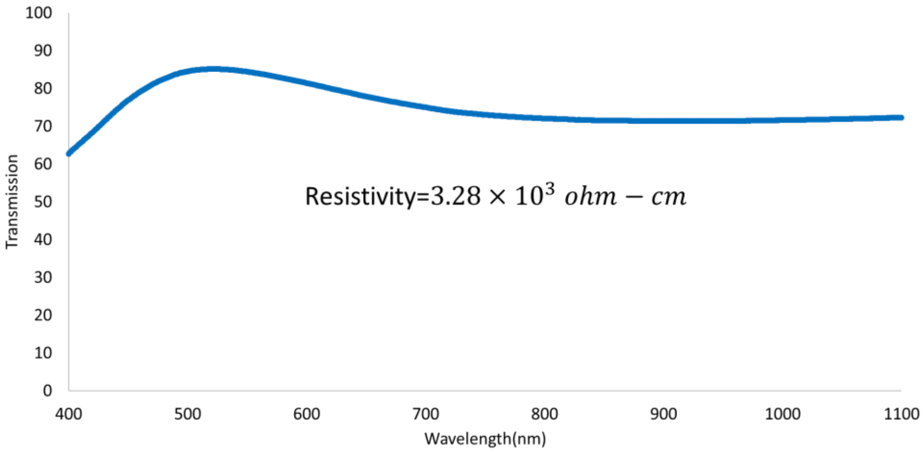

Fig 5.11: NiO_x Transmission

The architecture of the PIN devices made using NiO_x and CdS is shown in Figure 5.12. The perovskite film was solution processed and the recipe for the same was developed by Liang Zhang.

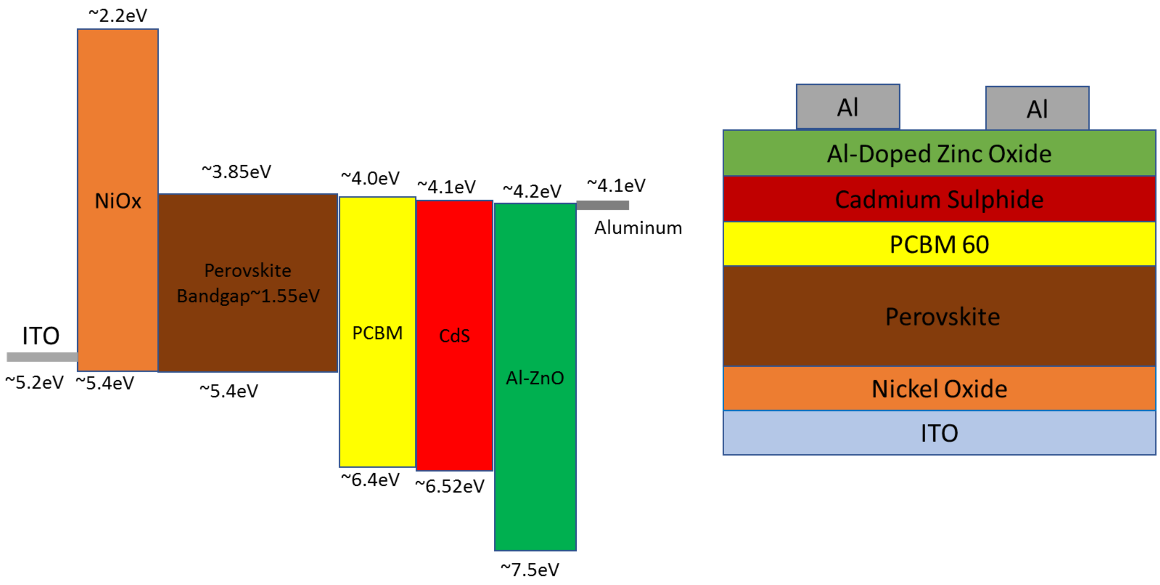

Fig 5.12: NiO_x and CdS based device– PIN architecture

The results of the NiO_x & CdS based device is shown in Figure 5.13.

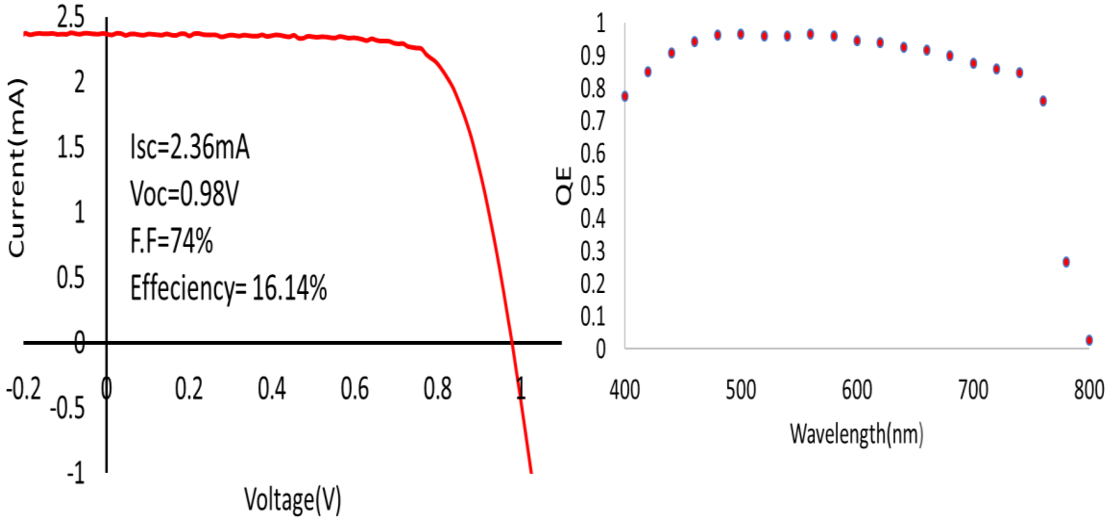

Fig 5.13: NiO_x and CdS based device – IV & QE results

CHAPTER 6

CONCLUSION

6.1. Conclusion

To summarize this work, high efficiency sequential and co-evaporated vapor devices were made using both NIP and PIN architecture. Some of the significant findings from this work are follows.

- High efficiency sequential NIP devices were made P3HT as p-type Type II heterojunction. The devices were consistent and thickness of P3HT was critical in attaining high efficiencies. Techniques such as vacuum annealing for removing excess MAI was introduced.
- The sequential NIP devices has voltage evolution and hysteresis. Voltage evolution was improved by reducing the amount of MAI; however hysteresis could not be solved by reducing MAI owing to charge trapping in undoped transport layers.
- PIN sequential devices made using doped organic transport layers did not have hysteresis and no voltage evolution.
- Consistent high efficiency PIN devices were made using Co-evaporator. The co-evaporated devices were made on FTO and ITO superstrates at room temperature, 50°C and 75°C. The substrate temperature was increased for grain enhancement, one of the highest efficiency PIN vapor device was fabricated.
- FTO/PTAA devices have improved voltage evolution to ITO/PTAA devices and this is due to the intrinsically larger grains formed on FTO/PTAA surface. In comparison, the

sequential PIN devices have no voltage evolution owing to both large grains and doped transport layers (New discovery)

- Co-evaporated NIP devices were made with a modified fabrication for grain enhancement. The devices had improved voltage evolution. Still, the co-evaporated NIP devices have hysteresis due to charge trapping in undoped TiO_2
- FAI perovskites were fabricated using NIP architecture, we were the first group to make FAI based devices using vapor approach.
- Thermal degradation study was carried out on both MAI and FAI based perovskites, FAI perovskites was found to be thermally more stable.
- Cadmium Sulfide and Nickel oxide film development was carried out using E-beam evaporator. CdS offers a pathway to use the device as the top cell in a tandem, protects the perovskite from plasma during ZnO sputtering and stops diffusion of moisture and mobile ions towars the contact.

REFERENCES

1. Enerdata. Available from: https://yearbook.enerdata.net/energy-consumption-data.html.
2. Blog, L.; Available from: http://www.lendogram.com/blog/wp-content/uploads/2016/04/renewable_energy_sources.gif.
3. Generator, L.A.; Available from: http://landartgenerator.org/blagi/archives/127.
4. Richard Perez, M.P.; Available from: 4. http://www.asrc.albany.edu/people/faculty/perez/Kit/pdf/a-fundamental-look-at%20the-planetary-energy-reserves.pdf.
5. DOE, U.S.; Available from: https://www.eia.gov/.
6. EnergyTrend. Available from: https://commons.wikimedia.org/wiki/File:Price_history_of_silicon_PV_cells_since_1977.svg.
7. Staff, A.N.; Available from: https://publishing.aip.org/publishing/journal-highlights/can-perovskites-and-silicon-team-boost-industrial-solar-cell.
8. Munsell, M.; Available from: https://www.greentechmedia.com/articles/read/solar-pv-prices-to-fall-below-1.00-per-watt-by-2020.
9. Wikipedia. Available from: https://en.wikipedia.org/wiki/Cadmium_telluride_photovoltaics.
10. Solar, F.; Available from: http://firstsolar.com/en/Technologies-and-Capabilities/PV-Modules/First-Solar-Series-4-Modules/CdTe-Technology.
11. Wesoff, E.; Available from: https://www.greentechmedia.com/articles/read/First-Solar-Hits-Record-22.1-Conversion-Efficiency-For-CdTe-Solar-Cell.
12. University, W.S.; Available from: https://www.eurekalert.org/pub_releases/2016-02/wsu-rmk022616.php.
13. NREL. Available from: http://www.nrel.gov/pv/.
14. Burschka, J., et al., *Sequential deposition as a route to high-performance perovskite-sensitized solar cells.* Nature, 2013. **499**(7458): p. 316-319.
15. Liu, M., M.B. Johnston, and H.J. Snaith, *Efficient planar heterojunction perovskite solar cells by vapour deposition.* Nature, 2013. **501**(7467): p. 395-398.
16. Wenk, H.R. and A. Bulakh, *Minerals: Their Constitution and Origin*. 2004: Cambridge University Press.
17. Yin, W.-J., T. Shi, and Y. Yan, *Unusual defect physics in CH3NH3PbI3 perovskite solar cell absorber.* Applied Physics Letters, 2014. **104**(6): p. 063903.
18. Fu, D. and M. Itoh, *Ferroelectricity in Silver Perovskite Oxides*. Ferroelectrics - Material Aspects. 2011.
19. Kronmüller, H. and S. Parkin, *Handbook of magnetism and advanced magnetic materials: Spintronics and magnetoelectronics*. 2007: John Wiley & Sons.
20. Li, C., et al., *Formability of ABX3 (X = F, Cl, Br, I) halide perovskites.* Acta Crystallographica Section B, 2008. **64**(6): p. 702-707.
21. Green, M.A., A. Ho-Baillie, and H.J. Snaith, *The emergence of perovskite solar cells.* Nat Photon, 2014. **8**(7): p. 506-514.
22. Eperon, G.E., et al., *Formamidinium lead trihalide: a broadly tunable perovskite for efficient planar heterojunction solar cells.* Energy & Environmental Science, 2014. **7**(3): p. 982-988.
23. Saliba, M., et al., *Cesium-containing triple cation perovskite solar cells: improved stability, reproducibility and high efficiency.* Energy & Environmental Science, 2016. **9**(6): p. 1989-1997.

24. Kumar, M.H., et al., *Lead-Free Halide Perovskite Solar Cells with High Photocurrents Realized Through Vacancy Modulation.* Advanced Materials, 2014. **26**(41): p. 7122-7127.
25. Chen, Q., et al., *The optoelectronic role of chlorine in CH3NH3PbI3(Cl)-based perovskite solar cells.* Nature Communications, 2015. **6**: p. 7269.
26. Sheng, R., et al., *Methylammonium Lead Bromide Perovskite-Based Solar Cells by Vapor-Assisted Deposition.* The Journal of Physical Chemistry C, 2015. **119**(7): p. 3545-3549.
27. Balaji, G., et al., *CH3NH3PbI3 from non-iodide lead salts for perovskite solar cells via the formation of PbI2.* Physical Chemistry Chemical Physics, 2015. **17**(16): p. 10369-10372.
28. Joshi, P.H., *Understanding the photostability of perovskite solar cell*, in *Electrical engineering*. 2016, Iowa State University.
29. Park, N.G., M. Grätzel, and T. Miyasaka, *Organic-Inorganic Halide Perovskite Photovoltaics: From Fundamentals to Device Architectures*. 2016: Springer International Publishing.
30. Wang, Q., et al., *Transition from the Tetragonal to Cubic Phase of Organohalide Perovskite: The Role of Chlorine in Crystal Formation of CH3NH3PbI3 on TiO2 Substrates.* The Journal of Physical Chemistry Letters, 2015. **6**(21): p. 4379-4384.
31. Quarti, C., et al., *Structural and optical properties of methylammonium lead iodide across the tetragonal to cubic phase transition: implications for perovskite solar cells.* Energy & Environmental Science, 2016. **9**(1): p. 155-163.
32. Stoumpos, C.C., C.D. Malliakas, and M.G. Kanatzidis, *Semiconducting Tin and Lead Iodide Perovskites with Organic Cations: Phase Transitions, High Mobilities, and Near-Infrared Photoluminescent Properties.* Inorganic Chemistry, 2013. **52**(15): p. 9019-9038.
33. Wehrenfennig, C., et al., *Charge carrier recombination channels in the low-temperature phase of organic-inorganic lead halide perovskite thin films.* APL Mater., 2014. **2**(8): p. 081513.
34. Topsöe, H.K., *Chemische untersuchungen homologer verbindungen.* Zeitschrift für Kristallographie, 1884. **8**: p. 246–296.
35. Mitzi, D.B., et al., *Conducting Layered Organic-inorganic Halides Containing <110>-Oriented Perovskite Sheets.* Science, 1995. **267**(5203): p. 1473-1476.
36. Mitzi, D.B., K. Chondroudis, and C.R. Kagan, *Organic-inorganic electronics.* IBM Journal of Research and Development, 2001. **45**(1): p. 29-45.
37. Kojima, A., et al., *Novel Photoelectrochemical Cell with Mesoscopic Electrodes Sensitized by Lead-Halide Compounds (2).* Meeting Abstracts, 2006. **MA2006-02**(7): p. 397.
38. Kojima, A., et al., *Organometal Halide Perovskites as Visible-Light Sensitizers for Photovoltaic Cells.* Journal of the American Chemical Society, 2009. **131**(17): p. 6050-6051.
39. Im, J.-H., et al., *6.5% efficient perovskite quantum-dot-sensitized solar cell.* Nanoscale, 2011. **3**(10): p. 4088-4093.
40. Snaith, H.J., *Perovskites: The Emergence of a New Era for Low-Cost, High-Efficiency Solar Cells.* The Journal of Physical Chemistry Letters, 2013. **4**(21): p. 3623-3630.
41. Kim, H.-S., et al., *Lead Iodide Perovskite Sensitized All-Solid-State Submicron Thin Film Mesoscopic Solar Cell with Efficiency Exceeding 9%.* Scientific Reports, 2012. **2**: p. 591.
42. Lee, M.M., et al., *Efficient Hybrid Solar Cells Based on Meso-Superstructured Organometal Halide Perovskites.* Science, 2012. **338**(6107): p. 643-647.
43. Heo, J.H., et al., *Efficient inorganic-organic hybrid heterojunction solar cells containing perovskite compound and polymeric hole conductors.* Nat Photon, 2013. **7**(6): p. 486-491.

44. Noh, J.H., et al., *Chemical Management for Colorful, Efficient, and Stable Inorganic–Organic Hybrid Nanostructured Solar Cells.* Nano Letters, 2013. **13**(4): p. 1764-1769.
45. Even, J., et al., *Importance of Spin–Orbit Coupling in Hybrid Organic/Inorganic Perovskites for Photovoltaic Applications.* The Journal of Physical Chemistry Letters, 2013. **4**(17): p. 2999-3005.
46. Mosconi, E., et al., *First-Principles Modeling of Mixed Halide Organometal Perovskites for Photovoltaic Applications.* The Journal of Physical Chemistry C, 2013. **117**(27): p. 13902-13913.
47. Sun, S., et al., *The origin of high efficiency in low-temperature solution-processable bilayer organometal halide hybrid solar cells.* Energy & Environmental Science, 2014. **7**(1): p. 399-407.
48. Xing, G., et al., *Long-Range Balanced Electron- and Hole-Transport Lengths in Organic-Inorganic CH₃NH₃PbI₃.* Science, 2013. **342**(6156): p. 344-347.
49. Wehrenfennig, C., et al., *Homogeneous Emission Line Broadening in the Organo Lead Halide Perovskite CH3NH3PbI3–xClx.* The Journal of Physical Chemistry Letters, 2014. **5**(8): p. 1300-1306.
50. Samiee, M., et al., *Defect density and dielectric constant in perovskite solar cells.* Applied Physics Letters, 2014. **105**(15): p. 153502.
51. Shockley, W. and H.J. Queisser, *Detailed Balance Limit of Efficiency of p-n Junction Solar Cells.* Journal of Applied Physics, 1961. **32**(3): p. 510-519.
52. Sha, W.E.I., et al., *The efficiency limit of CH3NH3PbI3 perovskite solar cells.* Applied Physics Letters, 2015. **106**(22): p. 221104.
53. Tauc, J., R. Grigorovici, and A. Vancu, *Optical Properties and Electronic Structure of Amorphous Germanium.* physica status solidi (b), 1966. **15**(2): p. 627-637.
54. Tauc, J., *Optical properties and electronic structure of amorphous Ge and Si.* Materials Research Bulletin, 1968. **3**(1): p. 37-46.
55. Lin, Q., et al., *Electro-optics of perovskite solar cells.* Nat Photon, 2015. **9**(2): p. 106-112.
56. Juarez-Perez, E.J., et al., *Photoinduced Giant Dielectric Constant in Lead Halide Perovskite Solar Cells.* The Journal of Physical Chemistry Letters, 2014. **5**(13): p. 2390-2394.
57. Almond, D.P. and C.R. Bowen, *An Explanation of the Photoinduced Giant Dielectric Constant of Lead Halide Perovskite Solar Cells.* The Journal of Physical Chemistry Letters, 2015. **6**(9): p. 1736-1740.
58. Miyata, A., et al., *Direct measurement of the exciton binding energy and effective masses for charge carriers in organic-inorganic tri-halide perovskites.* Nat Phys, 2015. **11**(7): p. 582-587.
59. Hu, M., et al., *Distinct Exciton Dissociation Behavior of Organolead Trihalide Perovskite and Excitonic Semiconductors Studied in the Same System.* Small, 2015. **11**(18): p. 2164-2169.
60. D'Innocenzo, V., et al., *Excitons versus free charges in organo-lead tri-halide perovskites.* Nature Communications, 2014. **5**: p. 3586.
61. Grancini, G., et al., *Role of microstructure in the electron–hole interaction of hybrid lead halide perovskites.* Nat Photon, 2015. **9**(10): p. 695-701.
62. Manser, J.S. and P.V. Kamat, *Band filling with free charge carriers in organometal halide perovskites.* Nat Photon, 2014. **8**(9): p. 737-743.

63. Stranks, S.D., et al., *Electron-Hole Diffusion Lengths Exceeding 1 Micrometer in an Organometal Trihalide Perovskite Absorber.* Science, 2013. **342**(6156): p. 341-344.
64. Nie, W., et al., *High-efficiency solution-processed perovskite solar cells with millimeter-scale grains.* Science, 2015. **347**(6221): p. 522-525.
65. Adhyaksa, G.W.P., et al., *Carrier Diffusion Lengths in Hybrid Perovskites: Processing, Composition, Aging, and Surface Passivation Effects.* Chemistry of Materials, 2016. **28**(15): p. 5259-5263.
66. Li, Y., et al., *Direct Observation of Long Electron-Hole Diffusion Distance in CH3NH3PbI3 Perovskite Thin Film.* Scientific Reports, 2015. **5**: p. 14485.
67. Shi, D., et al., *Low trap-state density and long carrier diffusion in organolead trihalide perovskite single crystals.* Science, 2015. **347**(6221): p. 519-522.
68. Dong, Q., et al., *Electron-hole diffusion lengths > 175 μm in solution-grown CH₃NH₃PbI₃ single crystals.* Science, 2015. **347**(6225): p. 967-970.
69. Duan, H.-S., et al., *The identification and characterization of defect states in hybrid organic-inorganic perovskite photovoltaics.* Physical Chemistry Chemical Physics, 2015. **17**(1): p. 112-116.
70. Chueh, C.-C., C.-Z. Li, and A.K.Y. Jen, *Recent progress and perspective in solution-processed Interfacial materials for efficient and stable polymer and organometal perovskite solar cells.* Energy & Environmental Science, 2015. **8**(4): p. 1160-1189.
71. Song, Z., et al., *Pathways toward high-performance perovskite solar cells: review of recent advances in organo-metal halide perovskites for photovoltaic applications.* Journal of Photonics for Energy, 2016. **6**(2): p. 022001-022001.
72. Kulkarni, S.A., et al., *Band-gap tuning of lead halide perovskites using a sequential deposition process.* Journal of Materials Chemistry A, 2014. **2**(24): p. 9221-9225.
73. Andalibi, S., et al., *Band gap engineering of organo metal lead halide perovskite photovoltaic absorber.* Optical and Quantum Electronics, 2016. **48**(4): p. 258.
74. Hoke, E.T., et al., *Reversible photo-induced trap formation in mixed-halide hybrid perovskites for photovoltaics.* Chemical Science, 2015. **6**(1): p. 613-617.
75. McMeekin, D.P., et al., *A mixed-cation lead mixed-halide perovskite absorber for tandem solar cells.* Science, 2016. **351**(6269): p. 151-155.
76. Berkley, U.; Available from: http://news.berkeley.edu/2016/11/07/major-advance-in-solar-cells-made-of-cheap-easy-to-use-perovskite/.
77. ASC. Available from: https://www.acs.org/content/acs/en/pressroom/presspacs/2016/acs-presspac-september-28-2016/toward-greener-inexpensive-solar-cells.html.
78. ; Available from: https://www.greentechmedia.com/articles/read/solar-pv-prices-to-fall-below-1.00-per-watt-by-2020.
79. Atlas, N.; Available from: http://newatlas.com/cheap-durable-perovskite-solar-cells/41618/.
80. Xinhua. Available from: http://news.xinhuanet.com/english/2016-10/24/c_135775776.htm.
81. Hailegnaw, B., et al., *Rain on Methylammonium Lead Iodide Based Perovskites: Possible Environmental Effects of Perovskite Solar Cells.* The Journal of Physical Chemistry Letters, 2015. **6**(9): p. 1543-1547.
82. Serrano-Lujan, L., et al., *Tin- and Lead-Based Perovskite Solar Cells under Scrutiny: An Environmental Perspective.* Advanced Energy Materials, 2015. **5**(20): p. 1501119-n/a.
83. Babayigit, A., et al., *Assessing the toxicity of Pb- and Sn-based perovskite solar cells in model organism Danio rerio.* Scientific Reports, 2016. **6**: p. 18721.

84. Times, L.A.; Available from: http://www.latimes.com/local/lanow/la-me-exide-cleanup-20160217-story.html.
85. EPA. Available from: https://cfpub.epa.gov/enforcement/cases/.
86. IPS. Available from: http://www.ipsnews.net/2004/08/environment-cleaning-up-lead-contamination-on-mexico-us-border/.
87. Bush, K.A., et al., *Thermal and Environmental Stability of Semi-Transparent Perovskite Solar Cells for Tandems Enabled by a Solution-Processed Nanoparticle Buffer Layer and Sputtered ITO Electrode.* Advanced Materials, 2016. **28**(20): p. 3937-3943.
88. Berhe, T.A., et al., *Organometal halide perovskite solar cells: degradation and stability.* Energy & Environmental Science, 2016. **9**(2): p. 323-356.
89. Hwang, I. and K. Yong, *Novel CdS Hole-Blocking Layer for Photostable Perovskite Solar Cells.* ACS Applied Materials & Interfaces, 2016. **8**(6): p. 4226-4232.
90. Sun, T.B.; Available from: http://www.baltimoresun.com/health/blog/bs-hs-lead-paint-grant-20150824-story.html.
91. Joshi, P.H., et al., *The physics of photon induced degradation of perovskite solar cells.* AIP Advances, 2016. **6**(11): p. 115114.
92. Chen, H., et al., *Extending the environmental lifetime of unpackaged perovskite solar cells through interfacial design.* Journal of Materials Chemistry A, 2016. **4**(30): p. 11604-11610.
93. Nie, W., et al., *Light-activated photocurrent degradation and self-healing in perovskite solar cells.* Nature Communications, 2016. **7**: p. 11574.
94. Leskar, K.J.; Available from: https://www.lesker.com/newweb/ped/organicmaterialseries.cfm.
95. Pankove, J.I., *Optical Processes in Semiconductors*. 1971: Dover.
96. Warwick. Available from: https://www2.warwick.ac.uk/fac/sci/physics/current/postgraduate/regs/mpags/ex5/phonons/indirect_absorption/.
97. Pankove, J.I., *Absorption Edge of Impure Gallium Arsenide.* Physical Review, 1965. **140**(6A): p. A2059-A2065.
98. Sturge, M.D., *Optical Absorption of Gallium Arsenide between 0.6 and 2.75 eV.* Physical Review, 1962. **127**(3): p. 768-773.
99. Hill, D.E., *Infrared Transmission and Fluorescence of Doped Gallium Arsenide.* Physical Review, 1964. **133**(3A): p. A866-A872.
100. Urbach, F., *The Long-Wavelength Edge of Photographic Sensitivity and of the Electronic Absorption of Solids.* Physical Review, 1953. **92**(5): p. 1324-1324.
101. Jackson, W.B. and N.M. Amer, *Direct measurement of gap-state absorption in hydrogenated amorphous silicon by photothermal deflection spectroscopy.* Physical Review B, 1982. **25**(8): p. 5559-5562.
102. Luciani, L., et al., *Sub-gap absorption study of defects in ion-implanted and annealed Si layers.* Applied Physics A, 1990. **50**(5): p. 495-498.
103. Wyrsch, N., et al., *How to reach more precise interpretation of subgap absorption spectra in terms of deep defect density in a-Si:H.* Journal of Non-Crystalline Solids, 1991. **137**: p. 347-350.
104. Samiee, M., et al., *Measurement of defect densities and Urbach energies of tail states in PTB7 solar cells.* Applied Physics Letters, 2014. **105**(13): p. 133511.
105. Moss, T.S. and T.D.F. Hawkins, *Infrared absorption in gallium arsenide.* Infrared Physics, 1961. **1**(2): p. 111-115.

106. McLean, T.P., *The absorption-edge spectrum of semiconductors*. 1960: Heywood and compnay.
107. M Gershenzon, D.G.t.a.R.E.D. in *Proceedings of the International Conference on the Physics of Semiconductors*. Exeter.
108. Neamen, D.A., *Semiconductor physics and devices: basic principles*. 2003: McGraw-Hill.
109. Streetman, B. and S. Banerjee, *Solid State Electronic Devices, Global Edition*. 2015: Pearson Education Limited.
110. Pierret, R.F., *Advanced Semiconductor Fundamentals*. 2002: Pearson Higher Education & Professional Group.
111. Nelson, J., *The Physics of Solar Cells*. 2003: Imperial College Press.
112. Esfahani, M.S., *Device physics of organic and perovskite solar cells*, in *Electrical and Computer Engineering*. 2015, Iowa State University.
113. Methessan, A. *Matthiessen's rule*. 1864; Available from: https://en.wikipedia.org/wiki/Electron_mobility.
114. Bowden, C.H.a.S. *Bulk Lifetime*. Available from: http://www.pveducation.org/pvcdrom/characterisation/bulk-lifetime.
115. Fox, A.M., *Optical Properties of Solids*. 2001: Oxford University Press.
116. Hull, R. and INSPEC, *Properties of Crystalline Silicon*. 1999: INSPEC, the Institution of Electrical Engineers.
117. Green, M.A., *Improved value for the silicon free exciton binding energy.* AIP Advances, 2013. **3**(11): p. 112104.
118. Knupfer, M., *Exciton binding energies in organic semiconductors.* Applied Physics A, 2003. **77**(5): p. 623-626.
119. Arkhipov, V.I. and H. Bässler, *Exciton dissociation and charge photogeneration in pristine and doped conjugated polymers.* physica status solidi (a), 2004. **201**(6): p. 1152-1187.
120. Muntwiler, M., et al., *Coulomb Barrier for Charge Separation at an Organic Semiconductor Interface.* Physical Review Letters, 2008. **101**(19): p. 196403.
121. Seager, C.H., *Grain boundary recombination: Theory and experiment in silicon.* Journal of Applied Physics, 1981. **52**(6): p. 3960-3968.
122. Fossum, J.G. and F.A. Lindholm, *Theory of grain-boundary and intragrain recombination currents in polysilicon p-n-junction solar cells.* IEEE Transactions on Electron Devices, 1980. **27**(4): p. 692-700.
123. Joshi, D.P. and D.P. Bhatt, *Theory of grain boundary recombination and carrier transport in polycrystalline silicon under optical illumination.* IEEE Transactions on Electron Devices, 1990. **37**(1): p. 237-249.
124. Wang, X. and Z.M. Wang, *High-Efficiency Solar Cells: Physics, Materials, and Devices*. 2013: Springer International Publishing.
125. McEvoy, A., L. Castaner, and T. Markvart, *Solar Cells: Materials, Manufacture and Operation*. 2012: Elsevier Science.
126. Hack, M., et al., *Minority-carrier diffusion lengths in amorphous silicon-based alloys.* Journal of Applied Physics, 1982. **53**(9): p. 6270-6275.
127. Sakata, I., M. Yamanaka, and T. Sekigawa, *Relationship between carrier diffusion lengths and defect density in hydrogenated amorphous silicon.* Journal of Applied Physics, 1997. **81**(3): p. 1323-1330.
128. van den Heuvel, J.C., R.C. van Oort, and M.J. Geerts, *Diffusion length measurements of thin amorphous silicon layers.* Solid State Communications, 1989. **69**(8): p. 807-810.

129. Shyam, A., *Fabrication of high quality, low bandgap amorphous Silicon and amorphous Silicon Germanium alloy solar cell by Chemical Annealing*, in *Electrical and Computer Engineering*. 2011, Iowa State University.
130. Wang, Y., et al., *Visible light driven type II heterostructures and their enhanced photocatalysis properties: a review.* Nanoscale, 2013. **5**(18): p. 8326-8339.
131. *Double diode model*. Available from: http://pveducation.org/pvcdrom/characterisation/double-diode-model.
132. Lindholm, F.A., J.G. Fossum, and E.L. Burgess, *Application of the superposition principle to solar-cell analysis.* IEEE Transactions on Electron Devices, 1979. **26**(3): p. 165-171.
133. education, P. *IV curve*. Available from: http://www.pveducation.org/pvcdrom/iv-curve.
134. education, P. *Short circuit current*. Available from: http://www.pveducation.org/pvcdrom/short-circuit-current.
135. education, P. *Open circuit Voltage*. Available from: http://www.pveducation.org/pvcdrom/open-circuit-voltage.
136. education, P. *Fill factor*. Available from: http://www.pveducation.org/pvcdrom/fill-factor-0.
137. ABET. *Solar spectrum*. Available from: http://abet-technologies.com/wp-content/uploads/Low-cost-Solar-Simulators-2015.pdf.
138. Vikram Dalal, M.L., James Booker, Ashok Vaseashta, Steven Hegedus. *Quantum Efficiency of Amorphous Alloy Solar Cells*. in *18th IEEE PVSC*. 1986.
139. Smestad, G.P., *Optoelectronics of Solar Cells*. 2002: Society of Photo Optical.
140. Brendel, R. and A. Goetzberger, *Thin-Film Crystalline Silicon Solar Cells: Physics and Technology*. 2003: Wiley.
141. Fahrenbruch, A. and R. Bube, *Fundamentals Of Solar Cells: Photovoltaic Solar Energy Conversion*. 2012: Elsevier Science.
142. education, P. *External quantum effeciency*. Available from: http://pveducation.org/pvcdrom/quantum-efficiency.
143. Pecharsky, V. and P. Zavalij, *Fundamentals of Powder Diffraction and Structural Characterization of Materials*. 2005: Springer US.
144. Scope, M. *X-ray diffractometer*. Available from: http://li155-94.members.linode.com/myscope/xrd/background/machine/.
145. Goldstein, J., *Scanning Electron Microscopy and X-ray Microanalysis: Third Edition*. 2003: Plenum.
146. Materials Science and Engineering, I.S.U. *SEM image*. Available from: http://www.mse.iastate.edu/research/laboratories/sem/microscopy/how-does-the-sem-work/college-electron-microscope/electron-optical-column/.
147. Cai, B., et al., *High performance hybrid solar cells sensitized by organolead halide perovskites.* Energy & Environmental Science, 2013. **6**(5): p. 1480-1485.
148. Wojciechowski, K., et al., *Sub-150 [degree]C processed meso-superstructured perovskite solar cells with enhanced efficiency.* Energy & Environmental Science, 2014. **7**(3): p. 1142-1147.
149. Wang, J.T.-W., et al., *Low-Temperature Processed Electron Collection Layers of Graphene/TiO2 Nanocomposites in Thin Film Perovskite Solar Cells.* Nano Letters, 2014. **14**(2): p. 724-730.
150. Bi, D., et al., *Using a two-step deposition technique to prepare perovskite (CH3NH3PbI3) for thin film solar cells based on ZrO2 and TiO2 mesostructures.* RSC Advances, 2013. **3**(41): p. 18762-18766.

151. Li, Y., et al., *Fabrication of Planar Heterojunction Perovskite Solar Cells by Controlled Low-Pressure Vapor Annealing.* The Journal of Physical Chemistry Letters, 2015. **6**(3): p. 493-499.
152. Du, T., et al., *Comparative Study of Vapor- and Solution-Crystallized Perovskite for Planar Heterojunction Solar Cells.* ACS Applied Materials & Interfaces, 2015. **7**(5): p. 3382-3388.
153. Malinkiewicz, O., et al., *Perovskite solar cells employing organic charge-transport layers.* Nat Photon, 2014. **8**(2): p. 128-132.
154. Momblona, C., et al., *Efficient methylammonium lead iodide perovskite solar cells with active layers from 300 to 900 nm.* APL Mater., 2014. **2**(8): p. 081504.
155. Chen, W., et al., *Efficient and stable large-area perovskite solar cells with inorganic charge extraction layers.* Science, 2015.
156. Malinkiewicz, O., et al., *Metal-Oxide-Free Methylammonium Lead Iodide Perovskite-Based Solar Cells: the Influence of Organic Charge Transport Layers.* Advanced Energy Materials, 2014. **4**(15): p. 1400345-n/a.
157. Subbiah, A.S., et al., *Inorganic Hole Conducting Layers for Perovskite-Based Solar Cells.* The Journal of Physical Chemistry Letters, 2014. **5**(10): p. 1748-1753.
158. Kim, B.-S., et al., *Fully vacuum–processed perovskite solar cells with high open circuit voltage using MoO3/NPB as hole extraction layers.* Organic Electronics, 2015. **17**: p. 102-106.
159. Teuscher, J., et al., *Control and Study of the Stoichiometry in Evaporated Perovskite Solar Cells.* ChemSusChem, 2015. **8**(22): p. 3847-3852.
160. Wang, S., et al., *Smooth perovskite thin films and efficient perovskite solar cells prepared by the hybrid deposition method.* Journal of Materials Chemistry A, 2015. **3**(28): p. 14631-14641.
161. Ono, L.K., et al., *Fabrication of semi-transparent perovskite films with centimeter-scale superior uniformity by the hybrid deposition method.* Energy & Environmental Science, 2014. **7**(12): p. 3989-3993.
162. Leyden, M.R., et al., *Large formamidinium lead trihalide perovskite solar cells using chemical vapor deposition with high reproducibility and tunable chlorine concentrations.* Journal of Materials Chemistry A, 2015. **3**(31): p. 16097-16103.
163. Luo, P., et al., *Chlorine-conducted defect repairment and seed crystal-mediated vapor growth process for controllable preparation of efficient and stable perovskite solar cells.* Journal of Materials Chemistry A, 2015. **3**(45): p. 22949-22959.
164. Chen, C.-W., et al., *Efficient and Uniform Planar-Type Perovskite Solar Cells by Simple Sequential Vacuum Deposition.* Advanced Materials, 2014. **26**(38): p. 6647-6652.
165. Ng, A., et al., *Efficiency enhancement by defect engineering in perovskite photovoltaic cells prepared using evaporated PbI2/CH3NH3I multilayers.* Journal of Materials Chemistry A, 2015. **3**(17): p. 9223-9231.
166. Longo, G., et al., *Perovskite solar cells prepared by flash evaporation.* Chemical Communications, 2015. **51**(34): p. 7376-7378.
167. Heo, J.H., et al., *Recent Progress of Innovative Perovskite Hybrid Solar Cells.* Israel Journal of Chemistry, 2015. **55**(9): p. 966-977.
168. Jeon, N.J., et al., *Solvent engineering for high-performance inorganic–organic hybrid perovskite solar cells.* Nat Mater, 2014. **13**(9): p. 897-903.

169. Ahn, N., et al., *Highly Reproducible Perovskite Solar Cells with Average Efficiency of 18.3% and Best Efficiency of 19.7% Fabricated via Lewis Base Adduct of Lead(II) Iodide.* Journal of the American Chemical Society, 2015. **137**(27): p. 8696-8699.
170. You, J., et al., *Improved air stability of perovskite solar cells via solution-processed metal oxide transport layers.* Nat Nano, 2016. **11**(1): p. 75-81.
171. Kottokkaran, R., et al. *Highly reproducible vapor deposition technique, device physics and structural instability of perovskite solar cells*. in *2015 IEEE 42nd Photovoltaic Specialist Conference (PVSC)*. 2015.
172. Chen, Q., et al., *Planar Heterojunction Perovskite Solar Cells via Vapor-Assisted Solution Process.* Journal of the American Chemical Society, 2014. **136**(2): p. 622-625.
173. Alexander, J.C., *Surface Modifications and Growth of Titanium Dioxide for Photo-Electrochemical Water Splitting*. 2016: Springer International Publishing.
174. Nowotny, J., *Oxide Semiconductors for Solar Energy Conversion: Titanium Dioxide*. 2011: Taylor & Francis.
175. Fuller, C.S. and J.A. Ditzenberger, *Diffusion of Lithium into Germanium and Silicon.* Physical Review, 1953. **91**(1): p. 193-193.
176. Tritsaris, G.A., et al., *Diffusion of Lithium in Bulk Amorphous Silicon: A Theoretical Study.* The Journal of Physical Chemistry C, 2012. **116**(42): p. 22212-22216.
177. Larue, J.C., *Lithium Diffusion in Silicon with Respect to Si Solar Cells.* physica status solidi (a), 1971. **6**(1): p. 143-151.
178. Chan, T.-L. and J.R. Chelikowsky, *Controlling Diffusion of Lithium in Silicon Nanostructures.* Nano Letters, 2010. **10**(3): p. 821-825.
179. Kleinschmidt, A.T., S.E. Root, and D.J. Lipomi, *Poly(3-hexylthiophene) (P3HT): fruit fly or outlier in organic solar cell research?* Journal of Materials Chemistry A, 2017.
180. Ameri, T., et al., *Performance Enhancement of the P3HT/PCBM Solar Cells through NIR Sensitization Using a Small-Bandgap Polymer.* Advanced Energy Materials, 2012. **2**(10): p. 1198-1202.
181. Abbas, H.A., et al., *High efficiency sequentially vapor grown n-i-p CH3NH3PbI3 perovskite solar cells with undoped P3HT as p-type heterojunction layer.* APL Mater., 2015. **3**(1): p. 016105.
182. Sachtler, W.M.H., G.J.H. Dorgelo, and A.A. Holscher, *The work function of gold.* Surface Science, 1966. **5**(2): p. 221-229.
183. Annica Andersson, et al., *Fluorine Tin Oxide as an Alternative to Indium Tin Oxide in Polymer LEDs.* Advanced Materials, 1998. **10**(11): p. 859-863.
184. Hao, F., et al., *Controllable Perovskite Crystallization at a Gas–Solid Interface for Hole Conductor-Free Solar Cells with Steady Power Conversion Efficiency over 10%.* Journal of the American Chemical Society, 2014. **136**(46): p. 16411-16419.
185. You, J., et al., *Moisture assisted perovskite film growth for high performance solar cells.* Applied Physics Letters, 2014. **105**(18): p. 183902.
186. Luxel. *Radak furnace*. Available from: http://luxel.com/products/thermal-evaporation-equipment/radak-and-oled-furnaces/.
187. LaMer, V.K. and R.H. Dinegar, *Theory, Production and Mechanism of Formation of Monodispersed Hydrosols.* Journal of the American Chemical Society, 1950. **72**(11): p. 4847-4854.
188. Baronov, A., et al., *A simple model of burst nucleation.* Physical Chemistry Chemical Physics, 2015. **17**(32): p. 20846-20852.

189. Voorhees, P.W., *The Theory of Ostwald Ripening.* Journal of Statistical Physics, 1984. **38**.
190. Wikipedia. *Ostwald Ripening*. Available from: https://en.wikipedia.org/wiki/Ostwald_ripening.
191. Ono, L.K., et al., *Organometal halide perovskite thin films and solar cells by vapor deposition.* Journal of Materials Chemistry A, 2016. **4**(18): p. 6693-6713.
192. Dysol. *MAI*. Available from: http://www.dyesol.com/products/dsc-materials/perovskite-precursors/methylammonium-iodide.html.
193. Zhou, Q., et al., *Enhancing performance and uniformity of CH3NH3PbI3−xClx perovskite solar cells by air-heated-oven assisted annealing under various humidities.* Scientific Reports, 2016. **6**: p. 21257.
194. Evangelos Vitoratos, S.S., Nikolaos Paliatsas, Konstantinos Emmanouil, Stelios A. Choulis, *Conductivity Degradation Study of PEDOT: PSS Films under Heat Treatment in Helium and Atmospheric Air.* Chemistry & Materials Science, 2012. **2**(1).
195. Vitoratos, E., et al., *Thermal degradation mechanisms of PEDOT:PSS.* Organic Electronics, 2009. **10**(1): p. 61-66.
196. Conings, B., et al., *Perovskite-Based Hybrid Solar Cells Exceeding 10% Efficiency with High Reproducibility Using a Thin Film Sandwich Approach.* Advanced Materials, 2014. **26**(13): p. 2041-2046.
197. Snaith, H.J., et al., *Anomalous Hysteresis in Perovskite Solar Cells.* The Journal of Physical Chemistry Letters, 2014. **5**(9): p. 1511-1515.
198. Tress, W., et al., *Understanding the rate-dependent J-V hysteresis, slow time component, and aging in CH3NH3PbI3 perovskite solar cells: the role of a compensated electric field.* Energy & Environmental Science, 2015. **8**(3): p. 995-1004.
199. Christians, J.A., J.S. Manser, and P.V. Kamat, *Best Practices in Perovskite Solar Cell Efficiency Measurements. Avoiding the Error of Making Bad Cells Look Good.* The Journal of Physical Chemistry Letters, 2015. **6**(5): p. 852-857.
200. Heo, J.H., et al., *Hysteresis-less inverted CH3NH3PbI3 planar perovskite hybrid solar cells with 18.1% power conversion efficiency*. Energy & Environmental Science, 2015. **8**(5): p. 1602-1608.
201. Kim, H.-S. and N.-G. Park, *Parameters Affecting I–V Hysteresis of CH3NH3PbI3 Perovskite Solar Cells: Effects of Perovskite Crystal Size and Mesoporous TiO2 Layer.* The Journal of Physical Chemistry Letters, 2014. **5**(17): p. 2927-2934.
202. Tao, C., et al., *17.6% stabilized efficiency in low-temperature processed planar perovskite solar cells.* Energy & Environmental Science, 2015. **8**(8): p. 2365-2370.
203. Ip, A.H., et al., *A two-step route to planar perovskite cells exhibiting reduced hysteresis.* Applied Physics Letters, 2015. **106**(14): p. 143902.
204. Wojciechowski, K., et al., *C60 as an Efficient n-Type Compact Layer in Perovskite Solar Cells.* The Journal of Physical Chemistry Letters, 2015. **6**(12): p. 2399-2405.
205. Richardson, G., et al., *Can slow-moving ions explain hysteresis in the current-voltage curves of perovskite solar cells?* Energy & Environmental Science, 2016. **9**(4): p. 1476-1485.
206. Cao, X., et al., *Modulating Hysteresis of Perovskite Solar Cells by a Poling Voltage.* The Journal of Physical Chemistry C, 2016. **120**(40): p. 22784-22792.
207. Almora, O., et al., *Noncapacitive Hysteresis in Perovskite Solar Cells at Room Temperature.* ACS Energy Letters, 2016. **1**(1): p. 209-215.
208. Chen, B., et al., *Origin of J–V Hysteresis in Perovskite Solar Cells.* The Journal of Physical Chemistry Letters, 2016. **7**(5): p. 905-917.

209. Momblona, C., et al., *Efficient vacuum deposited p-i-n and n-i-p perovskite solar cells employing doped charge transport layers.* Energy & Environmental Science, 2016. **9**(11): p. 3456-3463.
210. Kim, J., et al., *Stable and null current hysteresis perovskite solar cells based nitrogen doped graphene oxide nanoribbons hole transport layer.* Scientific Reports, 2016. **6**: p. 27773.
211. Wu, C.-G., et al., *High efficiency stable inverted perovskite solar cells without current hysteresis.* Energy & Environmental Science, 2015. **8**(9): p. 2725-2733.
212. Zhao, Y., et al., *Anomalously large interface charge in polarity-switchable photovoltaic devices: an indication of mobile ions in organic-inorganic halide perovskites.* Energy & Environmental Science, 2015. **8**(4): p. 1256-1260.
213. Xiao, Z., et al., *Giant switchable photovoltaic effect in organometal trihalide perovskite devices.* Nat Mater, 2015. **14**(2): p. 193-198.
214. Leijtens, T., et al., *Mapping Electric Field-Induced Switchable Poling and Structural Degradation in Hybrid Lead Halide Perovskite Thin Films.* Advanced Energy Materials, 2015. **5**(20): p. 1500962-n/a.
215. Deng, Y., Z. Xiao, and J. Huang, *Light-Induced Self-Poling Effect on Organometal Trihalide Perovskite Solar Cells for Increased Device Efficiency and Stability.* Advanced Energy Materials, 2015. **5**(20): p. 1500721-n/a.
216. Joshi, P., et al. *Physics of instability of perovskite solar cells*. in *2016 IEEE 43rd Photovoltaic Specialists Conference (PVSC)*. 2016.
217. Mizusaki, J., K. Arai, and K. Fueki, *Ionic conduction of the perovskite-type halides.* Solid State Ionics, 1983. **11**(3): p. 203-211.
218. Narayan, R.L. and S.V. Suryanarayana, *Transport properties of the perovskite-type halides.* Materials Letters, 1991. **11**(8–9): p. 305-308.
219. Kuku, T.A., *Ionic transport and galvanic cell discharge characteristics of CuPbI3 thin films.* Thin Solid Films, 1998. **325**(1–2): p. 246-250.
220. Azpiroz, J.M., et al., *Defect migration in methylammonium lead iodide and its role in perovskite solar cell operation.* Energy & Environmental Science, 2015. **8**(7): p. 2118-2127.
221. Meloni, S., et al., *Ionic polarization-induced current–voltage hysteresis in CH3NH3PbX3 perovskite solar cells.* Nature Communications, 2016. **7**: p. 10334.
222. Haruyama, J., et al., *First-Principles Study of Ion Diffusion in Perovskite Solar Cell Sensitizers.* Journal of the American Chemical Society, 2015. **137**(32): p. 10048-10051.
223. Eames, C., et al., *Ionic transport in hybrid lead iodide perovskite solar cells.* Nature Communications, 2015. **6**: p. 7497.
224. Walsh, A., et al., *Self-Regulation Mechanism for Charged Point Defects in Hybrid Halide Perovskites.* Angewandte Chemie International Edition, 2015. **54**(6): p. 1791-1794.
225. Yuan, Y., et al., *Photovoltaic Switching Mechanism in Lateral Structure Hybrid Perovskite Solar Cells.* Advanced Energy Materials, 2015. **5**(15): p. 1500615-n/a.
226. Yuan, Y. and J. Huang, *Ion Migration in Organometal Trihalide Perovskite and Its Impact on Photovoltaic Efficiency and Stability.* Accounts of Chemical Research, 2016. **49**(2): p. 286-293.
227. Wang, H.-H., et al., *Improving the TiO2 electron transport layer in perovskite solar cells using acetylacetonate-based additives.* Journal of Materials Chemistry A, 2015. **3**(17): p. 9108-9115.
228. Aldrich, S.

229. Bi, C., et al., *Non-wetting surface-driven high-aspect-ratio crystalline grain growth for efficient hybrid perovskite solar cells.* Nature Communications, 2015. **6**: p. 7747.
230. Wang, Q., C. Bi, and J. Huang, *Doped hole transport layer for efficiency enhancement in planar heterojunction organolead trihalide perovskite solar cells.* Nano Energy, 2015. **15**: p. 275-280.
231. Seo, J., J.H. Noh, and S.I. Seok, *Rational Strategies for Efficient Perovskite Solar Cells.* Accounts of Chemical Research, 2016. **49**(3): p. 562-572.
232. Elschner, A., et al., *PEDOT: Principles and Applications of an Intrinsically Conductive Polymer*. 2010: CRC Press.
233. Borriello, I., G. Cantele, and D. Ninno, *\textit{Ab initio} investigation of hybrid organic-inorganic perovskites based on tin halides.* Physical Review B, 2008. **77**(23): p. 235214.
234. Zhumekenov, A.A., et al., *Formamidinium Lead Halide Perovskite Crystals with Unprecedented Long Carrier Dynamics and Diffusion Length.* ACS Energy Letters, 2016. **1**(1): p. 32-37.
235. Han, Q., et al., *Single Crystal Formamidinium Lead Iodide (FAPbI3): Insight into the Structural, Optical, and Electrical Properties.* Advanced Materials, 2016. **28**(11): p. 2253-2258.
236. Aldrich, S. *Poly(methyl methacrylate)*. Available from: http://www.sigmaaldrich.com/catalog/product/aldrich/445746?lang=en&region=US.
237. El-Mellouhi, F., et al., *Enhancing Intrinsic Stability of Hybrid Perovskite Solar Cell by Strong, yet Balanced, Electronic Coupling.* Scientific Reports, 2016. **6**: p. 30305.
238. Aguiar, J.A., et al., *In situ investigation of the formation and metastability of formamidinium lead tri-iodide perovskite solar cells.* Energy & Environmental Science, 2016. **9**(7): p. 2372-2382.
239. Bag, M., et al., *Kinetics of Ion Transport in Perovskite Active Layers and Its Implications for Active Layer Stability*. Journal of the American Chemical Society, 2015. **137**(40): p. 13130-13137.